

**DEVELOPMENT OF MULTI-PHASE CORE THERMAL
HYDRAULIC MODELS FOR FUEL MELTING DURING
SEVERE ACCIDENTS**

By
ANUJ DUBEY
ENGG02201405005

Indira Gandhi Centre for Atomic Research, Kalpakkam

A thesis submitted to the
Board of Studies in Engineering Sciences
In partial fulfillment of requirements
for the Degree of
DOCTOR OF PHILOSOPHY
of
HOMI BHABHA NATIONAL INSTITUTE



March, 2021

Homi Bhabha National Institute¹

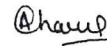
Recommendations of the Viva Voce Committee

As members of the Viva Voce Committee, we certify that we have read the dissertation prepared by Shri Anuj Dubey entitled “Development of multi-phase core thermal hydraulic models for fuel melting during severe accidents” and recommend that it may be accepted as fulfilling the thesis requirement for the award of Degree of Doctor of Philosophy.

Chairman – Dr. S. Murugan



Guide / Convener – Dr. Anil Kumar Sharma

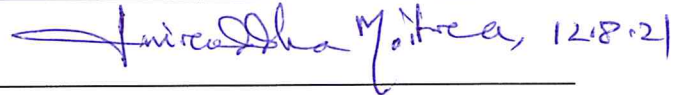


Co-guide -

Examiner -



Member 1- Dr. Aniruddha Moitra



Member 2- Dr. K. Devan



Member 3- Dr. T. Sundararajan



Final approval and acceptance of this thesis is contingent upon the candidate's submission of the final copies of the thesis to HBNI.

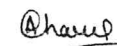
I/We hereby certify that I/we have read this thesis prepared under my/our direction and recommend that it may be accepted as fulfilling the thesis requirement.

Date: 12-08-2021

Place: KALPAKKAM

Signature

Co-guide (if any)



Signature

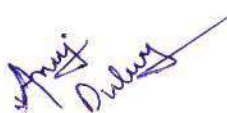
Guide

¹ This page is to be included only for final submission after successful completion of viva voce.

STATEMENT BY AUTHOR

This dissertation has been submitted in partial fulfilment of requirements for an advanced degree at Homi Bhabha National Institute (HBNI) and is deposited in the Library to be made available to borrowers under rules of the HBNI.

Brief quotations from this dissertation are allowable without special permission, provided that accurate acknowledgement of source is made. Requests for permission for extended quotation from or reproduction of this manuscript in whole or in part may be granted by the Competent Authority of HBNI when in his or her judgment the proposed use of the material is in the interests of scholarship. In all other instances, however, permission must be obtained from the author.



Anuj Dubey

DECLARATION

I hereby declare that the investigation presented in the thesis has been carried out by me. The work is original and has not been submitted earlier as a whole or in part for a degree / diploma at this or any other Institution / University.


Anuj Dubey

List of publications arising from the thesis

Journal

1. “Reactor Dynamics of In-pin Fuel Motion in Fast Breeder Reactors”, Dubey A., Sathiyasheela T., Sharma A. K., *Nuclear Engineering and Design*, **2018**, 340, 431-446.
(Doi: <https://doi.org/10.1016/j.nucengdes.2018.10.010>)
2. “In-pin fuel motion dynamics for beginning of life core in fast breeder reactors”, Dubey A., Sathiyasheela T., Sharma A. K., *Nuclear Engineering and Design*, **2019**, 347, 31-44.
(Doi: <https://doi.org/10.1016/j.nucengdes.2019.03.014>)
3. “Modelling, verifications and safety feedback assessment of annular fast reactor fuel pins with severe accident code MITRA”, Dubey, A., Sharma, A. K., *Nuclear Engineering and Design*, **2020**, 364, 110684.
(Doi: <https://doi.org/10.1016/j.nucengdes.2020.110684>)
4. “Investigation of alternative annular fuel pin designs for mitigation of the unprotected transient overpower accident”, Dubey, A., Sharma, A. K. (Under communication to *Annals of Nuclear Energy*)

Chapters in books and lectures notes

1. “Reactivity Effects of In-Pin Fuel Motion in Modern Fast Breeder Reactors”. Dubey, A., Sathiyasheela, T., Sharma, A. K., *Advances in Interdisciplinary Engineering*, **2019**, Lecture Notes in Mechanical Engineering. Springer, Singapore.
(Doi: https://doi.org/10.1007/978-981-13-6577-5_6)

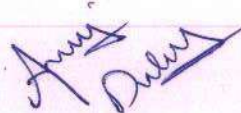
Conferences

1. “Reactor Dynamics Analyses of Fuel Melting in Fast Reactors under UTOPA”, Dubey A., Sathiyasheela T., Sharma A. K., *Proceedings of the 7th International and 45th National Conference on Fluid Mechanics and Fluid Power (FMFP)*, IIT Bombay, Mumbai, India (December 10–12, **2018**).
2. “Modelling and Verifications of Fast Reactor Fuel Melting and Multi-phase Flow Code MITRA”, Dubey A., Sathiyasheela T., Sharma A. K., *Proceedings of the 25th National and 3rd International Heat and Mass Transfer Conference (IHMTTC)*, IIT Roorkee, India (December 28–31, **2019**).

3. Dubey A., Sathiyasheela T., Sharma A. K. “Bheeshan durghatna mein parmaanu indhan ke galan evam fission gas ke risaav ka bhautikeeya adhyayan”, Urja ke kshetra mein bhaarteeya vigyaan evam takneeke pragati, *Akhil Bharatiya Hindi Vaigyanik Sangoshthi*, Kalpakkam, India (January 9–10, 2020).

Others

1. “Comparisons of Reactivity Feedbacks Under UTOPA in Fast Reactors”, Sathiyasheela T., John R., Dubey A., Srinivasan G. S., Devan K. (Under communication to Nuclear Engineering and Design)
2. Sathiyasheela T., Dubey A., Srinivasan G. S., Devan K. “UTOPA Studies of BOL Core with in-pin Fuel Motion”, FBR 1 & 2 / IGCAR/30920/DN/1004/Revision A, March 2020.
3. Sathiyasheela T., Dubey A., Srinivasan G. S., Devan K. “UTOPA Studies of FBR 1 & 2 BOL Core with in-pin Fuel Motion”, SAS-294/Revision A, March 2020.
4. Sathiyasheela T., Dubey A., Srinivasan G. S., Devan K. “Comparisons of Feedback under UTOPA in FBR 1 & 2”, SAS-297/Revision A, June 2020.


Anuj Dubey

असतो मा सद्गमय ।
तमसो मा ज्योतिर्गमय ।
मृत्योर्मा अमृतं गमय ।

बृहदारण्यक उपनिषद् १.३.२८

*“From untruth lead us to Truth.
From darkness lead us to Light.
From death lead us to Immortality.”*

Brihadaranyaka Upanishad 1.3.28

Acknowledgements

It is my delight to thank my teachers, family members, and friends, without whom this work would not have been possible.

I express my deepest gratitude towards my supervisor, Prof. Anil Kumar Sharma. I consider myself fortunate to have received such an admirable guide, who has also been a major source of inspiration for me from the beginning. He taught me the art of writing research articles and motivated me to work in a disciplined, time-bound manner. He permitted me to freely tackle research problems without losing sight of the practical aspects of the program. I owe my success to him.

It would not have been possible for me to tackle the dynamically coupled nature of the research topic without receiving tremendous technical support from Smt. T. Sathiyasheela. I pay my sincere gratitude to her for allowing me to work freely in an inter-disciplinary environment.

I consider myself fortunate to have worked under the most distinguished professors in my Doctoral Committee. I thank Prof. S. Murugan, Committee Chairman, for his suggestions and encouragement. I would also like to express my gratitude towards Prof. K. Devan, Head, Reactor Neutronics Division, for his support in administrative matters as well as his technical suggestions. His guidance allowed me to overcome some difficult moments, for which I am deeply indebted to him. I thank Prof. A. K. Moitra and Prof. T. Sundararajan of the Department of Mechanical Engineering, IIT Madras, for their encouragement and oversight. I would also like to thank Sri. P. Puthiyavinayagam, Director (Ex), Reactor Design Group, for being a source of great inspiration for me from the beginning.

I thank Jaisankar Sir and my friends Parth, Niraj and Bala Sundaram, who helped me several times out of the goodness of their hearts. I mention my close friends Arpita, Alaka, Fayaz, Ijee, Jayanthi, Ronit, Shradha, Shubhra, Surojit, and Teena, who made my stay in IGCAR joyful. Finally, I thank my kind mother, Mrs. Uma Dubey, my gracious sister, Ms. Garima Dubey and my loving father, Mr. Girish Chandra Dubey, for providing unwavering support during the difficult phases of this work.

Anuj Dubey

Contents

List of publications arising from the thesis	ix
Acknowledgements	xiii
Contents	xv
Summary.....	xxi
List of figures.....	xxiii
List of tables	xxxix
Nomenclature	xxxv
Chapter 1 Introduction	1
1.1 Overview of sodium cooled fast reactors	1
1.2 Beyond design basis events in SFR systems	7
1.3 Inherent safety features of SFR	8
1.4 Role of fuel squirting in SFR safety	13
1.5 Specialized test reactors	15
1.5.1 TREAT reactor	15
1.5.2 EBR-II reactor	15
1.5.3 CABRI reactor	15
1.6 Major challenges in modelling molten fuel relocation	18
1.7 Literature review	19
1.7.1 Experimental studies	20
1.7.2 Computational tools.....	25
1.7.2.1 Available mathematical models.....	25
1.7.2.2 Tools for fuel squirting.....	27
1.7.2.3 Tools for in-pin fuel motion	28
1.7.3 Reactor safety studies	30
1.7.4 Summary and gap areas.....	32
1.8 Major challenges and motivation	36
1.9 Aim of the present work: outline of the thesis.....	37
1.10 Closure	41

Chapter 2 Computational Methodology	43
2.1 System specifications	43
2.1.1 Brief outline of reactor core	43
2.1.2 Fuel subassembly and pin parameters	46
2.2 Computational terminologies.....	49
(i) Melting point	49
(ii) Melt interface radius.....	49
(iii) Solidus radius	49
(iv) Melt mass fraction.....	50
(v) Reactor over-power.....	50
(vi) Fuel density.....	50
2.3 Reactor neutronics methodology	51
2.3.1 Necessary perturbation worth data.....	51
2.3.2 PREDIS: pre-disassembly phase analysis code system	54
2.3.3 UTOP specification (single pin models).....	57
2.3.4 Molten fuel relocation feedback	58
2.4 Experimental benchmark data	59
2.4.1 E9 test.....	59
2.4.2 E9bis test.....	62
2.5 Salient working description of MITRA code	64
2.6 Closure	67

Chapter 3 Development of an Advanced Multi-phase Thermal Hydraulic Model and Investigation of Melt Relocation in Fast Reactors	68
---------------------------------------------------------------------------------------------------------------------------------------------	-----------

3.1 Mathematical modelling of the problem.....	69
3.1.1 The physical problem	69
3.1.2 Phase-change heat transfer	70
3.1.3 Multi-phase flow	74
3.1.4 Dimensional analysis and flow regimes	76
3.1.5 Molten fuel thermal expansion	78
3.1.6 Crust solidification model	79
3.1.7 Particle viscosity model	82

3.1.8	Escape of fission gases towards plena	83
3.1.9	Closure laws.....	86
3.1.10	Governing equations of the advanced multiphase flow model	88
3.1.11	Fuel-clad gap conductance model	91
3.2	Salient features of the numerical algorithm	92
3.2.1	Discretization and stability criteria.....	92
3.2.2	Mass conservation residual and flux corrections.....	94
3.2.3	Calculation procedure	96
3.3	Results and discussion	98
3.3.1	Grid independence analysis	98
3.3.2	Optimization of the free volume gas escape model.....	101
3.3.3	Experimental validation (CABRI-E9bis test)	103
3.3.4	Melt motion predictions under fast reactor conditions.....	107
3.3.4.1	Results for case study I.....	109
3.3.4.2	Results for case study II	111
3.3.5	Investigation of fuel mass relocation.....	113
3.4	Closure.....	119

Chapter 4 Reactor Dynamics Investigation of In-pin Fuel Motion during Unprotected

Transient Overpower Accidents.....		121
4.1	Numerical modelling.....	122
4.1.1	Model system	122
4.1.2	Problem description and assumptions	123
4.1.3	In-pin fuel motion solver	125
4.1.4	Neutronic/Hydrodynamic coupling algorithm.....	127
4.1.4.1	Selection of a suitable data-transfer period.....	129
4.1.5	Computational procedure	131
4.2	Results and discussion	132
4.2.1	Whole-core simulation of UTOP (without melt relocation feedback)	134
4.2.2	Whole core simulation of UTOP (best estimate case studies).....	135
4.2.2.1	Results for Case I.....	135
4.2.2.2	Results for Case II.....	137
4.2.2.3	Reactor dynamics of in-pin fuel motion (Cases I & II)	139

4.2.3	Whole core simulation of UTOP (conservative case studies)	141
4.2.3.1	Results for Case III	141
4.2.3.2	Results for Case IV	142
4.2.3.3	Reactor dynamics of in-pin fuel motion (Cases III & IV)	144
4.2.4	Impact of in-pin fuel motion on accident outcome	146
4.2.5	Thermodynamic assessment of molten fuel vaporisation	148
4.2.6	Effect of reactor parameters	151
4.2.6.1	Effect of core burnup	151
4.2.6.2	Effect of reactivity insertion rate	152
4.3	Closure	154

Chapter 5 Development of a Fission Gas Release Solver and Investigation of Melt Relocation in Alternative Axial Blanket Designs 157

5.1	Modelling of fission gas pressurization force	158
5.1.1	Mathematical and numerical modelling	158
5.1.1.1	Underlying physical mechanisms	158
5.1.1.2	Intra-granular fission gas release	159
5.1.1.3	Inter-granular fission gas release	161
5.1.1.4	Transient fission gas release	162
5.1.1.5	Development of a fission gas release solver (FGR)	164
5.1.1.6	Outline of MITRA algorithm	166
5.1.2	Results and discussion	168
5.1.2.1	Model validation and inter-code verifications	168
5.1.2.2	Transient fission gas release during UTOP	176
5.1.2.3	Effect of fission gas pressurization on melt hydrodynamics and relocation	180
5.1.2.4	Effect on whole-core melt propagation	187
5.2	Modelling of melt motion in alternative geometrical designs	189
5.2.1	Mathematical and numerical modelling	189
5.2.1.1	Problem definition and assumptions	190
5.2.1.2	Governing equations and boundary conditions	192
5.2.1.3	Incorporation of a bulk freezing model	193
5.2.1.4	Grid modifications	194
5.2.2	Results and Discussion	195

5.2.2.1	Validation of bulk freezing model	195
5.2.2.2	Effect of completely annular blanket column	196
5.2.2.3	Effectiveness of partially annular top and bottom blanket columns	199
5.3	Closure	203
Chapter 6 Concluding Remarks and Future Work.....		206
6.1	Conclusions.....	206
6.2	Scope for future work.....	209
Appendix A: Thermo-physical properties		210
Appendix B: Discretized equations		214
Appendix C: User instruction manual		219
Bibliography		227

Summary

The main objective of the work presented in this thesis is to simulate the melting and relocation of annular, mixed oxide ((U-Pu)-O₂) nuclear fuel during unprotected transient overpower accidents in sodium-cooled fast reactors (SFR). The study emphasizes on a physically consistent resolution of the underlying fluid dynamics, and on the dynamic coupling between melt relocation and reactor neutronics. As a first step, a multi-phase core thermal hydraulic model is developed with advanced features that can capture the rate of fuel melting as well as the interaction between the hydrodynamic effects of gravity, pressure, melt freezing, surface tension, liquid thermal expansion, and inter-phase momentum exchange. The complete set of governing equations are solved with an explicit finite difference method, and the resultant numerical algorithm is employed towards the simulation of the CABRI-E9bis (in-pile) transient overpower test. The simulation results are compared with experimental findings, and the agreement is found to be excellent. As a second illustration, the model is extended towards typical fast reactor conditions to predict the practically relevant fluid flow and relocation behaviour. It is found that there is a net relocation of molten fuel from high neutron density region (core-mid plane) to relatively low neutron density region (top and bottom of fissile column), which averts an undesirable increase in fuel mass near the core mid-plane. Therefore, the relocation is found to be advantageous towards the inherent safety of fast reactors.

To investigate the propagation of fuel melting throughout the reactor core and to determine its impact on SFR safety, a dynamic (neutronic/hydrodynamic) coupling algorithm is developed with the help of in-house reactor dynamics code, PREDIS. An optimization of the developed algorithm is carried out to minimize the computational costs. Subsequently, whole core simulations of unprotected transient overpower accidents (UTOP) in both equilibrium and beginning-of-life (BOL) core conditions are carried out with best and conservative estimates of the external reactivity insertion. Estimates of the propagation of melting inside the SFR core, the resultant relocation feedback, major

controlling parameters, and the impact on the accident scenario are presented. A comparison of the results with de-coupled, equivalent UTOP simulations reveals the impact on the safety margin of SFR. A thermodynamic assessment of molten fuel is also carried out to address the possibility of fuel vaporisation at high temperatures during UTOP.

For a physically consistent representation of the microstructural gas release processes involved in the pressurization of molten fuel, a dedicated fission gas release solver (FGR) is subsequently developed and coupled with the multi-phase flow model. Extensive validation of the resultant algorithm (MITRA) is carried out against the results of steady-state experiments, FEAST-OXIDE code and the CABRI-2 transient overpower tests. The algorithm is subsequently utilized to investigate the realistic impact of fission gas pressurization on melt motion. Results show that regardless of the burnup level, the fission gas release-induced pressurization force is unable to influence the melt motion significantly, and the agglomerated melt column remains constrained by the effects of solidification. Effects of the modelling improvements on the accident outcome are examined through a consolidated, whole-core, conservative simulation of UTOP.

To investigate the possibility of a highly advantageous fuel relocation out of the active core through suitable design modifications, a bulk freezing model is incorporated with the modelling framework. The algorithm is subsequently employed towards the simulation of melt motion in alternative fuel pin geometries consisting of completely annular and partially annular axial blanket columns. It is found that the melt relocates out of the active core once a threshold amount of melting is breached, and the amount of fuel relocated out of the active core is a function of the melt mass fraction. The provision of a minimal number of annular blanket pellets (~ 5–15) situated next to the annular fuel pellets can be an effective and optimal choice for obtaining the highly advantageous fuel relocation out of the active core. The study has highlighted the utility of annular axial blanket designs as one of the viable means for enhancing the safety margins of current and future fast reactors.

List of figures

Figure	Title	Page
Figure 1.1:	Schematic layout of a liquid sodium cooled, pool-type fast reactor.	2
Figure 1.2:	Typical SFR fuel subassembly and fuel pin.	4
Figure 1.3:	Schematic diagram of a typical CSR subassembly (PFBR [19]).	6
Figure 1.4:	View of the CABRI reactor from above. Major components are: 1: Experimental test loop, 2: Hodoscope channel, 3: Control rods, 4: Transient rods, 5: Driver fuel subassemblies. [42]	16
Figure 1.5:	Schematic layout of CABRI reactor core.	17
Figure 2.1:	Configuration of FBR-500 core at beginning of equilibrium cycle [15].	44
Figure 2.2:	Schematic diagram of FBR-500 fuel subassembly and fuel pin [52,83]	47
Figure 2.3:	Axial profile of fuel void worth [89].	52
Figure 2.4:	Single CSR withdrawal worth data utilized in UTOP simulations. (a) Differential worth profile (b) Integral worth profile [91]	54
Figure 2.5:	Schematic diagram of 2-D (r-z) grid utilized in PREDIS for FBR-500 computations [30].	55
Figure 2.6:	Power trace and flow rate conditions for the CABRI-E9bis test [33]	63
Figure 2.7:	Salient working description of MITRA code.	65
Figure 3.1:	General schematic of the problem domain.	70
Figure 3.2:	Schematic diagram of in-pin fuel motion in annular mixed oxide fuel pins during UTOP.	75
Figure 3.3:	Nodes of the multi-phase flow spatial mesh (Velocity locations are staggered; Area of flow is variable)	93
Figure 3.4:	Model domain discretization	100

Figure 3.5: Molten fuel volume fraction as a function of axial position, melt mass fraction and rate of gas escape through the plenum. (a) $c = -2.0$, and (b) $c = -0.1$.	102
Figure 3.6: CABRI-E9bis melt interface profile (R_{int}/R_o ; end of transient).	104
Figure 3.7: Melting and solidification history for E9bis test.	105
Figure 3.8: E9bis thermal and molten fuel flow schematic (Elevation is with reference to BFC)	106
Figure 3.9: Melt motion in equilibrium fuel under SFR conditions: (a) Thermal map of the fuel column (b) Axial distribution of melt mass (plot is applicable for a single pin of the central subassembly; total fuel mass in one FBR-500 pin is 0.225 kg)	110
Figure 3.10: Melt motion in fresh fuel under fast reactor conditions: (a) Thermal map of the fuel column for Zone-1 fuel pin (b) Axial distribution of melt mass (single pin).	112
Figure 3.11: The temperature of molten fuel ($T_{f,l}$) as a function of axial position and melt mass fraction. Plots are specific to Case-II. In locations with absence of molten fuel, the plot shows the pellet inner surface temperature ($T_{f,wall}$).	113
Figure 3.12: A summary of melt relocation in annular fast reactor fuel pins under UTOP transient. Total fuel mass for a single fuel pin is 0.225 kg (7.5, 15 ... 30 % are melt mass fractions).	114
Figure 3.13: Fuel mass relocation in annular fast reactor pins subjected to UTOP. (a) 7.5 % melt mass, (b) 15 % melt mass, (c) 22.5 % melt mass and (d) 30 % melt mass. (Total fuel mass in central subassembly = 48.8 kg)	116
Figure 3.14: Melt relocation safety feedback characteristics.	118
Figure 4.1: Flow-chart of in-pin fuel motion solver	126
Figure 4.2: Flow-chart of the inter-disciplinary computational algorithm (Each zone represents single phase-change and fluid flow solver)	128

Figure 4.3: Reactor power history during UTOP without the consideration of melt relocation feedback.	135
Figure 4.4: Whole core melting and in-pin fuel motion for Case I (Equilibrium core condition; Best estimate; stabilized state; $t = 750 s$)	136
Figure 4.5: Temperature histories for Case-I (Zone-1 fuel pin; best estimate)	137
Figure 4.6: Whole core melting and in-pin fuel motion for Case II (BOL core condition; Best estimate; stabilized state; $t = 750 s$)	138
Figure 4.7: Temperature histories for Case-II (BOL core, Zone-I, best estimate)	139
Figure 4.8: Transient behaviour of reactor during UTOP (Cases I & II; best estimate): (a) Net reactivity vs. time, (b) Reactor power vs. time	140
Figure 4.9: Reactor dynamics response of fast reactor under best estimate case study of UTOP: (a) Case I (Equilibrium condition) and (b) Case II (BOL condition)	140
Figure 4.10: Schematic of in-pin fuel motion in fast breeder reactor for Case III (Conservative, equilibrium core simulation; I, II...IV represent fuel zones; Filled region inside fuel cavity indicates presence of molten fuel column)	142
Figure 4.11: Temperature histories for Case-III (Equilibrium core, Zone-I, conservative estimate)	142
Figure 4.12: Schematic of in-pin fuel motion in fast breeder reactor for Case IV (Conservative, BOL core simulation; I, II...IV represent fuel zones; Filled region inside fuel cavity indicates presence of molten fuel column; $t = 750 s$)	143
Figure 4.13: Temperature time history of Zone-I fuel pin for BOL core under the conservative estimate (Case-IV)	144
Figure 4.14: Transient behaviour of a 500 MWe fast reactor during UTOP (conservative analysis): (a) Net reactivity vs. time and (b) Reactor power vs. time.	145

Figure 4.15: Reactor dynamics plots for conservative simulations of UTOP: (a) Case-III (Equilibrium core) and (b) Case-IV (BOL core).	145
Figure 4.16: P-H data plots for molten fuel (Saturation vapour curve of molten fuel marks the boundary between liquid and vapour phases; P-H data is specific to Zone-1)	149
Figure 4.17: Comparison between BOL (best estimate) and equilibrium (conservative) cases (external reactivity insertion is approximately equal for both cases)	151
Figure 4.18: Reactivity insertion rate study: (a) Power history, (b) Reactivity history.	153
Figure 5.1: A brief outline of the developed code.	167
Figure 5.2: Results of verifications against UO ₂ sample irradiation tests. Fission gas release curves of FGR are compared with FEAST-OXIDE curves along with experimental data [126,130].	170
Figure 5.3: Power profile for the FBTR MOX fuel irradiation test	171
Figure 5.4: State of gas retention in FBTR MOX test pin. (a) Distribution of retained gases within the fuel pellet stack. (b) Retention of fission gases along the radius of the fuel pellet at the location of peak power. (dark regions signify minimum quantity of retained gas.)	172
Figure 5.5: Comparison of E9 test data with gas release obtained from MITRA simulation [33].	174
Figure 5.6: Comparison of E9 test data with melt profile obtained from MITRA simulation	175
Figure 5.7: E9bis test: (a) Melt column time history (b) Melt mass as a function of time (upper and lower limits specify the respective extents of the melt column; $z = 0.75\ m$ signifies top of fuel column, $z = 0\ m$ signifies bottom of fuel column)	176
Figure 5.8: Gas retention coefficient, F_g , as a function of the dimensionless pellet radius (R/R_o) and fuel burnup level. (peak power location)	178

Figure 5.9: The release of fission gases due to melting as a function of transient time and peak fuel burnup.	179
Figure 5.10: Evolution of the melt column as a function of the melt mass fraction and peak fuel burnup. Melt occupies the region between the top and bottom curves. (Core mid-plane is located at $z = 0.5 \text{ m}$)	184
Figure 5.11: Pellet inner surface temperature ($T_{w,i}$) as a function of z and Bu_{max} . Each plot represents the temperature when melt mass = 5 %. The region occupied by melt is indicated by the flat profile (Elevation is with respect to z_b).	184
Figure 5.12: A generalized schematic of in-pin fuel motion in SFR conditions. (a) Thermal mapping of the fuel pellet stack during various stages of melting (0, 5, ... 35 % denote the melt mass fractions; pellet radius is exaggerated for clarity) (b) Axial variation of molten fuel mass (M_l) inside the cavity. (fuel mass = 0.225 kg/pin).	185
Figure 5.13: Melt relocation feedback as a function of fuel burnup and melt mass fraction (a) 0–3 atom percent (b) 4–7 atom percent (fuel mass removal worth analyses are constrained to central subassembly, $W_{max} = -41 \text{ pcm}$).	186
Figure 5.14: Thermal mapping of FBR core (equilibrium state) subjected to UTOP ($t = 750 \text{ s}$); Zone 1, 2, 3 and 5 undergo fuel melting. Maximum melting occurs in Zone 1 (central subassembly).	188
Figure 5.15: Reactor response a function of time (a) Reactor power history (b) Relocation feedback for zones (1-5). (Equilibrium core (previous) represents results where radial variation in gas retention is neglected; Equilibrium core (MITRA) represents results where the radial variation is incorporated)	188
Figure 5.16: Comparison between earlier and current UTOP simulations; (a) Core averaged melt fraction history (b) Whole core melt feedback history.	189

Figure 5.17: Problem domain	190
Figure 5.18: Comparison of the melt column evolution with the crust formation and bulk freezing models. Results are for E9bis test.	195
Figure 5.19: Sensitivity of melt relocation to geometric design variation (entry of fuel in annular top blanket occurs at melt fraction = 34.2 %).	197
Figure 5.20: In-pin fuel motion in case of annular upper blanket pellets. (a) Thermal mapping of the fuel and axial blanket columns during various stages of melting (0, 10, ... 40 % denote the melt mass fractions). (pellet radius is exaggerated for clarity) (b) Axial variation of melt mass inside a single fuel subassembly ($z_t = 1.3\text{ m}$).	197
Figure 5.21: Sensitivity of the melt relocation feedback to geometric variation.	198
Figure 5.22: Melt column evolution as a function of the top blanket geometry (Z_{bl} = length of top blanket cavity).	200
Figure 5.23: Fuel relocation in top blanket column as a function of top blanket geometrical design (melt mass is specific to central subassembly; total fuel mass is 48.8 kg).	201
Figure 5.24: Melt relocation feedback as a function of top blanket geometrical configuration and time.	201
Figure 5.25: Simulation results for partially annular bottom blanket case studies. (a) Melt column evolution. (b) Mass of fuel removed from the active core (melt mass is specific for the central subassembly).	202
Figure 6.1: Summary and highlights of the thesis.	208
Figure A1: Enthalpy versus temperature plot for mixed oxide fuel. In the mushy state, latent heat and sensible heat exchange occur simultaneously.	211
Figure C.1: An example input file ('pfbr27-bol.n1')	219
Figure C.2: Enthalpy-temperature data input files	220

Figure C.3: MITRA Run time output- steady state variables (Transient time = 0.0 s) 224

List of tables

Table No.	Title	Page
Table 2.1:	FBR-500 core parameters (dual data represents inner/outer core region values).	44
Table 2.2:	Relevant parameters of BOL and equilibrium cores (inner/outer core) [79,80].	45
Table 2.3:	Fuel subassembly grouping for FBR-500 (\dot{m}_{ct} = coolant mass flow rate in 1 subassembly) [15,80].	46
Table 2.4:	FBR-500 fuel specifications (I: inner core region; O: outer core region) [79,84,85].	48
Table 2.5:	Material void worth data for FBR-500 equilibrium core [82].	52
Table 2.6:	Zone-wise fuel void worth distribution ($\% W_f / \sum W_f$) [82,89].	53
Table 2.7:	UTOP parameters for single fuel pin study	57
Table 2.8:	Annular fuel specifications for CABRI-2 test series. (Gen: generation, ret retention) [33,34]	60
Table 2.9:	CABRI-2 annular fuel pin test conditions. (Transient undercooling and maximum power hold-up conditions are applicable only for E9bis) [33,34,72]	61
Table 3.1:	Grid independence study.	98
Table 3.2:	Grid size details (dimensions are for fast reactor case study)	99
Table 3.3:	Sensitivity of melt motion with respect to the rate of escape of fission gases towards plenum. The deviations (%) are with respect to the preceding data ($100(\rho_{f,curr} - \rho_{f,prev}) / \rho_{rel,prev}$).	103
Table 3.4:	Results of CABRI-E9bis [33] benchmarking study	107
Table 3.5:	Table of fuel mass redistribution due to melting and motion. Mass relocation is with reference to 217 fuel pins of the central subassembly. (t = time instant (s); X_{max} = Peak linear power (kW/m))	114

Table 4.1: Nuclide number density at beginning of equilibrium core ($\text{barn}^{-1} \text{cm}^{-1}$)	125
Table 4.2: Table of sensitivity of neutronic/hydrodynamic coupling algorithm towards the data-exchange period (Δt_{exc}). All the deviations are with respect to the first case.	130
Table 4.3: Table of severe accident case studies (B & C stand for best estimate and conservative respectively; banking depth is from TFC; withdrawal speed = 2 mm/s)	133
Table 4.4: Table of comparison of fast reactor dynamics with and without the inclusion of the in-pin fuel motion feedback (ρ_{rel}). Each value represents the maximum value of the variable. All reactivity values are in dollar (\$).	147
Table 4.5: Molten fuel P-H data (ΔH = excess enthalpy required for vaporization)	150
Table 4.6: Parametric analysis of reactivity insertion rate	152
Table 5.1: Verification data for fuel samples irradiated in FR-2 reactor	169
Table 5.2: Specifications of FBTR-MOX test pins [131].	171
Table 5.3: E9 validation results	173
Table 5.4: Response of annular MOX fuel pin under UTOP at various burnup levels ($FGR_{t=0}, FGR_{t=120}$ are the fission gas release before and after the transient; radial melt is at $t = 120$ s, $S_f, S_g, F_{g,avg}$ are at peak power location ($z = 0.75$ m))	177
Table 5.5: Melt motion as a function of the melt mass fraction and fuel burnup	181
Table 5.6: Geometrical parameters of the modified fuel pin.	191
Table 5.7: Grid size details for the alternative fuel pin geometry.	194
Table B.1: Definition of discretized multi-phase flow coefficients	218
Table C.1: MITRA input files (n=1: IRN; IRN = total number of fuel and blanket channels in the core).	219
Table C.2: MITRA input variables	222
Table C.3: MITRA subroutines and functions	225

Table C.4: Output files (n=1: IRN; IRN = total number of fuel and blanket channels in the core). 226

Nomenclature

<i>A</i>	Area, m ²
<i>b</i>	Constants used in fission gas thermal conductivity correlations
<i>Bu</i>	Fuel burnup, atom percent
<i>C</i>	Fission gas atom concentration (atoms·m ³), constants used in several expressions, specific heat
<i>d</i>	Characteristic diameter, m
<i>D</i>	Diffusion coefficient (m ² ·s ⁻¹), coefficients for heat diffusion equations, Diameter (m)
<i>dop</i>	Doppler broadening
<i>e</i>	Enthalpy of source mass, J·kg ⁻¹
<i>E</i>	Fraction of edge bubbles connected to free volume
<i>F</i>	Localized gas retention coefficient, Force (N·m ⁻¹), Fraction of face bubbles connected to the edge bubbles
<i>Fr</i>	Fission gas release fraction
<i>g</i>	Gravitational acceleration, m·s ⁻²
<i>G</i>	Smear density of molten fuel, kg·m ⁻³ , Coefficients for thermal conductivity of gas mixture
\dot{G}	Gas atom deposition rate to the grain boundary due to intra-granular bubble migration, atoms·m ⁻³ ·s ⁻¹
<i>Gen</i>	Fission gas generation
<i>h</i>	Heat transfer coefficient, W·m ² ·K ⁻¹
<i>H</i>	Enthalpy, J·kg ⁻¹
<i>K</i>	Conductivity (W·m ⁻¹ ·K ⁻¹), fission gas atom generation (atoms·m ⁻³ ·s ⁻¹), nucleation rate constant of bubbles (s ⁻¹)
<i>L</i>	Length of column (m), a reference to a particular axial grid number
\dot{m}	Mass flow rate, kg·s ⁻¹
<i>melt</i>	A reference to the initiation of melting
<i>M</i>	Mass, kg
<i>Mol</i>	Molecular mass, kg·mole ⁻¹
<i>n</i>	Gas moles

Nu	Nusselt number
o	Fraction of liquid in mushy fuel
p	Fuel porosity
P	Pressure ($\text{N}\cdot\text{m}^{-2}$), Peak linear power ($\text{kW}\cdot\text{m}^{-1}$)
q	Heat flux ($\text{W}\cdot\text{m}^{-2}$), constants used in fission gas thermal conductivity relations
\dot{Q}	Heat generation, $\text{W}\cdot\text{m}^{-3}$
r	Radial coordinate, m, bubble radius, m
R	Radius (m), a gas constant ($\text{J}\cdot\text{mole}^{-1}\cdot\text{K}^{-1}$)
Re	Reynold's number
Ret	Fission gas retention
S	A fluid mass source term ($\text{kg}\cdot\text{m}^{-1}\cdot\text{s}^{-1}$), an inter-granular bubble volume fraction
t	Time, s
T	Temperature, °C
V	Velocity ($\text{m}\cdot\text{s}^{-1}$), Volume (m^3)
W	Fuel mass removal worth, pcm
x	Stoichiometric deviation
X	Linear heat rating ($\text{W}\cdot\text{m}^{-1}$), Fraction of intra-granular gas atoms arriving at inter-granular face bubbles
y	PuO_2 mole fraction
Y	Yield fraction of noble gas atom from fission
z	Axial coordinate, m

Greek Symbols

α	Multi-phase fluid volume fraction, solid particle fraction, a thermal expansion coefficient
β	A delayed neutron fraction, pcm
ρ	Density ($\text{kg}\cdot\text{m}^{-3}$), feedback (pcm)
ϕ	Azimuthal coordinate
τ	Wall friction force, $\text{N}\cdot\text{m}^{-1}$

σ	Surface tension ($\text{N}\cdot\text{m}^{-1}$), Stefan-Boltzmann constant
μ	Dynamic viscosity ($\text{kg}\cdot\text{m}^{-1}\cdot\text{s}^{-1}$)
ω	A burnup-dependent parameter for the fuel thermal conductivity correlation

Subscripts

a	A reference to ambient or room temperature
ax	Fuel axial expansion feedback
b	A reference to the bottom-most location within the fuel column, intra-granular bubbles
BB	Bottom blanket
bs	A reference to the bottom-most axial grid number inside the multi-phase flow domain, which is not blocked by solidification
bu	Discontinuous phase bubble in multi-phase flow
cav	Pellet cavity
c	Clad, constants used in multiple equations and correlations
ci	Clad inner surface
co	Clad outer surface
ct	Coolant
D	Inter-phase drag-force
dop	Doppler feedback
e	Inter-granular edge bubble
eff	effective
exc	Data exchange
f	Fuel phase, inter-granular face bubble
FV	A reference to discretized coefficients of fuel momentum conservation
g	Gas phase (also referred as G), dissolved gas atoms
gap	Fuel-cladding gap
gb	Gas atoms in intra-granular gas bubbles
gr	Fuel grain
He	Helium
ht	Heat transfer domain

<i>i</i>	Fluid phase, a reference to the pellet inner radius
<i>i – j</i>	Liquid-gas interface
<i>in</i>	A reference to the coolant inlet temperature
<i>int</i>	Melt interface
<i>Kr</i>	Krypton
<i>l</i>	Liquid-state, a reference to the lower-most location within the bottom blanket
<i>liq</i>	Liquidus
<i>low</i>	Lower plenum (also LP)
<i>m</i>	A reference to the axial location of the core mid-plane
<i>max</i>	maximum
<i>n</i>	Nominal or steady-state
<i>N</i>	Number of radial nodes
<i>o</i>	Pellet outer surface
<i>p</i>	Solid particle
<i>pin</i>	Internal environment of pin
<i>r</i>	Relative between two fluid phases
<i>rel</i>	Melt relocation, gas atoms released to the free volume
<i>s</i>	Solid-state
<i>sat</i>	Saturation
<i>sol</i>	Solidus
<i>t</i>	A reference to the top-most location within the fuel column, total gas atoms within fuel grain
<i>top</i>	A reference to the top-most location within the upper plenum
<i>TB</i>	Top blanket
<i>ts</i>	A reference to the top-most axial grid number inside the multi-phase flow domain, which is not blocked by solidification
<i>tuc</i>	Transient undercooling
<i>u</i>	A reference to the upper-most location within the top blanket
<i>U</i>	Universal
<i>up</i>	Upper Plenum (also <i>UP</i>)

<i>vm</i>	Virtual mass
<i>VM</i>	A reference to the discretised coefficients of virtual mass terms
<i>w, i</i>	wall-fluid interface
<i>Xe</i>	Xenon

Abbreviations

BFC	Bottom of fissile column
BOL	Beginning of life
EBR	Experimental breeder reactor
EOL	End of life
EQL	Equilibrium
FBR	Fast Breeder Reactor
FCMI	Fuel-clad mechanical interaction
FGR	Fission gas release
LHR	Linear heat rating
LOF	Loss of flow
MITRA	Multi-phase In-pin Thermal hydraulic Relocation Algorithm
MMF	Melt mass fraction
MWe	Electrical capacity in Megawatt
MWth	Thermal capacity in Megawatt
PFBR	Prototype fast breeder reactor
SFR	Sodium fast reactor
TFC	Top of fissile column
TUCOP	Transient under-cooling and over-power
UTOP	Unprotected transient over-power

Chapter 1

Introduction

Sodium-cooled fast reactors have demonstrated remarkable operational performance with high uranium utilization and thermal efficiencies of up to 45 %, while simultaneously breeding fissile material. It was a fast reactor that illuminated four 200-watt light bulbs and marked the world's first electrical power generation through nuclear fission. More than 400 reactor years of operational experience have been accrued, with a particularly satisfactory in-service performance during the previous two decades [1]. Unlike thermal reactors, fast reactors are not designed in their most reactive configuration, and hence their potential for a core disruptive accident poses a major safety concern [2]. Consequently, avoidance of large-scale core disruption is one the most important objectives in the design of fast reactors. Accordingly, diverse safety shutdown and passive decay heat removal systems are incorporated in fast reactor design, which practically eliminate the chances of severe core damage [3]. Nevertheless, the absolute elimination of accidents can never be guaranteed in any safety system. Therefore, events with an extremely low probability of occurrence, which might lead to conditions more severe than those considered in the plant design (beyond design basis), are also studied to manage their course and eliminate major radiological consequences [4]. The safety analysis of such a beyond design basis event for current and future fast reactors forms the background of the research presented in this thesis.

1.1 Overview of sodium cooled fast reactors

The long-term goal of India's nuclear power programme is to develop an advanced Thorium (Th^{232})-Uranium (U^{233}) fuel cycle and utilize the abundant natural reserves of Thorium to meet the country's growing energy needs [5]. Pressurized Heavy

Water Reactors (PHWR) and Light Water Reactors (LWR) based on Uranium (U^{235}) form the first stage of the programme. Fissile Plutonium (Pu^{239}) is a by-product of these reactors. Sodium-cooled fast reactors (SFR) based on Pu^{239} with the blanket around the core consisting of depleted Uranium (primarily U^{238}) from PHWR and Thorium form the second stage of the programme. The aim of the second stage is to convert fertile nuclei (U^{238} , Th^{232}) into additional fissile nuclei (Pu^{239} , U^{233}) for the sustainable growth of India's nuclear power capacity. A Prototype Fast Breeder Reactor (PFBR) with 500 MWe capacity is currently under commissioning in Kalpakkam [6]. Six more SFR with similar capacity are envisaged in future [7].

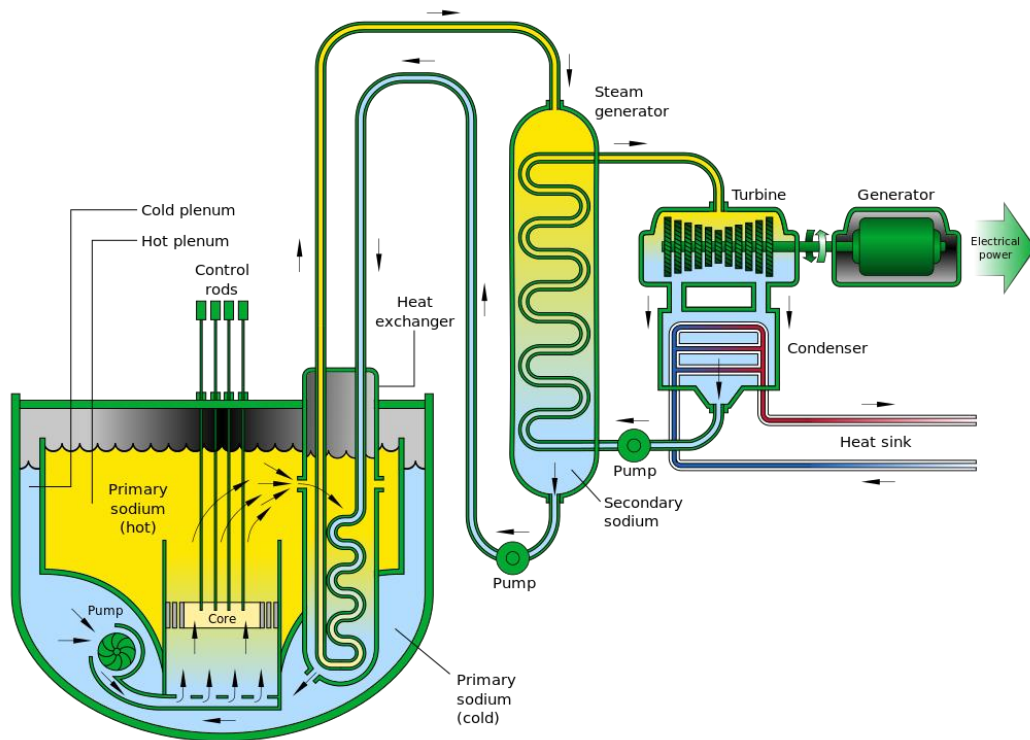


Figure 1.1: Schematic layout of a liquid sodium cooled, pool-type fast reactor.

Consider the basic layout of an SFR (Refer Fig. 1.1). Heat generated from nuclear fission inside the reactor core is extracted by the primary sodium circuit and supplied to the secondary sodium circuit through an intermediate heat exchanger (IHX). The secondary sodium circuit transfers heat to the power generating steam circuit through a

steam generator. Through the steam circuit, thermal energy is supplied to steam turbines, leading to electrical power generation. SFR can be categorized among the ‘loop’ and ‘pool’ type designs. The loop type design (for e.g., India’s FBTR [8], Japan’s MONJU [9]) refers to an SFR in which the IHX and primary sodium pumps (PSP) are installed in a hot cell adjacent to the reactor vessel. Sodium flows from the reactor vessel to the hot cell through piping. The pool-type SFR refers to a system in which the IHX and PSP are installed within the reactor vessel itself (for e.g., Britain’s PFR [10]). The latter design practically eliminates the ‘loss-of-coolant’ scenario typically considered in the safety analysis of thermal reactors.

SFR fuel is generally designed in the form of cylindrical pellets, which are stacked together inside stainless-steel cladding tubes (Refer Fig. 1.2). The stack of fuel pellets is called the ‘fuel column’. Stacks of fertile blanket pellets, called blanket columns, are normally positioned both above and below the fuel column. Fission gas plenum, designed to accommodate the gaseous fission products released from fuel, are provided either above the top blanket or below the bottom blanket columns. A helical spring is typically installed in the top plenum to ensure that the pellets remain fixed in their intended position during transport and handling. Top and bottom plugs seal the pellets from the environment outside the cladding. This assembly is called a ‘fuel pin’. A bond gas (Helium) with high thermal conductivity is filled inside the pin before sealing, to decrease the thermal resistance of the pellet-cladding gap. Fig. 1.2 shows the presence of a cavity inside the fuel column. Such a cavity is either formed by fuel restructuring, or can be introduced during fabrication [11]. Fuel pellets designed with central cavities are known as ‘annular’ pellets, and the pins housing such pellets are called annular fuel pins. Annular pellets offer considerable advantages over conventional solid pellets in

terms of fuel-clad mechanical interaction and total achievable energy extraction [12]. PFBR, European Sodium Fast Reactor (ESFR) and the Indian FBR-1 will be utilizing the annular pin design [6,13,14].

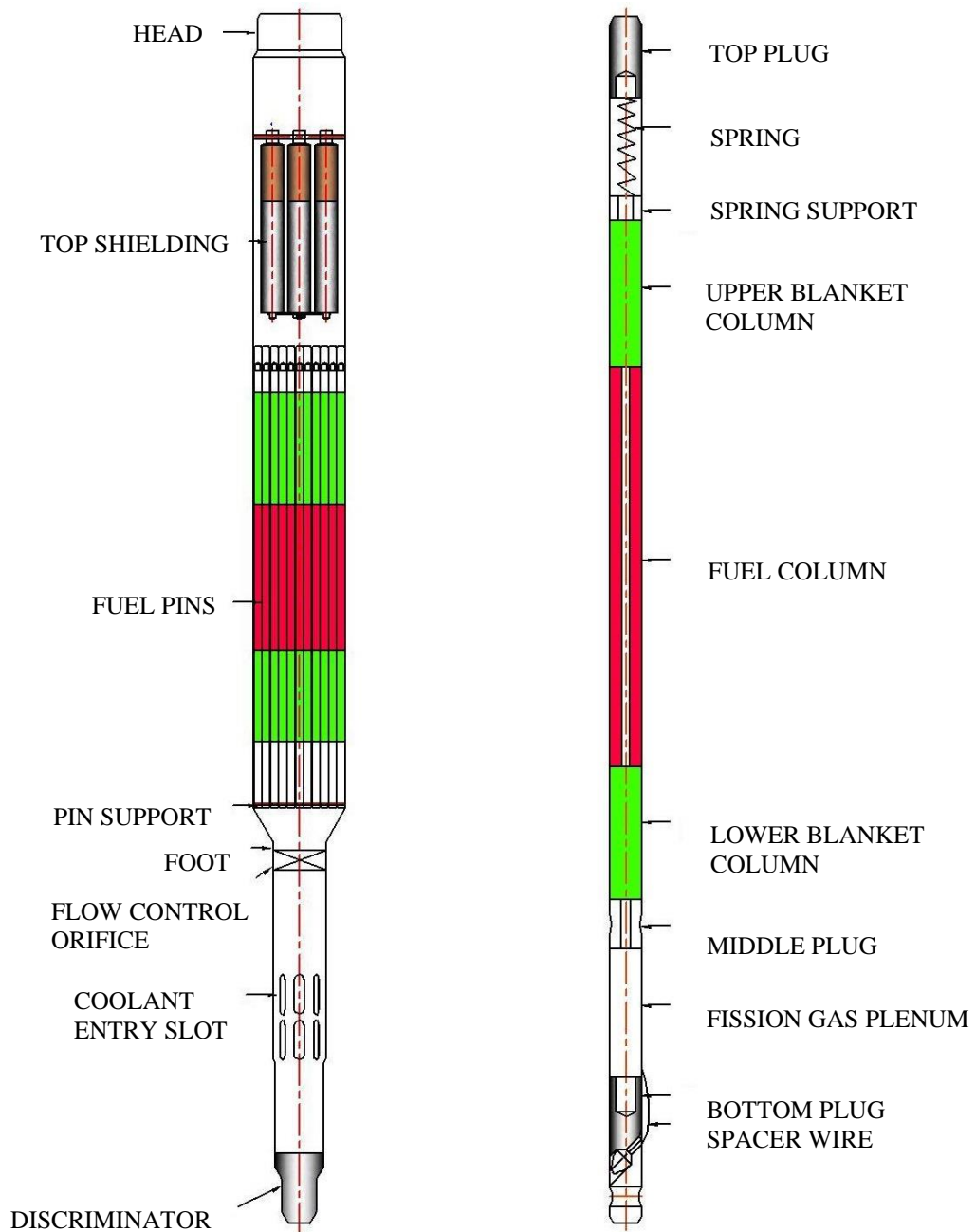


Figure 1.2: Typical SFR fuel subassembly and fuel pin.

The fuel pins are arranged in the form of bundles inside hexagonal, stainless steel units called fuel subassemblies (Refer Fig. 1.2). Each subassembly contains several fuel

pins, which are typically installed with helical spacer wires to support the pin bundle and to assist in inter-channel coolant mixing [15]. Liquid sodium within the cold pool enters the subassemblies through the entry slots located near the foot and flows through the pin bundle, extracting heat from the clad outer surface. It exits through the head of the subassemblies into the hot pool and loses its thermal energy in the IHX.

An SFR core loaded for the first time with un-irradiated or fresh fuel, in preparation for its first-core cycle, is said to be in the *'beginning-of-life'* condition [16]. Irradiation results in the fission of heavy nuclei and a corresponding decrease in the heavy atom number density. The loss of fissile nuclei is quantified in terms of the fuel burnup, which is defined as the percentage of fissile nuclei that have undergone fission (atom percent). At the end of each fuel cycle, a fraction of fuel subassemblies is replaced with fresh fuel subassemblies. After a few cycles, the core reaches the *'equilibrium'* condition, in which the configuration of the reactor core at the start of any cycle is identical to the configuration at the start of the previous cycle. Both the fuel, absorber material, and structural material undergo several thermo-mechanical and chemical changes during irradiation. For e.g., the fuel-cladding gap, which is open for fresh fuel, gets closed after a short time under irradiation due to fuel cracking, swelling and differential thermal expansion of fuel and clad [17]. Gap closure decreases the thermal resistance to heat flow and thereby influences the fuel temperature. Hence, safety studies are generally carried out with due consideration to both the above-described core conditions.

Prominent safety features incorporated in modern SFR systems consist of two diverse and independent decay heat removal systems, two independent, diverse, and fast-acting safety shutdown mechanisms, a core catcher plate, and a reactor containment

building [13]. The decay heat removal systems maintain the core at a safe temperature during planned shutdown periods and station blackout incidents [18]. The two diverse shutdown mechanisms are designed to terminate any untoward incident well before initiation of damage in the reactor core [19]. A schematic diagram of a typical control rod subassembly used in the shutdown mechanisms is presented in Fig. 1.3. The subassembly consists of a stationary sheath and a mobile control and safety rod (CSR). Multiple absorber pins containing neutron absorber (for e.g., B_4C) pellets are housed inside the CSR.

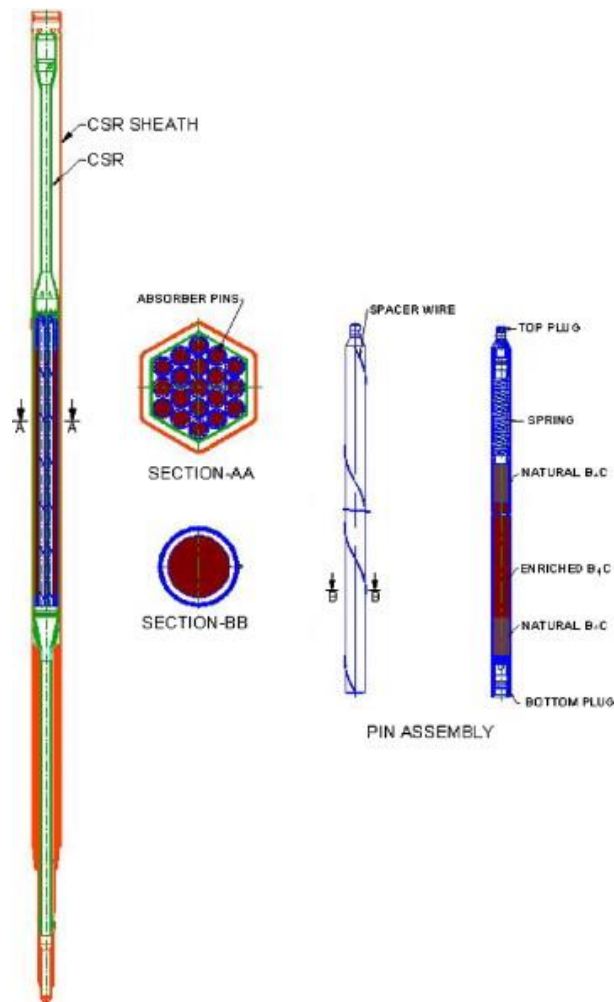


Figure 1.3: Schematic diagram of a typical CSR subassembly (PFBR [19]).

The shutdown systems of most SFR are equipped with interlocks to prevent the withdrawal of two or more rods simultaneously. A small, maximum speed of

withdrawal (typically ~ 2 mm/s) is purposely designed into the system to prevent any rapid increase in the rate of fission. Each safety provision has been subjected to extensive testing and scrutiny over decades of technological development and is backed up by considerable operational experience. Hence, modern SFR systems have rendered core disruptive accidents to extremely low levels of probability.

1.2 Beyond design basis events in SFR systems

Beyond Design Basis Events (BDBE) are hypothetical accidents that are assumed to occur in case of a complete breach of the safety envelope of the reactor design. Under BDBE analysis, it is assumed that an accident initiating event, typically within the purview of the reactor safety envelope, occurs, in response to which, both the primary and secondary shutdown systems fail to bring the reactor to a safe state [4]. The hypothetical and simultaneous failure of multiple safety systems falls outside the single-fault criterion for design basis events (DBE). Despite the extremely low probability of occurrence, these events could pose a major public health hazard, if the radioactive material within the reactor vessel is not confined adequately. The international nuclear safety advisory group (INSAG), in its report on the basic safety principles for nuclear power plants, highlights the importance of incorporating BDBE in safety analysis to ensure the mitigation of radiological consequences [4]. With the introduction of a new event categorization system, BDBE are now split in two components: Design Extension Condition-A (without core melting), and Design Extension Condition-B (with core melting) [20]. The International Atomic Energy Agency (IAEA), in its safety guidelines, recommends the analysis of those DEC (B) that can challenge the integrity of the containment, to provide inputs for the design of containment and other safety provisions. For SFR systems, three types of perturbations can upset the steady-state operation [21]:

(a) change in the reactivity, (b) change in the coolant flow rate, and (c) change in the coolant inlet temperature. Accordingly, the three enveloping severe accident conditions in SFR safety analysis are as follows:

- (i) Unprotected Loss of Heat Sink (ULOHS): An unexpected failure of the normal heat removal system, accompanied by the simultaneous failure of all safety shutdown systems.
- (ii) Unprotected Transient Over-power (UTOP): An unexpected withdrawal of a CSR, or the passage of a large bubble through the core, accompanied by the simultaneous failure of all the safety shutdown systems.
- (iii) Unprotected Loss of Flow (ULOF): A sudden and complete failure of the primary coolant flow system, accompanied by the simultaneous failure of all the safety shutdown systems.

Over the decades, considerable research efforts have led to the identification of ‘inherent safety mechanisms’, some of which are unique to SFR systems and can be incorporated into the reactor design to mitigate the consequences of the above outlined accidents passively. The mechanisms relevant to the present work are briefly introduced as follows.

1.3 Inherent safety features of SFR

For a nuclear reactor to generate the desired power at a constant rate, the rate of neutron production through fission reactions must be equal to the rate of neutron losses caused by absorption and leakage. A deviation from this condition leads to a time dependence of the neutron population, and consequently the rate of heat generation. An effective neutron multiplication factor (K_{eff}) represents the time dependence in terms of the ratio of number of neutrons in one generation to that in the preceding generation.

Another useful parameter to represent the rise or fall of the reactor power is the reactivity (ρ), which is defined as the fractional change in the effective multiplication factor $\left(\frac{k_{eff}-1}{k_{eff}}\right)$. Common terminologies used to express ρ are percent milli or pcm (10^{-5}), percent or cent (10^{-2}) and Dollar (\$). One Dollar is defined as the threshold between a critical or stable state ($\rho = 0$) and a prompt-critical state ($\rho = \beta$), where β represents the fraction of delayed neutrons in the total neutron population. Delayed neutrons are produced in a small fraction by ‘delayed neutron precursors’, which are fission products with excitation energies high enough to make possible the emission of a neutron.

Reactivity is a function of macroscopic cross sections, which involve the atomic number densities of materials in the system. As the neutron reaction cross-sections and number densities of materials depend on temperature, a change in reactor power can influence the core temperature and hence the reactivity. Spatial movement of material can also disturb the number densities, thereby influencing the reactivity. Such variations in the reactivity can affect the inherent stability of a nuclear reactor during upset conditions. Mathematically, these variations are incorporated by splitting the reactivity in two components ($\rho = \delta\rho_{ext} + \delta\rho_{feed}$). The external influences, such as the insertion of positive reactivity via a control rod, are represented by $\delta\rho_{ext}$, whereas the temperature and movement related influences are represented by the so-called ‘feedback reactivity’ ($\delta\rho_{feed}$). As outlined above, research has led to the recognition of beneficial inherent safety features in SFR systems. Each feature is represented in the reactor kinetics calculations through a respective $\delta\rho_{feed}$. Prominent reactivity feedbacks identified for SFR systems, and their associated impact on reactor safety are briefly introduced as follows [22]:

- (a) Fuel Doppler: The resonance peaks in the neutron absorption cross-sections undergo the so-called ‘Doppler broadening’ with rise in temperature. The result is an increase in the reaction rates for both fissile and fertile nuclei. However, temperature rise of the principal fertile nuclei (U^{238}) results in a relatively larger increase in the effective rate of parasitic capture, which generates a beneficial negative reactivity feedback. The fuel Doppler feedback provides a crucial, negative temperature coefficient, particularly in mixed-oxide fuel based SFR.
- (b) Fuel axial expansion: The rise in fuel temperature under an upset condition leads to the expansion of fuel pellets in both the radial and axial directions. The radial expansion of fuel pellets does not influence the radial expansion of the core itself, since it is accommodated either by the gap between fuel pellets and cladding, or by the elasticity of the cladding steel. However, the axial expansion of fuel pellets effectively increases the height of the core. The increased height results in an increased neutron leakage through the radial border of the core, which generates a beneficial, negative reactivity feedback. This feedback is an important inherent safety mechanism for both oxide and metal fuel based SFR systems.
- (c) Control rod driveline expansion feedback: The CSR drive mechanism is generally immersed partially within the hot pool. An increase in the core outlet temperature results in a corresponding increase in the hot pool and the CSR drive mechanism temperatures. The thermal expansion of the CSR drive mechanism leads to an effective insertion of CSR in the reactor core, which generates a negative reactivity feedback.
- (d) Core radial expansion: Rise in the overall core temperature leads to radial thermal expansion of structural components of the core. A minor increase in the effective

diameter of the core increases the space between the fuel subassemblies, which leads to a corresponding negative reactivity feedback.

(e) Sodium thermal expansion and boiling: Liquid metals such as sodium are weak neutron moderators, i.e., they tend to decrease the speed of fast neutrons slightly. A change in the core temperature affects the density and mass of liquid sodium, which influences the reactivity. The nature of this feedback is exceedingly space dependent [23]. For e.g., the occurrence of coolant boiling near the top of the active core increases the neutron leakage, whereas the corresponding reduction in coolant density reduces the neutron moderation. The increased leakage tends to dominate the decrease in moderation, leading to a negative reactivity feedback. However, boiling in the central region of the core reduces moderation without a significant rise in neutron leakage. Therefore, large-scale loss of coolant generates a positive reactivity feedback in commercial sized, ((U-Pu)-O₂) fuel, homogeneous core SFR [16]. For small-sized SFR (for e.g., EBR-II), neutron leakage is much more dominant. ULOF and ULOHS tests conducted in EBR-II have demonstrated passive shutdown without damage to the reactor core, based on the negative reactivity feedbacks associated with rise in coolant, fuel and structural temperatures [24].

(f) Fuel compaction: One of the crucial safety related aspects of SFR systems is that the compaction of fuel in the event of a core meltdown can generate a large positive reactivity feedback [2]. The coolant, stainless steel cladding and fuel pellets situated within the highest neutron density regions are most susceptible to degradation/phase-change during severe accidents. In case of cladding and fuel pellets, phase-change results in the formation of molten fluid in a localized region. Due to the tendency of fluids to undergo deformation readily in the presence of

shear stresses, the molten material flows under the influence of hydrodynamic forces. The resultant relocation of material results in a corresponding reactivity feedback. The magnitude and nature of this feedback (positive or negative) generally depends upon: (a) the fluid dynamics of the molten material under consideration, (b) material mass involved in relocation, and (c) location of melting within the core. If the molten material collapses downwards under the influence of gravity, a large, positive reactivity feedback can arise. The phenomenon is commonly referred to as ‘fuel slumping’ or ‘fuel compaction’, and is utilized in conservative safety studies [22].

(g) Molten fuel relocation: A striking feature of SFR discovered in UTOP related experiments is the dispersive flow of molten fuel in the axial direction of the core, both before and after the failure of cladding. The movement within the pin before clad-failure is commonly known as ‘fuel squirting’ [22]. The movement outside the pin after clad-failure is called ‘fuel sweep-out’. Fuel squirting is a rapid, hydrodynamic movement of molten fuel inside the cavity of fuel pellets. It typically occurs at high velocities of the order of 40 m/s inside the fuel column [25], and leads to the relocation of molten fuel from the active core to either the fertile blanket [26], or the gas plena. Both fuel squirting and fuel sweep-out remove molten fuel from the vicinity of the active core. The loss of fissile nuclei from the core generates a negative reactivity feedback [22].

If somehow the negative reactivity feedback mechanisms fail to mitigate the severe accident, the reactor may undergo large-scale meltdown and attain an uncoolable configuration. Under such circumstances, if the core collapses and becomes prompt-critical ($\rho = 1 \$$), a rapid power excursion and core material vapourization may occur

[2]. Due to significantly high material vapour pressures, such a power rise will ultimately be terminated by the physical disassembly of the core material. Conservative safety studies of the physical disassembly are normally carried out to identify the uppermost limit of threat to the containment [3]. The severe accident phenomenology prior to the attainment of an un-coolable configuration is broadly categorized as the ‘pre-disassembly phase’ of a core disruptive accident [27]. The desired outcome of inherent safety is the complete neutronic shutdown of the reactor within the pre-disassembly phase in a relatively benign manner. In this context, it is important to examine the fuel squirting feedback, which is expected to mitigate UTOP even prior to clad failure.

1.4 Role of fuel squirting in SFR safety

In general, the above reactivity feedbacks are well established and intrinsic to the safety envelope of all modern SFR designs. However, the same cannot be unanimously stated for fuel squirting, despite several experimental demonstrations of its effectiveness. Squirting was first established as an accident mitigating mechanism through experiments conducted in the TREAT reactor [25]. Thereafter, multiple experimental studies further established the utility of the mechanism for UTOP mitigation [26,28,29]. Based on the widespread evidence, squirting was utilized as a prominent negative reactivity feedback in the safety assessment of India’s PFBR [3]. However, the assessment was further extended to include the control rod driveline expansion feedback, in order to demonstrate inherent safety of PFBR against UTOP even without the squirting feedback [30].

Findings that contested the above approach first emerged from the UTOP experiments conducted in the EBR-II reactor. It was found that although squirting took

place in solid fuel pins, it did not occur in annular fuel pins [31]. Further evidence to dispute the established fuel squirting hypothesis arrived from the experiments conducted in the CABRI reactor, located in Cadarache (France) [32]. In a number of UTOP tests performed with annular fuel pins, squirting remained absent [33]. Instead, a new type of relocation mechanism, termed ‘in-pin fuel motion’ was reported for the first time. The main difference between squirting and in-pin fuel motion was that while squirting led to a rapid removal of melt from the active core, in-pin fuel motion led to a relatively much slower relocation within the confinement of the annular pellet cavity (Refer Fig. 1.2). Studies showed that in-pin fuel motion failed to disperse fuel away from the active core, except in certain uncommon circumstances, such as the fragmentation of blanket pellets prior to the test [33], or excessively high rise in reactor power [34]. Based on these experimental findings, Papin, in a book chapter on the behavior of fast reactor fuel under accident conditions, discounted fuel squirting as an accident mitigating mechanism during UTOP [35]. Similar views were also expressed by the Argonne National Laboratory (ANL) in their technical report on severe accident mitigation in fast reactors [36].

A significant disagreement in the approaches adopted towards fuel squirting and its impact on SFR safety is evident. A deeper exploration of literature is needed to: (a) highlight the reasons for the disagreement, (b) identify experimental findings of maximum relevance towards India’s SFR program, and (c) examine the available theoretical models of fuel squirting for their utility in safety analysis. First, a short description of the experimental facilities used to study fuel squirting is provided. Second, the major challenges in mathematical modeling of molten fuel relocation are

discussed. Subsequently, a compact and thorough literature review is carried out to fulfill the above highlighted goals.

1.5 Specialized test reactors

1.5.1 TREAT reactor

The Transient Reactor Test (or TREAT) facility is an air-cooled, graphite moderated, thermal-spectrum test reactor located in Idaho National Laboratory, USA [37]. The purpose of the facility is to evaluate different types of fuel designs under accident conditions by generating transient neutron fluxes. The facility is equipped with a hodoscope, which can monitor the axial fuel motion in space-time [38]. The underlying principle of this device is the detection of fast fission neutrons which escape through an opening in the biological shield, amid a background of thermal neutrons and gamma radiation.

1.5.2 EBR-II reactor

Experimental Breeder Reactor-II (EBR-II) is a sodium fast reactor constructed by Argonne National Laboratory in Idaho, USA [39]. The objectives of this reactor were to demonstrate the feasibility of fast reactors as power plants and to demonstrate on-site recycling of spent fuel [40]. Later, it proved to be a remarkably effective test reactor due to the presence of fast neutron spectrum and capability of creating slow transients.

1.5.3 CABRI reactor

Located in Cadarache (France), CABRI is an experimental, thermal neutron spectrum based research reactor built for testing nuclear fuel under severe accident conditions [41]. Some of the studies performed in this reactor are important for this thesis. For clarity in the subsequent review, the main features of the reactor are briefly introduced as follows:

CABRI is a pool-type, light water moderated reactor with a maximum steady-state power level of 25 MW. A picture of the reactor core taken from above shows the major core components and their positions (Refer Fig. 1.4). The driver core consists of: (a) Six percent enriched, UO_2 based fuel rods with 80 cm fissile length, (b) Six control rod subassemblies with tubes containing Hafnium (23 each), (c) Four transient rod subassemblies with tubes containing ^3He (24 each), (d) graphite reflector and (e) light water coolant at a pressure of ~ 1.2 atm.

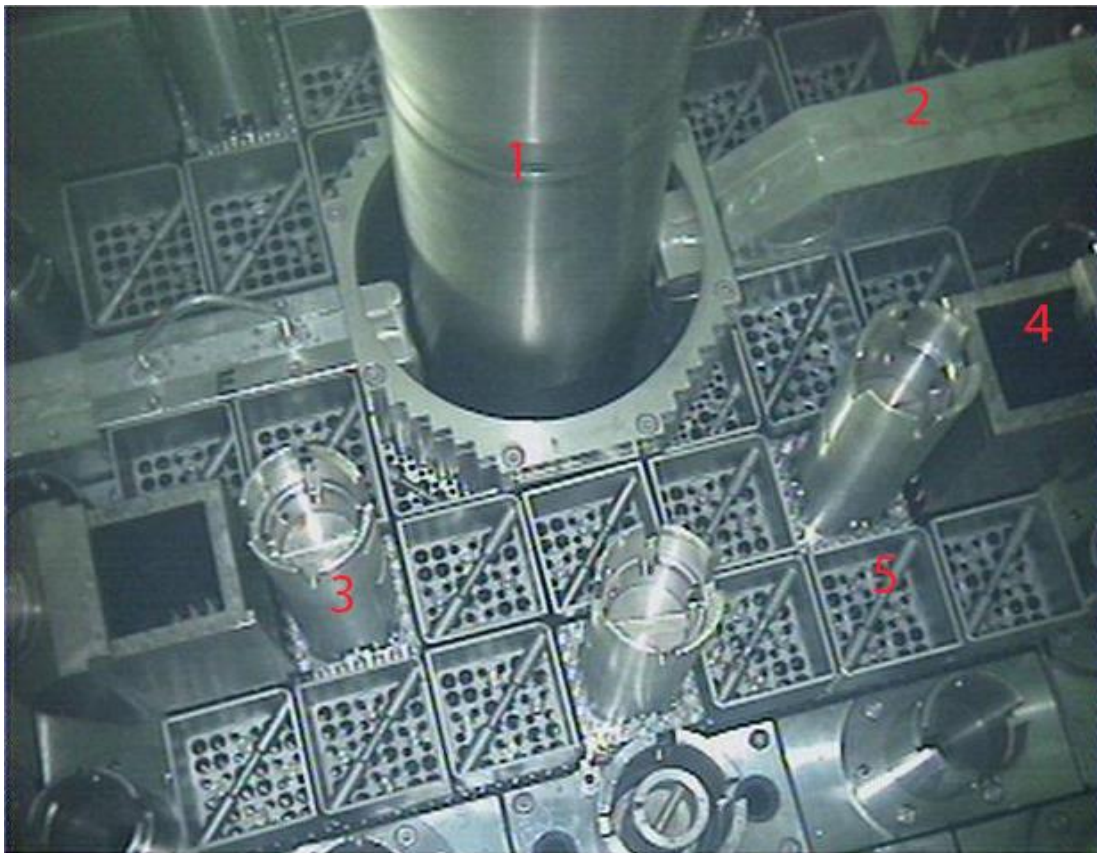


Figure 1.4: View of the CABRI reactor from above. Major components are: 1: Experimental test loop, 2: Hodoscope channel, 3: Control rods, 4: Transient rods, 5: Driver fuel subassemblies. [42]

Figure 1.5 presents a schematic diagram of the reactor core and the experimental sodium loop. The loop is made up of both in-pile and out-of-pile components. The test section is inserted into the in-pile part (fixed at the core centre) before conducting experiments. The test pin is housed inside a 12 mm diameter Niobium tube at the radial centre of the

core. Liquid sodium flows through the annular channel in between the fuel pin and the tube. The tube is thermally insulated at its outer surface with Argon (white space outside test channel) and a Molybdenum reflector.

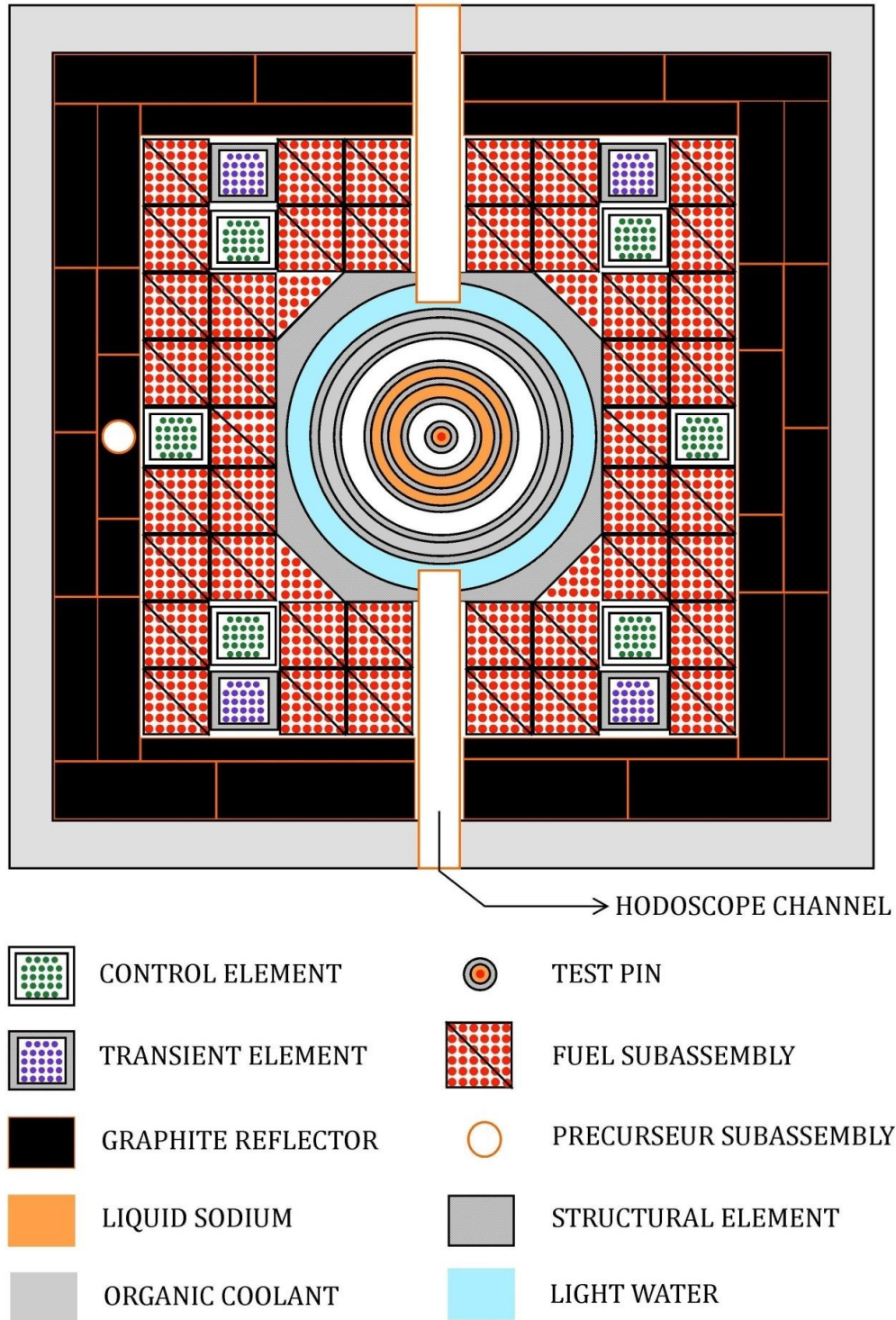


Figure 1.5: Schematic layout of CABRI reactor core.

Sodium inlet and by-pass flow systems ensure the desired mass flow rate within the test channel (concentric sodium rings outside Argon insulation). The entire sodium loop is kept in a vacuum environment inside the test section (white space outside sodium channels). A detailed schematic of the test section is presented by Flores et al. [43]. A reactivity injection system allows the realization of overpower by depressurization of ^3He from the transient rods situated among the driver fuel subassemblies. The rods are connected to an out-of-pile discharge tank through a set of fast-acting and control valves [35]. The rate of reactivity insertion is controlled by regulating the rate of ^3He discharge from the transient rods. The system is capable of injecting reactivity of up to 4 \$/s in a duration less than 0.01 s, by opening the fast-acting valves [44]. For slower rates of reactivity insertion, the valves are opened sequentially [45]. The external reactivity insertion is countered by the Doppler Effect and other delayed feedbacks until a new equilibrium is reached. The control rods are completely dropped at the end of the transient to regulate the total energy deposited in the test pin. The parameters of the reactivity injection system are the initial absorber pressure, control valve aperture, control rod drop instant, steady-state temperature and power [45]. A heat balance method is used to evaluate the steady-state core power, by measuring the rise in coolant temperature for an accurately monitored flow rate [44]. Boron-lined ionization chambers are calibrated to correspond to the steady-state power measured by the heat balance method. Cobalt and gold disk and wire dosimeters are used to measure the axial flux profile in both the driver subassemblies and the experimental test section.

1.6 Major challenges in modelling molten fuel relocation

Theoretical treatment of material relocation in the reactor core requires the prescription of hydrodynamic forces acting on the molten mass within the available

flow space. In case of fuel relocation within the annular fuel pin, this space is the inner cavity of fuel pellets. The characteristic length (or inner diameter of pellet) is small (~ 2 mm), while the length is of the order of one meter. Besides gravity (body force), the surface-acting forces are: (a) Capillary, (b) Viscous, (c) Inter-phase momentum exchange (drag, virtual mass), and (d) Pressure forces. The flow is also affected by a temperature gradient along the length of the flow space, which may solidify molten fuel. This may lead to increased inter-molecular cohesive forces, leading to rise in fluid viscosity by several orders of magnitude [46]. Solidified fuel can also choke the melt cavity. Inter-phase momentum exchange occurs due to the presence of two fluids in the flow space (Fluid 1- Molten fuel, Fluid 2- fission gas mixture). [47]. Pressure forces are generated by the release of fission gases, that were originally trapped inside the fuel microstructure [48]. The relative dominance of one force over the other dictates the hydrodynamics. Naturally, the flow behaviour reported in experimental literature differs vastly [25,31,33]. Any computational modelling effort must take the above challenges in account to represent the physics of molten fuel relocation appropriately.

1.7 Literature review

Nuclear fuel rods (or pins) have a simple geometrical design and straight forward application, i.e., heat generation and radioactivity containment. The underlying physics, however, is not simple. From the beginning to the end of its life, the pin undergoes several thermo-mechanical and chemical changes. Therefore, in accidents, the melting and relocation of fuel and cladding become a function of these changes (for e.g., burnup, swelling, irradiation history) along with the conditions of the upset event. To predict the phase-change, relocation and resultant reactivity feedbacks, the scientific community relies on (a) specialized test reactors (for e.g., TREAT, CABRI) and (b)

comprehensive computational tools with experimental validation. Finally, reactor safety assessments are carried out based on the collected information to categorize the impact of each mechanism. This review therefore addresses the available literature in three parts, viz., experimental studies, computational tools, and reactor safety assessment studies.

1.7.1 Experimental studies

Tests were performed in the TREAT reactor (Section 1.5.1) to evaluate the fuel-clad mechanical interaction for ceramic fuel during a sudden, large reactivity insertion. In one of these tests (C3C), an expulsion of molten fuel out of the active zone was noticed for the first time [49]. It was found that fuel had escaped out of the test pin (in molten state) at such a high velocity that it even penetrated a capillary tube (0.8 mm diameter) outside the pin. This expulsion was attributed to a large pressure force caused by the release of fission gases from the molten fuel microstructure. Based on the hypothesis that the expulsion could provide an advantageous negative reactivity feedback, a series of tests were carried out [25,50,51]. It was found that a fast insertion of external reactivity ($\sim 5 \text{ } \$/\text{s}$) resulted in a large expulsion of fuel before the steel cladding could fail [25]. In the report of one such test (PINEX-2), the term ‘fuel squirting’ was used for the first time. Molten fuel was squirted out of the fissile column at a high speed ($\sim 30\text{-}40 \text{ m/s}$) up to the fission gas plenum. This movement could mitigate a sudden reactivity insertion in SFR systems. Some concerns about the applicability of squirting towards commercial SFR remained unaddressed:

(a) The tests were carried out with fuel pins specifically designed to promote squirting.

The fuel, insulator, and reflector pellets were designed with annular geometry to create an internal flow channel between the fuel pellet cavity and at least one (upper

or lower) gas plenum. However, typical SFR fuel pins have solid blanket pellets, which confine the internal flow channel within the fissile column.

- (b) The reactivity insertion rate (5 $\$/s$) was unrealistic with regards to UTOP in SFR systems. Safety provisions in modern SFR ensure that the rate of reactivity insertion remains small (few C/s) [35].
- (c) The test pin did not include axial blanket columns, which are generally present in SFR fuel pins [52].

Out of the above, concern (c) was addressed with follow-up experimental studies [50][26]. Three types of blanket and plenum geometries were tested to determine the optimal design for squirting: (Design I) solid bottom blanket, annular top blanket; (Design II) annular bottom blanket, solid top blanket; and (Design III) annular bottom blanket, annular top blanket. All the pins had a direct pathway between the fuel column and at least one gas plenum. The reactivity insertion rate was fixed at 3 $\$/s$. It was found that in the presence of axial blanket pellets, molten fuel could not enter the gas plena in any of the three tests. Instead, it froze in the blanket column, choking the flow channel. Maximum squirting occurred in Design 1, followed by Design 2 and Design 3. It was theorized that in Design 1, molten fuel temperature must have been highest at the time of entry in the top blanket. It therefore penetrated the greatest distance, leading to maximum squirting.

A series of five tests were conducted in EBR-II (Section 1.5.2) with mixed oxide fuel and different fuel pin designs to address the above concerns [31]. Each test was conducted on a different type of fuel (aggressive (high smear density, thin clad), moderate and advanced (annular fuel) design). Nineteen pre-irradiated fuel pins were used in each test. Pins with aggressive parameters failed. Pins with moderate and

advanced parameters did not fail up to 100 % over-power. Fuel-clad mechanical interaction was the dominant failure mechanism. Molten cavity pressurization and melt thermal expansion played an important role in failure. It was found that under typical UTOP conditions in modern SFR, the probability of failure was not a function of the rate of power rise. Annular fuel design mitigated fuel-clad mechanical interaction very effectively by letting fission gases escape to the plenum and providing space for thermal expansion of molten fuel. In some solid fuel pins, a squirting distinct from the PINEX tests was observed. The mechanism is briefly described as follows:

Fuel melting in solid pins leads to the formation of a melt cavity enclosed by solid fuel from all sides. With further rise in power, this cavity grows in the axial and radial directions. If sufficient melting occurs, the cavity grows up to TFC. Here, high cavity pressure forces the blanket pellets upwards, resulting in the relocation of some molten fuel mass and solid fuel pellet fragments from the fissile to fertile column. For clarity in subsequent discussion, this squirting is hereafter referred to as *solid fuel squirting*. None of the annular fuel pins exhibited squirting involving melt relocation from the fissile to the fertile region.

The first test series carried out in the CABRI reactor (called CABRI-1) involved ‘fast’ transients, i.e., large reactivity insertion within a few hundred micro-seconds [32]. UTOP in SFR systems typically involves a small rate of unexpected reactivity insertion (few C/s) due to the safety provisions incorporated in the reactor design [35]. Doppler and axial expansion feedbacks counter the external reactivity insertion. The net result of these kinetic mechanisms is a slow rise in SFR power ($\sim 1\text{--}3\%$ P_n/s) [35]. Therefore, beginning in the late nineties, a new series of tests (CABRI-2) was taken up to test the behaviour of SFR fuel under such conditions [33,53]. Subsequently, CABRI-FAST

series was taken up to establish the fuel-clad mechanical interaction (FCMI), margin-to-failure and power-to-melt for annular pins with improved cladding (SCARABIX; 15-15 Ti CW clad) [34]. To simulate UTOP conditions in the test reactor, the transient rods were depressurized at a slow rate. A uniform rate of power rise ($\sim 1\% P_n/s$) was therefore achieved in all the tests. The annular MOX fuel pins had inner and outer pellet diameters of ~ 2 mm and 7.27 mm, respectively. Fissile length for each pin was 75 cm. Despite the significantly high transient power levels achieved in the E9 (134.7 kW/m, 223 % P_n/s), E9bis (107,5 kW/m, 181 % P_n/s), PF1 (88.3 kW/m, 213 % P_n/s) and MF2 (124.7 kW/m, 315 % P_n/s) tests, none of the annular fuel pins underwent failure. Results relevant to the melting, relocation, and squirting behaviour of MOX based, annular fuel pins, which are to be utilized in India's upcoming SFR, are outlined as follows:

Charpenel et. al. [33] have presented detailed experimental results on fuel melting and relocation during UTOP. Based on the neutron radiographs and axial cuts of test pins, as well as the hodoscope readings, it is reported that annular fuel exhibits a relocation mechanism distinctly different from the conventionally understood fuel squirting. This motion, known as 'in-pin fuel motion', can result in the relocation of molten fuel up to the top of the fissile column, if significant rise in power and melting occur. Based on the segregation of metallic fission products from the melt, it is concluded that the movement is slow in nature. In-pin fuel motion has been unanimously observed in all the UTOP tests with annular fuel pins. If the blanket pellets are completely intact prior to the accident, the melt can remain confined inside the fissile length despite a significantly high rise in power and substantial melting. Therefore, with in-pin fuel motion, the probability of fuel removal from the active core is quite small under typical UTOP conditions.

Charpenel et. al. [33] have also shown that a small amount of fuel can penetrate the top blanket column, if the top blanket pellets are fractured a-priori (E9bis test). Fuel melting in this test began in less than thirty seconds. After a substantial amount of melting, a few grams of fuel were relocated from the fissile column to the gaps present between the fragmented top blanket pellets. Based on the hodoscope readings, the time of relocation was determined to be between sixty-five to sixty-nine seconds. The test proved that even with in-pin fuel motion, fuel removal from the active core is possible. However, due to sensitivity constraints of the motion measuring device (hodoscope), a clear picture of the fuel motion within the fissile column remains unavailable.

A significantly large resistance to failure of annular MOX fuel pin during UTOP was established. Even at exceedingly high transient power levels, the pins did not undergo failure. In one of the tests (E9bis), a notch was introduced in the cladding steel at the peak power node. Furthermore, a partial reduction in the coolant flow rate was implemented to initiate failure. Despite the imposition of such severe conditions, the pin resisted failure successfully. However, the imposition of UTOP on a solid MOX pin resulted in failure at a relatively much lower power level. Therefore, annular MOX fuel pins were found to provide a strong advantage over solid fuel pins with regards to resistance towards failure under UTOP. Consequently, the potential for pre-failure fuel melting and relocation in annular fuel pins is immense and must be taken in account in the safety studies.

Fukano et. al [34] have reported squirting in annular fuel pins during UTOP, under an excessively high rise in power. In the MF2 test, fuel squirted through a melt cavity in the blanket pellets up to a distance of ~ 3 cm from the top of fissile column (TFC). Squirted fuel came in direct contact with the cladding steel at TFC. The blanket

pellets of the test pin were completely solid by design, and literature does not reveal the presence of any prior fragmentation. The radius of the melt cavity (~ 0.45 mm) created within the blanket pellets was smaller in comparison with the prefabricated cavity inside fuel pellets (1.015 mm). Localized coolant boiling (near TFC) was also observed at the instant of squirting. It was reported that coolant boiling, and molten fuel-clad contact were inter-connected events. However, the sequence of events is unknown, i.e., whether boiling resulted in molten fuel-clad contact, or whether fuel squirting led to clad heat-up and coolant boiling. It may be noted that the coolant flow rate (0.11 kg/s) was much smaller as compared to E9 (0.153 kg/s), which may have caused localized boiling and squirting in this test. The mass of fuel squirted out of the fissile column is unavailable. From the radiographic images, this mass appears to be a few grams. These results show that in annular fuel pins, a few grams can be squirted out of the fissile column at excessively high-power levels during UTOP. Such squirting may occur simultaneously with coolant boiling. However, if a vacant space is available in the top blanket pellets prior to the accident, fuel can be relocated out of the fissile column at a relatively lower power level without coolant boiling [33].

1.7.2 Computational tools

1.7.2.1 Available mathematical models

Chen et al. [54] developed a 1-D enthalpy formulation based model for capturing the phase-change heat transfer in nuclear fuel rods. Shrivastava et al. [55] developed a model to capture the natural convection in molten fuel trapped inside the fuel rods. McCord et al. [56] et al. developed analytical solutions for melting driven by internal heat generation. Kamiyama et. al [57] developed a fuel freezing model for calculating the distance of penetration in cold channels. These studies did not consider the

challenges associated with modelling phase-change in annular pellet geometry. The problem domain was considered completely solid prior to the start of melting. Therefore, the presence of gas phase was neglected. Molten fuel was either considered stationary [54] or assumed to occupy the fluid flow domain entirely. Furthermore, the effects of fission gas release induced pressurization and melt freezing in cold regions were not addressed. These assumptions rendered the above mathematical models unsuitable for application towards annular fuel pins.

Manchon et. al [58] studied the vaporisation of molten fuel during a core disruptive accident. Total core melt-down was assumed to have occurred prior to fuel vapour expansion, thus exposing fuel to the coolant ambient pressure. In UTOP, molten fuel is contained inside the fuel pin with high internal pressure until cladding failure. The vapour saturation temperature for a high-pressure environment is significantly greater in comparison with the corresponding temperature for the coolant ambient pressure. Studies focused on molten fuel vaporization under such pre-failure conditions are scarce in literature.

Multi-phase flow models can become ill-posed for certain ranges of independent variables. An ill-posed model generates divergences in the numerical solution. A method of characteristics analysis has revealed the regions of real and complex characteristics with regards to the 1-D multi-phase flow equations of the RELAP5 code [59]. A linear stability analysis has further revealed the ill-posed regions and the growth rates of numerical disturbances [60]. Sodium thermophysical properties have also been incorporated in the RELAP5 code framework to enable its utilization in SFR thermal hydraulics analysis [61]. An uncertainty analysis of RELAP5 has also been carried out [62]. However, the code architecture does not address the modelling challenges specific

to annular pellet geometry. For instance, the mass source terms in RELAP5 are derived from liquid-vapour phase change, whereas the mass source terms needed for the present study involve solid/liquid phase change. Another challenge that arises in the simulation of fuel squirting through RELAP5 is the transient variation in the flow geometry, which must be accommodated in both the heat-transfer and multi-phase flow models. Furthermore, flow blockage caused by the solidification of molten fuel requires a dedicated solidification module. The above challenges need to be addressed before the application of RELAP5 towards fuel squirting.

1.7.2.2 Tools for fuel squirting

Modelling efforts for capturing fuel squirting began in the late 1970s, soon after its discovery. The first such code, PINEX-AR [63], was developed for analysis of squirting observed in the PINEX-2 test (Section 1.7.1). The code assumed slug flow as the dominant flow regime [64]. To calculate the slug velocity, pressure drop between the melt cavity and fission gas plena was calculated, since an internal flow channel was created in the test [25]. PINEX-AR was integrated in the UK whole core accident code, FRAX [65]. A major limitation of this tool is that its validation is confined to PINEX tests, which do not represent typical UTOP conditions and fuel specifications.

The FUMO-E code [66] was also validated with the PINEX-2 and PINEX-3 experiments. Studies with this code were able to conclude that (a) In case of a relatively slower transient (~ 50 cents/s), even if an open pathway was available to the plenum, the melt was more likely to freeze in the annular blanket/reflector pellets and (b) Melt freezing and plugging were dominated by crust-build up instead of a bulk freezing process. This code was integrated in the MELT-IIIB code system [67]. The validation was not extended to slow rate of reactivity insertion ($\sim 1\text{--}3$ cents/s) since such tests had

not been carried out at that time. Mathematical framework of FUMO-E was not published in available literature.

Experimental reports of a new type of squirting (solid fuel squirting, Refer Section 1.7.1), led to a shift in code development towards solid fuel pins [68]. PINACLE, built as a part of the SAS-4A code, could predict squirting in metallic and oxide fuelled solid pins (Section 1.7.1). However, its validation with the melt motion data of annular fuel pins (CABRI-E9, E9bis) may not be possible since it assumes a homogenous flow model [69]. This is appropriate for solid fuel, wherein the melt and fission gases are locked inside a small volume and their movements are intricately coupled. However, this is not the case with annular fuel.

1.7.2.3 Tools for in-pin fuel motion

The ASTEC-Na code system is a pre-disassembly phase simulation tool for analysis of protected and unprotected accidents in SFR [70]. It derives its thermo-mechanical models from the LWR code SCANAIR [71] as well as the ICARE models of the ASTEC V2 integral code system [70]. Improvements such as the development of cladding mechanics, fission gas release and sodium boiling models suited to SFR, experimental validation and inter-code verifications have been achieved [72] [73]. Validation database includes UTOP, transient under-cooling and overpower and ULOF experiments [43]. With regards to in-pin fuel motion, a model 'FOAM' is incorporated. Based on the 'EJECT' model of the SAS-SFR code [74], FOAM calculates fuel melting, gas release, axial motion, melt freezing and heat transfer between relocated and solid fuel. Validation of FOAM is performed against the E7, E9 and LT2 tests, among which only E9 [33] is relevant to the Indian SFR UTOP analysis [30], due to its slow power ramp. Results such as transient fission gas release and melt radius are validated with

experimental data. With regards to in-pin fuel motion (E9) and fuel squirting (LT2), evolution of the fuel inner radius at the peak power node is detailed. The state of the fuel column during the transient is detailed (LT2). A rare instance of fuel escape to the plena is described (LT2). Results are compared with the predictions of SAS-SFR code [75], descended from the SAS4A safety analysis code system. SAS-SFR is considered as the reference code for analysis of the pre-disassembly phase of severe accidents in SFR [76]. Further validation of ASTEC-Na is reported to be under progress [72]. Experimental validation of both the codes against the melt motion behaviour during slow rates of reactivity insertion, for e.g., E9, as well as the clearly recorded blanket penetration in E9bis [33], is currently unavailable. Mathematical modelling involved in these codes, that may be applicable for India's current and future SFR, is not published in available literature. Furthermore, India does not have the license to use these codes.

A preliminary melting and multi-phase flow model was previously developed for melt motion inside annular fast reactor fuel pins [77]. The model could represent nuclear fuel melting and the resultant multi-phase flow using conventional macro-channel closure laws. Validation of the model was carried out against the thermal parameters of the CABRI-E9 test. However, challenges associated with modelling molten fuel relocation (outlined in Section 1.6) were not addressed appropriately (for e.g., small hydraulic diameter, melt freezing on colder pellet surfaces, increase in viscosity of partially solidified melt). As a preliminary benchmarking exercise, the model was employed to simulate the CABRI-E9bis test, in which fragmented top blanket pellets were penetrated by molten fuel between 65-69 s [33]. With this model, as soon as melting began, the melt travelled rapidly to the bottom-most node of the cavity and solidified, despite the experimental observations regarding slow motion [77].

Furthermore, the penetration of the top-most fuel node did not take place at all. Hence, the available model gave inconsistent results with regards to the benchmark in-pin fuel motion data. It is evident that there is a need to develop an advanced multi-phase flow model which can address the modelling challenges and generate results consistent with the benchmark in-pin fuel motion data.

1.7.3 Reactor safety studies

The Argonne National Laboratory (ANL) has evaluated the effectiveness of in-pin fuel motion for reactor safety [36]. The report states that the effectiveness of in-pin fuel motion as a safety feedback (during UTOP) may be limited due to freezing of fuel in the colder regions (particularly for annular, mixed-oxide fuel pins, which are to be used in Indian fast reactors). Freezing may lead to blockage of the internal flow pathway, whereas easy escape of fission gases may prevent strong pressure forces. In a comprehensive summary of the CABRI-2 tests, Papin states that no significant reactivity feedback is expected in annular fuel pins [35]. This is true based on two pre-conditions: (a) the melt remains limited to the fissile height of the pin and (b) the melt mass remains small. However, if these conditions are violated and a significant amount of melting takes place, the impact of in-pin fuel motion on SFR safety cannot be neglected. In fact, it is experimentally proven that given sufficient melting, the melt can relocate: (a) as far as the top of the active region (E9) (b) beyond the active region (E9bis) [33]. Since the relocation is dynamically coupled with its reactivity feedback, it will affect the core reactivity, and must be taken in account. Computation of the relocation reactivity feedback requires analysis of the whole core of SFR to determine the extent of propagation of melting and the consequential fuel relocation in each core channel. SFR safety studies that incorporate the mechanics of in-pin fuel motion in the

safety paradigm are scarce in literature. Furthermore, studies have not addressed the experimentally proven relocation of fuel beyond the active region, despite the possibility of a strong, negative reactivity feedback.

From the perspective of Indian SFR safety studies, an earlier reactor safety assessment utilized the fuel squirting feedback for the mitigation of UTOP accident [3]. The study was based on an ample evidence of squirting in solid fuel pins at low rates of reactivity insertion [29]. It was theorized that since the resistance to fuel squirting was greatest in solid fuel pins and comparatively smaller in annular fuel pins, the likelihood of squirting was greater in case of the latter. However, data obtained from CABRI-2 and CABRI-FAST test series has proven that the dominant relocation mechanism in annular fuel pins under UTOP is in-pin fuel motion. Fuel ejection from the active core is severely constrained and is only possible under exceptional circumstances, such as: (a) if the top blanket pellets are fragmented a-priori and significant melting occurs [33], or (b) if there is an excessively high rise in reactor power ($(315 \% P_n)$) accompanied with coolant boiling [34]. Even under such conditions, the mass of fuel squirted out of the fissile column appears to be small. In view of such experimental evidence, the methodology of Indian SFR safety assessment needs to be updated.

Sathiyasheela et. al. [30] have demonstrated the effectiveness of inherent safety features of a medium-sized SFR (500 MWe) towards UTOP mitigation using the indigenously developed code 'PREDIS'. It is reported that negative reactivity feedbacks (control rod driveline expansion, fuel Doppler and axial expansion) eliminate the external reactivity insertion and bring the reactor to a safe state, without extensive core damage. The study neglected the fuel squirting feedback. However, in the absence of a fuel relocation tool, it was assumed that molten fuel remained stationary. Since fuel

relocation influences the overall fuel temperature distribution, it also influences the fuel Doppler and axial expansion feedbacks. Therefore, India's SFR safety analysis codes require a computational tool dedicated to pre-failure molten fuel relocation to incorporate its practical impact on SFR accident kinetics.

1.7.4 Summary and gap areas

Previous experimental studies have revealed three broad categories of pre-failure fuel relocation, viz., annular fuel squirting [25], solid fuel squirting [28] and in-pin fuel motion [33,34]. From the perspective of contemporary fast breeder reactors (for e.g., India's PFBR [13], FBR-600 [6]) in-pin fuel motion is the most important category of displacement, due to: (a) associated test parameters (1-5 C/s and annular fuel pellet design), which are also expected during UTOP, and (b) high failure threshold of annular fuel pins under UTOP, which ensures significant in-pin fuel motion prior to clad failure. Experimental test series conducted in the CABRI reactor have provided the most detailed and relevant information on the characteristics of in-pin fuel motion [33,34]. In particular, the E9bis test has revealed the transient time at which molten fuel penetrates the gaps between the fragments of the top blanket pellets [33]. However, the fast neutron detection device (hodoscope) is unable to generate a clear picture of the melt motion as a function of time due to sensitivity constraints.

The available thermal models [54,55] on nuclear fuel melting are confined to solid pellet geometry. The challenges associated with annular pellet geometry (for e.g., axial relocation of melt, presence of fission gases) are not addressed with these models (Refer Section 1.6). Pressure forces generated by transient fission gas release are hypothesized as the main driver behind both annular fuel squirting [25] and solid fuel squirting [28]. However, the available thermal models omit the effect of transient fission gas release.

Therefore, these models cannot be applied towards the simulation of fuel relocation in annular fuel pins. Furthermore, most fuel vaporization studies are focused on the phenomena after clad failure, and do not address the vaporization concerns before clad failure [58].

Previous computational tools dedicated to fuel relocation in fast reactor fuel pins are confined to annular fuel squirting and solid fuel squirting [66,68]. Therefore, their direct application towards India's SFR safety analysis is not possible. Present safety assessment codes with dedicated computational tools for in-pin fuel motion are ASTEC-Na (FOAM) [72], and SAS-SFR [75]. Both codes are experimentally validated against the thermal and fission gas release data of benchmark experiments [53]. However, validation of their in-pin fuel motion tools with the corresponding benchmark data, which is most relevant for India's SFR safety requirements, is unavailable. Their corresponding mathematical models are not published in open literature. A melting and multiphase flow model intended for in-pin fuel motion in annular fuel pins is previously published [77]. However, this model is unable to generate relocation predictions that are consistent with the benchmark in-pin fuel motion data.

Previous reactor safety studies have neglected the reactivity feedback of in-pin fuel motion based on the assumptions of limited melting, fuel freezing and confinement of melt mass inside the fissile height [35,36]. On the contrary, a safety study of PFBR has cited fuel squirting as the dominant accident mitigation mechanism in UTOP [3], based on the experimental evidence of squirting in solid fuel pins. Sathiyasheela et. al [30] have demonstrated the inherent safety of an SFR system similar to the Indian PFBR [13], by using the control rod driveline expansion feedback. However, molten fuel has been assumed to remain stationary due to the absence of a dedicated computational tool.

Experimental studies have clearly shown that if extensive melting does occur, in-pin fuel motion can relocate the melt up to the top of the fissile column [33]. Significant variations exist in the axial power profile within the fuel column. Therefore, even if the melt remains trapped inside the fuel column, it can undergo relocation from a high neutron density region (for e.g., core mid-plane), to a low neutron density region (for e.g., top/bottom of fuel column). Such a relocation will give rise to a negative reactivity feedback. Conversely, if fuel is relocated from the top-most region of the active core to the core mid-plane (due to gravity), the resultant reactivity feedback will be positive. Such a relocation can result in severe consequences. SFR safety studies that address the neutronics effects of in-pin fuel motion are scarce. Whole-core investigations of UTOP in modern SFR systems that utilize computational tools dedicated to in-pin fuel motion [72,75] are unavailable.

Benchmark experiments have also proven that fuel relocation out of the active core region is possible with annular fuel pins even under slow reactivity insertion rates [33,34]. Such a relocation can be highly advantageous towards SFR safety. Particularly, the presence of small gaps in the top blanket pellets has been shown to remove melt out of the active core at a reasonably moderate level of power rise. Computational tools capable of simulating this phenomenon are scarce in literature.

From the review, the following gap areas in literature are revealed:

- ❖ An adequate theoretical description of the fluid dynamics of in-pin fuel motion continues to pose a challenge in the field of nuclear reactor thermal hydraulics. A need is felt to develop an advanced mathematical model which can represent the underlying physical phenomena appropriately and generate flow predictions in consistence with experimental findings. The model should be able to bring out a

clear picture of the pre-failure molten fuel relocation behaviour and supplement the limitations of previous experimental results.

- ❖ A dedicated computational tool is required to investigate the fluid dynamics of in-pin fuel motion under modern SFR conditions and to determine the basic nature of relocation, i.e., whether melt is relocated away the core mid-plane or towards it. For its reliability, the tool should be comprised of well-benchmarked mathematical models, particularly for melt relocation.
- ❖ For a realistic assessment of the consequences of in-pin fuel motion on SFR safety, it is necessary to address the intrinsic coupling between the hydrodynamics and reactor neutronics. It is also necessary to extend the computational analysis to the whole core to estimate the practical magnitude of the relocation reactivity feedback and its controlling parameters.
- ❖ There is a need to address the likelihood of molten fuel vaporisation prior to clad failure in modern SFR systems. A basic study can be carried out using the above-described computational tool by comparing the peak temperature of molten fuel with the corresponding saturation vapour temperature.
- ❖ Due to the importance of fission gas release induced pressure forces in both annular fuel squirting and solid fuel squirting, it is essential to develop mathematical models that can represent the physics of these forces appropriately in case of in-pin fuel motion. Since the magnitude of these forces is largely dependent on the transient rate of gas release from molten fuel, there is a need to develop a robust model for the same, which can then be coupled with the advanced multi-phase flow and thermal models. The consolidated computational tool, comprising of all the models, can be used to assess the importance of pressure forces in modern SFR during UTOP.

- ❖ From the experimental results, a scope for significant improvement in the inherent safety of future SFR systems is identified. The scope calls for computational investigations of melt relocation inside alternative fuel pin designs, which may facilitate early removal of molten fuel from the active core region. Such an investigation requires a dedicated computational tool that can simulate the physics of melt penetration in the blanket pellets appropriately.

1.8 Major challenges and motivation

From the diverse set of gap areas, a dedicated computational tool has emerged as the primary requirement for a physically appropriate integration of pre-failure molten fuel motion in the reactor safety assessment of India's upcoming fast reactors. The code should be able to (a): resolve the important hydrodynamic effects, (b) generate predictions that are consistent with the benchmark in-pin fuel motion data, and (c) couple the reactor neutronics aspects of fuel relocation with its hydrodynamics, to resolve the dynamically coupled nature of the problem. The computer codes that have been developed for the numerical prediction of pre-failure molten fuel motion in SFR can be listed as follows: PINEX-AR, FUMO-E, PINACLE, ASTEC-Na (FOAM) and SAS-SFR [63,66,68,72,75]. The PINEX-AR and FUMO-E codes are based on the experimental database of the PINEX test series. Their scope is limited to rapid reactivity insertion rates, which are not applicable to UTOP conditions in modern SFR. The PINACLE module is a part of the SAS4A code system [76]. Although it is an appropriate model for melt relocation inside completely solid fuel pins, its framework is unsuitable for annular fuel pins due to the assumption of homogeneous multi-phase flow [69]. The FOAM model of the ASTEC-Na code system and the SAS-SFR code are relevant tools for studying the pre-failure fuel relocation in India's current and future

SFR. However, validation of both tools with the benchmark in-pin fuel motion data for annular, MOX fuel pins under postulated UTOP conditions (1-5 C/s) in modern SFR systems is not published [72]. This benchmarking is essential for a reliable assessment of the pre-failure molten fuel relocation reactivity feedback, which is required for the safety analysis of India's future SFR. Furthermore, India does not have the license to use the above-described code systems. A model for melting and multiphase flow inside annular fuel pins has been previously published [77]. However, the model is unable to generate motion predictions that are consistent with the benchmark in-pin fuel motion data. Hence a long-standing need has been identified as the development of a dedicated computational tool for integrating the pre-failure molten fuel relocation in the safety assessment of India's current and future fast reactors. The necessity of developing such a computational tool and its utilization in reactor safety analysis is the primary motivation of the present work.

1.9 Aim of the present work: outline of the thesis

Motivated by the above considerations, the main objective of the work presented in this thesis is to develop a computational tool for the simulation of mixed oxide ((U-Pu)-O₂) fuel melting and relocation in sodium-cooled fast breeder reactors during unprotected transient overpower accidents. The study emphasizes on capturing the complex interplay of hydrodynamic forces, including the pressure forces generated by transient fission gas release, as well as addressing the dynamic coupling between melt hydrodynamics and reactor neutronics. The required computational tool must be able to resolve the hydrodynamics of fuel relocation appropriately and generate results that are consistent with the benchmark experimental data. Consistent with the challenges and gap areas outlined above, following topics are investigated in this thesis:

❖ Development of an Advanced Multi-phase Thermal Hydraulic Model and Investigation of Melt Relocation in Fast Reactors: An advanced mathematical model is developed with the following modelling efforts: (a) Crust formation model is developed to simulate the solidification of molten fuel in relatively cooler regions. (b) Particle viscosity model is developed to simulate the increase in cohesive forces between the molecules of partially solidified fuel (c) A smear density formulation is added to represent the thermal expansion of molten fuel at high temperatures. (d) A free volume model is added to represent the escape of fission gases through inter-pellet gaps to the fission gas plena. (e) Based on a dimensional analysis, mini-channel flow regime constraints are incorporated in the closure laws of multiphase flow to represent the effects of surface tension. The resultant set of governing equations involving energy conservation in fuel, clad and coolant as well as multiphase flow (mass, momentum, and energy conservation) are solved following an explicit finite difference numerical scheme.

Based on the above unified approach of melting and multi-phase flow modelling, an advanced numerical algorithm is devised that can capture the rate of fuel melting and resolve the hydrodynamic effects of gravity, pressure (due to fission gas release), viscosity (due to solidification), drag, virtual mass and surface tension. Numerical simulations are performed for the CABRI-E9bis test. The corresponding results are compared with the experimental data quoted in literature, leading to successful validation of the algorithm. Subsequently, the benchmarked model is extended to predict the melt motion characteristics expected in a single fuel pin of a typical, medium-sized (500 MWe), pool-type, liquid-sodium cooled fast breeder reactor (FBR-500) [3]. The sensitivity of the relocation towards burnup is assessed by

comparative analysis of equilibrium and BOL fuel pins. Numerical simulations of the transient power rise typical to UTOP in modern SFR are carried out for both fuel pins. Furthermore, the effect of fission gas escape to the plenum is analysed. Finally, a mass relocation analysis is carried out to study the effect of in-pin fuel motion on the axial distribution of fuel mass. The present study is aimed at developing novel predictions of the fluid dynamics of in-pin fuel motion expected in fast breeder reactors. The study is also aimed at addressing the concerns of severe consequences due to melt relocation towards high neutron density regions (for e.g., core mid-plane).

- ❖ Reactor Dynamics Investigation of In-pin fuel motion during Unprotected Transient Overpower Accidents: As apparent from the intrinsic coupling between the hydrodynamics and the reactor dynamics of melt relocation, realistic assessment of the impact of in-pin fuel motion on severe accidents requires that appropriate attention be given to both aspects. Furthermore, fuel melting may propagate radially from the central subassembly towards outer fuel subassemblies, depending upon the reactor over-power level and radial power distribution in the core. Therefore, the benchmark-proven numerical algorithm is utilized for the development of an interdisciplinary computational algorithm with the help of the in-house point kinetics code, PREDIS. A simple and robust parallel processing technique is developed to extend the numerical algorithm to the entire SFR core and to address the above-mentioned intrinsic coupling. An optimization study is carried out to enhance the efficiency of the coupled system. Subsequently, coupled hydrodynamic/neutronic simulations of UTOP are carried out for FBR-500 reactor core. In view of the sensitivity of melt displacement towards core condition, the simulations are carried out for both BOL and equilibrium core conditions. Best estimate as well as

conservative simulations of each core are carried out to address the uncertainties in the control rod withdrawal worth, fuel Doppler and material removal worth. The propagation of melting in the reactor core and the associated reactor dynamics are studied for each case. Comparative analysis of UTOP with and without in-pin fuel motion feedback is carried out to address the impact of in-pin fuel motion on the inherent safety of SFR. A thermodynamic analysis of molten fuel is carried out to investigate the potential of fuel vaporisation prior to clad failure. Finally, the effects of core condition and reactivity insertion rate on the melt propagation and relocation feedback are studied. The aim of the present study is to investigate the propagation of melting in the BOL and equilibrium cores of fast reactors during UTOP with due consideration of the neutronics aspects of melt relocation. The study is also aimed at developing realistic estimates of the reactor neutronics impact of in-pin fuel motion on the severe accident progression.

- ❖ Development of a Fission Gas Release Solver and Investigation of Melt Relocation in Alternative Axial Blanket Designs: In response to the finding of appreciable sensitivity in the fluid flow, fuel mass relocation and progression of UTOP towards the core configuration, a dedicated steady-state and transient fission gas release solver (FGR) is subsequently developed and integrated with the benchmark-proven numerical algorithm. Emphasis is placed on the mechanistic representation of the micro-scale gas release mechanisms at the intra-granular, inter-granular and transient gas release levels. First, steady-state validation of FGR solver is performed using isothermal gas release data, FBTR mixed-oxide fuel irradiation test and the results of the FEAST-OXIDE code, whereas transient validation is performed against the E9 test conducted in CABRI reactor. The resultant Multi-phase In-pin Thermal

hydraulic Relocation Algorithm (MITRA) is also verified against the E9bis melting and displacement data for the sake of experimental consistency.

With appropriate representation of the micro-scale fission gas release processes, investigation of the transient gas release in a single fuel pin is carried out with the consolidated computational tool, MITRA. Next, the realistic effect of burnup dependent transient fission gas release on fuel melting and relocation behaviour is investigated. Next, a consolidated whole-core simulation of UTOP in equilibrium core (conservative case) is carried out with MITRA to determine the effects of modelling improvements on the accident progression. The aim of the present study is to investigate the realistic impact of fission gas release on melting, relocation, and progression of UTOP accident. Finally, to investigate a highly desirable fuel relocation out of the active core through suitable fuel pin design modifications, MITRA is augmented further to simulate multi-phase flow in annular blanket pellets and the fission gas plena. To achieve this, the previously developed crust formation model is replaced with a bulk freezing model, which can capture the breakage of solidified crust and further penetration of fuel in the blanket column. Subsequently, numerical simulations of UTOP with geometrically modified fuel pin designs are carried out. The study is aimed at investigating the potential for improvement in the inherent safety features of current and future SFR.

1.10 Closure

The chapter presents a brief academic background of this thesis. The role of fuel squirting in safety analysis of SFR is described. Major modelling challenges are discussed in brief. From a thorough review, gap areas in the current literature are highlighted, and the finally the main motivation, aim and scope of work are brought out

clearly. The next chapter describes the computational methodologies adopted towards severe accident simulation in terms of system specifications and reactor neutronics, as well as a working description of an indigenously developed computational tool MITRA.

Chapter 2

Computational Methodology

In this chapter, the methodologies used to simulate the unprotected transient overpower accident, viz., fast reactor system specification, reactor neutronics modelling, experimental benchmark data, and salient features of the indigenously developed code MITRA are detailed. The chapter begins with the technical specification of the SFR system utilized for severe accident simulation. Thereafter, various computational terminologies needed to describe molten fuel relocation are discussed. This is followed by reactor neutronics data needed for severe accident simulation and reactor kinetics methodology. Experimental results utilized for code benchmarking are discussed. Finally, salient features of MITRA code are described in short to illustrate its working methodology.

2.1 System specifications

2.1.1 Brief outline of reactor core

The present study utilizes a 500 MWe, pool-type, liquid sodium cooled, fast breeder reactor for the simulations of the unprotected transient overpower accident. The specifications of this system are similar to a medium-sized, mixed-oxide ((U-Pu)-O₂) fuelled SFR system (for e.g., PFBR [13]). A schematic diagram of the selected SFR (hereafter FBR-500) core presents the arrangement of fuel, blanket, control safety rod (CSR), diverse safety rod (DSR) and reflector subassemblies (Refer Fig. 2.1). The fuel subassemblies are grouped between the inner and outer core regions, based on their Pu-239 enrichment. Table 2.1 presents the basic parameters of the core. Primary and backup shutdown systems consist of 9 CSR and 3 DSR, respectively. Radial blanket subassemblies containing depleted UO₂ pins are provided outside the outer core region.

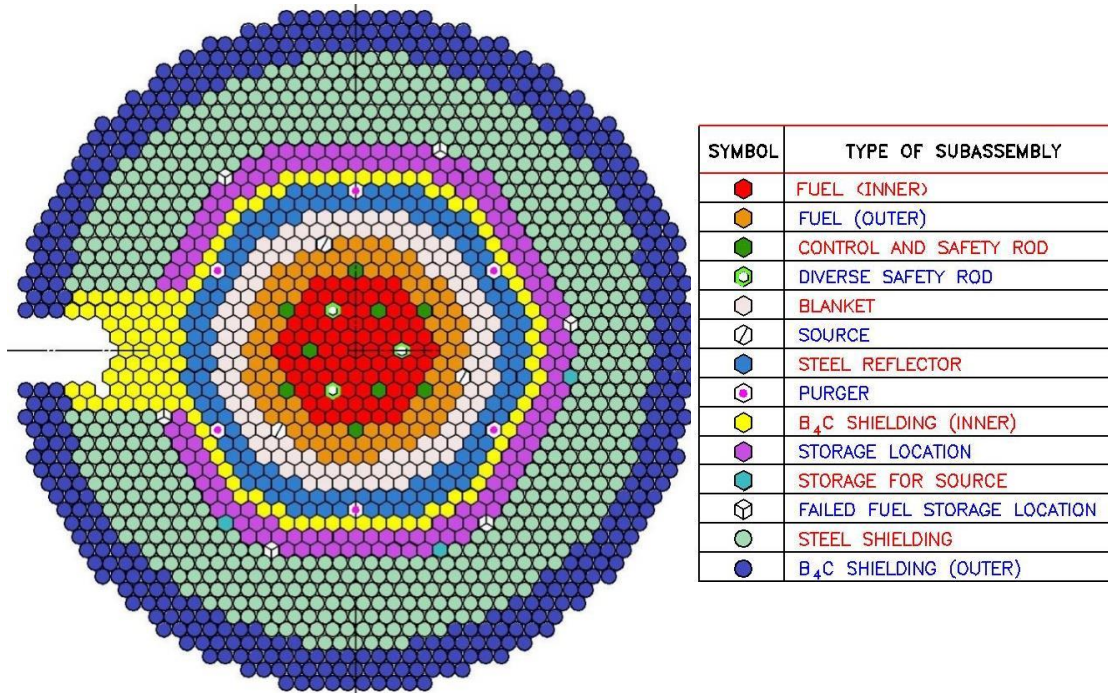


Figure 2.1: Configuration of FBR-500 core at beginning of equilibrium cycle [15].

Table 2.1: FBR-500 core parameters (dual data represents inner/outer core region values).

Parameter	Value
Total heat generation (MW)	1250
Fuel type	((U-Pu)-O ₂)
Core enrichment (Pu/(U+Pu)), %	20.7/27.7
Fissile length, L (m)	1
Number of pins per fuel subassembly	217
Number of pins per blanket subassembly	61
Number of CSR rods	9
Number of DSR rods	3
Inlet coolant temperature, $T_{ct,in}$ (°C)	397

The equilibrium core configuration is arrived from the beginning-of-life configuration after two fuel cycles of 180 effective full power days [78]. Table 2.2

presents the core averaged burnup levels, fuel phase-change temperatures [79] and number of subassemblies for both core configurations. Both the radial and axial power profiles become flatter as the reactor core transitions from BOL to equilibrium configuration. Hence, the maximum linear heat rating (X_{max}), defined as the heat generation per unit length of a fuel pin (located in the highest power region), at its peak power elevation, is greater in case of BOL core. Core enrichment levels and inlet coolant temperatures are equivalent for the two cores.

Table 2.2: Relevant parameters of BOL and equilibrium cores (inner/outer core) [79,80].

Parameter	BOL	Equilibrium
X_{max} (kW/m)	45	41
Bu_{avg} (atom percent)	0	3
$T_{solidus}$ (K)	2998/2962	2983/2947
$T_{liquidus}$ (K)	3038/3010	3023/2995
No. of fuel subassemblies	88/90	85/96
No. of blanket subassemblies	114	120

All fuel and blanket subassemblies in the core are connected hydraulically with a common inlet and outlet coolant plenum, i.e., all subassemblies experience equivalent inlet and outlet pressures. Coolant flow zones applicable to FBR-500 are prescribed based on the core radial power profile [15]. Orifice plates with different flow resistances are built into the foot of the subassemblies to ensure that the flow rate is proportional to the power generation, so that the steady-state clad hotspot temperatures remain below the design threshold in all the subassemblies [81]. Accordingly, the FBR-500 core is divided in four inner-core, three outer-core, and three radial blanket channels for safety studies [82] (Refer Table 2.3).

Table 2.3: Fuel subassembly grouping for FBR-500 (\dot{m}_{ct} = coolant mass flow rate in 1 subassembly) [15,80].

Zone	No. of sub-assemblies	(% $X_{max}/X_{max,I}$)		\dot{m}_{clnt} (kg/s)
		BOL	Equilibrium	
I	1	100	100	35.8
II	30	94.3	94.8	35.8
III	24	85.3	86.6	31.4
IV	30	77.9	79.9	28.8
V	30	86.7	90.2	34.1
VI	42	69	72.7	28.8
VII	24	52.1	55.3	20.8

Maximum power generation occurs in Zone-1 (central subassembly), followed by Zone-2 (thirty subassemblies) and Zone-5 (thirty subassemblies at the beginning of outer core). The radial power variation is defined as the ratio of zone-wise peak LHR (X_{max}) and Zone-I peak LHR ($X_{max,I}$). The power is greater in Zone-V as compared to Zones-III and IV, due to relatively higher enrichment in the outer-core (Refer Table 2.3). Flattening of the radial power profile during the transition from BOL to equilibrium configuration is evident from the data. Similarly, flattening of the axial power profile is evident from the axial peak factor for the equilibrium core (~ 1.241 , Zone-I) as opposed to the BOL core (~ 1.246 , Zone-I).

2.1.2 Fuel subassembly and pin parameters

The study is focused on annular fuel pellet design, which is to be employed in current and future SFR, such as PFBR, European Sodium Fast Reactor (ESFR [14]), and FBR-600 [6]. Schematic diagrams of the fuel subassembly, fuel pin and their cross-sectional views are presented in Fig. 2.2. The prefabricated cavity present inside the

fuel pellets is closed by solid blanket pellets at its axial boundaries. A helical spacer wire supports the pin and promotes cross-channel mixing of liquid sodium.

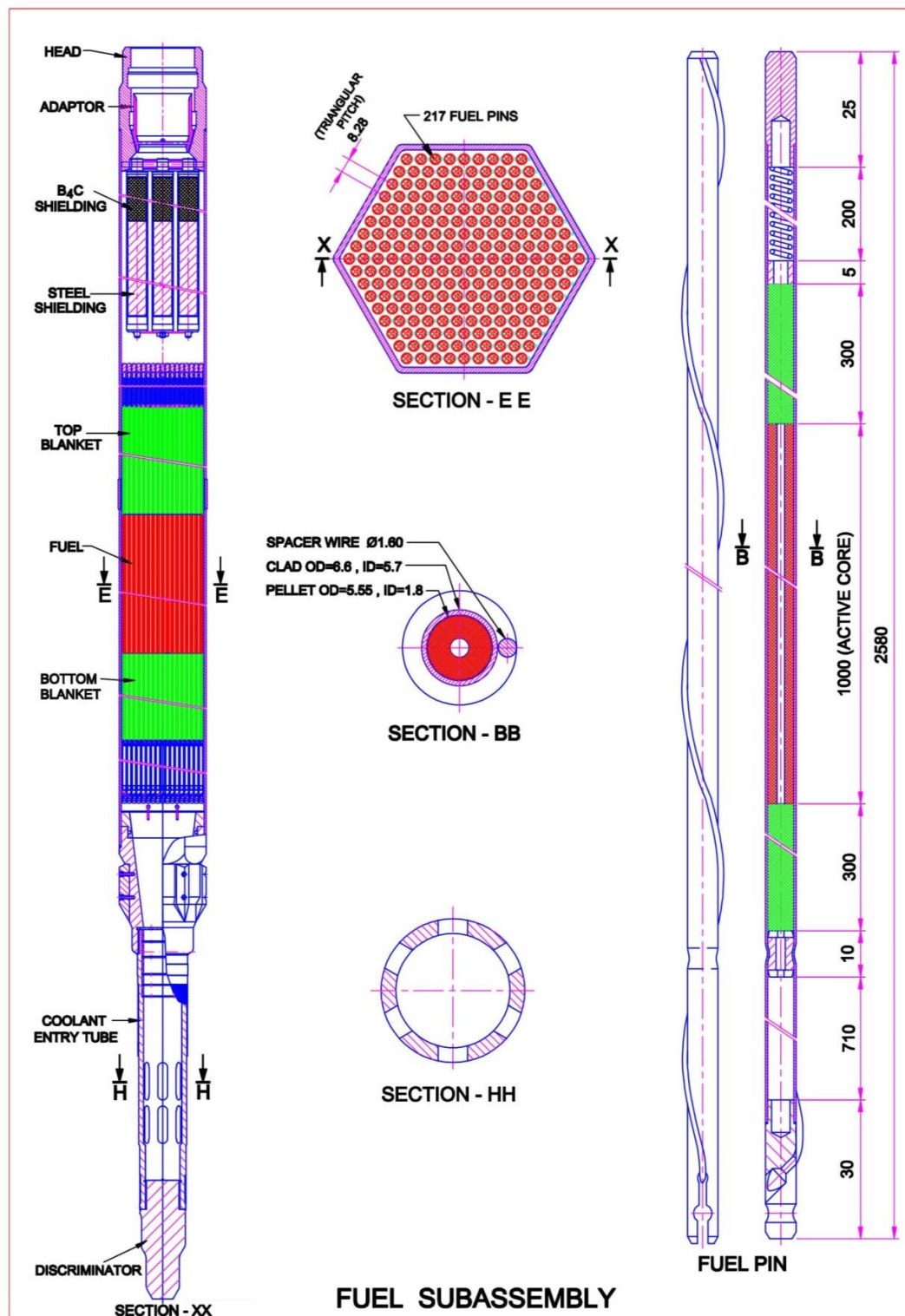


Figure 2.2: Schematic diagram of FBR-500 fuel subassembly and fuel pin [52,83].

Table 2.4: FBR-500 fuel specifications (I: inner core region; O: outer core region) [79,84,85].

Parameter	Sign	Value
Fuel inner radius, mm	R_I	0.9
Fuel outer radius, mm	R_O	2.775
Inner clad radius, mm	R_{CI}	2.85
Outer clad radius, mm	R_{CO}	3.3
Fuel column length, m	L	1
Top blanket length, m	L_{TB}	0.3
Bottom blanket length, m	L_{BB}	0.3
Deviation from stoichiometry	x	0.02
Theoretical fuel density (kg/m^3)	TD	11063/11097
Fuel pellet density (kg/m^3)	ρ_{sol}	10565 (I), 10598 (O)
Smeared density (% TD)	-	90
Mass of fuel per pin (kg)	-	0.225
Length of upper plenum	L_{UP}	0.2
Length of lower plenum	L_{LP}	0.71
Clad material	-	D9

The pin bundle arrangement within a hexagonal, stainless-steel wrapper is visible in Fig. 2.2 (Cross-sectional view E-E). Multiple slots in the foot of the subassembly act as coolant inlet points. Orifice plates can be seen above these entry points. Geometrical and thermo-physical specifications of the fuel pin are detailed in Table 2.4. The data is published in the Appendix-A of ‘Fast Spectrum Reactors’ [84]. Theoretical fuel density

is derived from well-established property correlations [79]. Fuel densities presented in Table 2.4 are defined below.

2.2 Computational terminologies

(i) Melting point

The melting points of mixed-oxide fuel are the solidus (T_{sol}) and liquidus (T_{liq}) temperatures, which indicate the beginning and completion of melting respectively [79]. Therefore, phase-change in MOX fuel is characterized by a mushy layer instead of a sharp melt interface [86]. Latent heat absorption occurs simultaneously with sensible heating within this zone. For modelling, the mushy layer is generally represented by a single melting point ($T_{int} = (1 - o)T_{sol} + oT_{liq}$) based on a linear interpolation between the solidus and liquidus points. An average melting point is used in the present work ($o = 0.5$). Appendix-A details the associated thermophysical property correlations.

(ii) Melt interface radius

The melt interface radius (r_{int}) denotes the approximate position of the mushy layer within the fuel pellet. Computationally, it is defined as follows:

$$r_{int} = \left(\frac{r_{i+1} - r_i}{T_{i+1} - T_i} \right) (T_{int} - T_i) + r_i, \quad T_i > T_{int} > T_{i+1} \quad \dots (2.1)$$

In the above equation, T_{i+1} and T_i are temperatures ($^{\circ}C$) of two radially consecutive fuel nodes situated at r_{i+1} and r_i .

(iii) Solidus radius

The solidus radius is analogous to the melt interface radius, except that it denotes the location of start of phase-change:

$$r_{sol} = \left(\frac{r_{i+1} - r_i}{T_{i+1} - T_i} \right) (T_{sol} - T_i - 273) + r_i, \quad T_i > T_{sol} > T_{i+1} \quad \dots (2.2)$$

The above radius indicates the outermost extent of the phase-change phenomena and is used to calculate the normalized radial melt extent ($\% R_{sol}/R_o$).

(iv) Melt mass fraction

It is used to quantify the amount of fuel melting for a single fuel pin. It is defined as the ratio of mass of fuel with temperature greater than (or equal to) the solidus temperature (T_{sol}), to the total fuel mass present inside a fuel pin at a given instant.

$$MMF (\%) = \frac{100 \int_{Z_b}^{Z_t} (R_o^2 - R_{sol}^2) dz}{(R_o^2 - R_i^2)(Z_b - Z_t)} \quad \dots (2.3)$$

In the above equation, R_i, R_o are the pellet inner and outer surface radii, Z_b, Z_t are the elevations at BFC and TFC, respectively. To quantify the amount of melting in the entire reactor core, a core averaged melt mass fraction is defined as follows:

$$MMF_{core} (\%) = \frac{\sum_{j=1}^{j=7} N_{FSA,j} MMF_j (\%)}{\sum_{j=1}^{j=7} N_{FSA,j}} \quad \dots (2.4)$$

In the above equation, $MMF_j (\%), N_{FSA,j}$ are the zone-wise melt mass fraction and number of fuel subassemblies respectively (Refer Table 2.3).

(v) Reactor over-power

It is generally defined as the percentage excess in reactor power with respect to the nominal power $\left(\frac{P(t) - P(t=0)}{P(t=0)} \% \right)$. Here, steady-state power (also denoted as nominal power (P_n)) exists at the start of the transient ($t = 0$). In the present work, to avoid confusion, the excess power definition is not used. Instead, the reactor over-power is simply represented by the ratio of the transient and nominal power levels ($\% P(t)/P_n$).

(vi) Fuel density

The theoretical density of nuclear fuel (TD) is generally defined at the standard operating temperature and pressure (STP) based on experimental correlations [79].

During fabrication, in-built porosity is introduced in the fuel pellets to improve the irradiation performance. Therefore, the physical density of fuel pellets (ρ_{sol}) is denoted as a fraction of the theoretical density ($\rho_{sol} = TD(1 - p)$), where p represents the fraction of in-built porosity. The liquid fuel density (simply ρ_f) does not involve in-built porosities and is hence evaluated directly from the thermophysical property correlations. Another parameter of interest for reactor neutronics is the smeared density of nuclear fuel, which is mathematically defined as follows:

$$\rho_{smear}(\% TD) = \left(\frac{100(R_o^2 - R_i^2)(1-p)}{R_o^2} \right) \quad \dots (2.5)$$

The density data associated with the FBR-500 pin is detailed in Table 2.4. Corresponding thermophysical property correlations are presented in Appendix-A.

2.3 Reactor neutronics methodology

2.3.1 Necessary perturbation worth data

The reactivity effects of any change in the core configuration (for e.g., material relocation, sodium voiding) are calculated with a perturbation analysis of the neutron multiplication factor [87]. A first order approximation of the perturbation theory is utilized based on the assumption that the perturbation being studied is so small that the difference between the perturbed and unperturbed neutron flux is negligible [88]. The technique is well established with multiple applications in safety studies of medium-sized SFR [30,82]. Change in reactivity caused by any perturbation is quantified in terms of a reactivity ‘worth’ (pcm/kg). For the present study, material removal worth data for fuel, coolant, and cladding steel is derived from literature (Refer Table 2.5). The fuel void worth is required to compute the fuel relocation feedback (Section 2.3.4). Normalized axial profiles of the fuel void worth for Zone-I (central subassembly) of

both BOL and equilibrium core configurations are presented in Fig. 2.3. Normalization is with respect to the maximum fuel mass removal worth of each configuration ($W_{max} = -41 pcm$, BOL; $W_{max} = -39 pcm$, equilibrium). Table 2.6 presents the distribution of the fuel void worth among the inner-core and outer-core channels.

Table 2.5: Material void worth data for FBR-500 equilibrium core [82].

Material	Void worth (pcm)
Fuel (inner core)	-18,908
Fuel (outer core)	-16,671
Fuel (axial blanket)	-10
Fuel (radial blanket)	-187
Coolant	+620
Steel	+3181

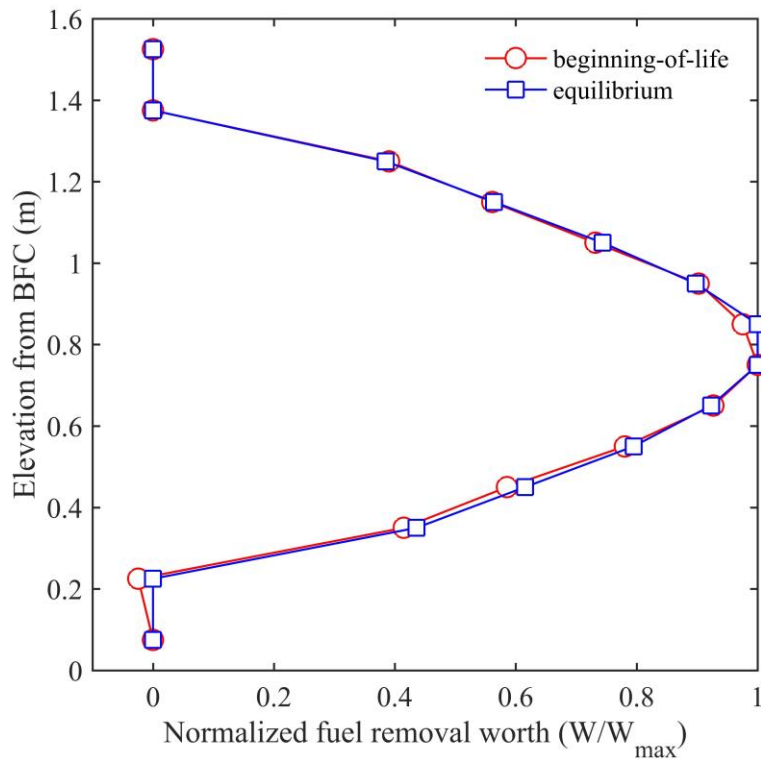


Figure 2.3: Axial profile of fuel void worth [89].

Removal of entire fuel mass from Zone-1 (central fuel subassembly) results in a negative reactivity feedback of -298 pcm (BOL) and -287 pcm (equilibrium) [82]. Removal of all fuel from Zone-2 subassemblies results in a negative feedback of -7931 pcm (BOL) and -7736 pcm (equilibrium). The relative impact of fuel removal for each zone depends upon the respective number of fuel subassemblies (Refer Table 2.3). Since Zone-1 consists of a single subassembly, the negative reactivity feedback generated due to fuel voiding is much smaller as compared to the other fuel zones. The delayed neutron fraction for both BOL and equilibrium cores is ~ 355 pcm [82].

Table 2.6: Zone-wise fuel void worth distribution ($\% W_f / \sum W_f$) [82,89].

Zone	BOL core	Equilibrium core
I	0.8	0.8
II	22.2	21.2
III	14.3	13.9
IV	15.6	15.4
V	19.4	19.8
VI	19.9	20.6
VII	7.8	8.1

In the present work, external reactivity insertion (ρ_{ext}) due to unexpected withdrawal of a single CSR with the simultaneous failure of the plant protection system is studied. The rate of insertion ($\frac{d\rho_{ext}}{dt}$) is a function of the differential worth of the CSR as well as the speed of withdrawal. A typical, slow speed of withdrawal (2 mm/s) is considered, based on the CSR design of a 500 MWe SFR [90]. The differential as well as integral worth of CSR are derived from the results of Devan et. al [91]. The CSR design consists of 65 % enriched B_4C in the centre (0.71 m) and natural B_4C (0.2 m) at

both the top and bottom ends (Refer Fig. 1.3). The differential and integral worth of the CSR are presented in Fig. 2.4. Typical banking depths of CSR for FBR-500 are between 0.3-0.4 m. For conservative analysis of UTOP, the errant CSR is withdrawn from a deeper location. Case-wise accident parameters for whole-core simulations are detailed in Chapter 4. Parameters for single pin studies are detailed in Section 2.3.3.

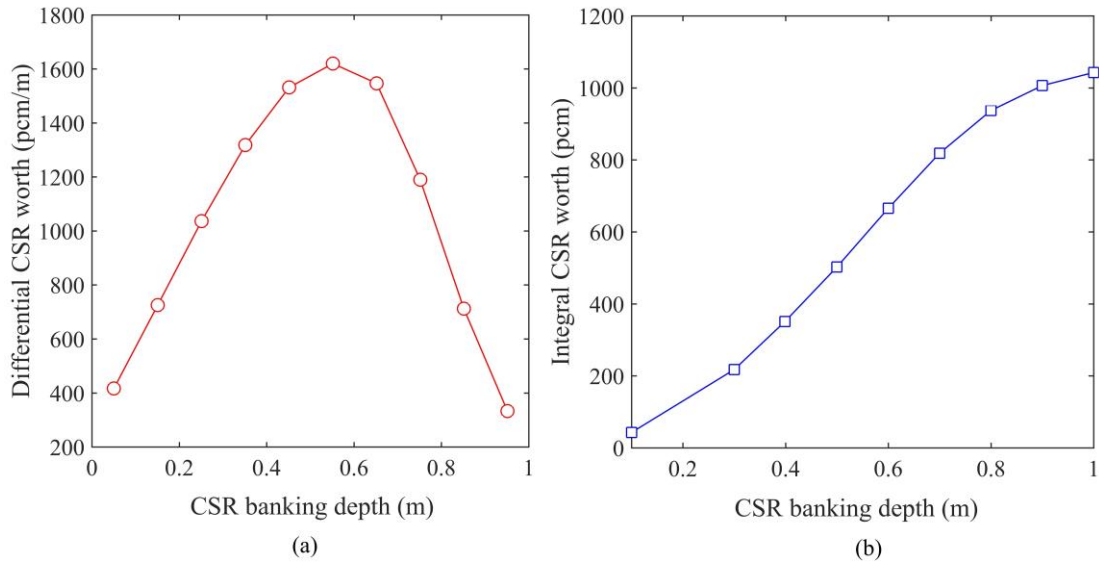


Figure 2.4: Single CSR withdrawal worth data utilized in UTOP simulations. (a) Differential worth profile (b) Integral worth profile [91].

2.3.2 PREDIS: pre-disassembly phase analysis code system

PREDIS is an in-house code for studying the dynamics of fast reactors during the pre-disassembly phase of core disruptive accidents [92]. It utilizes a 2-D cylindrical ($r \times z$) model of the reactor core [30]. The core is divided into ten radial channels to represent the seven fuel and three blanket zones of FBR-500 (Refer Table 2.3). The code uses a representative single pin model for each radial zone to compute the transient phenomena in the corresponding group of fuel and blanket subassemblies. Axially, the core is divided in fourteen segments, among which ten uniform-sized divisions are created in the fissile column and two larger, uniform-sized divisions are created in both the top and bottom axial columns (Refer Fig 2.5). Within each mesh, ten cylindrical

divisions are further provided in the fuel pellet geometry to evaluate the radial temperature distribution, which is used to evaluate the fuel Doppler and fuel axial expansion feedbacks. Nodes for clad and coolant are provided in each mesh to evaluate the corresponding transient temperature changes, which are also used to evaluate reactivity feedbacks. Experimental validation studies of PREDIS are carried out against the European LOFA benchmark problem and up to onset of sodium boiling in the BN800 benchmark exercise [82].

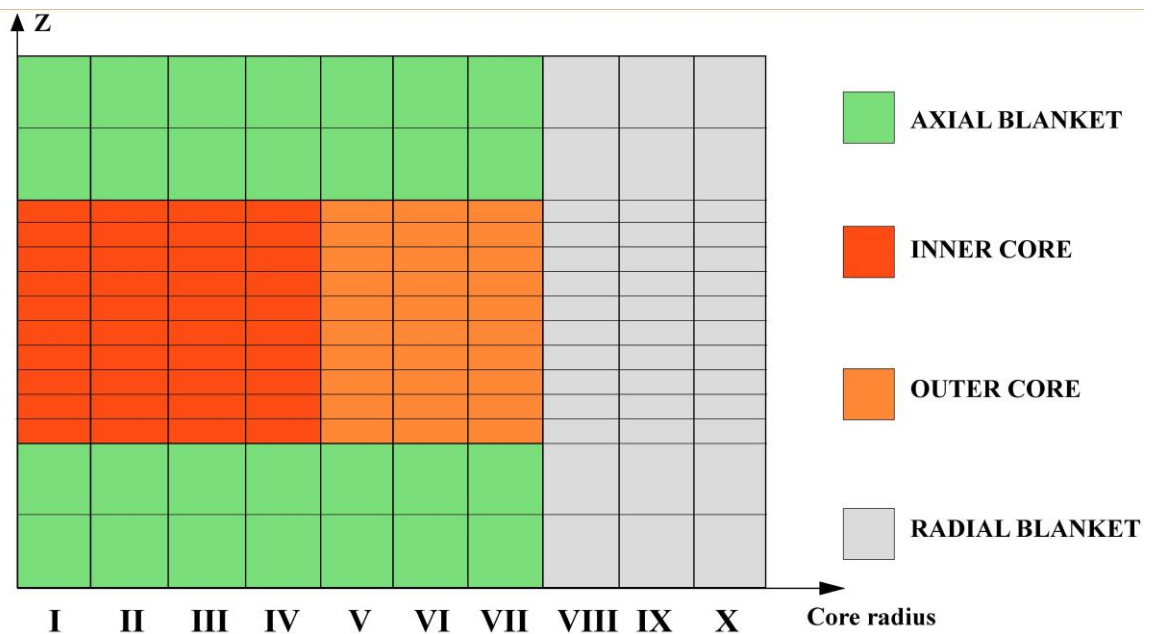


Figure 2.5: Schematic diagram of 2-D (r-z) grid utilized in PREDIS for FBR-500 computations [30].

For a 500 MWe fast reactor core (for e.g., PFBR), Eigen value separation between the fundamental mode and the first mode is greater than 5000 pcm, which indicates that the use of point kinetics model is justified [93]. The governing equations are as follows [23,92]:

$$\frac{dP(t)}{dt} = \left(\frac{\rho - \beta}{\Lambda} \right) P(t) + \sum_{j=1}^{j=6} \lambda_j C_j(t), \quad j = 1, 2, \dots, 6 \quad \dots (2.6)$$

$$\frac{dC_j(t)}{dt} = \frac{\beta_j}{\Lambda} P(t) - \lambda_j C_j(t), \quad j = 1, 2, \dots, 6 \quad \dots (2.7)$$

$$\rho = \rho_{ext} + \rho_{feed} \quad \dots (2.8)$$

$$\rho_{feed} = \rho_{Dop} + \rho_{f,axexp} + \rho_{c,axexp} + \rho_{ct} + \rho_{rad} + \rho_{cr} + \rho_{ves} + \rho_{sl} \quad \dots (2.9)$$

In the above equations, $P(t)$ is the total neutronic power (Watt), ρ is the net reactivity, β is the total delayed neutron fraction ($\beta = \sum_{j=1}^{j=6} \beta_j$), Λ is the prompt neutron generation time ($\Lambda = \frac{1}{K_{eff}}(s)$), λ_j is the decay constant of the j^{th} precursor (s^{-1}), C_j is the delayed neutron precursor concentration of the j^{th} group (Watt), ρ_{ext} is the external reactivity insertion, and ρ_{feed} is the total reactivity feedback. Reactivity feedbacks due to fuel Doppler (ρ_{Dop}), fuel axial expansion ($\rho_{f,axexp}$), clad axial expansion ($\rho_{c,axexp}$), combined coolant expansion and voiding feedback ($\rho_{ct} = \rho_{ct,exp} + \rho_{ct,void}$), core radial expansion (ρ_{rad}), control rod driveline expansion (ρ_{cr}), vessel expansion (ρ_{ves}) and fuel slumping (ρ_{sl}) are incorporated in ρ_{feed} depending upon their significance in a given accident scenario. The core radial expansion feedback consists of the expansion effects of the grid plate and flowering of fuel subassemblies. Doppler coefficient in the present study is derived from the work of Harish et. al [82]. Feedback calculation procedure is derived from the work of Sathiyasheela et. al [30]. Simulation starts with the evaluation of core temperature distribution at a steady, nominal power level and a secondary, higher power level. The temperature and power coefficients, defined as the change in reactivity resulting from an increase in temperature and core power level respectively [11], are determined by the differences in temperature corresponding to the two power levels. The steady state data serves as input for the transient computation. Time march from the moment of accident initiation ($t = 0$ s) begins with iterations of the point kinetics and thermal hydraulics models. External reactivity is introduced in the point kinetics model through Eq. (2.8). Change

in power, evaluated through Eq. (2.6), results in a change in core temperature. Total feedback reactivity (ρ_{feed}) is evaluated through Eq. (2.9), for which each feedback magnitude relevant to the accident scenario is calculated. PREDIS stops the transient computations if: (a) the core becomes prompt-critical ($\rho = \beta$), (b) localized boiling of fuel initiates at the peak power region, or (c) the core attains a stable state and remains in it for a long enough period to permit operator action in practical situations ($t > 500$ s). In case of the first two outcomes, PREDIS additionally prepares input files for the disassembly phase analysis code VENUS [94].

2.3.3 UTOP specification (single pin models)

Table 2.7 presents the accident parameters utilized for studying fuel behaviour with single pin models. The parameters are based on the reactor kinetics of an unexpected CSR withdrawal from a banking depth of 50 cm. Associated differential CSR worth data and speed of withdrawal are described earlier in Section 2.3.1.

Table 2.7: UTOP parameters for single fuel pin study.

Parameter	Value
Ramp rate (% P_n/s)	1
Transient time (s)	120
Maximum power level (% P_n)	220

Simulation of CSR withdrawal in FBR-500 with PREDIS results in an initial reactivity insertion rate of ~ 3.5 pcm/s, which decreases to ~ 0.7 pcm/s towards the completion of withdrawal. Four inherent reactivity feedbacks ($\rho_{Dop}, \rho_{f,axexp}, \rho_{ct,exp}, \rho_{c,axexp}$) are activated, while the other feedbacks are neglected for the purpose of conservatism. Consequently, the rate of power rise ranges between 1.17 % P_n/s ($t = 148$ s) to 0.3 % P_n/s ($t = 250$ s). Therefore, a generalized, nominal

rate of power rise (1 % P_n/s) is selected for studying fuel behaviour with single pin models. Such a slow rate is typically postulated for most modern SFR systems [35]. The maximum power level (220 %) is applicable for both BOL and equilibrium fuel pins. The purpose is to generate a substantial amount of melting in both fuel pins and study the entire range of fuel relocation behaviour from the start of melting up to the complete occupation of pellet cavity.

2.3.4 Molten fuel relocation feedback

In the present work, an additional reactivity feedback (ρ_{rel}) is added to the feedback reactivity defined in Eq. (2.9). The definition of ρ_{rel} is as follows:

$$\rho_{rel} = \sum \frac{(M_{steady} - M_{transient})}{M_{steady}} (W_k) \quad \dots (2.10)$$

$$M_{steady} = (M_s + M_l)|_{t=0} \quad \dots (2.11)$$

$$M_{transient} = (M_s + M_l)|_{t>0} \quad \dots (2.12)$$

$$M_{sol} = \pi(R_o^2 - R_{int}^2)\Delta z \cdot \rho_{f,s} \quad \dots (2.13)$$

$$M_{liq} = \alpha_f \cdot \pi R_{int}^2 \Delta z \cdot \rho_{f,l} \quad \dots (2.14)$$

In the above equations, $M_s, M_l, M_{steady}, M_{transient}$ are the local fuel masses for solid state, liquid state, original state ($t = 0$ s) and transient state ($t = 0$ s). The product of change in local fuel mass during transient ($M_{steady} - M_{transient}$) and fuel void worth per kg fuel ($\frac{W_k}{M_{steady}}$) is summed from the bottom of lower blanket (z_l) to the top of upper blanket (z_u) to obtain the total fuel relocation feedback. The fuel outer pellet radius (R_o) is defined in Table 2.4, whereas the melt interface radius (R_{int}) is defined in Section 2.2. Fuel densities ($\rho_{f,s}, \rho_{f,l}$) for solid and liquid states are defined in Appendix-A (thermo-physical properties). The inclusion of blanket columns in the summation ensures that even if fuel is somehow entrained inside the blanket pellets, the effect is

duly accounted in the calculation. The above definition accounts for the pre-failure fuel relocation observed in the benchmark experiments, wherein molten fuel remains trapped within the fissile column throughout. Fuel mass removal from a given location generates a negative reactivity perturbation in Eq. (2.10). Addition of the same mass to a different location generates a positive reactivity perturbation. If the relocation is from a relatively low fuel void worth (for e.g., axial ends of the fuel column) to a high fuel void worth (for e.g., core mid-plane), the net ρ_{rel} is positive. Similarly, relocation from the core mid-plane to the axial ends generates a negative reactivity feedback.

2.4 Experimental benchmark data

Emphasis is placed on comprehensive experimental validation of the developed models for consolidating the reliability of the computational tool. Benchmarking studies have been carried out against the results of the CABRI reactor in subsequent chapters. The studies require a description of the experimental methodology and the various test parameters. Main features of the test reactor have been presented earlier in Chapter 1 (Section 1.5.3). Benchmark experiments and their outcomes are presented as follows:

2.4.1 E9 test

The objective was to evaluate the margin to failure of an annular mixed oxide fuel pin under UTOP conditions. It was conducted using an OPHELIE-6 fuel pin (annular fuel; solid blanket; SS316 CW clad) irradiated in the *Phénix* reactor [95] (Refer Table 2.8 for fuel specification). The test conditions are briefly summarized in Table 2.9. During UTOP, the presence of negative feedbacks (fuel Doppler, fuel axial expansion) leads to an approximately linear rise in power. To reproduce the same, a uniform power ramp of 1.1 % P_n/s ($P_n = 60.3 \text{ kW}/m, t = 0 \text{ s}$) was implemented over the pin until the power level reached 234 % ($P_{max} = 134.7 \text{ kW}/m, t = 119 \text{ s}$). A constant coolant

mass flow rate was maintained throughout ($\dot{m}_{ct} = 0.153 \text{ m}^3/\text{kg}$). Thermal spectrum resulted in power depression along the radius of the fuel pellets ($\frac{X_l}{X_o} = 0.45$). This is a departure from fast reactor conditions. It was minimized by establishing a high steady state power ($X_{t=0} = 60.3 \text{ kW/m}$), which led to significantly higher fuel temperature as compared to End of Life (EOL) conditions.

Table 2.8: Annular fuel specifications for CABRI-2 test series. (Gen: generation, ret retention) [33,34]

Parameter	E9	E9bis
Fuel pin	OPHELIE-6	OPHELIE-6
Fuel pellet	Annular	Annular
Blanket pellet	Solid UO ₂	Solid UO ₂ *
Inner radius of pellet (m)	1.0×10^{-3}	1.0×10^{-3}
Outer radius of pellet (m)	3.635×10^{-3}	3.635×10^{-3}
Outer radius of clad (m)	4.325×10^{-3}	4.325×10^{-3}
Inner radius of clad (m)	3.75×10^{-3}	3.75×10^{-3}
Plutonium mole-fraction (%)	0.145	0.14
Length of fuel column (m)	0.75	0.75
Length of upper blanket (m)	0.2	0.2
Length of lower blanket (m)	0.2	0.2
Maximum burnup (at. %)	4.9	4.73
Upper plenum volume (m ³)	8.1×10^{-6}	8.1×10^{-6}
Lower plenum volume (m ³)	30.13×10^{-6}	30.13×10^{-6}
Fuel porosity (%)	4.5	4.5
Plenum pressure (MPa, 400°C)	1.2	1.2
EOL peak power (kW/m)	30.5	30.5
(Xe + Kr) Gen. (mm ³ STP g ⁻¹)	1014	1014**

*Bottom blanket pellets are fully solid; at least one top blanket pellet is fragmented.

** Data taken for OPHELIE-6 pin; E9bis specific data unavailable.

Table 2.9: CABRI-2 annular fuel pin test conditions. (Transient undercooling and maximum power hold-up conditions are applicable only for E9bis) [33,34,72]

Parameter	E9	E9bis
Fuel pin	OPHELIE-6	OPHELIE-6
Rate of power rise ($\% P_n/s$)	1.1	0.95
$X_{max,t=0}(kW/m)$	60.3	59.4
$X_{max,t=t_{max}}(kW/m)$	134.7	107.5
Radial depression (X_I/X_o)	0.45	0.45
$\Delta T_{Na,t=0}(^{\circ}C)$	180	180
$t_{max}(s)$	118	88
$\Delta t_{hold}(s)$	-	195.1
$\dot{m}_{ct,t=0}(kg/s)$	0.153*	0.153**
$\Delta t_{TUC}(s)$	-	28.4
$\Delta \dot{m}_{ct,final}(kg/s)$	-	0.092

*flow rate = $((0.643 \text{ m}^3/\text{kg})/3600) * 857.71 (\rho_{ct})$

**flow rate based on E9 due to approximately equal steady state power

Fuel melting was first detected at an LHR of $\sim 73 \text{ kW/m}$. Post-irradiation analysis revealed a maximum melt fraction of 57 %. At the peak power node, only a $500 \mu\text{m}$ thick layer of solid fuel remained between the melt and cladding steel. The melt extent ($\% R/R_o$) was found to be 86.2 %. In the lower portion, melting extended almost up to BFC ($z_{melt,b} = 0.016 \text{ m}$), while in the upper portion, melting did not reach TFC ($z_{melt,t} = 0.69 \text{ m}, z_t = 0.75 \text{ m}$).

Neutron radiographs and axial cuts of the test pin provided information on the fuel relocation behaviour. The main characteristics were as follows: Molten fuel relocated up to the top of the fuel column, where it was stopped by the solid blanket

pellets. Metallic fission products did not accumulate at the top of the fuel column, despite relocation up to this level. This showed that the duration of the motion was long enough to allow segregation of metallic products from liquid fuel. This segregation was not observed in the CABRI-1 tests, indicating that the motion in E9 test was much slower in comparison. Hence, annular fuel squirting, typical to rapid reactivity insertion (for e.g., PINEX-2 [25]), did not occur. Natural convection of molten fuel was concluded to be insignificant, since post-irradiation analyses showed multiple bubbles distributed throughout the melt. If natural convection had been significant, then the bubbles would have agglomerated into a single bubble (by their buoyancy).

Large amount of transient gas release took place ($F_{t=0} = 53.6\%$, $F_{t_{max}} = 82.6\%$). Fission gases were liberated completely out of the molten fuel, and partially from fuel that did not melt. The pin did not fail despite high level of power (223 %) and melting (57 %). Fuel-clad mechanical interaction was insignificant despite the large amount of melting (since no significant change was observed in the clad diameter).

2.4.2 E9bis test

The objective was to investigate the possibility of molten fuel ejection in case of adventitious failure of annular fuel pin. An OPHELIE-6 pin (Refer Table 2.8 for specifications) was deliberately weakened by creating a notch at the peak power location. A unique (and fortunate) feature of this pin was the presence of fragmented pellets in the top blanket prior to the test [33]. Central node power at steady state was kept much higher than EOL level at *Phénix* to negate the effect of thermal neutron spectrum ($X_{t=0} = 59.4\text{ kW/m}$). The pin was subjected to a uniform power ramp of 0.95 % (P_n/s) until the power reached its maxima ($X_{t_{max}} = 107.5\text{ kW/m}$, Refer Fig. 2.6). Thereafter, the power was held constant for a period ($\Delta t_{hold} = 195.1\text{ s}$). In the

last 28.4 s of this period, transient under-cooling, and over-power (TUCOP) condition was imposed to increase the possibility of clad failure. The flow was linearly reduced up to 60 % of its steady state level. However, the cladding steel did not fail.

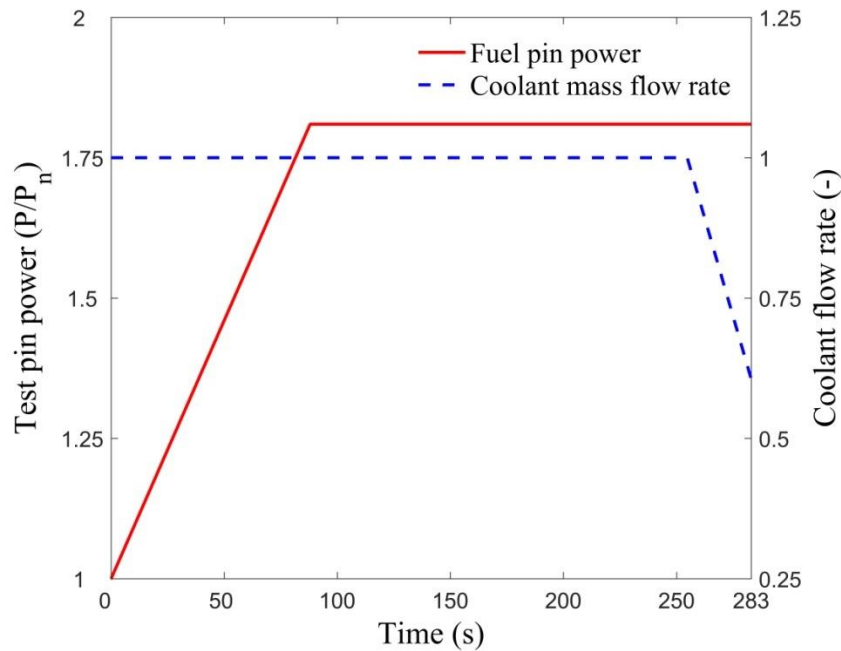


Figure 2.6: Power trace and flow rate conditions for the CABRI-E9bis test [33].

Major results of the test are as follows:

Fuel melting was detected when the highest power node reached a linear power ≈ 73 kW/m. Post-irradiation analysis revealed a maximum melt mass fraction between 40-50 %. The exact magnitude could not be determined due to the relocation of fuel from the fissile to fertile region. The maximum melt extent ($\% R/R_0$) was 82 ± 2 %. The lower and upper melt extents were 0.095 m ($z_{melt,b}$) and 0.635 m ($z_{melt,t}$).

There were wide gaps present between the fragments of the top blanket pellets (unlike E9). Between ($t = 65 - 69$ s), large spikes were observed in the hodoscope readings. These spikes could only be explained by the entrance of molten fuel in the gaps of the top blanket (confirmed in post-irradiation analysis). Hence the timing of melt penetration into the upper blanket pellets was recorded. Other motion

characteristics were analogous to E9. Instead of squirting, a slow in-pin fuel motion occurred. The motion-detecting device (hodoscope) could detect the loss of fuel upon melting at any axial location within the fuel column. Because of the sensitivity of the device towards neutron self-shielding effect, the corresponding gains caused by fuel relocation could not be detected. Therefore, significant loss of fuel in the upper portion of the fuel column was detected at 90 kWm^{-1} , and the corresponding area of gain could not be identified. Consequently, a clear picture of the melt motion within the fuel column was not obtained.

Subjecting the pin to the maximum power level for an extensive hold-up period and initiating a partial loss of flow towards the end of this period resulted in a considerable rise in outer fuel temperature. It is known that there is an extensive release of intra-granular gases to the grain boundaries at high temperatures during transients [96]. Consequently, a significant amount of transient fission gas release occurred in the outer pellet regions which did not undergo melting [33]. In the regions where melting occurred, the fission gases were liberated completely ($F_{t=0} = 53.6 \%$, $F_{t_{max}} = 81 \%$). Despite the extreme conditions, the stainless-steel cladding (SS316-CW) did not fail. A practically relevant change in the measurement of the clad outer diameter before and after the test was not found. No significant FCMI occurred during the test [33].

2.5 Salient working description of MITRA code

A robust code is developed to integrate the pre-failure melting and relocation behaviour of mixed-oxide ((U-Pu)-O₂) nuclear fuel in the safety assessment of India's current and future fast reactors. Mathematical models of heat transfer, multi-phase flow and fission gas release are developed and implemented into a code named 'MITRA' (Multi-phase In-pin Thermal hydraulic Relocation Algorithm).

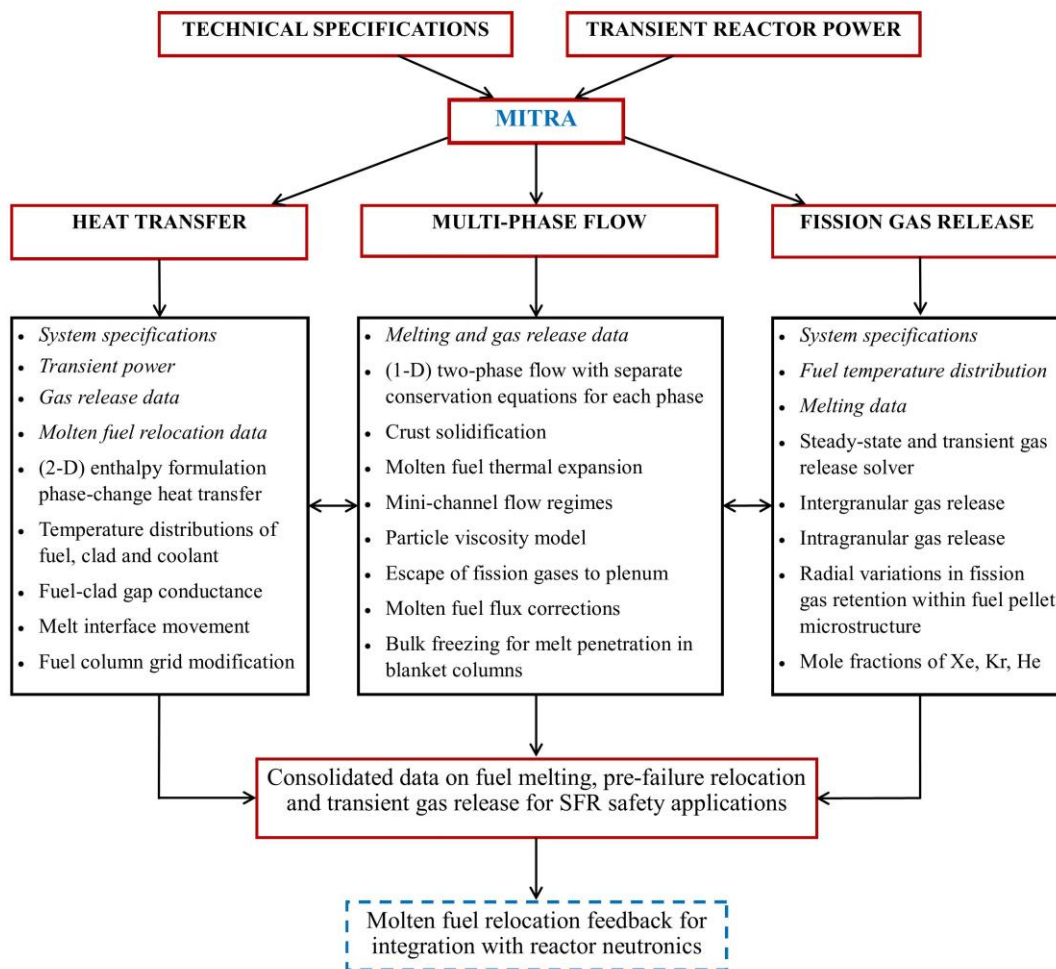


Figure 2.7: Salient working description of MITRA code.

The code is written in FORTRAN-95 programming language. A block diagram of the code shows the basic working methodology and salient features (Refer Fig. 2.7). In-depth investigations of pre-failure fuel relocation and whole-core melt propagation during UTOP are carried out using this code [89,97–100]. Basic input requirements are technical specifications of the SFR system under study and transient parameters (for e.g., reactor power, coolant mass flow rate). Transient input required by each model is provided by the other two models through a dynamic coupling within the code framework. A user instruction manual presents the input/output file system and necessary guidelines to use the code (Refer Appendix-B).

Heat transfer- Geometrical and thermo-physical parameters of fuel pin, transient changes in reactor power, coolant flow rate, multi-phase flow data (for e.g., axial distribution of melt volume fraction, melt temperature) and gas release data (for e.g., moles of Xenon, Krypton and Helium) are required as input. The model tracks the solid/liquid melt interface, modifies the computational grid based on the interface movement and numerical stability requirements, and generates source terms for introduction in the multi-phase flow equations.

Multi-phase flow- Computational grid modifications and fluid mass source terms calculated in the heat-transfer model, and fission gas release data (steady state fission gas release, fission gas retention within fuel pellet microstructure) are the required inputs. Emphasis is placed on addressing the major modelling challenges associated with pre-failure molten fuel relocation, outlined earlier in Chapter 1 (Section 1.6), and validation against benchmark experimental data. Salient features of this model are highlighted in Fig. 2.7. Basic methodology of melt freezing is crust formation combined with the enhancement in viscosity of partially solidified melt. A much simpler approach, i.e., bulk freezing, is also introduced to simulate melt penetration in fertile blanket columns.

Fission gas release- The model is built for both steady-state irradiation and transient simulations. Both model versions use the fuel temperature distribution data as input and are therefore coupled with the heat transfer model. Melt interface radius is an input for the transient version. A salient feature is the capability to provide both radial and axial variations in fission gas retention within the fuel pellet microstructure to the multi-phase flow model. Mole fractions of gaseous fission products are utilized in the gap

conductance calculations of the heat-transfer model. The model is built as a subroutine within the MITRA framework.

Experimental benchmarking of the above models is carried out in subsequent chapters. With the combined computational results, a consolidated database on pre-failure fuel melting, in-pin fuel motion and transient fission gas release behaviour is generated for SFR safety applications. In the present work, the database has been used to evaluate the molten fuel relocation feedback (ρ_{rel} , Refer Section 2.3.4) for integration with the reactor neutronics computations. Fuel void worth data is an additional input required for the same (Refer Section 2.3.1).

2.6 Closure

Specifications of SFR system, core configuration and fuel design parameters utilized for severe accident simulation are detailed. Basic mathematical terminologies used in the present work are defined. Perturbation theory-based fuel void worth data and CSR worth data essential for reactor neutronics computations is presented. Methodology of reactor kinetics modelling with in-house code PREDIS, reactivity feedback calculations and UTOP parameters for single pin models are briefly explained. Definition of melt relocation reactivity feedback is laid down. Working methodology and salient features of the indigenously developed in-pin fuel motion code MITRA are briefly described. The next chapter presents the development of a multi-phase core thermal hydraulic model with advanced features as a first step towards the fulfilment of the objectives of this thesis.

Chapter 3

Development of an Advanced Multi-phase Thermal Hydraulic Model and Investigation of Melt Relocation in Fast Reactors

In this chapter, a transient, thermal hydraulic model is developed for numerical simulation of mixed oxide ((U-Pu)-O₂), nuclear fuel melting and motion in a multi-phase environment, with particular emphasis on appropriate representation of the underlying physical mechanisms. As a first step, a 2-D mathematical model for heat transfer and melting of nuclear fuel is integrated with a 1-D multi-phase flow model, which consists of separate, volume averaged equations for two fluids (Fluid 1: - molten fuel, Fluid 2:- gaseous fission products). Subsequently, the combined melting and multiphase flow model is developed further by the inclusions of: (a) mini-channel flow regimes based on dimensional analysis of the flow, (b) smear density formulation to represent the thermal expansion of molten fuel at high temperatures, (c) crust formation model to simulate solidification in relatively cooler regions, (d) particle viscosity model to simulate the rise of inter-molecular cohesive forces in partially solidified fuel, and (e) free volume model to represent the escape of fission gases through inter-pellet gaps to the fission gas plena. The complete set of governing equations involving energy conservation in fuel, clad and coolant as well as multi-phase flow (mass, momentum, and energy conservation) are solved following an explicit finite difference numerical scheme. Based on the above unified approach of melting and multi-phase flow modelling, an advanced numerical algorithm is devised that can capture the rate of fuel melting and resolve the hydrodynamic effects of gravity, pressure (due to fission gas release), viscosity (due to solidification), cavity blockage, drag, virtual mass and surface

tension. Numerical simulations are performed for the CABRI-E9bis test, and the results are compared with the experimental data quoted in literature.

As a second illustration, the benchmark-proven algorithm is extended to capture the fluid flow as well as fuel mass relocation characteristics expected in fast breeder reactor conditions. To achieve the above goals, the following specific tasks are carried out:

- (i) Optimization of the free volume gas escape model
- (ii) Investigation of melt motion under typical fast breeder reactor conditions (Equilibrium and Beginning-of-life fuel).
- (iii) Fuel mass relocation analysis to determine the possibility of an undesirable increase in fuel mass near the core mid-plane during UTOP.

3.1 Mathematical modelling of the problem

3.1.1 The physical problem

The present work investigates the melting and associated multi-phase flow of mixed-oxide nuclear fuel inside a cylindrical geometry bounded radially by annular fuel pellets and axially by solid blanket pellets (Refer Fig. 3.1). Fuel column consisting of annular pellets is placed between upper and lower blanket columns consisting of solid pellets. The fuel-cladding gap is visible between pellets and cladding. Maximum heat generation occurs in the fuel pellets. The coolant (sodium) extracts heat from the clad surface through forced convection. Consequently, all the fuel pellets attain the highest and lowest temperatures at their inner and outer surfaces, respectively. The gap between fuel and clad can be opened or closed, depending upon the thermal expansion, and swelling of pellets and steel cladding. The free volume of the pin consists of upper and

lower plena, pellet cavity, and fuel-clad gap. A helical spring usually occupies the upper plenum volume partially.

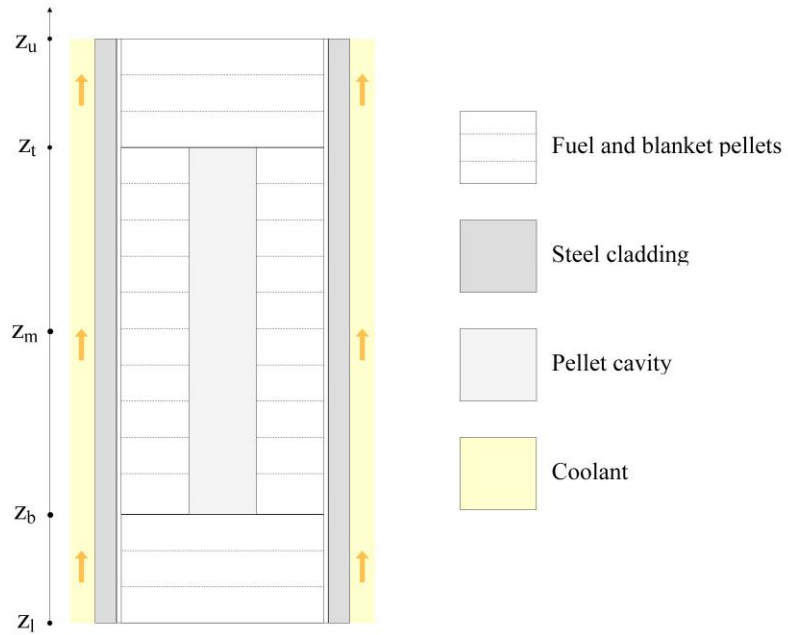


Figure 3.1: General schematic of the problem domain.

3.1.2 Phase-change heat transfer

The transient, cylindrical heat diffusion equation can be solved to simulate the heat-up during upset conditions in nuclear fuel elements, if the target substances do not undergo a change of state [101]:

$$\frac{1}{r} \frac{\partial}{\partial r} \left(Kr \frac{\partial T}{\partial r} \right) + \frac{\partial}{\partial z} \left(K \frac{\partial T}{\partial z} \right) + \frac{1}{r^2} \frac{\partial}{\partial \phi} \left(K \frac{\partial T}{\partial \phi} \right) + \dot{Q} = \rho C_p \frac{\partial T}{\partial t} \quad \dots (3.1)$$

The above governing equation can be suitably simplified based on the following assumptions [77]:

- i. The heat transfer is axisymmetric with respect to the azimuthal coordinate, i.e., $T \neq f(\phi)$.
- ii. The axial heat diffusion in the steel cladding is negligible compared to the radial heat diffusion.

While the axisymmetric condition in the azimuthal coordinate is justified based on geometry, the second boundary condition is based on: (a) small area for heat transfer in axial direction due to the thin geometry of the steel cladding and (b) significant heat extraction by forced convection at the outer surface of cladding, resulting in maximum heat diffusion in the radial direction. To derive the governing equation for energy conservation in the coolant, the following elemental form can be derived from the Reynold's transport theorem [102]:

$$\rho C_p \left(\frac{\partial T}{\partial t} + V_r \frac{\partial T}{\partial r} + \frac{V_\phi}{r} \frac{\partial T}{\partial \phi} + V_z \frac{\partial T}{\partial z} \right) = - \left(\frac{1}{r} \frac{\partial}{\partial r} (r q_r) + \frac{1}{r} \frac{\partial q_\phi}{\partial \phi} + \frac{\partial q_z}{\partial z} \right) \quad \dots (3.2)$$

Simplifications can be carried out with the help of the following assumptions:

- iii. The coolant channel is approximated as an annular flow area located concentrically outside the cladding steel. The area of this channel ($2\pi R_{co} \Delta r$) is equivalent to the average coolant flow area per fuel pin in the subassembly.
- iv. The heat transfer is approximately uniform for all fuel pins in a single fuel subassembly.

Integrating Eq. (3.2) along the radial coordinate, and substituting the above defined boundary conditions, results in the following 1-D governing equation for coolant energy conservation:

$$\rho_{ct} A_{ct} C_{ct} \frac{\partial T_{ct}}{\partial t} = -\rho_{ct} A_{ct} C_{ct} V_{ct} \frac{\partial T_{ct}}{\partial z} + 2\pi K_{ct} \left[r \frac{\partial T_{ct}}{\partial r} \right]_{r=R_{co}}^{r=R_{co}+\Delta r} + A_{ct} \frac{\partial}{\partial z} \left(K_{ct} \frac{\partial T_{ct}}{\partial z} \right) \dots (3.3)$$

For further simplification, the following assumptions are considered:

- v. The coolant channels in a fuel subassembly have approximately equal temperature distributions along the z-axis.
- vi. The axial, diffusive, heat flux in the coolant channel is negligible in comparison to the axial, convective heat flux.

The boundary condition (v) is aimed at simplifying the problem domain to tackle the complexities of multi-phase flow. Using this assumption, an adiabatic boundary condition can be considered on the outer surface of the coolant channel ($\left. \frac{\partial T_{ct}}{\partial r} \right|_{r=R_{co}+\Delta r} = 0$). Finally, the boundary condition (vi) follows from the high coolant flow velocity ($\sim 7 \text{ m} \cdot \text{s}^{-1}$) during UTOP, which renders the diffusive heat flux negligible in comparison to the advective heat flux. This condition is limited to UTOP and cannot be applied in severe accident scenarios involving loss of coolant flow. The above-described assumptions lead to the following simplified energy conservation equations in the fuel/blanket pellets, clad and coolant:

$$\frac{1}{r} \frac{\partial}{\partial r} \left(K_f r \frac{\partial T_f}{\partial r} \right) + \frac{\partial}{\partial z} \left(K_f \frac{\partial T_f}{\partial z} \right) + \dot{q} = \rho_f C_f \frac{\partial T_f}{\partial t} \quad \dots (3.4)$$

$$\frac{1}{r} \frac{\partial}{\partial r} \left(K_c r \frac{\partial T_c}{\partial r} \right) = \rho_c C_c \frac{\partial T_c}{\partial t} \quad \dots (3.5)$$

$$\rho_{ct} A_{ct} C_{ct} \frac{\partial T_{ct}}{\partial t} = -\rho_{ct} A_{ct} C_{ct} V_{ct} \frac{\partial T_{ct}}{\partial z} - 2\pi K_{ct} \left. r \frac{\partial T_{ct}}{\partial r} \right|_{r=R_{co}} \quad \dots (3.6)$$

In problems involving phase-change, it is more suitable to change the dependent variable to specific enthalpy (H_f). This technique is known as the enthalpy method [54,103]. Now, the transient heat conduction equation easily accommodates the rejection or absorption of latent heat at the phase-change interface [104]. The difficulty arises when, upon melting, the liquid undergoes displacement due to hydrodynamic forces, leaving the original site of melting. To accommodate frequent removal or addition of the liquid fuel, the model utilizes a grid modification mechanism [77]. This mechanism ensures that one node remains positioned continually on the melt interface as it travels, while neighboring nodes are created or destroyed, depending upon the presence or absence of liquid phase, and numerical stability constraints. These modifications result in the final energy conservation equations as follows [89]:

$$\rho_f(T_f) \frac{\partial H_f}{\partial t} = \dot{Q}(z, t) + \frac{1}{r} \left(\frac{\partial}{\partial r} \left(K_f(T_f) r \frac{\partial T_f}{\partial r} \right) \right) + \frac{\partial}{\partial z} \left(K_f(T_f) \frac{\partial T_f}{\partial z} \right) \quad (R_{ht} < r < R_o) \quad (3.7)$$

$$\rho_c C_c \frac{\partial T_c}{\partial t} = \frac{1}{r} \left(\frac{\partial}{\partial r} \left(K_c r \frac{\partial T_c}{\partial r} \right) \right) \quad (R_{ci} < r < R_{co}) \quad \dots (3.8)$$

$$\rho_{ct} A_{ct} \frac{\partial H_{ct}}{\partial t} = h_{ct} (2\pi R_{co}) (T_{co} - T_{ct}) - \rho_{ct} A_{ct} V_{ct} \frac{\partial H_{ct}}{\partial z} \quad \dots (3.9)$$

In the above equations, ρ_f, H_f, T_f, K_f are the density, enthalpy, temperature, and thermal conductivity of nuclear fuel, \dot{Q} is the volumetric rate of heat generation; ρ_c, C_c, T_c, K_c are the clad density, specific heat, temperature and thermal conductivity, R_o, R_{ci}, R_{co} are the radii of fuel outer surface, clad inner and clad outer surface respectively, $R_m = \frac{(R_o + R_{ci})}{2}$, R_{ht} is the inner radii of heat conduction domain, $\rho_{ct}, A_{ct}, H_{ct}, T_{ct}, V_{ct}$ are the coolant density, effective flow area, enthalpy, temperature and velocity. Note that in Eq. (3.9), the heat-transfer from clad to coolant is represented by a convective term, which is physically equivalent to the radial heat diffusion term in Eq. (3.6). The definitions of fuel enthalpy (H_f), solidus and liquidus temperatures (T_{sol}, T_{liq}) are detailed in Appendix-A (Eq. (A4-A10)) for the purpose of brevity. Figure A1 displays the enthalpy-temperature plot for ((U-Pu)-O₂) based on these equations. The boundary conditions of the model are defined as follows:

$$K_f(T_f) \frac{\partial T_f}{\partial r} \Big|_{r=R_o} = h_{gap} \left(\frac{R_m}{R_o} \right) (T_{ci} - T_o) \quad \dots (3.10)$$

$$K_f(T_f) \frac{\partial T_f}{\partial r} \Big|_{r=R_{int}} = \frac{(h_{w,f} A_{w,f} (T_{f,int} - T_{f,l}) + h_{w,g} A_{w,g} (T_{f,int} - T_g))}{2\pi R_{int}} \quad \dots (3.11)$$

$$K_f(T_f) \frac{\partial T_f}{\partial r} \Big|_{r=0} = 0 \quad \dots (3.12)$$

$$K_c \frac{\partial T_c}{\partial r} \Big|_{r=R_{co}} = h_{ct} (T_{ct} - T_{co}) \quad \dots (3.13)$$

$$K_c \frac{\partial T_c}{\partial r} \Big|_{r=R_{ci}} = h_{gap} \left(\frac{R_m}{R_{ci}} \right) (T_{co} - T_o) \quad \dots (3.14)$$

The top and bottom surfaces of the respective upper and lower blanket stacks are justifiably adiabatic ($\left. \frac{\partial T_f}{\partial z} \right|_{z=Z_l} = \left. \frac{\partial T_f}{\partial z} \right|_{z=Z_l} = 0$). The contact area ($A_{w,i}$) represents the direct contact between a fluid-phase (i) and the solid fuel surrounding it. It is proportional to the fluid volume fraction ($A_{w,i} = \alpha_i 2\pi R_{int}$, where R_{int} = melt interface radius). This ensures smooth transition between multi-phase flow regimes and avoids numerical instability. As an initial condition, the fuel, blanket, clad and coolant domains are given a uniform temperature distribution, equivalent to the coolant inlet temperature ($T_{ct,inlet} \cong 390 - 400 \text{ }^\circ\text{C}$).

3.1.3 Multi-phase flow

Melting first starts at the inner edge of those fuel pellets which experience highest neutron flux (Figure 3.2). As the melt interface travels radially outwards, both the melt and fission gases enter the cavity. The local pressure (P_{cav}) depends on the gas phase density (ρ_g), constant (R_g) and temperature (T_g). Now, the movement of the melt depends on the force resultant, which can be determined by integrating the Navier-Stokes's equations over the melt volume. Such an approach becomes difficult in case of complex flows, since, it requires accurate knowledge of the liquid-gas interface [105]. The problem can be simplified by attempting to formulate equations, which govern volume averaged fluid quantities. A generalized statement for the conservation of an extensive, vectoral or scalar, physical property F_i ($F_i = \rho_i f_i dV_i$) pertaining to the matter which constitutes phase i , in a volume V_i , can be written as follows [47]:

$$\begin{aligned} \frac{\partial}{\partial t} \int_{V_i} \rho_i f_i dV_i = & \int_{S_i} (-\rho_i f_i u_i + \phi_i) n_i dS_i + \int_{S_{int}} (-\rho_i f_i (u_i - w) + \phi_i) n_i dS_{int} + \\ & \int_{V_i} \rho_i \theta_i dV_i \end{aligned} \quad \dots (3.15)$$

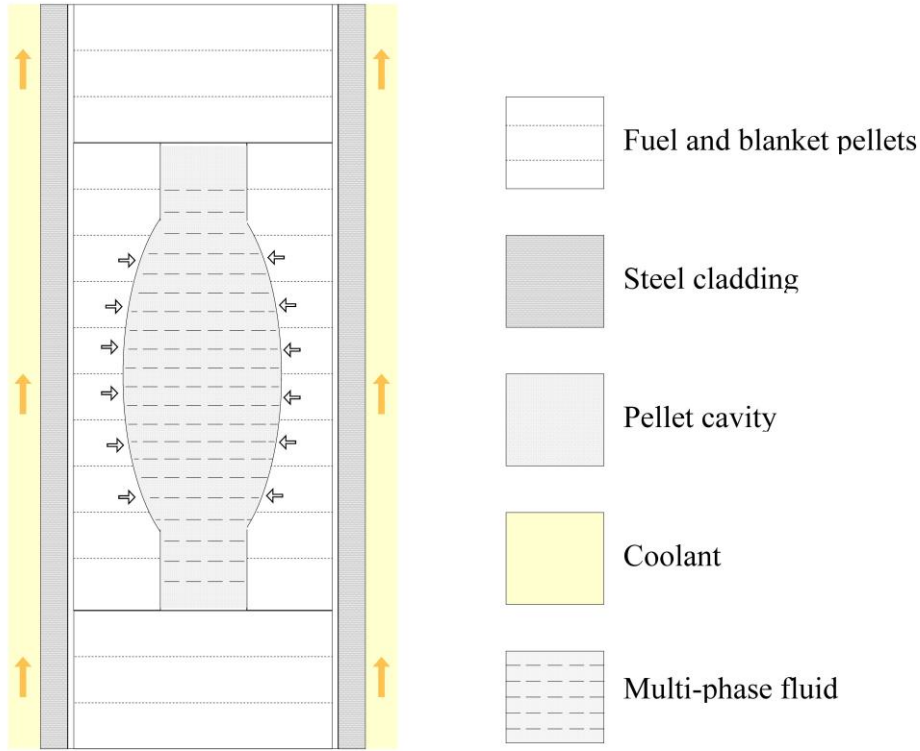


Figure 3.2: Schematic diagram of in-pin fuel motion in annular mixed oxide fuel pins during UTOP. Multi-phase fluid refers to molten fuel and fission gas mixture.

The above equation reduces to 1-D multi-phase conservation equations for mass, momentum and energy using a volume averaging technique in the radial and azimuthal coordinates. Accordingly, 1-D multi-phase conservation equations in a molten environment have been proscribed [48]:

$$\frac{\partial}{\partial t}(\alpha_i A \rho_i) + \frac{\partial}{\partial z}(\alpha_i A \rho_i V_i) = \alpha_i A S_i \quad \dots (3.16)$$

$$\frac{\partial}{\partial t}(\alpha_i A \rho_i V_i) + \frac{\partial}{\partial z}(\alpha_i A \rho_i V_i^2) = \alpha_i A S_i V_{s,i} - \frac{\partial}{\partial z}(\alpha_i A P) + p \frac{\partial}{\partial z}(\alpha_i A) - \alpha_i A \rho_i g - A \tau_{fr,i} - drag_i \quad \dots (3.17)$$

$$\frac{\partial}{\partial t}(\alpha_i A \rho_i H_i) + \frac{\partial}{\partial z}(\alpha_i A \rho_i H_i V_i) = \alpha_i A S_i \left(e_{s,i} + \frac{1}{2} (V_{s,i} - V_i)^2 \right) + \alpha_i A \frac{DP}{Dt} - \frac{\partial}{\partial z}(\alpha_i A q_i) + \alpha_i A \rho_i \dot{q}_i + V_i (A \tau_{fr,i} + drag_i) \quad \dots (3.18)$$

Eq. (3.18) is derived through the procedure described in literature [48]. Using the above equations as a framework, certain modifications were carried out [77]. Evaluation

of the resultant model indicated the need for development of an advanced multi-phase thermal hydraulic model which would predict melt motion in consistence with experimental results (Refer Section 1.7.2.3). The present study attempts to derive such a model. Effort is directed at the development of improved closure laws which represent the underlying physical mechanisms appropriately. These efforts are detailed in the subsequent sections.

3.1.4 Dimensional analysis and flow regimes

To determine the dominant hydrodynamic effects, the various non-dimensional groups involved in the flow are derived using Buckingham's pie theorem [106]:

$$F(V_f, V_g, t, \rho_f, \mu_f, g, D, d, \Delta P, \sigma, \rho_g) = 0 \quad \dots (3.19)$$

Here, μ_f , σ , ρ_f are the viscosity, surface tension and density of molten fuel respectively, D is the diameter of fuel cavity, d_d is the characteristic diameter of the disperse phase, ΔP is the time averaged pressure difference (over the time scale, t), and ρ_g is the density of gas phase (mixture of bond gas with fission gases). Considering D, μ_f, ρ_f as the repeating variables (since $n = 3$), the following non-dimensional groups are obtained [89]:

$$\pi_1 = \frac{\rho_f V_f D}{\mu_f}, \pi_2 = \frac{\rho_f V_g D}{\mu_f}, \pi_3 = \frac{\rho_f^2 d^3 g}{\mu_f^2}, \pi_4 = \frac{\mu_f t}{\rho_f D^2}, \pi_5 = \frac{d}{D}, \pi_6 = \frac{\rho_f D^2 \Delta P}{\mu_f^2}, \pi_7 = \frac{\rho_g}{\rho_f}, \pi_8 = \frac{\rho_f D \sigma}{\mu_f^2} \quad \dots (3.20)$$

While π_1 clearly represents the molten fuel Reynolds number (Re_f), further familiar groups may be derived by inter-multiplication of the other π groups as follows:

$$Eo = \frac{(\rho_f - \rho_g) D^2 g}{\sigma}, Fr = \frac{V_f^2}{g D}, Eu = \frac{\Delta P}{\rho_f V_f^2} Re_{bu} = \frac{\rho_f V_f d}{\mu_f}, \alpha_d = \frac{d^2}{D^2} \quad \dots (3.21)$$

Here, Eo , Fr , Eu are the Eotvos, Froude and Euler numbers respectively, Re_{bu} is the bubble Reynolds number, α_d is the volume fraction of the disperse phase and V_r is the inter-phase relative velocity. Using the melt displacement data of the CABRI-E9bis test, orders of the system velocity and time scales are obtained [33]. Details of the test are compiled in Chapter 2 (Section 2.4.2). Considering the time between melt initiation ($t = 26$ s) and upper blanket penetration ($t = 65 - 69$ s), the flow time scale can be fixed (~ 40 s). The hydraulic diameter of the flow is equivalent to the pellet inner diameter ($D_I = 0.002$ m). Molten fuel density at the melting temperature is 8800 $kg \cdot m^{-3}$ (Refer Eq. A (12–15)), whereas the gas phase density within the cavity is much smaller ($\rho_g \sim 5 - 6$ $kg \cdot m^{-3}$) [33]. Surface tension at the melting temperature is ~ 0.513 $N \cdot m^{-1}$ [107]. Using the above data, the order of magnitude of the Eotvos number can be determined (~ 0.67). The Eotvos number criteria for identifying small conduit flows is given by Brauner, who has reported that in case of $Eo \leq 2\pi$, surface tension is dominant and the flow regimes differ from regular channel regimes [108]. The dominance of surface tension in the hydrodynamics results in the so called ‘mini-channel’ flow regimes. Experimental study for gas-liquid flow in vertical mini-channels shows the existence of the following flow regimes [109]:

- (a) *Annular flow*: Gas phase occupies maximum volume. Gas travels in a single, mostly continuous stream. The liquid phase forms a film between the solid boundary and the gas phase. Both the liquid and gas phases are continuous.
- (b) *Intermittent (or slug) flow*: Gas phase forms slugs which travel inside the liquid film. The space between two consecutive slugs is occupied by the liquid phase. Since the gas phase travels in the form of slugs, the liquid phase is continuous.

(c) *Dispersed bubble flow*: Gas phase travels in the form of bubbles which are dispersed throughout a continuous liquid phase. The liquid phase occupies maximum volume. This regime only exists at low gas volume fractions.

These flow regimes are incorporated in the present multi-phase flow model. Note that a dispersed droplet flow is not included above, since at low fuel volume fraction, the liquid phase assumes the shape of a film under the annular flow regime. Therefore, the liquid phase remains in contact with the solid wall in all the above regimes. To ensure the same mathematically: (a) melt flow is constrained within locations where the melt volume fraction is greater than a nominal value ($\alpha_f > 0.02$) and (b) the contact area between the melt and the solid fuel boundary is never allowed to become zero. Combined, these steps avoid dispersed droplet flow and ensure that the melt behaves like a continuous phase, which is consistent with experimental data for vertical mini channels. Due to the absence of these constraints, an earlier developed model predicted near instantaneous entrainment of the melt in the bottom-most fuel pellets of E9bis, which is erroneous (Refer Section 1.7.2.3 for details).

3.1.5 Molten fuel thermal expansion

The heat generated inside molten fuel is diffused radially across the solid/liquid interface (R_{int}) because of forced convection heat transfer between the clad outer surface and the coolant. In the absence of melting, at a given location, the heat generated within molten fuel is diffused across the pellet inner surface (R_I). In the former case, the boundary temperature is high ($T_{int} \cong 2730^\circ\text{C}$). Consequently, the molten fuel attains even higher temperatures, particularly near the peak power region ($T_f > 3500^\circ\text{C}$). Since molten fuel is free to expand in the annular pellet cavity at least until a significant amount of melting has taken place, its density decreases significantly ($\rho_{f,l} =$

8252 kg · m⁻³) [110]. Therefore, a need was felt to accommodate the liquid fuel thermal expansion in the multi-phase flow equations. To fulfill this need, an attempt is made to introduce an alternative dependent variable, known as smeared density of molten fuel, in the conservation equations. The smeared density is defined as the product of the physical density and the volume fraction ($G_f = \alpha_f \rho_f$). In the Eq. (3.16), the dependent parameter is α_f . Through this modification, the dependent parameter is changed to G_f :

$$\frac{\partial}{\partial t}(G_f A) + \frac{\partial}{\partial z}(G_f AV_i) = \alpha_i AS_i \quad \dots (3.22)$$

In the above equation, the variation in ρ_f is accommodated through corresponding changes in α_f , while simultaneously maintaining the conservation of mass. All the flux terms are changed accordingly, leading to a flexible formulation in which the fuel volume fraction is not fixed from the start of the solution. Through the energy conservation equation, the molten fuel temperature is evaluated and utilized in Eq. (A.14-A.15) to calculate the melt density ($\rho_{f,l}$). In an explicit manner, the magnitude of $\rho_{f,l}$ is updated in the next time-step, after the solution of fuel mass conservation equation. This results in the evaluation of a modified α_f , which is consistent with the change in density. The importance of the present modification is evident in the experimental benchmarking detailed in Section 3.3.3.

3.1.6 Crust solidification model

Axial variation in the neutron density results in a cosine power profile within the fuel column, with the maxima situated close to the core mid-plane. Furthermore, the dominance of surface tension ensures that upon melting, the melt remains in contact with the inner surface of fuel pellets continuously (Refer Section 3.1.4). Consequently,

as melting begins near the core mid-plane, molten fuel rapidly encounters adjacent, relatively cooler fuel pellets which are yet to undergo melting. Therefore, freezing begins immediately adjacent to the peak power region. On the other hand, the addition of excess fuel mass at the inner surface of adjacent fuel pellet increases the overall heat generation in the corresponding axial plane. Consequently, as further fuel is deposited at the inner surface, the temperature of the frozen fuel also increases. Additionally, continued power rise during UTOP also increases the local heat generation. Ultimately, the temperature at the innermost surface of the frozen fuel breaches the melt interface temperature, resulting in initiation of melting at this location. Now, the melt again encounters an unmolten surface and undergoes the same process. The result of such a continuous melting and freezing phenomena is a gradual, trickling motion from the peak power region towards the bottom of the fissile column. Mathematical representation of the above phenomena requires the evaluation of heat diffusion in an annular pellet with added frozen fuel mass. Furthermore, the frozen fuel must be removed from the multi-phase conservation equations. Once melting begins at the frozen surface, the reverse process must be carried out. An expression representing the mass transfer between the heat diffusion and multi-phase flow domains is derived as follows:

$$\rho_{f,sol} \frac{\partial A_{cav}}{\partial t} = \frac{\partial(\alpha_f \rho_f A_{cav})}{\partial t} \quad \dots (3.23)$$

In the above equation, the molten mass is transferred to the inner surface of the annular fuel pellet, based on the following prior conditions: (a) Both the molten fuel ($T_{f,l}$) and pellet inner surface (T_{wall}) temperatures must be lower than 98 % of the solidus temperature (T_{sol}), (b) the molten fuel volume fraction must be within a range ($10^{-3} < \alpha_f < 0.2$). These conditions ensure that freezing is carried out only at locations where it is physically feasible, while simultaneously maintaining

computational stability. The upper limit of α_f is rarely encountered in the computations since freezing is found to occur prominently near the lower limit. The rate of decrease of pellet cavity area is proportional to the rate of arrival of molten fuel mass from an adjacent axial location. A discretized formulation of the above mechanism is detailed for further clarity:

$$A_{cav}^{t+\Delta t} = A_{cav}^t \left(1 - \frac{\alpha_f^t \rho_{f,l}^t}{\rho_{s,f}} \right) \quad \dots (3.24)$$

In the above equation, the molten fuel mass at the end of time step (Δt) is deleted, while the cavity's cross-sectional area (A_{cav}) is reduced in proportion to the mass frozen within the time-step. Prior to the beginning of solidification, the interface radius (R_{int}) is kept fixed at the pellet inner radius (R_I). The index marker (D_{int}), which identifies the interface node in the 2-D arrays, for e.g., temperature, is accordingly fixed ($D_{int} = N_{cav} + 1 + 1$). The number of radial nodes within the cavity are $N_{cav} + 1$. As long as the thickness of frozen fuel remains less than the radial grid size (Δr), the interface radius is simply shifted to the new pellet inner radius, while D_{int} is left unchanged. However, once thickness of frozen fuel breaches Δr , a new radial node is created at R_{int} . In doing so, D_{int} is reduced by one digit. Now, the new, inner-most fuel node consists of a thickness greater than Δr . Such a grid (greater than Δr) does not create numerical instabilities.

The discretized form of the enthalpy formulation ensures that these geometrical changes are accounted for in the computations (Refer Eq. (B.1)). Finally, once R_{int} decreases sufficiently to warrant a second node creation at a nominal position, the above process is repeated, if A_{cav} remains greater than 4 % of the initial area (πR_I^2). Once this condition is also breached, the corresponding axial node is considered as choked with

frozen fuel. This condition ensures the prevention of numerical instabilities in the multi-phase conservation equations. In case of such a flow blockage, the axial boundary of the multi-phase flow domain (Z_{bs}) is changed to the choked location (Z_k). Numerically, the bottom surface index (L_{bs}) is changed to the choked node.

3.1.7 Particle viscosity model

Once a small amount of melting has occurred, the molten fuel stops freezing completely. Instead, it either attains higher temperature due to internal heat generation, or undergoes partial solidification, i.e., its temperature is greater than T_{sol} but lower than T_{liq} . In such a state, there is an appreciable rise in viscosity of the melt due to increased intermolecular cohesive forces [111]. In the absence of this enhancement, the earlier developed model predicted immediate relocation to the bottom of the pellet cavity at a high speed (Refer Section 1.7.2.3). The results of CABRI-2 test series have shown that this is a physically unrealistic result [33]. Therefore, the rise in viscosity is duly accounted through the integration of the particle viscosity model [112].

$$\mu_f = \begin{cases} \mu_f|_{T_{liq}} \left\{ (1-\alpha_p) + \frac{f\alpha_{p,max}\alpha_p}{\alpha_{p,max}-\alpha_p} \right\}, \alpha_p = \frac{T_{liq}-T_f}{T_{liq}-T_{sol}} (T_{sol} \leq T_f \leq T_{liq}) \\ 0.000988e^{4620T_f^{-1}} (T_f > T_{liq}) \end{cases} \quad \dots (3.25)$$

In the above equation, the dynamic viscosity of fuel (μ_f) depends on the temperature (T_f), the fraction of solid particles in the melt (α_p) and a fitting parameter (f). The particle viscosity model predicts near infinite viscosity for particle fractions greater than 0.62 ($\alpha_{p,max}$), which is intended to render the melt mass immovable [57]. To incorporate the same in the multi-phase flow model and avoid numerical instabilities simultaneously, a high finite viscosity is used under these conditions. A sensitivity analysis of the magnitude shows that the movement of molten fuel in the upward

direction is significantly slowed down if the coefficient C_{VF1} in Eq. (B.10) is updated with the particle viscosity.

While the crust formation model simulates the downward trickling movement of molten fuel, the particle viscosity model ensures a slow upward movement, which is in consistence with experimental observations of the CABRI-2 tests. This upward movement is fundamentally driven by liquid fuel thermal expansion. In the numerical model, mass conservation residuals are produced at the sites of high viscosity since the melt expands while remaining immobile at the same time. These residuals are numerically processed to create velocity corrections at the sites of large viscosity. The corrected velocities result in an upward motion which is proportional to the extent of thermal expansion. Liquid viscosity is derived from IAEA recommendation [107,110].

3.1.8 Escape of fission gases towards plena

Noble gas atoms are generated within the fuel microstructure as a by-product of nuclear fission. An intricate mechanism governs the movement of these atoms within the fuel microstructure. While some gas atoms can diffuse through the fuel matrix up to the grain boundaries and are eventually released to the open volume inside the fuel pin, other gas atoms remain trapped inside the microstructure either at the intra-granular or inter-granular level. The gas atoms released from solid fuel collect in the open volume of the pin (V_{pin}). An approximate equilibrium exists between the gas pressures in the plena, fuel-clad gap, and pellet cavity during steady-state irradiation. By adding the ideal gas equations for all free volumes, the internal pin pressure (P_{pin}) can be expressed as a function of the total moles of released gases (n_{Xe}, n_{He}, n_{Kr}), free volumes ($V_{gap}, V_{cav}, V_{up}, V_{low}$) and respective temperatures as follows [113] (SAS4A-DEFORM):

$$P_{pin} = \frac{(n_{Xe} + n_{He} + n_{Kr})R_U}{\sum_{Z_l}^{Z_u} \frac{V_{gap,k}}{T_{gap,k}} + \frac{V_{low}}{T_{low}} + \frac{V_{up}}{T_{up}} + \sum_{Z_t}^{Z_b} \frac{V_{cav,k}}{T_{cav,k}}} \quad \dots (3.26)$$

Here, R_U is the universal gas constant. Elevations denote the bottom of pellet cavity (Z_b), top of pellet cavity (Z_t), bottom of lower blanket (Z_l) and top of upper blanket (Z_u). In UTOP, melting of fuel at the inner pellet surface releases the gases retained initially within the fuel microstructure to the inner pellet cavity. This release is captured by the gas mass source term (S_g) in Eq. (3.47), which is essentially a rate of release ($kg \cdot m^{-1} s^{-1}$). Using the molecular mass of noble gas mixture (Mol_{Xe-Kr}), it can be converted to a molar rate of release. Transient gas release rates ($\frac{dn_{Kr}}{dt}$, $\frac{dn_{Xe}}{dt}$) are calculated by integrating the molar rate of release from bottom (Z_b) to top (Z_t) of the fuel column. Expressions for transient analysis are as follows:

$$\frac{dn_{Kr}}{dt} = \int_{Z_b}^{Z_t} \frac{S_g}{Mol_{Xe-Kr}} \left(\frac{Y_{Kr}}{Y_{Xe} + Y_{Kr}} \right) dz \quad \dots (3.27)$$

$$\frac{dn_{Xe}}{dt} = \int_{Z_b}^{Z_t} \frac{S_g}{Mol_{Xe-Kr}} \left(\frac{Y_{Xe}}{Y_{Xe} + Y_{Kr}} \right) dz \quad \dots (3.28)$$

$$\frac{dn_{cav}}{dt} = \int_{Z_b}^{Z_t} \frac{S_g}{Mol_{Xe-Kr}} dz \quad \dots (3.29)$$

$$P_{pin} = \frac{(n_{up} + n_{low} + n_{gap})R_U}{\sum_{Z_l}^{Z_u} \frac{V_{gap,k}}{T_{gap,k}} + \frac{V_{low}}{T_{low}} + \frac{V_{up}}{T_{up}}} \quad \dots (3.30)$$

$$\Delta n_{cav,k}^{t+\Delta t} = [1 - e^{-ct}] \left(\frac{P_{cav,k}^t - P_{pin}^t}{\frac{T_{cav,avg}^t}{V_{cav,avg}^t} + \left(\sum_{Z_l}^{Z_u} \frac{V_{gap,k}}{T_{gap,k}} + \frac{V_{low}}{T_{low}} + \frac{V_{up}}{T_{up}} \right)^{-1}} \right) \frac{1}{R_U} \quad \dots (3.31)$$

The transient pin pressure is a function of moles of gases in the upper plenum ($n_{up} = \frac{P_{pin} V_{up}}{R_U T_{up}}$), lower plenum ($n_{low} = \frac{P_{pin} V_{low}}{R_U T_{low}}$), and fuel-clad gap ($n_{gap} = \sum_{Z_l}^{Z_u} \frac{P_{pin} 2\pi R_{gap,k} \Delta z_k \cdot gap_k}{R_U T_{gap,k}}$). Approximate pressure equilibrium is assumed between these

free volumes. The plena temperature (T_{low}, T_{up}) are equal to the surrounding coolant temperature ($T_{ct}|_{z=Z_l}, T_{ct}|_{z=Z_u}$). In the pellet cavity, an excess gas pressure builds up due to the release of fission gases on melting ($\frac{dn_{cav}}{dt}$). This excess pressure reduces gradually due to gas escape through the inter-pellet gaps. A discretized form of the escape term is expressed in Eq. (3.31). Here, the moles of gas escaping through the inter-pellet gaps ($\Delta n_{cav,k}^{t+\Delta t}$) within time-step (Δt) depends on the pin pressure (P_{pin}^t), local cavity pressure ($P_{cav,k}^t$), temperature ($T_{low}, T_{up}, T_{cav,avg}^t, T_{gap}^t$), gap volume ($V_{gap,k} = \sum_{Z_l}^{Z_u} 2\pi r_{gap,k} g_{ap,k} \Delta z_k$), plena volume (V_{low}, V_{up}) and an exponential constant (c). The total gas escape from the cavity is found by algebraic summation ($\Delta n_{cav}^{t+\Delta t} = \sum_{Z_b}^{Z_t} \Delta n_{cav,k}^{t+\Delta t}$). This formulation removes sudden mathematical perturbations in the momentum conservation equations (Eq. (3.45–3.46)). At the same time, it ensures that the cavity pressure (P_{cav}) remains connected to the pin pressure (P_{pin}). This enables a robust simulation of melt hydrodynamics. Assuming an equilibrium condition between the gas plena and fuel-clad gap, the corresponding changes in gas content are as follows:

$$\Delta n_{up}^{t+\Delta t} = \frac{\Delta n_{cav}^{t+\Delta t}}{\left(\sum_{Z_l}^{Z_u} \frac{V_{gap,k}}{T_{gap,k}} + \frac{V_{low}}{T_{low}} + \frac{V_{up}}{T_{up}} \right)} \frac{V_{up}}{T_{up}} \quad \dots (3.32)$$

$$\Delta n_{low}^{t+\Delta t} = \frac{\Delta n_{cav}^{t+\Delta t}}{\left(\sum_{Z_l}^{Z_u} \frac{V_{gap,k}}{T_{gap,k}} + \frac{V_{low}}{T_{low}} + \frac{V_{up}}{T_{up}} \right)} \frac{V_{low}}{T_{low}} \quad \dots (3.33)$$

$$\Delta n_{gap,k}^{t+\Delta t} = \frac{\Delta n_{cav}^{t+\Delta t}}{\left(\sum_{Z_l}^{Z_u} \frac{V_{gap,k}}{T_{gap,k}} + \frac{V_{low}}{T_{low}} + \frac{V_{up}}{T_{up}} \right)} \frac{V_{gap,k}}{T_{gap,k}} \quad \dots (3.34)$$

From the above, the next time step values are derived ($n_{cav,k}^{t+\Delta t} = n_{cav,k}^t - \Delta n_{cav}^{t+\Delta t}$, $n_{low}^{t+\Delta t} = n_{low}^t + \Delta n_{low}^{t+\Delta t}$, $n_{up}^{t+\Delta t} = n_{up}^t + \Delta n_{up}^{t+\Delta t}$, $n_{gap,k}^{t+\Delta t} = n_{gap,k}^t + \Delta n_{gap,k}^{t+\Delta t}$).

To further isolate the melt hydrodynamics, these computations occur once in 50,000 two-phase flow time steps ($\Delta t_{pressure} = 0.25 \text{ s}$, $\Delta t_{two-phase} = 5 \times 10^{-6} \text{ s}$, $\Delta t_{heat} = 10^{-3} \text{ s}$) [89]. An optimization study aimed at investigating the flow perturbations caused by gas removal from the cavity, is presented in the subsequent sections.

3.1.9 Closure laws

Regarding the above defined multi-phase conservation equations, a critical issue is the prescription of the inter-phase as well as boundary interaction terms (Refer Eq. (3.17–3.18)). In general, empirical correlations are developed for describing these terms. However, the effect of mini-channel regimes must be duly considered in their definition. Another crucial aspect is the maintenance of numerical stability in the computations, which requires a smooth transition between the proscribed flow regimes. Accordingly, appropriate definitions are developed for these terms in this section. First, the law for pressure closure is stated, based on the assumption of equivalent local pressure within both phases at any axial location [48,68,114]:

$$P_{cav} = P_f = P_g = \rho_g R_g T_g \quad \dots (3.35)$$

Next, the inter-phase momentum interactions are described in terms of the well-known drag and virtual mass forces [115,116]:

Inter-phase momentum exchange:

$$F_D = \left\{ \begin{array}{l} \frac{A_{f-g} \rho_g C_D |V_r| V_r \sqrt{\alpha_g}}{2}, C_D = 0.005(1 + 75\alpha_f) \quad (\alpha_f < 0.26) \\ \frac{3\alpha_g C_D \rho_f A_{cav} |V_g| V_g}{4d_{bu}}, C_D = \frac{24}{Re_{bu}} \quad (\alpha_f \geq 0.26; Re_{bu} < 16) \\ \frac{3\alpha_g C_D \rho_f A_{cav} |V_g| V_g}{4d_{bu}}, C_D = \frac{24}{Re_{bu}} (1 + 0.1 Re_{bu}^{0.75}) (\alpha_f \geq 0.26; Re_{bu} \geq 16) \end{array} \right\} (3.36)$$

$$F_{vm} = -\alpha_g C_{vm} \rho_f A_{cav} \left(\frac{\partial}{\partial t} (V_f - V_g) + V_g \frac{\partial}{\partial z} (V_f - V_g) \right) \quad \dots (3.37)$$

The drag force (F_D) is a function of interfacial area per unit axial length (A_{f-g}), gas density (ρ_g), drag coefficient (C_D), relative velocity between the phases ($V_r = V_f - V_g$), gas volume fraction (α_g), fuel volume fraction (α_f), area of cavity (A_{cav}), hydraulic diameter of gas bubble (d_{bu}) and bubble Reynolds's number ($Re_{bu} = \frac{\rho_f |V_r| d_{bu}}{\mu_f}$). The expressions are based on the mathematical relations detailed by Kolev for annular and bubble flow [115,117]. The condition for transformation from annular to transition flow ($\alpha_f = 0.26$) is based on a maximum packing density consideration, which has scope for improvement. The virtual mass force has been developed out of necessity, since the exclusion of this force in fission gas momentum conversation (Eq. (3.17)) leads to divergence [77]. The virtual mass coefficient ($C_{vm}=0.5$) is fixed [115]. The lift force is not incorporated in the present analysis since: (a) fluid motion predominantly occurs in the axial direction, while motion in the radial direction is constrained by the flow geometry (Section 1.6), and (b) information regarding the radial velocities ($V_{f,r}, V_{g,r}$) is lost during volume averaging (Section 3.1.3). Information regarding the liquid-gas interface is incorporated through the flow regimes (Section 3.1.4).

Inter-phase heat exchange:

$$Nu_{f-g} = 2, \quad h_{f-g} = \frac{Nu_{f-g} K_g}{d_{bu}}, \quad q_{f-g} = h_{f-g} A_{f-g} (T_f - T_g) \quad \dots (3.38)$$

The liquid-gas interfacial heat exchange (q_{f-g}) is a function of the interfacial heat transfer coefficient (h_{f-g}), gas thermal conductivity (K_g), hydraulic diameter of bubble/slug (d_{bu}), interfacial area (A_{f-g}) and the fluid temperatures (T_f, T_g). The Nusselt number is specific for low velocity ($V_r = 0$), gas-liquid flow [64]. The validation study has shown that the flow velocities of both molten fuel and fission gases are small, and the flow is laminar in nature (Refer Section 3.3.3). The effect of liquid-gas heat transfer

on the melt temperature is negligible, since the heat capacity of the gas-phase is considerably smaller in comparison with molten fuel ($\rho_f C_{p,f} \gg \rho_g C_{p,g}$).

Friction with solid boundary:

$$\tau_{w,i} = \frac{1}{8} A_{w,i} \rho_i V_i |V_i| f_{Darcy}, Re_i = \frac{2\rho_i V_i R_{cav}}{\mu_i}, f_{Darcy} = \begin{cases} \frac{64}{Re_i} & (Laminar) \\ 0.316 Re_i^{-0.25} & (Turbulent) \end{cases} \quad \dots (3.39)$$

Here, the friction force ($\tau_{w,i}$) is a function of the fluid contact area with solid boundary per unit length ($A_{w,i}$), fluid density (ρ_i), velocity (V_i), Darcy friction factor (f_{Darcy}), cavity radius (R_{cav}) and the dynamic viscosity (μ_i) (Refer Section 3.1.7).

Solid boundary heat transfer:

$$q_{w,i} = h_{w,i} A_{w,i} (T_{w,i} - T_i), h_{w,i} = \frac{2K_i}{r_{cav}} \quad \dots (3.40)$$

Here, the heat exchange at the fluid-solid boundary ($q_{w,i}$) is a function of the heat transfer coefficient and contact area at the solid boundary ($h_{w,i}, A_{w,i}$), solid boundary temperature ($T_{w,i}$), fluid temperature (T_i), fluid thermal conductivity (K_i) and cavity radius (r_{cav}). The formulation of the heat transfer coefficient is based on the following assumptions: (a) convective heat transfer is negligible as compared to the conductive heat transfer, since melt motion is slow in nature. (Refer Section 2.4.1). (b) Temperature variation inside the melt is linear along the r-axis. (c) Radial coordinate at which the local melt temperature T_f equals the liquid-phase temperature ($T_{f,l}$) is half of the interface radius ($r_{cav}/2$) [68].

3.1.10 Governing equations of the advanced multiphase flow model

The above modelling additions, coupled with the volume averaged governing equations, lead to the derivation of the following mathematical model for multi-phase flow of molten fuel and fission gases inside the annular pellet cavity [89]:

$$\frac{\partial(\alpha_g \rho_g A)}{\partial t} + \frac{\partial(\rho_g \alpha_g A V_g)}{\partial z} = S_g \quad \dots (3.41)$$

$$\frac{\partial(G_f A)}{\partial t} + \frac{\partial(G_f A V_f)}{\partial z} = S_f \quad \dots (3.42)$$

$$\alpha_f A \rho_f \frac{\partial H_f}{\partial t} + \frac{\partial(\alpha_f A \rho_f H_f V_f)}{\partial z} = S_f (e_{sf} - H_f) + H_f \frac{\partial(\rho_f \alpha_f A V_f)}{\partial z} - \frac{\partial(\alpha_f A q_f)}{\partial z} + \alpha_f A \rho_f Q_f - q_{f-g} + q_{w,f} \quad \dots (3.43)$$

$$\alpha_g A \rho_g \frac{\partial H_g}{\partial t} + \frac{\partial(\alpha_g A \rho_g H_g V_g)}{\partial z} = S_g (e_{sg} - H_g) + H_g \frac{\partial(\rho_g \alpha_g A V_g)}{\partial z} - \frac{\partial(\alpha_g A q_g)}{\partial z} + q_{f-g} + q_{w,g} \quad \dots (3.44)$$

$$\frac{\partial(\alpha_f A \rho_f V_f)}{\partial t} + \frac{\partial(\alpha_f A \rho_f V_f^2)}{\partial z} = -\alpha_f A \frac{\partial P_{cav}}{\partial z} - \alpha_f A \rho_f g - \tau_{w,f} - F_D + F_{vm} \quad \dots (3.45)$$

$$\frac{\partial(\alpha_g A \rho_g V_g)}{\partial t} + \frac{\partial(\alpha_g A \rho_g V_g^2)}{\partial z} = -\alpha_g A \frac{\partial P_{cav}}{\partial z} - \alpha_g A \rho_g g - \tau_{w,g} + F_D - F_{vm} \quad \dots (3.46)$$

$$S_f = \frac{dA_{cav}}{dt} \rho_{f,sol}, \quad S_g = S_f F_g \quad \dots (3.47)$$

α_g, ρ_g, V_g are the local volume fraction, density, and velocity of gas phase, G_f, V_f are the local smeared density and velocity of molten fuel ($G_f = \alpha_f \rho_f$), S_g, S_f are the source terms which account for the addition of fission gases and fuel into the cavity upon melting, $F_g =$ coefficient of gas retention ($F_r = m_g/m_f$) where m_g, m_f are the masses of fission gas and fuel inside a node, $H_i =$ Phase specific enthalpy ($i = f, g$). $e_{si} =$ Phase specific enthalpy at the location of the melt interface. $q_i =$ Phase specific diffusive heat transport, $Q_i =$ heat generation (W/kg). $q_{i-j} =$ Heat transfer between the two phases (W/m), $q_{w,i}$ is the phase-specific wall heat transfer, A is the cross-sectional area of cavity, P_{cav} is the cavity pressure, g is the gravitational acceleration, $\tau_{w,i}$ is the wall shear stress, F_D is the drag force between the two phases, and F_{vm} is the virtual mass force. The vector of unknown variables for Eq. (3.41–3.46) is $[G_f \ H_f \ \rho_g \ H_g \ V_g \ V_f]^T$.

In the Eq. (3.47), a change in cavity area (A_{cav}) due to melting causes the generation of a non-zero source term (S_f). In turn, S_f results in a non-zero gas phase source term (S_g). The entry of S_f, S_g in Eq. (3.41–3.42) causes an increase in the molten fuel volume fraction (α_f) and the gas phase density (ρ_g) (Figure 3.2 presents gas release during melting schematically). This leads to a rise in local pressure (P_{cav}) (Refer Eq. 3.35). The rise in pressure sets up a dispersive pressure gradient in the momentum conservation equation (Refer Eq. (3.45–3.46)). The right-hand side of these equations combines the dispersive pressure gradient with the forces of gravity, wall friction, inter-phase friction and virtual mass in the calculation of the resultant force. The boundary conditions are as follows:

$$\frac{\partial v_i}{\partial z}\Big|_{z=Z_b} = 0, \quad \frac{\partial v_i}{\partial z}\Big|_{z=Z_t} = 0, \quad q_i|_{z=Z_b} = -K_i \frac{\partial T_f}{\partial z}\Big|_{z=Z_b}, \quad q_i|_{z=Z_t} = -K_i \frac{\partial T_f}{\partial z}\Big|_{z=Z_t} \dots (3.48)$$

Here, $z = Z_b, Z_t$ initially represent the solid blanket pellet surfaces at the bottom and top of the annular pellet cavity, respectively. In case of solidification and complete blockage, the corresponding boundary for fluid flow shifts to the location of the blockage. If the blocked region melts again, the boundary shifts back to the corresponding solid blanket pellet surface.

In the context of the above presented governing equations, it is important to mention that the present model does not attempt to model the radial variations in the fission gas retention coefficient (F_g , refer Eq. (3.47)). The use of a constant F_g at any given axial location, regardless of the melt interface radius, is a consequence imposed using an empirical correlation for the evaluation of the burnup dependent fission gas release fraction [12]. However, the radial variations can be important towards the estimation of the localized pressurization, as evident from the pressure closure law (Eq.

(3.35)) and the momentum conservation equations (Eq. (3.45–3.46)). This aspect is addressed through the development of a fission gas release solver in Chapter 5.

3.1.11 Fuel-clad gap conductance model

Gap conductance (h_{gap}) is an important thermal parameter which affects the fuel temperature significantly. It combines the following three phenomena: (a) fuel-clad heat transfer via direct contact (b) fuel-gas-clad heat transfer, also known as gap heat transfer and (c) fuel-clad radiation heat transfer. At the start of irradiation, the gap width between fuel pellet and clad is maximum. With increase in burnup, thermo-mechanical phenomena (swelling, cracking and relocation, thermal expansion) result in complete gap closure. Similarly, during transient heat-up, thermal expansion of high temperature fuel also results in gap closure. Roughness of the fuel and clad surfaces affects the direct contact heat transfer. The release of fission gases during steady-state or transient changes the conductivity of the mixture of gases present between the two surfaces. A mechanistic model for transient applications should provide: (a) Smooth transition between open-gap and closed-gap heat transfer (b) Expressions for the three heat transfer modes that integrate without generating abrupt fluctuations in the temperature field. A model proposed by Dharmadurai [118] does not fulfil these requirements appropriately, as it generates fluctuations upon fuel-clad gap closure. A modified jump-distance model developed by Ross and Strout is more suitable in this regard [119,120]:

$$h_{gap} = h_{gas} + h_{solid} + h_{rad} \quad \dots (3.49)$$

$$h_{gas} = \frac{K_g}{(R_{Cl}^t - R_O^t) + (j_f + j_c) + C_{gap,1}(\delta_c + \delta_f)} \quad \dots (3.50)$$

$$h_{solid} = \frac{C_{gap2} K_s}{\delta_{eff}^{(2C_{gap3}-1)}} \left(\frac{P_{gap}}{H} \right)^{C_{gap3}} \quad \dots (3.51)$$

$$h_{rad} = \sigma_B \left(\frac{1}{\varepsilon_f} + \frac{1}{\varepsilon_c} - 1 \right)^{-1} (T_O^2 + T_{Cl}^2)(T_O + T_{Cl}) \quad \dots (3.52)$$

$$j_f = \left(\frac{2-a_{mix}}{a_{mix}} \right) \frac{(2\pi R_m T_O)^{1/2} K_g}{(\gamma+1)C_v P_{pin}}, j_c = \left(\frac{2-a_{mix}}{a_{mix}} \right) \frac{(2\pi R_m T_{Cl})^{1/2} K_g}{(\gamma+1)C_v P_{pin}} \quad \dots (3.53)$$

$$a_{mix} = \frac{\sum_{i=1}^3 a_i X_i M_i^{-1/2}}{\sum_{i=1}^3 X_i M_i^{-1/2}} \quad \dots (3.54)$$

$$K_g = \sum_{i=1}^3 \frac{K_i}{1 + \sum_{\substack{j=1 \\ j \neq i}}^3 \frac{G_{ij} X_j}{X_i}} \quad \dots (3.55)$$

SAS-4A DEFORM literature provides expressions for jump distances, mixture thermal conductivity, mixture accommodation coefficient, and other terms ($C_{gap,1} = 1.98e^{-1.23365 \times 10^{-8} P_{pin}}$, $C_{gap,2} = 0.638$, $C_{gap,3} = 0.67$) [113]. Effective surface roughness and thermal conductivity of the gap depend upon the individual roughness and conductivities of the two surfaces $\left(\delta_{eff} = \left(\frac{\delta_f^2 + \delta_c^2}{2} \right)^{1/2}, K_s = \frac{2K_c K_f}{(K_c + K_f)} \right)$. Gas mixture thermal conductivity is a result of the kinetic theory of gases. SAS-4A DEFORM considers only two components in Eq. 3.55 (Helium and Xenon). The present model also considers the thermal conductivity of Krypton. Appendix-A details the gas thermal conductivity correlations (Refer Eq. A. (23–25)). Results show that this reduces the gap conductance, which increases the amount of melting. The accommodation coefficients are evaluated on the basis of well-established models available in literature [121].

3.2 Salient features of the numerical algorithm

3.2.1 Discretization and stability criteria

The basic framework of the numerical algorithm rests on the finite difference method, with an adaptive grid that adjusts in accordance with the melt interface motion as well as the presence/absence of molten fuel at an axial location. Temporal derivatives

are discretized explicitly, whereas spatial derivatives are discretized centrally. The underlying assumptions are as follows:

(a) A discretized node represents a control volume (CV) sufficiently small enough, such that any dependent variable (say, E) can be considered to vary linearly inside it. Therefore, an integral over the CV can be expressed as a product of the variable at the mid-point with the volume inside it. ($\int_{z_{k-1/2}}^{z_{k+1/2}} y dz = y_k \Delta z$)

(b) The time-step is small enough so that the definite integral of any dependent variable can be expressed as a product of the variable at any given instant with the time-step.

$$\left(\int_t^{t+\Delta t} E dt = E^{t+\theta\Delta t} \Delta t\right).$$

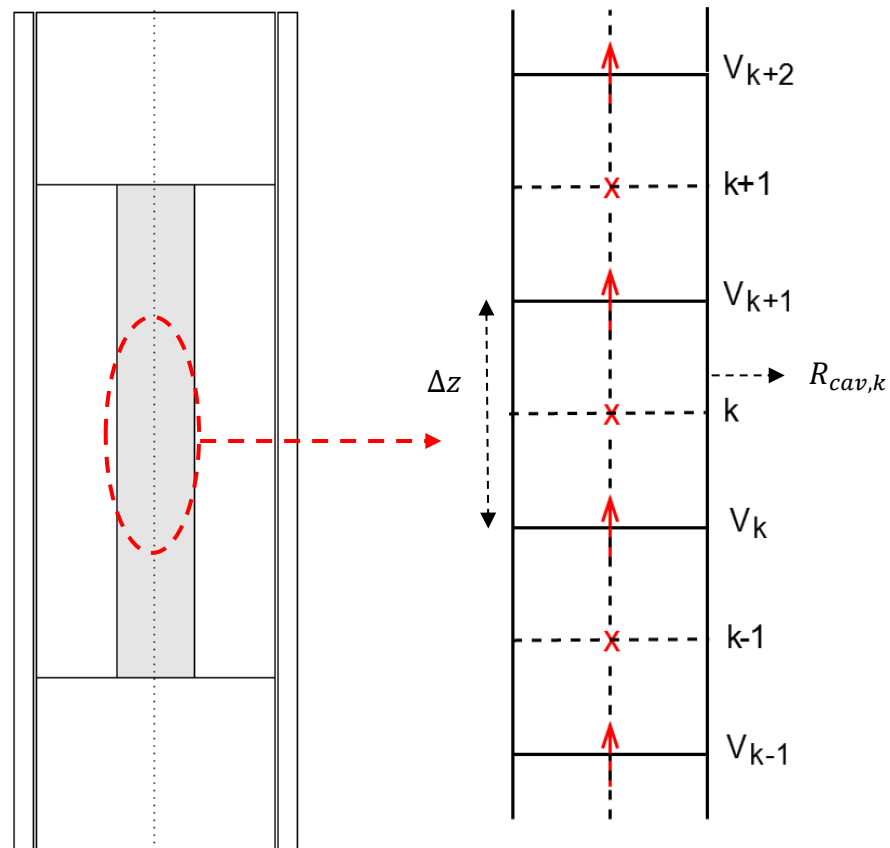


Figure 3.3: Nodes of the multi-phase flow spatial mesh (Velocity locations are staggered; Area of flow is variable).

Appendix-B presents the discretized equations, flux definitions, coefficients, and boundary conditions. A staggered mesh is used for the velocity nodes (Refer Fig. 3.3). An upwind scheme is used for calculating the mass, momentum, and enthalpy fluxes. At the upper and lower flow boundaries, all fluxes except diffusive heat fluxes are set to zero. The use of pressure at the end of time-step ($P_{cav}^{t+\Delta t_2}$) in the momentum conservation equation introduces an extent of implicitness in the formulation (Refer Eq. (B.9-B.10)). Different stability criteria are required for the enthalpy formulation (Δt_1) and multi-phase flow (Δt_2) models [54,122]:

$$\Delta t_1 = \min \left\{ \begin{array}{l} \frac{\rho_f C_f (T_f) \Delta r^2}{2K_f (T_f)} \\ \frac{\rho_c C_c \Delta r_c^2}{2K_c} \end{array} \right. , \Delta t_2 < \frac{\Delta z}{|V_g|} \quad \dots (3.56)$$

An additional constraint on Δt_2 arises from the reduction in A_{cav} due to melt freezing (Refer Section 3.1.6), since A_{cav} affects the coefficients of the discretized multi-phase flow equations. To maintain stability of the solution up to cavity blockage ($A_{cav} \leq 0.04\pi R_i^2$), the required Δt_2 values are significantly smaller in comparison with values obtained from the above expression (Refer Section 3.3.1).

In the above context, it is important to mention a region of frequent instability in the numerical algorithm. These instabilities arise when α_f approaches unity. If unconstrained, the multi-phase flow equations (Eq. (B.4-B.10)) frequently generate G_f values greater than ρ_f , which is physically inconsistent. To tackle such sources of divergence, the following technique has been incorporated in the numerical algorithm.

3.2.2 Mass conservation residual and flux corrections

The conservation of mass is numerically verified at the end of each heat-transfer time step by calculating the following residual:

$$Res_f = \sum_{z=Z_{bs}}^{z=Z_{ts}} \pi((R_{int}^2 - R_i^2))\rho_{f,s}\Delta z - \sum_{z=Z_{bs}}^{z=Z_{ts}} \alpha_f A_{cav}\rho_{f,l}\Delta z \quad \dots (3.57)$$

Along with physical consistency, another important reason for ensuring mass conservation is the intrinsic link between fuel mass and relocation reactivity feedback. A fuel mass residual will reflect as fuel voiding/positive reactivity in the computation (Refer Eq. (2.10)). Hence, a small residual can also impact the accident. It is observed that a conservation residual less than 10^{-4} kg per fuel pin does not generate any significant impact on the accident outcome. Additionally, it is found that in numerical simulations with the developed numerical algorithm, the conservation residual reaches a maximum magnitude of $10^{-5} - 10^{-6}$ kg.

A critical issue faced in the numerical algorithm is the prescription of the flux corrections for control volumes experiencing melt thermal expansion. Freezing of molten fuel on relatively cooler pellet surfaces leads to nil velocity, in accordance with the particle viscosity model. However, because of continued melting, heat-up and the associated melt thermal expansion, eventually, the physical density (ρ_f) becomes smaller in comparison with the smeared density (G_f), particularly near the peak power region. Consequently, the solution diverges since the melt volume fraction (α_f) now exceeds unity. Physically, this situation correlates with a classical, variable-density, incompressible flow problem, wherein a net outward mass flux occurs due to thermal expansion. To evaluate the equivalent, net outward flux for the current problem, the following expression is derived from Eq. (B.4):

$$(G_f A_{cav} V_f)_{k+\frac{1}{2}}^t \Big|_{corr} = (G_f A_{cav} V_f)_{k+\frac{1}{2}}^t + \frac{(G_f^{t+\Delta t} - \rho_f^{t+\Delta t})}{C_{F3}} \quad \dots (3.58)$$

The above correction ensures the conservation of mass at each node while simultaneously generating a net outward mass flux because of thermal expansion. The

new velocity obtained from the corrected mass flux is used subsequently in the energy and momentum flux calculations.

3.2.3 Calculation procedure

Steady-state calculations are carried out prior to the beginning of transient simulation. Eq. (B.1) is solved to obtain the distribution of enthalpy ($H_f^{t+\Delta t_1}$) within the fuel and blanket columns. Comparison of enthalpies with an enthalpy vs. temperature database based on Eq. (A.4-A.10) yields the temperature distribution ($T_f^{t+\Delta t_1}$). The database is constructed a-priori and allows simple incorporation of the temperature, mole-fraction (y) and state ($0 \leq o \leq 1$) dependent fuel specific heat $C_f(T_f, y, o)$ into the algorithm. Thereafter, Eq. (B.2-B.3) give the clad and coolant temperature distributions ($T_c^{t+\Delta t_1}, T_{ct}^{t+\Delta t_1}$). Since only gases are present in the central hole at steady state, cavity calculations remain limited to gas phase ($i = g$ only). First, the gas phase density ($\rho_g^{t+\Delta t_2}$) is obtained from Eq. (B.7). Subsequently, Eq. (B.8), (3.35), and (B.9) are solved in sequence to obtain gas phase enthalpy and temperature ($H_g^{t+\Delta t_2}, T_g^{t+\Delta t_2}$), cavity pressure ($P_{cav}^{t+\Delta t_2}$) and gas phase velocity ($V_g^{t+\Delta t_2}$) respectively. This sequence is repeated for each node of the pellet cavity (bottom-most to top-most node). Upon achieving convergence in T_f throughout the fuel nodes, the steady state computations are halted. A stepwise solution procedure for the UTOP transient is described as follows:

- (i) With the initiation of transient ($t = 0$ s), rise in reactor power results in rise in the fuel enthalpy. The heat-transfer and gas-phase conservation equations are solved as a continuation of the steady-state calculations described above. Additionally, $H_f^{t+\Delta t_1}$ is compared with the interface enthalpy (H_{int} , function of T_{int}) to detect melting at any axial location. Once melting begins at a particular

node, the melt-interface ($R_{int}^{t+\Delta t_1}$) position is determined using radial interpolation [77]. Geometrical modifications are carried out to ensure that one fuel node continuously travels with the melt interface. The mass source terms of both phases (S_f, S_g) are calculated for addition in the multi-phase flow conservation equations.

- (ii) After melting has begun, multi-phase governing equations are solved for both phases ($i = f, g$). Solution of Eq. (B.4-B.5) at each cavity node provides $G_f^{t+\Delta t_2}$ and $\alpha_f^{t+\Delta t_2}$ respectively. Solution of Eq. (B.6) provides $H_{f,l}^{t+\Delta t_2}$, which when compared with the fuel enthalpy vs. temperature database provides molten fuel temperature ($T_{f,l}^{t+\Delta t_2}$). Eq. (A.4-A.10) use $T_{f,l}^{t+\Delta t_2}$ to derive the fuel density $\rho_{f,l}^{t+\Delta t_2}$, which is used in Eq. (B.5) in the next time-step. Thereafter, Eq. (B.7), (B.8), (3.35), and (B.9) are solved in sequence to obtain $\rho_g^{t+\Delta t_2}, T_g^{t+\Delta t_2}, P_{cav}^{t+\Delta t_2}$ and $V_g^{t+\Delta t_2}$ respectively. If at any staggered velocity node, $\alpha_f^{t+\Delta t_2} > 0.02$ holds true for either of the neighbouring nodes (k or $k - 1$, Figure 3.3), then Eq. (B.10) is solved for molten fuel phase velocity ($V_f^{t+\Delta t_2}$). This condition is in accordance with the flow regime constraints developed in Section 3.1.4 [89]. Eq. (3.25) provides the expression for dynamic viscosity.
- (iii) During the time march, if the molten fuel enthalpy $H_{f,l}$ at any cavity node is less than H_{sol} , then the fuel mass present in the node solidifies on the cavity wall. The solidified fuel mass is re-transferred to the domain of enthalpy formulation and geometrical changes are carried out in accordance [77].
- (iv) Time marching proceeds within the cavity domain until the marching period equals the heat transfer time step ($m\Delta t_2 = \Delta t_1$). Once this occurs, enthalpy

formulation is solved for the next Δt_1 , and steps $(i - iv)$ are repeated. After a pre-fixed march period ($250 \times \Delta t_1$), Eq. (A.1-A.3) are solved to update K_f .

- (v) At the end of each heat transfer time-step, the axial distributions of α_f , ρ_f and R_{int} are used in Eq. (2.10–2.14) to arrive at the in-pin fuel motion (or relocation) feedback. The entire procedure is repeated until the end of the transient.

3.3 Results and discussion

3.3.1 Grid independence analysis

In this section, grid sensitivity study is carried out to determine the optimum mesh size. Zone-1 fuel pin specifications are used for the study. A typical, slow-ramp, transient overpower condition is simulated using multiple mesh sizes. Table 3.1 displays the results of the analysis. The maximum in-pin fuel motion feedback generated during the transient ($\rho_{rel_{max}}$) is selected for the grid independence study because it is a function of the space-time distribution of multiple heat-transfer and fluid flow variables ($R_{int}, S_f, T_{f,w}, T_{f,l}, \alpha_f$). Therefore, achieving convergence in ρ_{rel} is equivalent to achieving convergence in the in-pin fuel motion behaviour. The deviations are defined as the percentage change in the peak relocation feedback upon adopting the current grid with respect to the previous (upper) grid.

Table 3.1: Grid independence study.

S.NO	Fuel grid size (axial x radial)	$\rho_{rel_{max}}$ (pcm)	Deviation (%)
1	10 x 10	-2.6523	-
2	20 x 20	-1.823	-31.2
3	30 x 30	-1.9213	5.4
4	40 x 40	-1.9288	0.4

The study shows that the deviation for the fourth mesh (40 axial x 40 radial) with respect to the third mesh (30 x 30) is 0.4 %. Therefore, the third mesh (30 axial x 30

radial) is used in the fuel column for further analysis. The reasons behind the non-linearity in the evolution of ρ_{rel} (Table 3.1) are as follows:

- (a) The crust solidification module generates a gradual downward relocation of molten fuel (Section 3.1.6). If enough molten fuel gets solidified at any axial node, fluid flow is blocked at that node. The change in the flow domain affects the evolution of α_f , $T_{f,l}$, S_f , and R_{int} . Once the cavity re-melts because of rise in power, these variables are affected again. In this way, repeated flow blockage and re-melting perturb the fluid flow variables linked with ρ_{rel} .
- (b) The phase-change heat transfer model combines the enthalpy formulation with a grid modification mechanism [54,77] to address the modelling challenges associated with annular fuel pellets (Section 1.6). A limitation of the resultant heat transfer model is that it generates perturbations in R_{int} and S_f at each instance of deletion of a solid fuel node from the heat-transfer domain. The perturbations for the coarsest grid (10×10) are greater than those for the finest grid (40×40).

The above-described periodic perturbations affect ρ_{rel} . The coarsest grid generates greater perturbations as compared to those generated by the finest grid. Hence, the evolution of ρ_{rel} in Table 3.1 remains non-linear for the coarse grid.

Table 3.2: Grid size details (dimensions are for fast reactor case study).

Model region	Δr (mm)	Δy (mm)
Fuel column	0.0625	33.33
Upper/lower blanket column	0.0625	150
Inner cavity	-	33.33
Clad	0.15	33.33/150 (fuel/blanket)

Grid dimensions employed for various parts of the problem domain are enlisted in Table 3.2. The upper and lower blanket columns and clad are discretized with 2×30 (axial x radial) and 34×3 (axial x radial) nodes, respectively. A general schematic of the employed grid is displayed in Fig. 3.4.

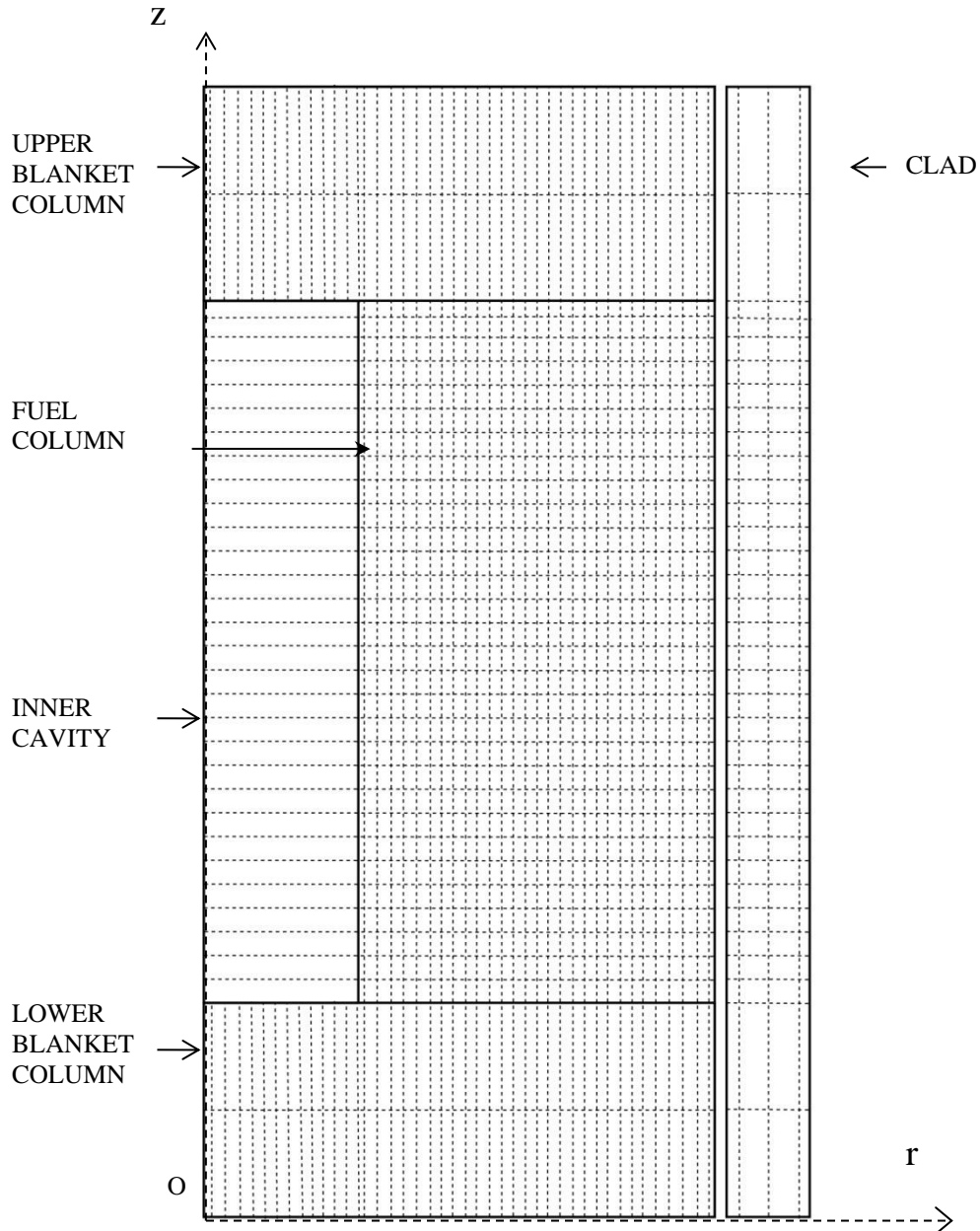


Figure 3.4: Model domain discretization.

All boundaries oriented parallel to the z -axis (axial direction) are described with half control volumes to capture the radial boundary conditions. The inner cavity is discretized using 1-D axial mesh with radius initially equal to fuel pellet inner radius

(R_l). Upon melting or solidification, the local cavity radius changes to the solid/liquid interface radius (R_{int}).

The algorithm employs a heat-transfer time step of 10^{-3} s (Δt_1). As for the multi-phase flow, the main stability concern arises in the gas-phase energy and momentum equations. It is found that in equilibrium core fuel, fluid flow time steps of $50 \mu s$ (prior to melting) and $10 \mu s$ (during melting) are sufficient to maintain stability. However, in the BOL core, the gas-phase density is much smaller due to absence of fission gases. Consequently, the solution requires smaller time steps of $10 \mu s$, $5 \mu s$ before and after melting, respectively. The necessity of reduced time-step after melting arises from the reduction in the equivalent cavity cross-sectional area ($\alpha_g A_{cav}$) of the gas-phase in locations that are nearly choked with frozen fuel.

A time step sensitivity study reveals the extent of convergence of the numerical algorithm for different multi-phase flow time steps ($\Delta t_2 = 20 \mu s, 15 \mu s, 10 \mu s$, and $5 \mu s$). ρ_{rel} values at $t = 100$ s during the single pin UTOP transient (Section 2.3.3) are compared for each Δt_2 . The values are -1.72 pcm, -2.07 pcm, -1.75 pcm, and -1.747 pcm for $20 \mu s, 15 \mu s, 10 \mu s$, and $5 \mu s$, respectively. The deviation (defined above) between the ρ_{rel} values for $10 \mu s$ and $5 \mu s$ is 0.28% . Therefore, the solution converges with the selected multi-phase flow time step ($\Delta t_2 = 10 \mu s$).

3.3.2 Optimization of the free volume gas escape model

Considering the presence of the gas-phase density (ρ_g) in the pressure closure equation, it can be stated that ρ_g plays a vital role in the evaluation of the pressure force in the molten fuel momentum equation (Refer Eq. (3.35) & (3.45)). The free volume model simulates the escape of fission gases from the annular pellet cavity to the plenum, resulting in a reduction in ρ_g . Consequently, the pressure field is perturbed, which leads

to an extraneous perturbation in the melt momentum conservation. Figure 3.5 presents an example of the changes in melt motion because of such pressure perturbations. The magnitude of the constant (c) represents the rate of escape through the inter-pellet gaps. For a large rate of escape (Fig. 3.5a), significant variations in the melt volume fraction (α_f) can be observed as compared to a small rate of escape (Fig. 3.5b). On the other hand, complete removal of the free volume gas escape model from the algorithm results in an unrealistic pressure within the annular cavity (~ 250 MPa) upon a large amount of melting, which cannot be sustained by the clad. The available literature has comprehensively proven the effective mitigation of fuel-clad mechanical interaction for annular fuel pins (Refer Section 1.7.1 [28,34]). Furthermore, under such a high pressure, the multi-phase flow tends to destabilize. Therefore, an optimization of the free volume gas escape model is required to eliminate the extraneous perturbations while simultaneously maintaining a realistic pressure within the annular pellet cavity.

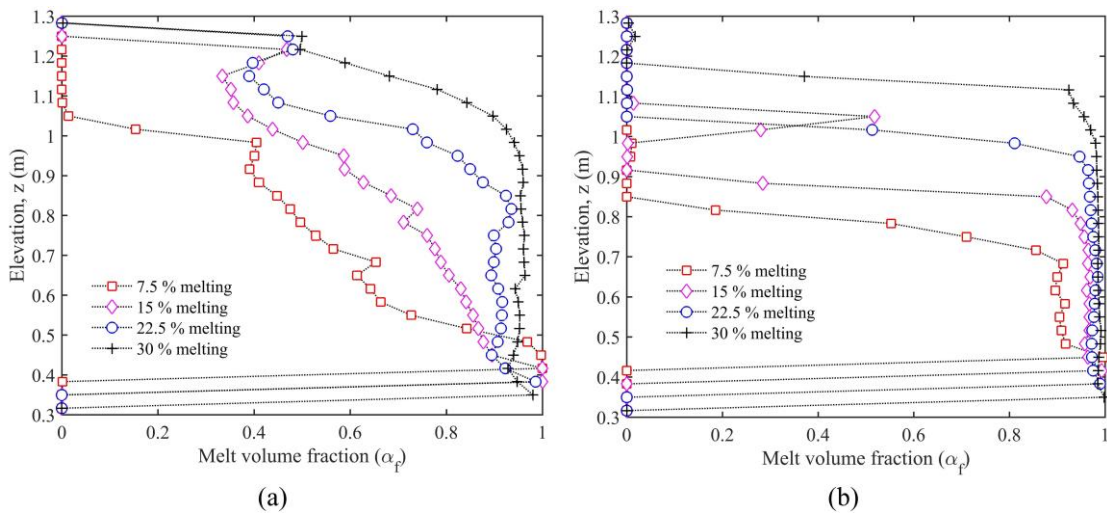


Figure 3.5: Molten fuel volume fraction as a function of axial position, melt mass fraction and rate of gas escape through the plenum. (a) $c = -2.0$, and (b) $c = -0.1$.

Table 3.3 presents a sensitivity analysis of the melt motion with respect to the fission gas escape rate. The table presents the melt relocation feedback magnitudes specific to the central fuel subassembly (Zone-1). The mathematical expressions used

in the calculation are detailed in Chapter 2 (Refer Eq. (2.10–2.14)). The deviations are least for the case of the least rate of escape. Based on the sensitivity study, the escape constant (-0.001) is selected for subsequent numerical simulations.

Table 3.3: Sensitivity of melt motion with respect to the rate of escape of fission gases towards plenum. The deviations (%) are with respect to the preceding data $(100(\rho_{f,curr} - \rho_{f,prev})/\rho_{rel,prev})$.

c	$\rho_{rel}(70 \text{ s})$ (%)	$\rho_{rel}(80 \text{ s})$ (%)	$\rho_{rel}(90 \text{ s})$ (%)	$\rho_{rel}(100 \text{ s})$ (%)
-2.0	-1.93	0.00	-3.00	0.00
-1.0	-1.91	-1.01	-2.24	-25.4
-0.5	-1.78	-6.85	-2.07	-7.65
-0.1	-1.91	7.64	-2.08	0.47
-0.05	-1.93	0.70	-2.03	-2.24
-0.01	-1.73	-10.5	-1.82	-10.4
-0.005	-1.58	-8.25	-1.75	-3.60
-0.001	-1.58	-0.48	-1.78	1.54

It is important to mention that the experimental benchmark data for the free volume gas escape model is scarce in literature. The plenum pressure (P_{pin}) (both before and after the transient) are generally measured through pin puncture tests [33]. However, the transient evolution of P_{pin} is not measured since destructive testing cannot be carried out during the transient. Hence, it remains difficult to validate the free volume gas escape model experimentally.

3.3.3 Experimental validation (CABRI-E9bis test)

This test was conducted on an OPHÉLIE-6 fuel pin (Refer Table 2.8 for specification). The pin contained fragmented upper blanket pellets [33]. Wide gaps between these pellet fragments were reported before the test. A uniform power ramp of 0.95 % P_n/s ($P_n = 59.4 \text{ kW}/m, t = 0 \text{ s}$) was implemented over the pin until the power level reached 181 % ($P_{max} = 107.5 \text{ kW}/m, t = 88 \text{ s}$). For the next 195 s, this level

was maintained. During the last ~ 28 s of this constant power period, the flow rate was reduced linearly at a rate of 1.4 % ($\dot{m}_{ct,n}/s$) until the end of the test (Refer Table 2.9). Fuel melting was detected at peak power = 73 kW/m. The melt penetrated the gaps in the upper blanket between 65-69 s, as per the on-site hodoscope data [33]. Based on the segregation of metallic fission products in the melt, it was concluded that the melt displacement occurred at a slow speed (Refer Section 2.4.1 for details).

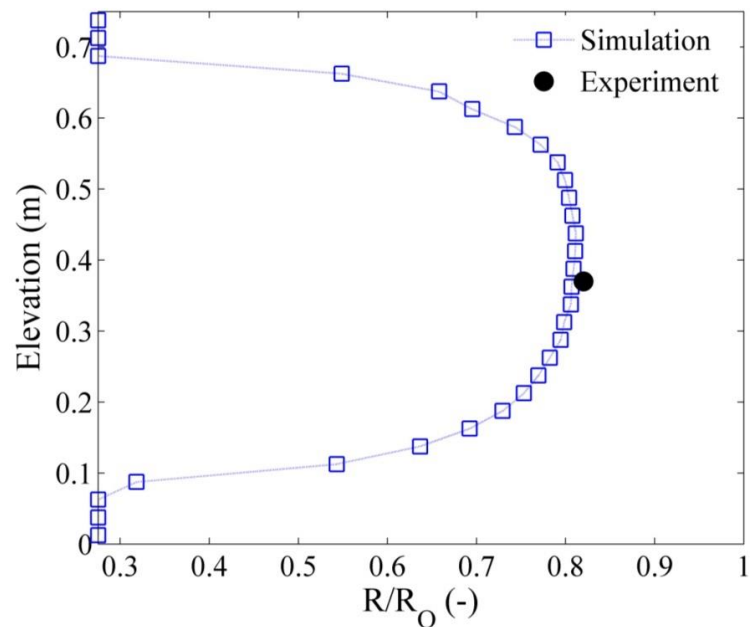


Figure 3.6: CABRI-E9bis melt interface profile (R_{int}/R_o ; end of transient).

As a first step, the thermal results of the simulation are compared with the test data. Figure 3.6 presents the numerically obtained melt interface profile at the end of transient ($t = 283$ s), as well as the physical measurement taken during the post-test examination. The top and bottom three nodes did not undergo melting since the position of the interface remained unchanged throughout. Here, the axial coordinate is with reference to the bottom of the fissile column (BFC). The maximum extension of the melt interface (81.1 %) occurred near the core mid-plane. The melt mass fraction signifies ratio of molten and total fuel masses. The solver calculates a maximum melt mass fraction of 39 % against experimental data of 40-50 %.

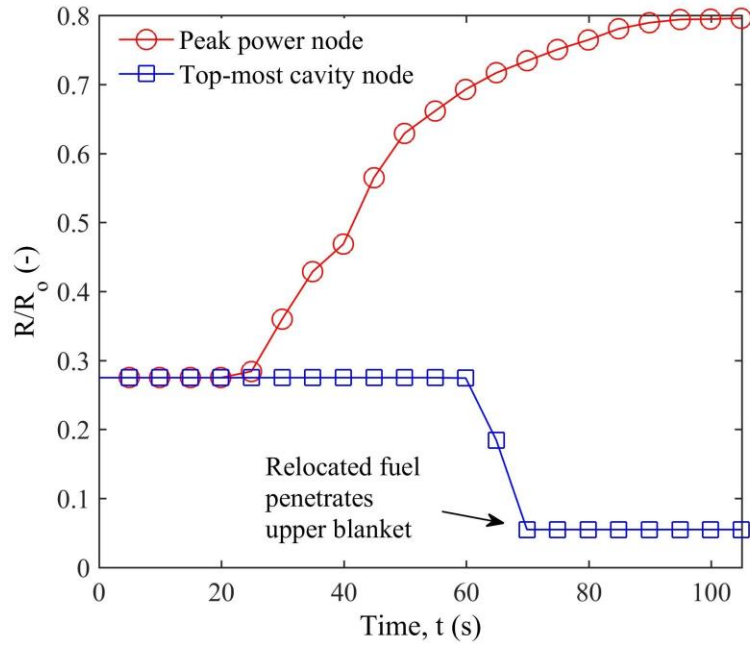


Figure 3.7: Melting and solidification history for E9bis test.

Second, let us examine the fluid flow behaviour. Simulation indicates complete blockage of the cavity top due to solidification of molten fuel at $t = 67$ s (Refer Fig. 3.7). This is an indication of penetration of the upper blanket at the same time. It is noted that the time of penetration is within the experimentally observed penetration period. The melt interface progression at the peak power node exhibits a change in slope ($t = 40$ s). This change reflects the extension of molten fuel column up to the peak power node, located near the core mid-plane (Refer Fig. 3.7 ($t = 40$ s)). Collection of molten fuel at this location increases the heat flux at the solid/liquid interface (or cavity radius), which results in the enhanced speed of radial melt progression [77]. The non-zero parameter (R/R_0) after 67 s is due to stability constraints imposed on the crust solidification model (Refer Section 3.1.6).

To describe the melt motion, a thermal schematic of the E9bis fuel column is presented in Fig. 3.8. In this figure, a slight downward relocation and solidification of molten fuel is visible at $t = 30$ s. This trend of downward relocation and solidification

continues until blockage of the cavity in the lower region ($t = 40$ s). Continuous power rise causes further downward relocation and blockage at a lower axial location. Simultaneously, a molten fuel column develops above the blockage. The downward relocation and upward lengthening of the molten fuel column continue. In this way, the length of the molten fuel column increases ($t = 60$ s).

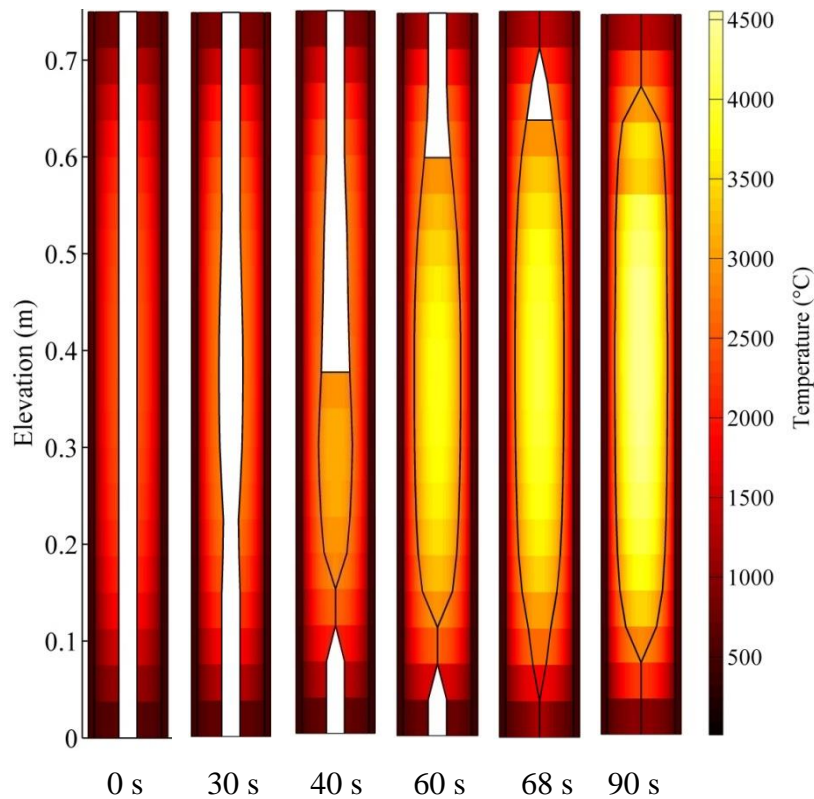


Figure 3.8: E9bis thermal and molten fuel flow schematic (Elevation is with reference to BFC).

High molten fuel temperature (4608 °C, maximum) results in extensive thermal expansion, which increases the molten fuel axial penetration (fuel vaporization concerns are addressed in Chapter 4). At a melt mass fraction of 26 % ($t = 67$ s), fuel completely occupies the top-most node. Around the same time ($t = 68$ s), molten fuel reaches the bottom of fuel column and solidifies ($t = 68$ s). Zero cavity radii at the bottom and top regions represent the resultant cavity closures. After some time ($t = 88$ s), the transient enters the maximum power period. The entire cavity gets occupied with molten fuel.

Table 3.4: Results of CABRI-E9bis [33] benchmarking study.

Parameter	Simulation	Experiment
Power to melt (kW/m)	72.4	72.7
Maximum melt radius (% Ro)	81.1	82 ± 2
Pin averaged melt mass fraction (%)	39	40-50
Time of penetration of upper blanket (s)	67	65-69
Upper melt extent (m/BFC)	0.675	0.635
Lower melt extent (m/BFC)	0.075	0.095

The flow field velocities predicted by the solver are low. Because of these low velocities and a small hydraulic diameter (mini channel), the flow is laminar. Clearly, the tendency of molten fuel to form a column just above the choked region is a result of the force of gravity. Additionally, the inability of fuel to move rapidly in both upwards and downwards directions is a result of melt freezing and the associated rise in viscous forces. Therefore, two important hydrodynamic forces governing the melt displacement are gravity and viscous forces. Furthermore, the major driving effect influencing the displacement up to the top of the fuel column is the thermal expansion of molten fuel. An excellent agreement between the model predictions and experimental results can be observed from Table 3.4. After the successful validation, the developed algorithm is confidently implemented towards the investigation of fuel behaviour during UTOP.

3.3.4 Melt motion predictions under fast reactor conditions

Next, the validated algorithm is utilized to simulate the fuel melting and multi-phase motion in SFR conditions under UTOP. The accident conditions for single pin studies have been described earlier in Chapter 2 (Section 2.3.3) and are not repeated here for the sake of brevity. The system chosen for analysis involves the typical, annular

fuel pin of a medium-sized SFR (Refer Table 2.4 for fuel specifications). This system is specifically chosen for the following reasons:

1. Since the CABRI reactor utilizes a thermal spectrum, neutron self-shielding effect inhibits nuclear fission in the inner region of fuel pellets. The result is a depression in volumetric heat generation (\dot{Q}) along the fuel pellet radius. In the available literature, a radial power depression factor of 0.45 is quoted for the CABRI-2 test series (Refer Section 2.4.1 for details). Consequently, the magnitude of \dot{Q} in molten fuel is considerably smaller as compared to the outer pellet region.
2. Under fast neutron spectrum, power depression across the fuel pellet radius is negligible. Therefore, \dot{Q} of molten fuel will be significantly greater in SFR conditions as compared to experimental conditions. Consequently, the melt temperature will be greater, which will affect the crust formation process as well as the melt viscosity.
3. The length of the active core region inside the CABRI reactor (0.75 m) is smaller as compared to the typical fast reactors under development and commissioning in India (1 m) [13]. Furthermore, the axial power profile applicable to the thermal spectrum of the CABRI reactor [45] is liable to differ from the power profile of SFR. Consequently, separate numerical simulations are required to investigate melt motion in typical fast reactor conditions.
4. The fuel pins tested in the CABRI experiments had been irradiated in the Phénix reactor up to intermediate burnup level (4 – 6 *atom percent*). However, typical SFR safety analysis also involves beginning-of-life (BOL) fuel, which: (a) does not contain fission gases and (b) has a different axial power profile specific to the BOL core.

Numerical simulations are performed for the following two fuel conditions:

Case I: Equilibrium fuel ($Bu = 3 \text{ atom percent}$)

Case II: BOL fuel (0 atom percent)

In consistence with the typical accident mechanism described in Section 2.3.3, a UTOP transient is simulated in the form of a slow, uniform rise in reactor power ($1 \% P_n/s$). Relevant thermophysical properties utilized in the simulations are described in Appendix-A. Fuel Specifications are detailed in Table 2.4. Steady-state operating parameters of both case studies are detailed in Table 2.2.

3.3.4.1 Results for case study I

(a) Melting

Figure 3.9a illustrates the transient heat-up and the subsequent melting followed by melt motion along the axis of the pellet cavity. The thermal maps are categorized based on the melt mass fraction to facilitate a comparison with Case-II in the subsequent section. The locations inside the pellet cavity filled with molten fuel ($\alpha_f \geq 0.8$) are colored and show the molten fuel temperature. The colorless (or white) locations show the presence of fission gases ($\alpha_g > 0.2$). The line separating the solid and liquid fuel represents the melt or interface radius (R_{int}). In locations without melt, the line simply represents the pellet inner surface radius (R_I). A cosine axial power profile exists inside the active core region. Consequently, the molten fuel located at the peak power location (core mid-plane; $z = 0.5 \text{ m}$) experiences the highest temperature as well as the greatest amount of melting. The temperature distributions for solid fuel, molten fuel, and clad are visible. The continuous coolant flow at the clad outer surface ensures relatively lower temperatures in the clad and outer areas of the fuel pellets. The axial power profile produces lower fuel temperatures in the lower and upper regions of the active core.

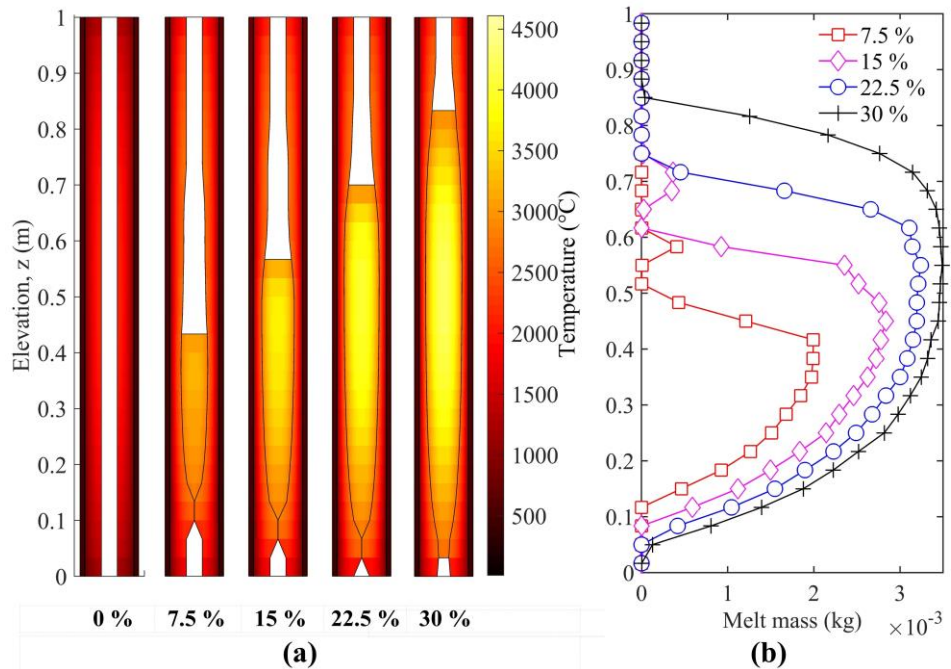


Figure 3.9: Melt motion in equilibrium fuel under SFR conditions: (a) Thermal map of the fuel column (b) Axial distribution of melt mass (plot is applicable for a single pin of the central subassembly; total fuel mass in one FBR-500 pin is 0.225 kg).

(b) *Melt motion*

A significant proportion of molten fuel agglomerates to form the so-called ‘melt column’ inside the pellets (Refer Fig. 3.9a). Note that this is analogous to the melt motion of the CABRI-E9bis test (Refer Fig. 3.8). The presence of such a column, characterized by high fuel volume fraction ($\alpha_f \geq 0.8$), immediately above the choked location remains a consistent feature throughout the transient. The white region above and below the column indicates that these areas are primarily occupied by the gas-phase. An axial plot of molten fuel mass (M_l) confirms the near absence of melt in the whitened locations (Refer Fig. 3.9b). The axial profile correlates with melt interface radius (r_{int}), since a larger r_{int} results in the melt column occupying a larger volume.

Due to the cosine variation in power, solidification of molten fuel occurs in colder regions, which leads to blockage. This impedes further downward flow, until the frozen fuel re-melts on account of rise in the reactor power. The cyclic process of freezing and

re-melting results in a so-called trickling, downward motion (Refer Section 3.1.6). Simultaneously, further melting in the central region, combined with significant thermal expansion of molten fuel, and high viscous resistance in the top region (due to solidification), result in a slow and upward flow of molten fuel. As a result, the molten fuel column, which was initially situated below the central node, grows at an approximately equal speed in both the upward and downward directions.

In this context, it is important to mention the contribution of the mini-channel flow regimes, which result in a continuous contact between the melt and pellet inner surface. Without a continuous contact, such a slow, experimentally consistent melt motion could not have been captured. The above-described trend continues until the end of the transient. It may be noted that the location of the melt column is well below the core mid-plane, at least for low melt mass fraction (7.5 %). This is a departure from the simulation results of the CABRI-E9bis test. It is deduced that this deviation is a result of the relatively flatter axial power profile employed in the present simulation, which accelerates the rate of re-melting [89].

3.3.4.2 Results for case study II

(a) Melting

Figure 3.10a illustrates the transient heat-up and the subsequent melting followed by melt displacement for the BOL fuel pin [97]. Since the steady-state operating parameters and thermophysical properties of the BOL fuel differ from the equilibrium fuel, the thermal maps are detailed for specific melt mass fraction levels instead of time instants to facilitate comparison with Case I. The axial variation in R_{int} is consistent with the cosine reactor power profile. The locations filled with molten fuel have noticeably undergone greater amount of melting as compared to other locations. This is

a consequence of the increased heat flux at the inner surface of fuel pellets adjacent to the melt column, which is mathematically represented by Eq. (3.11).

(b) Melt motion

Figure 3.10 provides a qualitative summary of the displacement behaviour in case of the BOL fuel pin. Major features of the displacement behaviour are as follows:

1. Melt agglomeration is a consistent phenomenon in both the case studies. However, the location of the melt column for BOL fuel is noticeably closer to the core-mid plane, specifically for 7.5–15 % melt mass fraction. In other words, the appreciable downward displacement observed in Case-I is decreased in Case-II.
2. The melt mass profiles, presented in Fig. 3.10b show the location of fuel within the cavity during the various stages of melting. A significant amount of melt mass is present above the melt column in the upper portion of the pellet cavity.

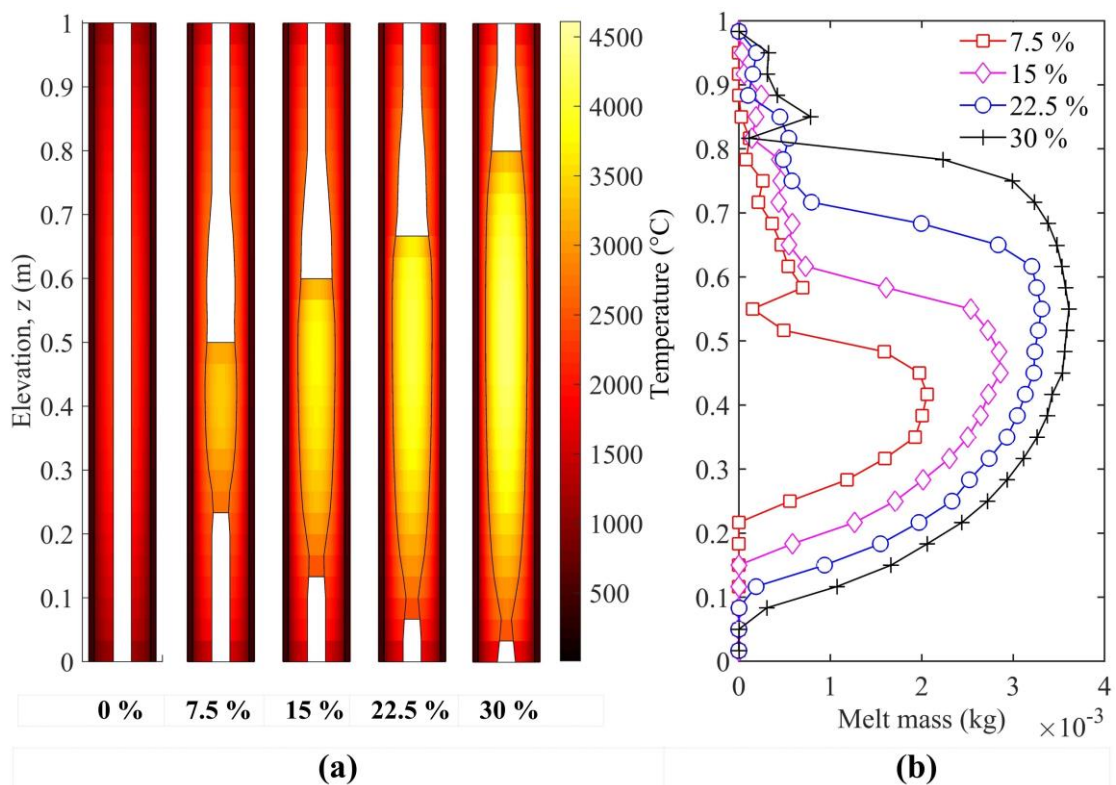


Figure 3.10: Melt motion in fresh fuel under fast reactor conditions: (a) Thermal map of the fuel column for Zone-1 fuel pin (b) Axial distribution of melt mass (single pin).

Figure 3.11 shows the temperature distribution within molten fuel ($T_{f,l}$) for the corresponding melt fractions. In the region above the agglomerate, $T_{f,l}$ is below the solidus temperature. The particle viscosity model (Eq. (3.25)) ensures a high viscosity (μ_f), which renders the melt immovable. Therefore, it does not agglomerate completely with the melt column below.

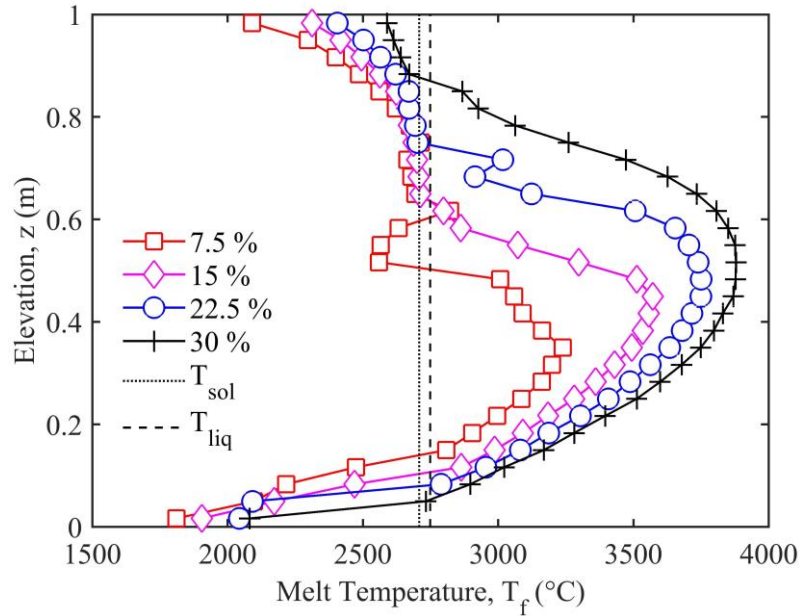


Figure 3.11: The temperature of molten fuel ($T_{f,l}$) as a function of axial position and melt mass fraction. Plots are specific to Case-II. In locations with absence of molten fuel, the plot shows the pellet inner surface temperature ($T_{f,wall}$).

3.3.5 Investigation of fuel mass relocation

The results of the above case studies are utilized to investigate the potential of an undesirable increase in fuel mass near the core mid-plane [97]. First, the melt mass profiles for both case studies are summarized in Fig. 3.12 to illustrate the progressive redistribution of molten fuel during the UTOP transient. For simplification of analysis, the fuel column is divided in three equal regions that represent the top (0–0.33 m), central (0.33–0.67 m), and bottom (0.67–1 m) axial segments. Elevations are with respect to BFC. For each region, the melt mass (M_l) and solid mass (M_s) are added

together to evaluate the total mass during the transient ($M_{transient}$). Mathematical definitions of the above terms are detailed in Chapter 2 (Refer Eq. (2.10-2.14). Here, all masses are calculated for Zone-I (central fuel subassembly) to facilitate ρ_{rel} computation subsequently ($M_f = 217 \times 0.225 \text{ kg}$). The transient mass is compared with the steady-state mass (M_{steady}) to determine the changes in fuel mass for the top, central, and bottom regions ($\Delta m = m|_t - m|_{t=0}$).

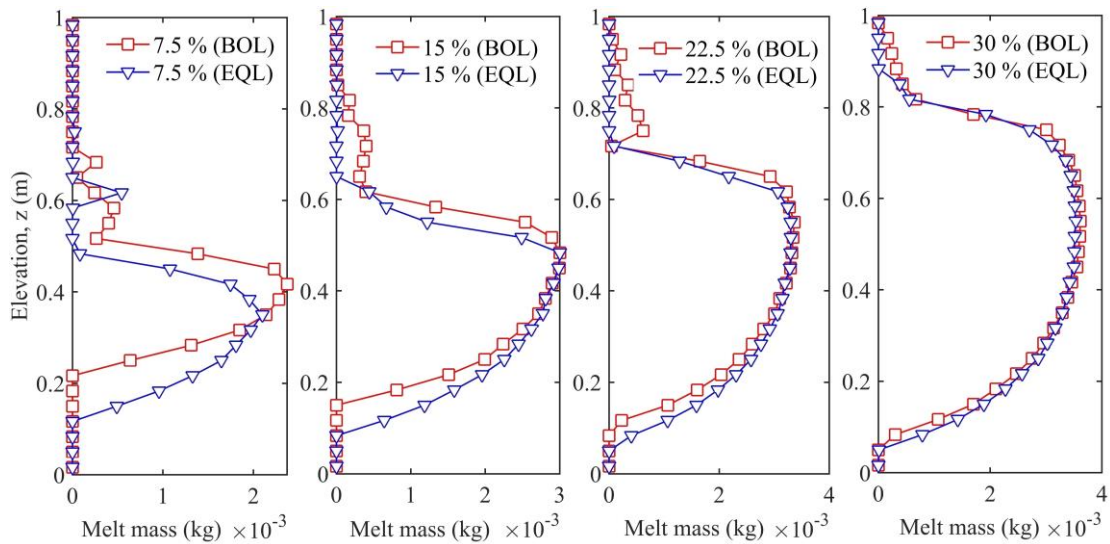


Figure 3.12: A summary of melt relocation in annular fast reactor fuel pins under UTOP transient. Total fuel mass for a single fuel pin is 0.225 kg (7.5, 15 ... 30 % are melt mass fractions).

Table 3.5: Table of fuel mass redistribution due to melting and motion. Mass relocation is with reference to 217 fuel pins of the central subassembly. (t = time instant (s); X_{max} = Peak linear power (kW/m))

MMF (%)	Case-I					Case-II				
	t	X_{max}	Δm_{cen}	Δm_{top}	Δm_{bot}	t	X_{max}	Δm_{cen}	Δm_{top}	Δm_{bot}
7.5	80	74.8	-0.66	-0.16	0.82	53	69.2	-0.40	-0.04	0.44
15	91	79.6	-0.37	-0.41	0.78	64	73.9	-0.20	-0.38	0.58
22.5	99	82.9	-0.30	-0.47	0.77	74	78.6	-0.14	-0.55	0.69
30	106	85.8	-0.67	0.04	0.63	86	84	-0.52	-0.21	0.73

Table 3.5 presents the results of the analysis. It is observed that in the central region (highest fuel void worth; Figure 2.3) surrounding the core mid-plane, the fuel mass is decreasing throughout the transient ($\Delta m_{cen} < 0$). A similar reduction can be seen in case of the top region. These losses are balanced by an equivalent gain in the bottom region. It is concluded that an undesirable increase in fuel mass near the core mid-plane is averted [97]. To clarify the physical mechanism responsible for the advantageous decrease in M_{cen} , the axial distribution of the fuel mass ($M_{transient}$) is presented in Fig. 3.13. The results of both case studies at equivalent melt mass fractions are plotted to facilitate the comparison of relocation behaviour. Important trends from Fig. 3.13 are as follows:

1. A prominent region of loss (fuel mass < 1.626 kg per node) can be seen above the core mid-plane in Fig. 3.13a. As melting continues, this region shifts upwards, until it is located close to the top of the fuel column (Refer Fig. 3.13d).
2. There is a prominent leftward shift in the data-points at the core mid-plane ($Z_m = 0.5$ m), as the melting increases from 7.5 % to 30 %. The leftward shift results in a prominent region of loss near the core-mid plane.
3. A prominent region of gain (fuel mass > 1.626 kg per node) continually exists in the lower portion of the fuel column. Initially, the region extends up to a location near the core-mid plane. However, as melting increases from 7.5 to 30 %, it shifts downwards and decreases in length. Simultaneously, the peak magnitude of the gain (near $z = 0$ m) continues to increase.

The above trends are readily explained through the thermal maps presented in Fig. 3.9–3.10 and the melt mass profiles presented in Fig. 3.12. For e.g., the upward shift in the topmost region of loss with melting is consistent with the upward growth of melt

columns, since it creates a corresponding upward increase in M_l . Increase in R_{int} for the top region with continued melting results in a decrease in M_s , while the absence of melt mass in the top region ensures a net decrease in $m|_{t,top}$ (7.5-22.5 % melt fraction).

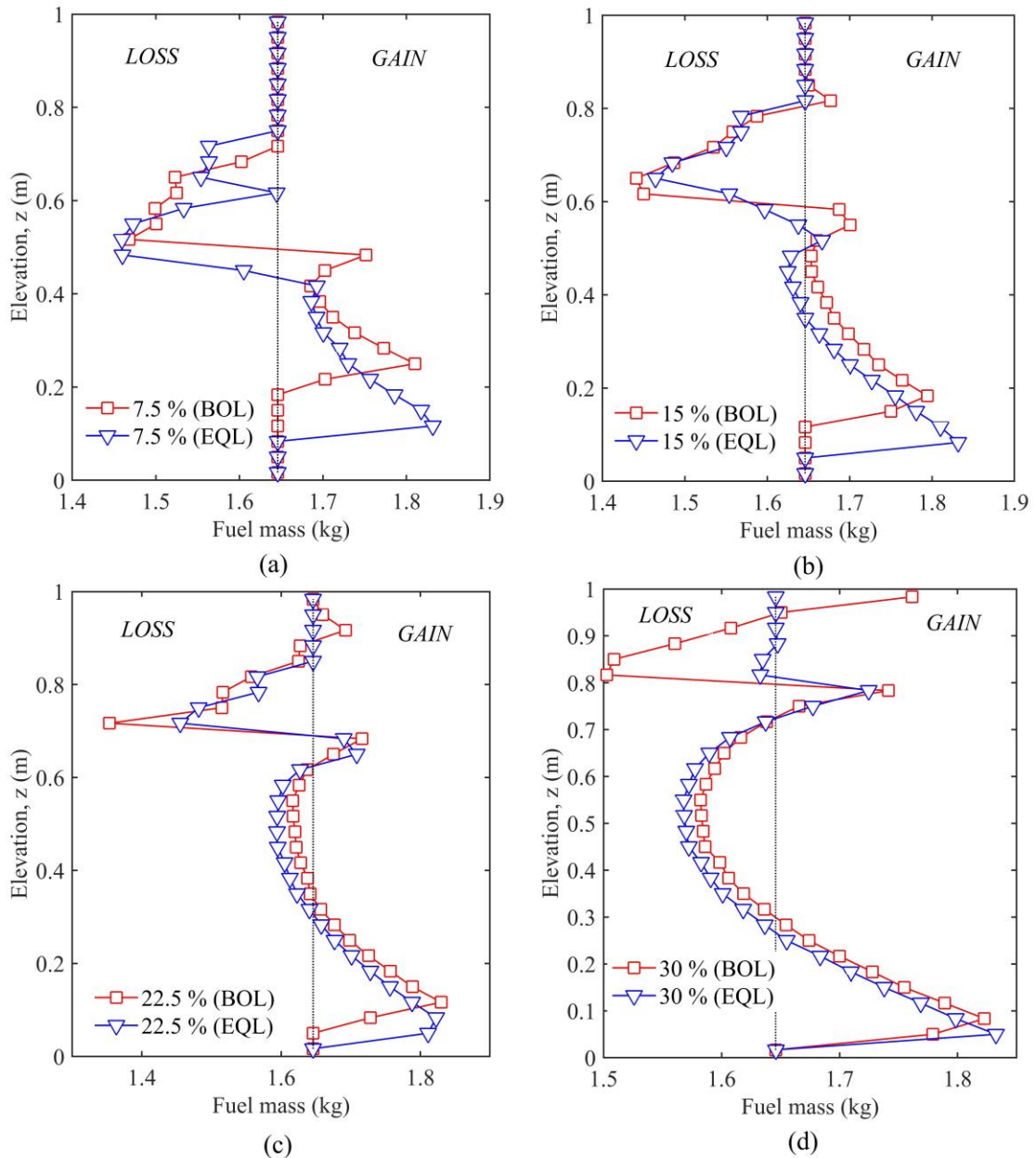


Figure 3.13: Fuel mass relocation in annular fast reactor pins subjected to UTOP. (a) 7.5 % melt mass, (b) 15 % melt mass, (c) 22.5 % melt mass and (d) 30 % melt mass. (Total fuel mass in central subassembly = 48.8 kg)

Similarly, the leftward shift in the nodes near the core mid-plane with increase in melting can be correlated with the melt temperature distribution presented in Fig. 3.11.

It is observed that at the core mid-plane, the melt temperature exceeds 3750°C , causing significant thermal expansion (Refer Eq. (A.15)). Consequently, liquid fuel density decreases significantly at the core mid-plane. Hence, despite increase in R_{int} (cavity radius), $M_{l,cen}$ does not increase significantly (Figure 3.12, 22.5–30 % melt fraction). However, $m_{s,cen}$ decreases with increase in R_{int} . Therefore, the net loss in the central region (Δm_{cen}) increases beyond 22.5 % melt fraction. This results in the aforementioned leftward shift.

Since the primary objective of the present investigation is to assess the impact of melt displacement on fast reactor safety, the above results are utilized for the determination of a melt relocation reactivity feedback (ρ_{rel} , Refer Eq. (2.10)). Figure 3.14 presents the characteristics of the feedback for both case studies. A clear difference is visible between the two cases up to 30 % melting. In this context, it is important to address the major differences between the melt displacement of the two case studies. In Case-I, the initial source of the negative feedback is the loss of fuel in the central segment due to downward displacement of melt. Further melting leads to filling of the core-mid plane with the melt agglomerate (Figure 3.12b). This leads to a temporary reduction in the fuel losses for the central segment (Refer Table 3.5, Δm_{top} for 15 % melt fraction). Simultaneously, the loss in the top segment (Δm_{top}) increases due to localized melting and downward motion. Consequently, the growth of the negative reactivity feedback is temporarily stalled. Continued melting and rise in melt temperature again increases the loss in the central region (above ~ 22.5 % melting). As a result of net outward mass flux, the losses in the top region are simultaneously reversed into a marginal gain. Since the fuel void worth is highest for the central region ($W_{f,cen}$), Δm_{cen} generates a negative reactivity perturbation (Eq. (2.10)) that is greater

in comparison with the combined positive reactivity perturbations of Δm_{top} and Δm_{bot} (magnitude-wise). Consequently, the negative reactivity feedback starts to increase for a second time.

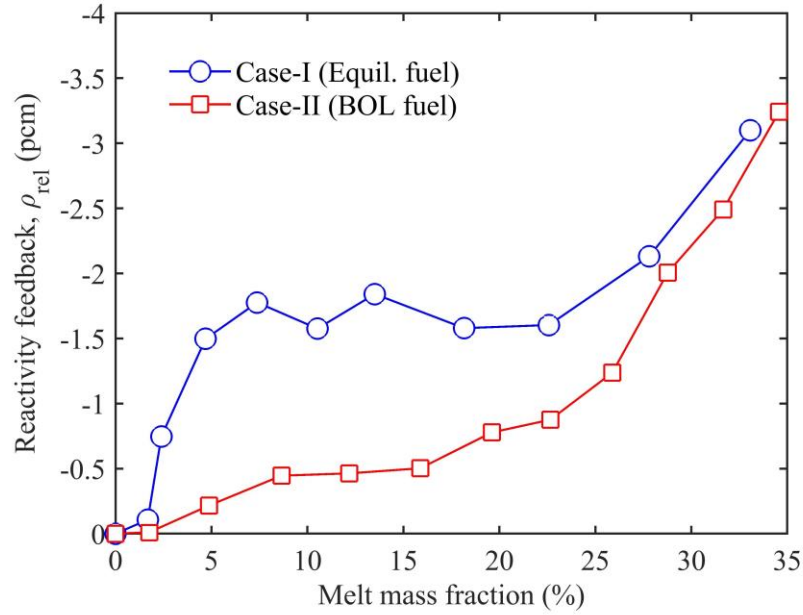


Figure 3.14: Melt relocation safety feedback characteristics.

In Case-II, the initial downward motion is decreased in comparison with Case-I (Refer Section 3.3.4.2(b)). Consequently, the loss of fuel in the central region (Δm_{cen}) is also comparatively smaller (Refer Table 3.5). As melting continues, the melt column grows upwards, leading to complete occupation of the central region. Therefore, $|\Delta m_{cen}|$ is reduced even further (15 % melt mass fraction). However, a considerable loss simultaneously appears in the top region due to melting and downward motion. Therefore, the reactivity feedback continues to increase marginally. Gradually, the heat-up and thermal expansion of molten fuel begins to decrease the fuel mass in the central region, causing an increase in $|\Delta m_{cen}|$. This results in a corresponding, gradual rise in the slope of the feedback curve.

3.4 Closure

In this chapter, first a multi-phase thermal hydraulic model is presented for numerical simulation of mixed oxide ((U-Pu)-O₂), nuclear fuel melting and motion, which considers the hydrodynamics of melt freezing, flow blockage, capillary effects, and gas escape to plenum, in addition to fission gas pressurization and conventional hydrodynamics. These effects are captured by devising an advanced multi-phase numerical algorithm based on a moving boundary, two-fluid, Eulerian, explicit finite difference approach. The variable density thermal expansion of molten fuel, combined with the freezing effects, can capture the slow, axially outward melt motion observed experimentally. This approach is distinctly different from the treatments available in literature, which rely on fission gas pressurization as a major driving force. Numerical simulations are performed for the E9bis experiment of the CABRI-2 test series, which provided unique data on melt displacement inside annular fuel pins during UTOP. The simulation results are compared with the experimental observations quoted in literature, and an excellent level of agreement is obtained. From these results, it can be concluded that liquid fuel thermal expansion and melt freezing can be the major hydrodynamic phenomena affecting melt displacement (in annular fuel) under the typically slow, over-power transient expected during UTOP in modern SFR.

As a second illustration, the benchmark-proven algorithm is extended to capture the fluid dynamics and relocation characteristics of melt that can be expected in a typical, medium-sized SFR. To achieve this purpose, typical fast breeder reactor accident conditions are simulated numerically with two basic SFR fuel conditions (Equilibrium and Beginning-of-life). From the results, the major conclusions are as follows:

- (i) As soon as melting begins, molten fuel starts to agglomerate into a melt column inside the annular pellets. The physical reasons responsible for such behaviour, identified by numerical analysis, are the cosine power profile, which results in a cyclic process of freezing and re-melting on immediately adjacent pellet surfaces, as well as the small hydraulic diameter of flow, which ensures constant contact between melt and pellet inner surface.
- (ii) As further rise in power takes place, the melt column grows axially outwards in both the upward and downwards directions.
- (iii) The size of the melt column is proportional to the amount of melting, numerically represented by the melt mass fraction.
- (iv) A significant downward displacement occurs early on after the onset of melting, particularly in Case-I (equilibrium fuel).
- (v) The undesirable increase in fuel mass near the core mid-plane is safely averted by the melt motion. On the other hand, a negative reactivity feedback emerges due to the decrease in total fuel mass in the high neutron density region around the core mid-plane.

This study has addressed the need for a theoretical description of the hydrodynamics of in-pin fuel motion in a manner consistent with the benchmark experimental data. Predictions of in-pin fuel motion pertinent to mixed-oxide fuelled fast breeder reactors have been established. The benchmark-proven model will be employed to investigate the propagation of melting in the entire reactor core and the resultant melt relocation feedback in detail in the next chapter.

Chapter 4

Reactor Dynamics Investigation of In-pin Fuel Motion during Unprotected Transient Overpower Accidents

In this chapter, the benchmark-proven, multi-phase thermal hydraulic model is utilized for the development of an inter-disciplinary computational algorithm with the help of the in-house point kinetics code, PREDIS. As apparent from the intrinsic coupling between the hydrodynamics and the reactor neutronics of melt displacement, a practical investigation of the impact of in-pin fuel motion on severe accidents requires appropriate attention towards both aspects. Furthermore, melting may propagate radially from the central subassembly towards outer fuel subassemblies, depending upon the reactor over-power level, fuel thermophysical properties and radial power distribution in the core. Therefore, a simple and robust parallel processing technique is developed to extend the multi-phase, thermal hydraulic model towards the entire reactor core and to address the above-mentioned intrinsic coupling. An optimization study is carried out to enhance the efficiency of the coupled system.

Subsequently, coupled hydrodynamic/neutronic simulations of UTOP are carried out for a typical, 500 MWe SFR. In view of the sensitivity of melt displacement towards core condition, the simulations are carried out for both BOL and equilibrium core conditions. Best estimate as well as conservative simulations of each core are carried out to address the uncertainties in the control rod withdrawal worth, fuel Doppler and material removal worth. The melt propagation characteristics in the entire reactor core are studied for each case. Comparative analysis of UTOP with and without the melt relocation feedback is carried out to determine its realistic impact on the safety of SFR. A thermodynamic analysis of molten fuel is carried out to investigate the potential of

fuel vaporisation. Finally, the effects of core condition and reactivity insertion rate on the accident scenario are studied. The aim of the present study is to investigate the propagation of melting in the BOL and equilibrium cores of SFR with due consideration of the neutronics aspects of melt relocation.

4.1 Numerical modelling

4.1.1 Model system

The model system for the present study consists of the active core of a typical, medium-sized SFR (FBR-500, Section 2.1.1). Schematic diagrams of the core layout and fuel subassembly have been presented earlier (Figure 2.1-2.2). Table 2.4 details the fuel specifications used in the present study. There are 181 fuel subassemblies in the reactor core, with 217 fuel pins in each subassembly. Spatial variations in power generation exist along the axial and radial coordinates of the reactor core, in addition to the radial variation in the coolant flow rate (\dot{m}_{ct}). As a result, the fuel, coolant, and clad temperatures are maximum in the central subassembly (or Zone-1), and minimum in the outermost fuel subassemblies. The innermost 85 and the remaining 96 fuel subassemblies comprise the inner and outer core regions, based on the PuO_2 mole-fraction (y). A system of division of these fuel subassemblies into seven hexagonal channels (or zones) is previously presented in Chapter 2. Radial power factors, coolant mass flow rates (per subassembly), enrichment levels and percentage radial distribution of the fuel void worth for each fuel zone are also described (Refer Table 2.2–2.3). A detailed description of the fuel void worth is presented in Section 2.3.1. In the table, the second innermost radial zone (or Zone-2) has the highest fuel void worth percentage, followed by the sixth and fifth radial zones. Therefore, even a slight modification in the fuel mass distributions of these zones will impact the reactivity feedback significantly.

4.1.2 Problem description and assumptions

Initially, the reactor core is generating a nominal amount of power under the steady-state operating condition. At time $t = 0$ s, a hypothetical, unwanted control rod withdrawal begins with the simultaneous and total failure of the shutdown systems, leading to the addition of an unbalanced positive reactivity into the reactor core. The speed of withdrawal is $2 \text{ mm} \cdot \text{s}^{-1}$, which causes a small rate of reactivity insertion ($\sim 0.7\text{--}3.5$ pcm/s, refer Section 2.3.3). Consequently, the reactor power starts rising at a slow rate, leading to fuel heat-up and eventual melting. Coolant flow continues at the nominal flow rate throughout the transient.

In the present study, the spatial variations in the power generation have been considered based on a first order perturbation worth analysis of a typical, medium-sized fast reactor [88]. It has been reported that the Eigen value separation between the fundamental mode and the first mode for medium-sized SFR (for e.g., PFBR), is substantial (~ 5000 pcm) [93]. Such a reactor core can be considered as tightly coupled, i.e., the radial and axial power profiles remain unchanged, whereas the magnitude of the linear heat rating (X) changes in proportion with the reactor overpower. Therefore, a point kinetics model has been utilized in the reactor dynamics calculations (Refer Section 2.3.2). Consequently, localized amplification of power near the initiating control rod has not been considered in the present study.

As the core temperature rises, reactivity feedbacks such as fuel Doppler, fuel axial expansion, control rod driveline expansion, core radial expansion, clad expansion, and coolant expansion, begin to influence the net reactivity. Since the present study is specifically focused on the reactor dynamics of in-pin fuel motion, a degree of conservatism is introduced by neglecting the core radial expansion feedback, which

assimilates the radial expansions of solid fuel, clad, wrapper and grid plate, as well as the control rod driveline expansion feedback [30,123]. Such a conservatism results in sufficient amount of fuel melting for a comprehensive investigation of the impact of in-pin fuel motion on fast reactor dynamics.

Unlike the experimental validation study described in Chapter 3 (Refer Section 3.3.3), there is a negligible attenuation of neutron flux along the fuel pellet radius. Therefore, in the present study, the rate of heat generation for a given zone is considered constant along the pellet radius ($X(z, t) \neq f(r)$). Furthermore, variation in the fission gas release along the pellet radius is neglected. Instead, the CEPTAR correlation is utilized for calculation of the gas mass source term at each axial node [12]. This assumption only affects the equilibrium core studies, since BOL core does not require fission gas release calculations. Chapter 5 addresses the impact of integrating these radial variations on the equilibrium core simulations.

Another important assumption considered in the present study is the treatment of molten fuel as a homogenous fluid. Table 4.1 presents the number densities of various nuclides under the equilibrium core condition. Upon melting, the oxides (U-Pu)-O₂, which are the primary substance in the melt, can be considered well-mixed since most of the thermophysical properties of both oxides are approximately equal. However, the segregation of metallic fission products from the melt has been observed experimentally [33]. From the nuclide density distribution presented in Table 4.1, it can be observed that the number density of metallic fission products is relatively smaller in comparison with the total density of U-Pu isotopes. Therefore, the above assumption can be considered as justifiable for the sake of simplicity.

Table 4.1: Nuclide number density at beginning of equilibrium core ($\text{barn}^{-1} \text{cm}^{-1}$) [88].

Isotope	Inner Core	Outer Core	Axial blanket
U-234	1.3388E-09	8.1889E-10	0.1958E-09
U-235	1.0917E-05	1.1028E-05	0.1719E-04
U-236	5.4474E-07	2.7615E-07	0.3949E-06
Np-237	6.4162E-07	3.8707E-07	0.1080E-06
U-238	5.2205E-03	4.8438E-03	0.7412E-02
Pu-239	9.0763E-04	1.2225E-03	0.6727E-04
Pu-240	3.5959E-04	4.7115E-04	0.1876E-05
Pu-241	7.0839E-05	9.5772E-05	0.5701E-07
Pu-242	2.0520E-05	2.6466E-05	0.7078E-09
Fission products	2.0847E-04	1.4729E-04	0.8608E-05
Pu-238	1.1222E-07	6.3432E-08	0.7137E-08
Am-241	1.6736E-06	1.6651E-06	0.1178E-08
Am-242	3.1260E-08	2.2302E-08	0.6838E-11

4.1.3 In-pin fuel motion solver

An advanced thermal hydraulic model for numerical simulation of fuel melting and fluid flow in a multi-phase environment has been presented in Chapter 3. Essentially, the developed model solves a physical system of a single fuel pin and a representative fuel channel. In the present study, an extension of the model is carried out to simulate the melting and fluid flow behaviour throughout the reactor core. Towards this goal, the numerical algorithm is converted into a ‘.exe’ executable file through a FORTRAN-95 compiler. The files, defined as in-pin fuel motion solvers, can read input data specific to a fuel channel (for e.g., thermophysical properties, coolant flow rate, steady state axial power distribution), and simulate the localized accident conditions. Based on the system of division of fuel subassemblies, seven separate in-pin fuel motion solvers are assigned to each fuel zone. Each solver simulates the melting

and fluid flow in a representative fuel pin which is thermally equivalent to all other fuel pins in the respective fuel zone.

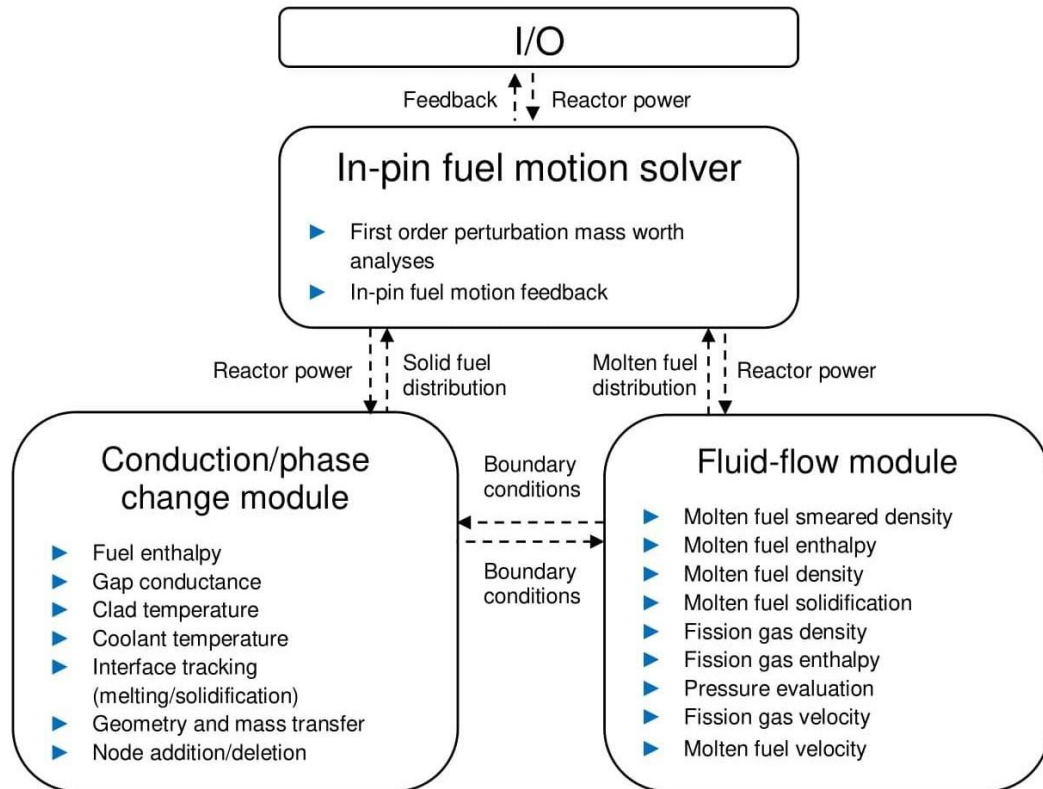


Figure 4.1: Flow-chart of in-pin fuel motion solver.

Figure 4.1 presents the calculation procedure involved in a typical in-pin fuel motion solver. The essential order of calculations is analogous to the procedure detailed in Section 3.2.3. The involved governing equations, boundary conditions and discretization schemes have been detailed in Chapter 3 and are not repeated here for the sake of brevity. However, the input and output data flow are modified to form an interface with PREDIS. Apart from the initial input data, the solver requires the transient power level to function. Additionally, the solver evaluates the melt relocation feedback (ρ_{rel}) with an earlier outlined method (Section 2.3.4), and utilizing the zone-specific fuel void worth data, calculates the melt relocation feedback for the respective zone, which is then extracted as the output data.

4.1.4 Neutronic/Hydrodynamic coupling algorithm

To develop a computational system for the whole core of a nuclear reactor, spatial variations in the thermal hydraulics, neutron flux and fuel thermophysical properties must be considered. Using the system of division described earlier in Chapter 2 (Section 2.1.1), as well as the separate solvers, the fuel melting and multiphase flow behaviour can be numerically simulated for the whole core. However, in the view of the intrinsic coupling between melt relocation and reactor neutronics, it is evident that any such numerical simulation of severe accident must parallelly incorporate reactor neutronics with the thermal hydraulics, to estimate the melt propagation as well the impact on reactor safety realistically. Furthermore, a major limitation of the developed numerical algorithm is the necessity of extremely small multi-phase flow time-steps ($\Delta t_2 \sim 10 - 50 \mu s$) to maintain numerical stability in the solution (Refer Section 3.3.1). It is also evident that to capture the melting and motion behaviour throughout the reactor core, numerical simulations must be performed for at least seven representative fuel pins (Refer Section 2.1.1). Therefore, the computational time needed for seven numerical simulations of up to 750 s will be significant. A parallel computational system can minimize the cost of whole core simulations.

In view of the above considerations, a parallel, inter-disciplinary computational algorithm is developed in the present study [89]. The in-pin fuel motion solvers are linked to the in-house reactor neutronics code PREDIS using a dynamic coupling mechanism (Refer Fig. 4. 2). Starting from steady state ($t = 0 s$), all the MITRA solver and PREDIS files (.exe format) execute a forward march in the time coordinate.

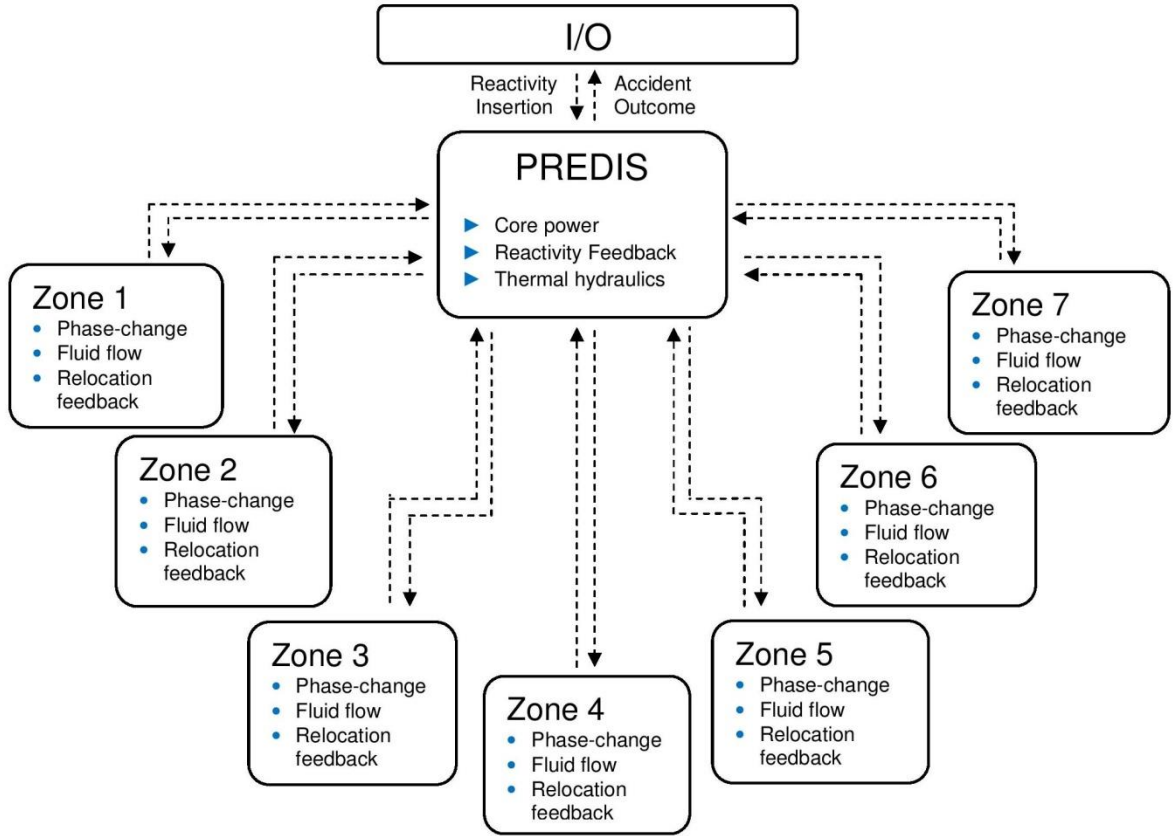


Figure 4.2: Flow-chart of the inter-disciplinary computational algorithm (Each zone represents single phase-change and fluid flow solver).

During this march, at a fixed time interval (or exchange period, Δt_{exc}), a data exchange module is activated inside each solver and PREDIS. These modules consist of do-while loops that iterate until they locate the target input file (‘.txt’ format) written by PREDIS. Subsequently, the modules read the input file to extract data and the associated input time. If this input time is equal to the solver’s respective transient time instant, within a margin of small tolerance, the data transfer module deletes the input file and writes an output file (‘.txt’ format) with the output data and the solver’s transient time instant. This output file in turn serves as an input file for PREDIS at the next Δt_{exc} during the time march. The allowable tolerance with respect to the transient time instant is taken as $2\Delta t_{exc}$. The purpose for using $2\Delta t_{exc}$ (and not Δt_{exc}) as the tolerance is to avoid floating point errors in the FORTRAN-95 platform. During the time-march, any

mismatch between the time instants of the parallel solvers is simply avoided by the deletion all the data-transfer files immediately after extraction of data. Hence, data files from an earlier time step are not read erroneously by any solver. In other words, the performance of the parallel processing algorithm remained unaffected by the magnitude of the tolerance, if the magnitude is greater than Δt_{exc} .

In case the tolerance is violated, the data exchange mechanism is halted automatically in PREDIS, and subsequently halted in the rest of the solvers. This mechanism enables parallel computation and captures the melt propagation in the whole core. In addition, it enables the assessment of the reactor dynamics of melt motion during UTOP. The procedure requires the following minimum system configuration to run successfully: Tetra-core processor with eight logical processors, 8 Gigabyte Ram, and Windows operating system.

4.1.4.1 Selection of a suitable data-transfer period

The data-exchange time (Δt_{exc}) controls the frequency of data transfer between the in-pin fuel motion solvers and PREDIS. The minimum value of Δt_{exc} is constrained by the maximum time-step of PREDIS (0.05 s) since the data exchange must occur only once within a single PREDIS time step. However, the algorithm can also function with a larger Δt_{exc} , if the solution remains numerically convergent. Furthermore, the reading-writing functions of the data-exchange module involve do-while loops, which essentially stall the computation until finding the target input (‘.txt’) file. Therefore, there is a considerable cost associated with the frequency of data-transfer. In the present study, an attempt is made to decrease the computational cost further by selecting an optimal data exchange frequency. A sensitivity study of the algorithm with respect to Δt_{exc} is presented in Table 4.2. The deviations are calculated with respect to the case

of minimum Δt_{exc} . It is observed that with increase in the data exchange period, there is a considerable deviation in the final (or stabilized) reactor power level, obtained at the end of the transient. However, the deviation decreases considerably for $\Delta t_{exc} = 0.2 \text{ s}$ ($< 1 \%$). Therefore, it is deduced that simulations may be carried out with this data-exchange period (0.2 s).

Table 4.2: Table of sensitivity of neutronic/hydrodynamic coupling algorithm towards the data-exchange period (Δt_{exc}). All the deviations are with respect to the first case.

S.No.	Δt_{exc} (s)	% P/P_n (t = 750 s)	Deviation (%)	Δt_{comp} (s)
1	0.05	192.0	-	5527.1
2	0.10	189.7	1.0	4709.7
3	0.15	183.6	-2.1	4340.7
4	0.20	189.1	0.7	4564.3

The deviations in Table 4.2 evolve non-linearly. This non-linearity is introduced by the inclusion of the instantaneous whole-core relocation feedback (ρ_{rel}) in the reactivity computations within PREDIS. With each Δt_{exc} , a new ρ_{rel} is fed to the net feedback reactivity. This creates minor oscillations in the trajectory of the reactor power profile. The frequency of these oscillations depends upon the magnitude of Δt_{exc} . Hence, the stabilized reactor power, captured at a single instant for all cases (t=750 s), does not evolve linearly in Table 4.2. However, the stabilized reactor powers ($P_{t=750 \text{ s}}$) for the minimum possible Δt_{exc} (0.05 s) and the selected Δt_{exc} (0.2 s) remain convergent. The computational time periods (t_{comp}) are obtained from a high-performance Intel Xeon workstation installed at the Computer Division, IGCAR. The time saved through the optimization on a nominal, Octa-core CPU is $\sim 1300 \text{ s}$ per simulation.

4.1.5 Computational procedure

The computational procedure followed in the in-pin fuel motion solvers are detailed in Section 3.2.3, whereas the modifications carried out to develop the dynamic coupling mechanism are presented in Section 4.1.3. The methodology of the reactor dynamics computations in PREDIS for the present work is as follows [97]:

- (i) Under the domain of PREDIS, the entire core is discretized into fuel and blanket zones (Figure 2.5). Each zone is represented by a single fuel pin, associated coolant flow and surrounding structure. The material removal worth for various core components such as fuel, clad, coolant and the withdrawal worth of control rods are obtained a-priori using a first order perturbation method (Refer Section 2.3.1) [88].
- (ii) Steady state computations are carried out using the design rated power level. The temperature distributions for fuel, clad and coolant are evaluated in each zone. Once convergence is obtained, the calculation proceeds to the transient.
- (iii) During the transient, PREDIS simulates the unprotected withdrawal of a single control rod with a constant speed of 2 mm/s. Using the CSR differential withdrawal worth presented earlier (Figure 2.4), the code inserts an external reactivity in the point kinetics equations (Eq. (2.6–2.8)).
- (iv) The code utilizes a point kinetics model for power computations. Point kinetic equations are solved to obtain the resultant neutron density and reactor power (Section 2.3.2). The power data is used to obtain thermal hydraulics data (fuel, clad and coolant temperature). Subsequently, the axial and radial thermal expansions of fuel, coolant and cladding along with melting and boiling (if any)

of core components are evaluated [82]. If coolant boiling initiates, the two-phase momentum, energy, and mass conservation equations for coolant are solved.

- (v) The temperature and thermal expansion data are employed to obtain the reactivity feedbacks due to fuel Doppler, coolant voiding (if any) and the expansions of fuel, coolant and clad. The methodology of the feedback calculations is detailed in Section 2.3.2 [30].
- (vi) PREDIS imports the relocation feedback using the dynamic coupling mechanism with the in-pin fuel motion solvers (Figure 4.2) to evaluate the total feedback reactivity. Steps (iv – vi) are repeated until the end of transient ($t = 750$ s).

Table 2.4 details the fuel specification used in the subsequent analyses. Table 2.3 details the radial variations in power generation inside the core. Appendix-A describes the thermo-physical properties. Solidus, Liquidus and melt interface temperatures decrease slightly with increase in burnup (Refer Eq. (A.9-A.11)). Grid independence study and the 2-D cylindrical grid (r, z) chosen for analysis are detailed in Section 3.3.1. For whole-core simulation, one executable file is assigned to each of the fuel channels for parallel processing (Section 4.1.4). Each file operates with the channel's respective fuel mass removal worth, coolant mass flow rate, power generation and material properties.

4.2 Results and discussion

In the present study, four separate cases of UTOP are considered, according to the core condition, banking depth, and differential withdrawal worth of a single CSR (Refer to the case-specific parameters in Table 4.3). The reactor core under study is

typical for a medium-sized, fast breeder reactor with an electrical output of 500 MW (Refer Section 2.1.1).

Table 4.3: Table of severe accident case studies (B & C stand for best estimate and conservative respectively; banking depth is from TFC; withdrawal speed = 2 mm/s) [30,97].

Case Study	Core condition	Banking depth (cm)	Withdrawal time (s)	Maximum insertion (\$)	$X_{max}(t = 0)$ (kW/m)
I	EQL (B)	30	150	0.57	41.6
II	BOL (B)	40	200	0.984	45.5
III	EQL (C)	40	200	0.98	41.6
IV	BOL (C)	50	250	1.48	45.5

The first case corresponds to the equilibrium core (EQL) condition, which is subjected to a nominal, unwanted control rod withdrawal. The second case corresponds to a similar, nominal control rod withdrawal for the beginning-of-life (BOL) core condition. Combined, these two cases reflect the best estimates of the accident conditions in SFR. The third case corresponds to a worst-case scenario for the equilibrium core, in which the control rod withdrawal occurs from a deeper location as compared to the nominal location. The intention behind such a conservative simulation is to address the uncertainties in the calculation methodology of the material void worth, Doppler broadening, and CSR withdrawal worth. Consequently, both the total external reactivity insertion and withdrawal time are greater as compared to Case-I. Similarly, the fourth case corresponds to a worst-case scenario for the BOL core, in which the total external reactivity insertion and withdrawal time are greater as compared to Case-II.

It may be noted that in Table 4.3, the maximum reactivity insertions and control rod banking depths are different for BOL and equilibrium cores. There are two reasons for the same: (a) when the reactor goes from BOL to equilibrium and subsequently to

end of life condition, there is a loss of reactivity. The reactor control rods are adjusted with increasing burnup to compensate this loss. As a result, the banking depth of control rods decreases with increasing core burnup. (b) The perturbation worth of core components changes with burnup due to fission product accumulation. Consequently, the available reactivity addition in an equilibrium core (under UTOP) is smaller in comparison with BOL core. The above-described phenomena are duly considered in the present work.

It should also be noted that the linear heat ratings presented in Table 4.3 correspond to the first zone, or the central subassembly (CSA), which experiences the highest power generation. Furthermore, it has been observed that although reactivity insertion occurs during the first 150–250 s, the reactor power tends to stabilize after a certain time-lag. To capture the final, stabilized state of the reactor core, the numerical simulations are carried out up to an extended period of 750 s.

4.2.1 Whole-core simulation of UTOP (without melt relocation feedback)

This section presents the results of preliminary, whole-core simulations carried out without coupling in-pin fuel motion with the reactor dynamics. The purpose is to establish the de-coupled accident progression for the above-described case studies, to evaluate the impact of in-pin fuel motion on reactor safety in the subsequent sections. Figure 4.3 shows the normalized reactor power history for each of the UTOP case studies mentioned in Table 4.3. The reactor power excursion in each case is proportional to the respective maximum external reactivity insertion. Hence, the power level is highest in case of BOL core (conservative, 1.48 \$), and lowest in case of equilibrium core (best estimate, 0.54 \$).

In this context, it is important to mention that the above power histories represent the extent of conservatism in the selected case studies. For e.g., it is previously mentioned that the present study only considers fuel Doppler, fuel axial expansion, clad expansion, and coolant expansion feedbacks in the dynamic simulations. This assumption permits the achievement of a sufficient amount of melting for a comprehensive analysis of the reactor dynamics of in-pin fuel motion. It is evident that if the reactor power reaches levels as high as presented in Fig. 4.3, a significant amount of melt propagation and coolant voiding can occur.

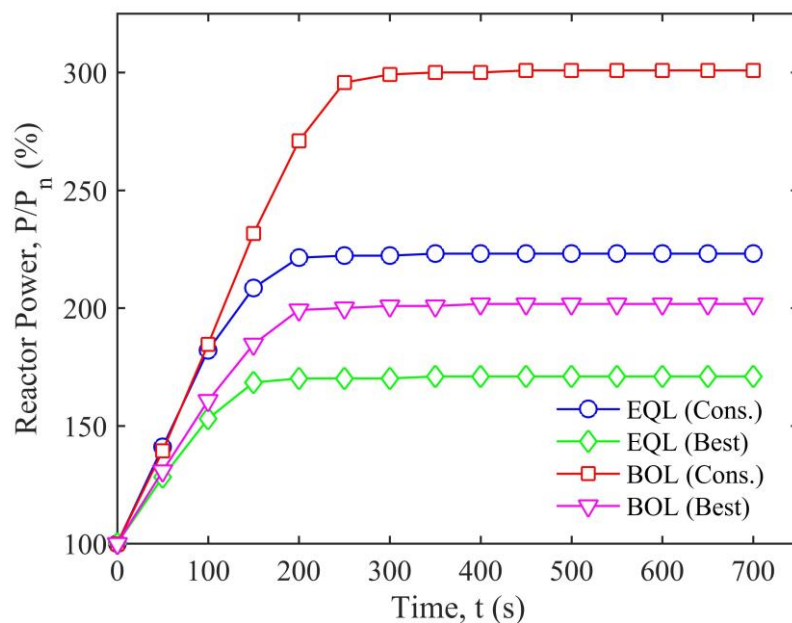


Figure 4.3: Reactor power history during UTOP without the consideration of melt relocation feedback.

4.2.2 Whole core simulation of UTOP (best estimate case studies)

4.2.2.1 Results for Case I

Figure 4.4 presents a schematic of the fuel columns of the seven representative fuel pins from each zone of the FBR-500 core at the end of the transient ($t = 750$ s). The figure presents a picture of the temperature distribution, quantum of melting, locations of solidification and the location of melt columns in each fuel zone of the

reactor core. It is evident that little or no melting has occurred in any of the zones except Zone-1. From the zone-wise radial power variation presented earlier in Chapter 2 (Table 2.3), it is known that maximum power density occurs in Zone-1, followed by Zone-2. Therefore, melting is unable to propagate outside Zone-1 (or the central subassembly). The melt fraction in Zone-1 at the end of the transient is 6 %.

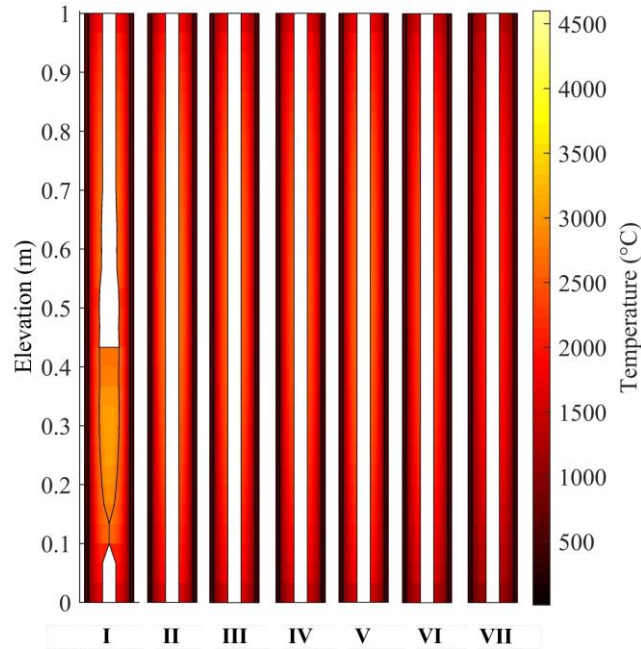


Figure 4.4: Whole core melting and in-pin fuel motion for Case I (Equilibrium core condition; Best estimate; stabilized state; $t = 750$ s).

Figure 4.5 presents a picture of the transient evolution of melting as well as the temperature histories of fuel, clad and coolant temperatures of Zone-I fuel pin. The focus is kept on Zone-I since it possesses the highest temperature in the core. Melting begins at $t = 131$ s, when the peak fuel temperature (T_f) exceeds the melt temperature (T_{int}) (Refer Eq. (A.11)). It is evident that the peak fuel temperature continues to increase beyond the instant of maximum control rod withdrawal ($t = 150$ s). The core attains a stabilized state after 250 s. The maximum temperatures of fuel, steel-clad and coolant are 3492 °C, 723 °C and 680 °C respectively. From these results, it is observed that both clad melting and coolant boiling are avoided by a substantial margin.

Furthermore, the melt column is located significantly below the core mid-plane ($z = 0.5 \text{ m}$), which indicates a downward melt motion in consistence with the results presented in Chapter 3 (Refer Section 3.3.4.1).

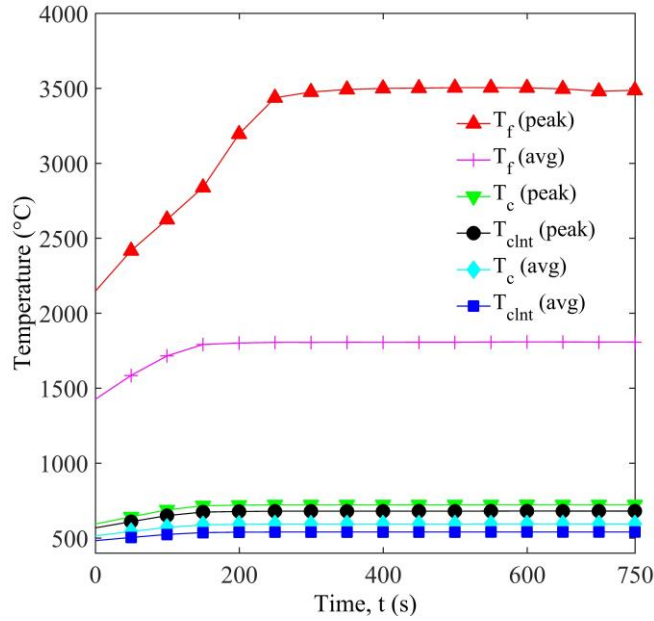


Figure 4.5: Temperature histories for Case-I (Zone-1 fuel pin; best estimate).

4.2.2.2 Results for Case II

Figure 4.6 presents a similar schematic of the BOL core fuel pins at the end of the transient ($t = 750 \text{ s}$). The thermal map, melt-interface profiles (R_{int}) and locations of the melt columns for each fuel zone are visible. The cavity width directly below the melt columns is decreased because of crust formation. The absence of complete cavity blockage in each zone is consistent with the motion characteristics presented in Chapter 3 (Refer Section 3.3.4.2). Furthermore, it is evident from the figure that melting has occurred in Zones 1, II, III and V. Therefore, unlike Case-I, damage has propagated to four fuel zones, amounting to a total of 85 fuel subassemblies (out of 181). The maximum melt mass fraction is 17 % in Zone-1. Again, the relative amount of melting in each zone is dependent on the radial power factors (Refer Table 2.3).

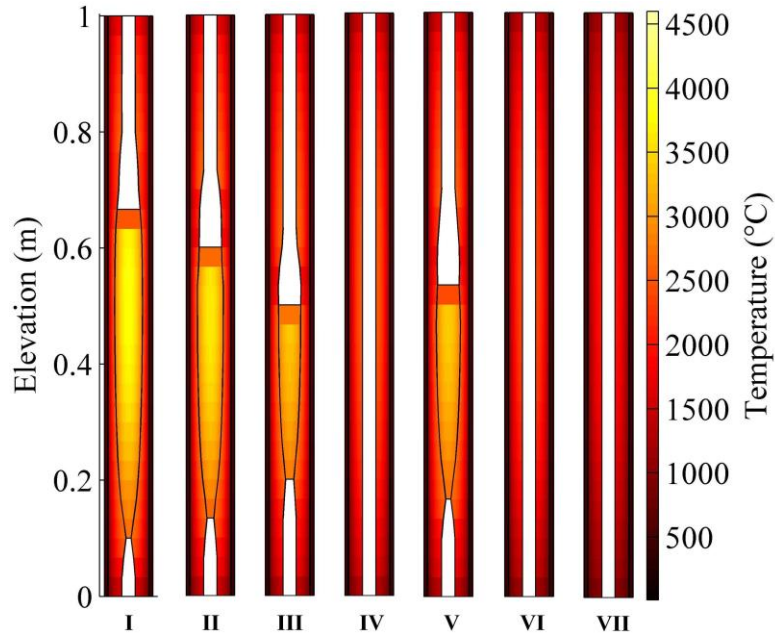


Figure 4.6: Whole core melting and in-pin fuel motion for Case II (BOL core condition; Best estimate; stabilized state; $t = 750$ s).

Figure 4.7 presents the temperature histories of the Zone-I fuel pin. Melting begins early in the transient ($t = 71$ s), due to: (a) considerable gap width in the core mid-plane region ($\sim 32 \mu m$, $t = 71$ s), which, combined with the presence of bond gas (Helium), translates in to a moderate gap conductance ($h_{gap} \sim 8230 W/m^2K$), and (b) greater steady state power level in case of fresh fuel ($X_{max} = 45 kW/m$) as compared to equilibrium fuel (Refer Table 2.2). It is clearly seen that the peak temperatures of molten fuel are higher in BOL core ($T_{f,peak} = 3907$ °C) as opposed to equilibrium core. The maximum coolant peak temperature in this case ($T_{ct,peak} = 701$ °C) shows that coolant voiding is avoided [107]. Similarly, the clad peak temperatures in this case ($T_{c,peak} = 748$ °C) indicates that the clad steel remains intact during the accident. Finally, it is observed that T_f stabilizes at ~ 250 s, which indicates a time lag after the instant of maximum rod withdrawal ($t = 200$ s, Refer Table 4.3).

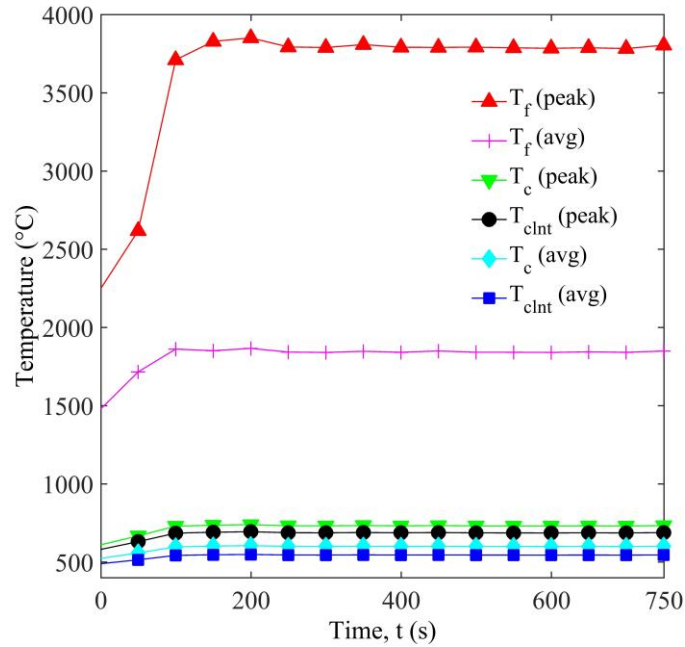


Figure 4.7: Temperature histories for Case-II (BOL core, Zone-I, best estimate).

4.2.2.3 Reactor dynamics of in-pin fuel motion (Cases I & II)

To understand the transient evolution of the accident in the above two case studies, the power and reactivity histories are presented in Fig. 4.8 [97]. Further insight can be gained from the reactivity feedback plots of the two case studies (Refer Fig. 4.9). It is seen that the external reactivity insertion is initially thwarted by the fuel Doppler and axial expansion feedbacks. With the beginning of fuel melting, an in-pin fuel motion feedback emerges and thwarts the net positive reactivity in both cases (Refer Fig. 4.8a). Consequently, the net positive reactivity begins to decrease, and the reactor power begins to stabilize. In Case-II (BOL core), the external reactivity insertion is completely neutralized at 250 s, which explains the stabilization of the peak fuel temperature at the same time (Refer Fig. 4.7).

In Case-I (equilibrium core), the reactor power continues to increase very slowly, even after complete withdrawal ($t = 150$ s). This is due to lack of melting in all the fuel zones except for Zone-I. It is found that the primary reasons for such a small amount

of melting are smaller external reactivity insertion, closure of fuel-clad gap width due to thermal expansion (Section 3.1.11) and smaller steady-state linear heat ratings in the case of equilibrium core (Refer Table 4.3; best estimate).

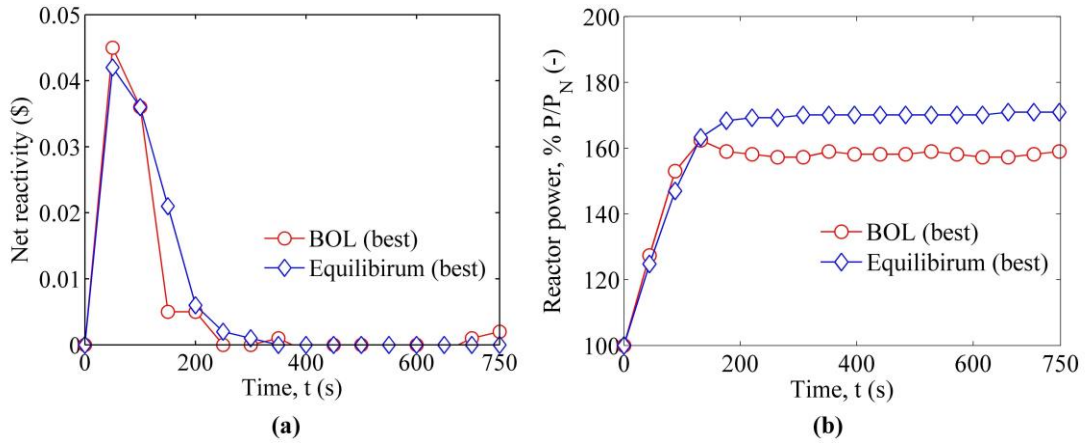


Figure 4.8: Transient behaviour of reactor during UTOP (Cases I & II; best estimate): (a) Net reactivity vs. time, (b) Reactor power vs. time.

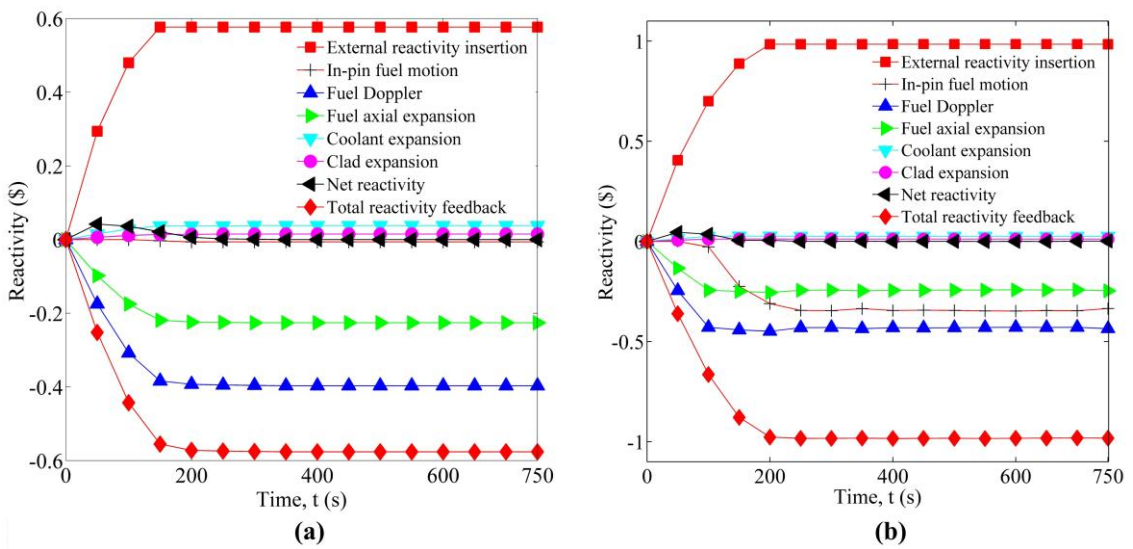


Figure 4.9: Reactor dynamics response of fast reactor under best estimate case study of UTOP: (a) Case I (Equilibrium condition) and (b) Case II (BOL condition).

The low level of melting results in negligible relocation, due to which, the in-pin fuel motion feedback is also small (-0.006 \$). As a result, the reactor power keeps rising even after complete withdrawal until the external reactivity is balanced slowly with other negative feedbacks (t = 357 s, Refer Fig. 4.8a). Consequently, the reactor finally stabilizes at a power level of 171 %, which is apparently greater than the stabilized BOL

power level of 159 % (Refer Fig. 4.8b). It may be noted that the stabilized, peak linear heat ratings ($X_{max}(t = 750), CSA$) of Cases I and II are 71.2 kW/m and 71.8 kW/m respectively.

4.2.3 Whole core simulation of UTOP (conservative case studies)

4.2.3.1 Results for Case III

Figure 4.10 presents a picture of the temperature distribution, melting, solidification and the location of the melt columns in each fuel zone of the 500 MWe SFR after the stabilization of power ($t = 750 \text{ s}$). From the figure, it is observed that melting has propagated in the first, third and fifth zones of the core, which also possess the highest radial power factors in decreasing order (Table 2.3). The remaining zones are intact until the end of the transient. Under the conservative simulation, a significantly greater amount of melting takes place in comparison with the best estimate. Furthermore, a clear, downward relocation is visible in the three molten zones, which is an indication of significant loss of fuel mass near the core mid-plane. The stabilized melt mass fractions in Zones I, II and V are 9.5 %, 3.3 % and 4 % respectively.

Figure 4.11 presents the temperature histories of the Zone-I fuel pin. It is evident that the peak molten fuel temperature begins to stabilize at 250 s ($T_{f,peak} = 3720 \text{ }^\circ\text{C}$) and increases slightly near the end of the transient ($T_{f,peak} = 3751 \text{ }^\circ\text{C}$). The peak coolant temperature ($T_{ct,max} = 701 \text{ }^\circ\text{C}$) is less than the sodium boiling point, $883 \text{ }^\circ\text{C}$ [107]. Similarly, the peak clad temperature is $746 \text{ }^\circ\text{C}$ respectively, which is significantly lower than the steel melting temperature.

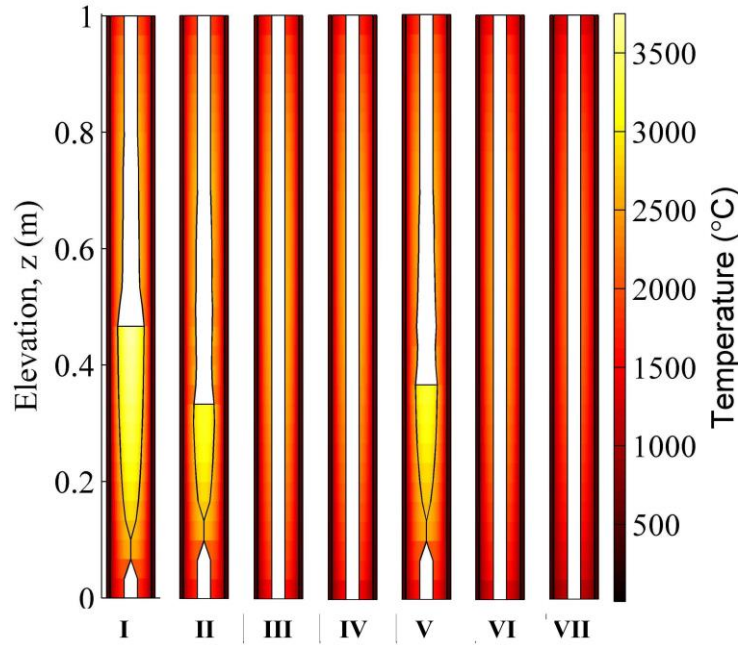


Figure 4.10: Schematic of in-pin fuel motion in fast breeder reactor for Case III (Conservative, equilibrium core simulation; I, II...IV represent fuel zones; Filled region inside fuel cavity indicates presence of molten fuel column).

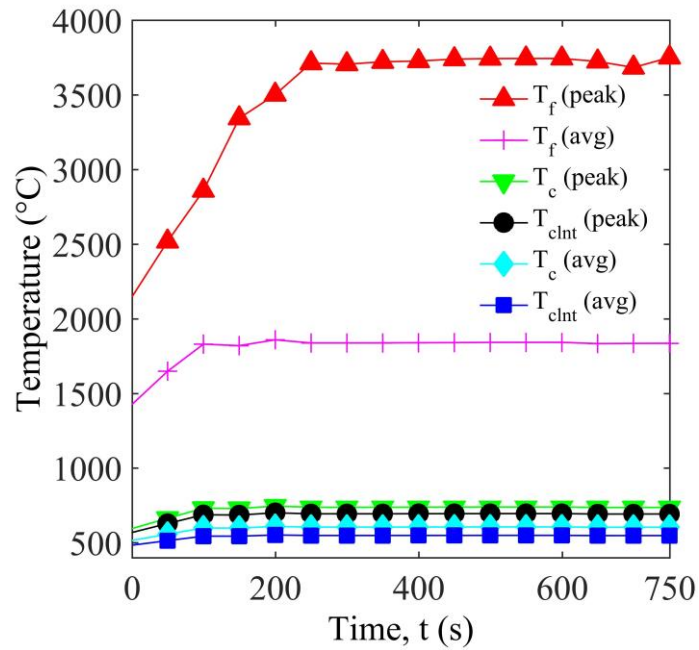


Figure 4.11: Temperature histories for Case-III (Equilibrium core, Zone-I, conservative estimate).

4.2.3.2 Results for Case IV

Figure 4.12 presents the stabilized state of the reactor core for the conservative simulation of UTOP in the BOL core condition. As discussed previously, the control

rod banking depth is greatest for this condition. Therefore, in this simulation, the resultant external reactivity insertion is also greatest (1.48 \$, Refer Table 4.3). Due to the same, extensive melting takes place in all fuel subassemblies of the core except for the outermost fuel Zone-VII. Elongated columns of molten fuel are formed in Zones I-V due to the extensive melting.

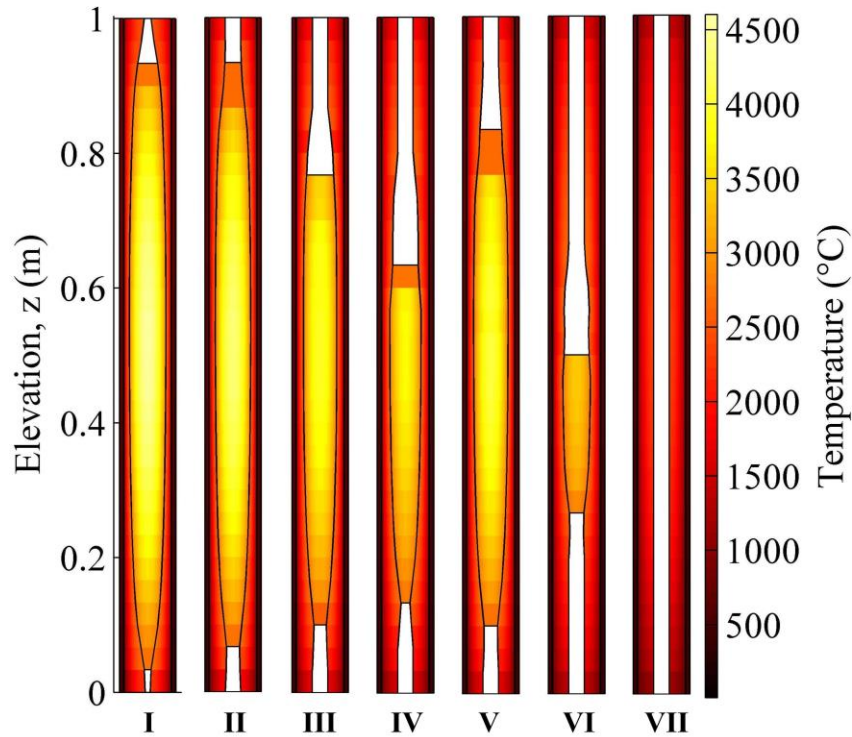


Figure 4.12: Schematic of in-pin fuel motion in fast breeder reactor for Case IV (Conservative, BOL core simulation; I, II...IV represent fuel zones; Filled region inside fuel cavity indicates presence of molten fuel column; $t = 750$ s).

The melt columns occupy the annular pellet cavity completely in Zones I and II. Highest melt mass fraction is 35 % in Zone-I, followed by 31 %, 26 %, 23 %, 16 % and 8 % in Zones II, V, III, IV and VI, respectively. The location of the melt column in Zone-VI is close to the core mid-plane, which is consistent with the slow, downward motion observed earlier in Chapter-3 (Refer Section 3.3.4.2).

Temperature time history of the Zone-1 fuel pin is shown in Fig. 4.13. Peak fuel temperature is highest in this case ($T_{f,max} = 4603$ °C). At such a high temperature,

vaporisation of molten fuel can occur (Refer Section 4.2.5 for further details). Peak coolant temperature ($T_{ct,max} = 786\text{ }^{\circ}\text{C}$) is still significantly less than the sodium boiling point, $883\text{ }^{\circ}\text{C}$ [107]. Clad peak temperature is $847\text{ }^{\circ}\text{C}$, which is also significantly less than the steel melting temperature. Experimental evidence regarding annular fuel pins indicates that cladding failure is unlikely to occur under the above described conditions, since annular fuel pins exhibit a very high threshold to failure [28,33,34] (Refer Section 2.4.2).

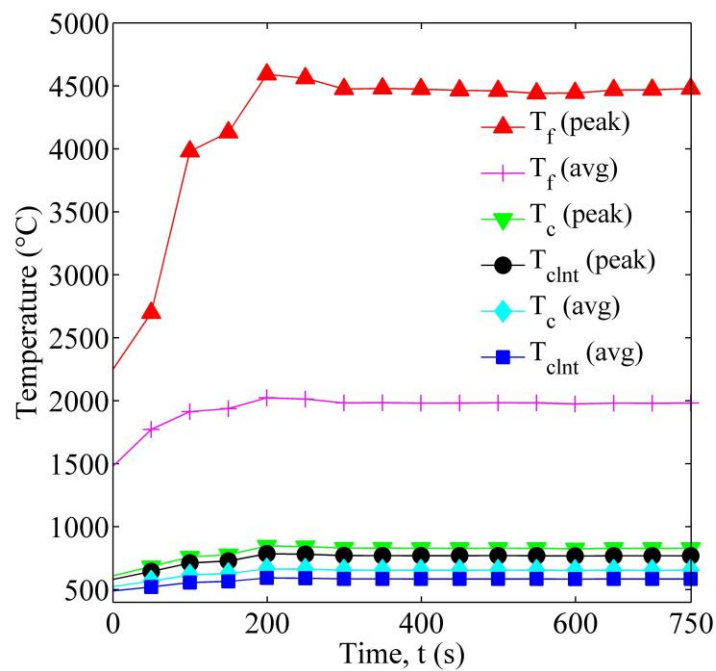


Figure 4.13: Temperature time history of Zone-I fuel pin for BOL core under the conservative estimate (Case-IV).

4.2.3.3 Reactor dynamics of in-pin fuel motion (Cases III & IV)

Figure 4.14 presents the reactor power and net reactivity histories for the conservative case studies [97]. It is observed that the net positive reactivity reaches a maximum magnitude of $0.054\text{ } \$$ and $0.056\text{ } \$$ in cases III and IV respectively early in the accident ($t \cong 48 - 50\text{ s}$). At this stage, the positive reactivity is countered essentially by the fuel Doppler and fuel axial expansion feedbacks, as seen in the reactivity feedback plots presented in Figure 4.15.

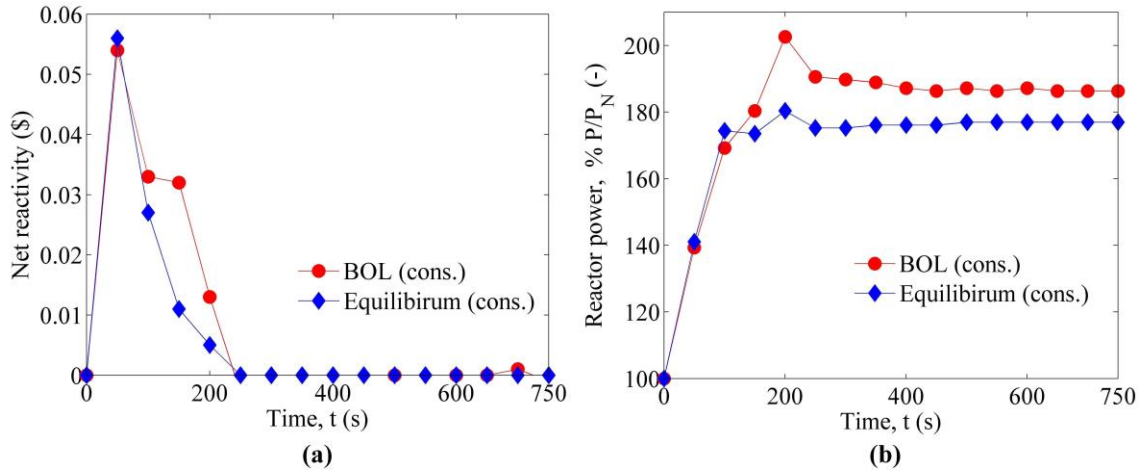


Figure 4.14: Transient behaviour of a 500 MWe fast reactor during UTOP (conservative analysis): (a) Net reactivity vs. time and (b) Reactor power vs. time.

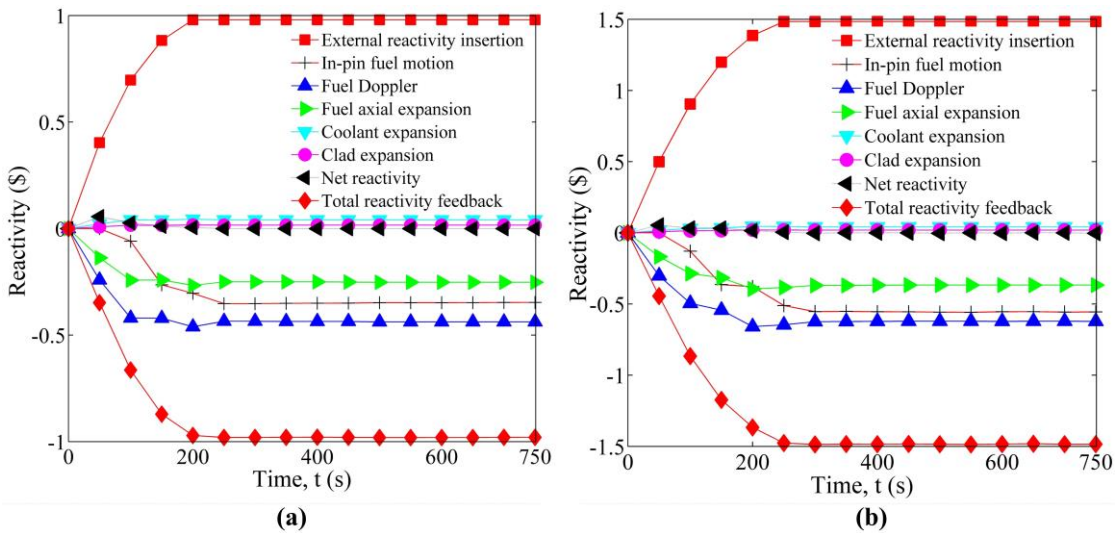


Figure 4.15: Reactor dynamics plots for conservative simulations of UTOP: (a) Case-III (Equilibrium core) and (b) Case-IV (BOL core).

With the start of melting at $t = 79$ s (Case III) and $t = 55$ s (Case IV), the in-pin fuel motion feedback emerges and begins to decrease the net reactivity. However, the reactor power continues to rise until the external reactivity is completely neutralized at $t = 230$ s (Case III) and $t = 208$ s (Case IV). Furthermore, there is a delay in the decrease of net positive reactivity in Case IV, as visible in Fig. 4.14a ($t = 100 - 160$ s). Consequently, the reactor power reaches a significant overpower ($P/P_n = 204\%$, $t = 199$ s). Due to extensive melting in six out of seven fuel zones, the in-pin fuel motion feedback attains a magnitude of -0.55 \$. The increased magnitude is consistent with

the results of Chapter 3 (Figure 3.14). Due to the increased negative feedback magnitude, the reactor power decreases, finally stabilizing at a slightly lower level ($P/P_n = 187\%$, $t = 750\text{ s}$). On the other hand, in Case-III, the positive reactivity is rapidly neutralized by the in-pin fuel motion feedback ($\rho_{rel} = -0.347\text{ \$}$), as visible in Fig. 4.14a. Consequently, the reactor overpower is curtailed effectively ($P/P_n = 182\%$, $t = 190\text{ s}$), leading to stabilization at 177% ($t = 750\text{ s}$).

It may be noted that the stabilized power in Case III is less than the corresponding power level for Case-IV. Such a trend is opposite to the best estimate case studies (Figure 4.8b). The reason for the opposing trend is as follows: There is a substantial amount of melting in Case III, leading to a considerable in-pin fuel motion feedback ($-0.347\text{ \$}$), which results in rapid neutralization of the external reactivity insertion. Consequently, the reactor power excursion is curtailed effectively. However, in Case-I, melting occurs only in one subassembly of equilibrium core, leading to an insignificant in-pin fuel motion feedback. Consequently, there is considerable time lag in the complete neutralization of external reactivity insertion. Hence, the reactor power continues to increase up to 171% , which is greater in comparison with BOL core (or Case-II).

4.2.4 Impact of in-pin fuel motion on accident outcome

Table 4.4 presents a comparison of the accident progression with ρ_{rel} against the progression without ρ_{rel} . The maximum values of the net reactivity (ρ), reactor power level (P/P_n), and the feedbacks due to in-pin fuel motion (ρ_{rel}), Doppler broadening (ρ_{Dop}) and fuel axial expansion ($\rho_{f,axexp}$) are summarized in the table. A significant reduction in the maximum power levels can be seen with ρ_{rel} . Consequently, other negative feedbacks are also smaller for the corresponding simulations. It is evident that

in-pin fuel motion reduces the power excursion during UTOP. Consequently, the number of degraded fuel subassemblies is also reduced significantly. The scale of the in-pin fuel motion feedback in comparison with the fuel Doppler and axial expansion feedbacks indicates its importance towards the safety paradigm.

Table 4.4: Table of comparison of fast reactor dynamics with and without the inclusion of the in-pin fuel motion feedback (ρ_{rel}). Each value represents the maximum value of the variable. All reactivity values are in dollar (\$).

Case	Inclusion of ρ_{rel}					Exclusion of ρ_{rel}			
	ρ	$\frac{P}{P_n}$ (%)	ρ_{rel}	ρ_{Dop}	$\rho_{f,axexp}$	ρ_{net}	$\frac{P}{P_n}$ (%)	ρ_{Dop}	$\rho_{f,axexp}$
I	0.042	171	-0.006	-0.397	-0.226	0.042	171	-0.401	-0.229
II	0.045	162	-0.345	-0.436	-0.247	0.054	202	-0.657	-0.392
III	0.056	182	-0.347	-0.438	-0.252	0.056	223	-0.666	-0.407
IV	0.054	204	-0.556	-0.622	-0.367	0.054	301	-0.983	-0.629

A secondary advantage of in-pin fuel motion is obtained through the apparent reduction in the reactor power level during the stabilization phase of the transient (Figure 4.8b, 4.14b). The reduction is a consequence of a gradual increase in the magnitude of ρ_{rel} during the time lag between full withdrawal and achievement of an approximate thermal equilibrium. During this time lag, melting continues to occur asymptotically in time, which leads to a greater melt mass fraction and a resultant increase in ρ_{rel} magnitude. Consequently, the net reactivity (ρ) acquires a small negative value, resulting in a gradual decrease in reactor power level. Moreover, the primary cooling system remains functional throughout this duration. This allows the operator to respond appropriately and restore the shutdown systems, thereby terminating the accident. Once the reactor is scrammed, the focus shifts to post-accident

decay heat removal, which is carried out either through the operational grade or safety grade decay heat removal systems [13].

4.2.5 Thermodynamic assessment of molten fuel vaporisation

Due to high temperatures during UTOP ($T_f > 3500\text{ }^\circ\text{C}$), molten fuel may vaporize within the confinement of pellet cavity. To verify the existence of vapour phase inside the cavity, the thermodynamic state of molten fuel is determined using two state variables, i.e., pressure and enthalpy [97]. Hence, the P-H plots for molten fuel, starting from melt initiation (melt mass fraction = 0 %, left extreme) to peak power excursion (maximum melt mass fraction, right extreme), are shown in Fig. 4.16. The x-axis represents the peak enthalpy of molten fuel, which occurs near the centre of the fuel column ($z = 0.5\text{ m}, r = 0\text{ m}$). The y-axis represents the external pressure (P_{cav}) felt by molten fuel at the same time. Since the power is highest in Zone-I, the plots specific to Zone-I are presented. The saturation vapour curve recommended by Breitung [124] divides the liquid and vapour regions of the plot. According to liquid-vapour equilibrium, vaporisation can occur if the saturation vapour pressure of molten fuel becomes equal to the external pressure. In the equilibrium core fuel pins, due to the generation and release of fission gases, the gas phase density (ρ_g) is high. Hence, the P_{cav} is also greater (Refer Eq. (3.35)). Therefore, the P-H plots for equilibrium cases are located higher up the abscissa (or pressure axis). Consequently, the saturation enthalpy corresponding to this range of pressure is large ($P_{cav} > 0.55\text{ MPa}, H_{sat} > 2.07\text{ MJ/kg}$). Moreover, upon melting, fission gases trapped within the solid fuel are also released. Hence, as the power rises and fuel melts, more gases are released, which further raises the external pressure felt by molten fuel. Therefore, the right extremes of

P-H plots for the equilibrium cases are far away from the saturation vapour curve, which implies low potential for existence of vapour phase.

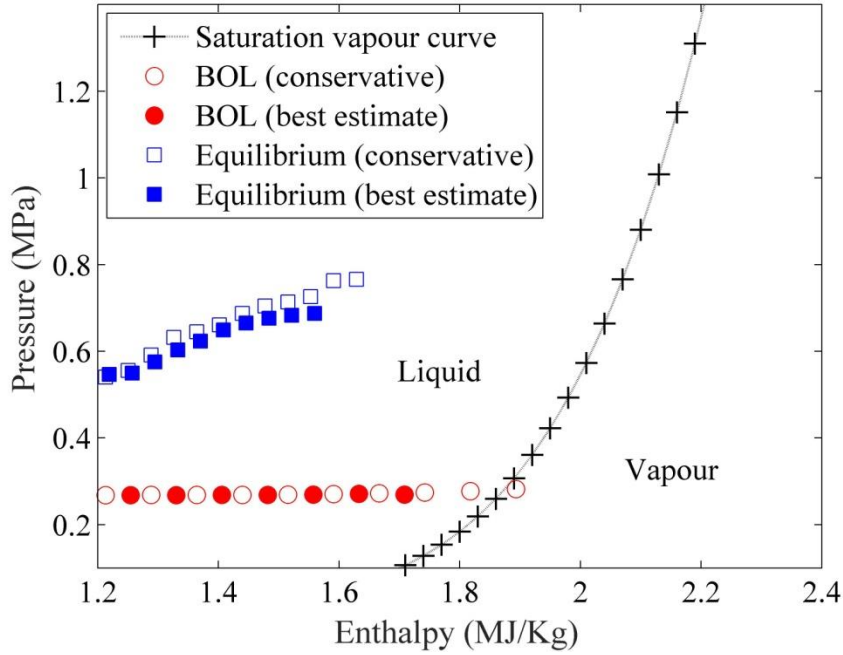


Figure 4.16: P-H data plots for molten fuel (Saturation vapour curve of molten fuel marks the boundary between liquid and vapour phases; P-H data is specific to Zone-1)

In the BOL core, fission gases are absent. The gas phase is comprised of bond gas only, due to which the gas phase density (ρ_g) is much lower than equilibrium core. Hence, the external pressure (P_{cav}) is also low. Therefore, the corresponding P-H data points are located downwards along the abscissa. Consequently, the corresponding saturation vapour enthalpy is least for BOL cases ($H_{sat} = 1.86 \text{ MJ/kg}$). Moreover, gas release upon melting is also nil ($S_g = 0$). When the molten fuel column begins to occupy the fuel cavity, the bond gases escape through the inter-pellet gaps to the plena. However, the total plena volume is much larger than the melt cavity volume, due to which, there is no appreciable pressurization during melting (Refer Table 2.4). This is reflected in the P-H plots (Refer Fig. 4.16, BOL cases), wherein the external pressure experienced by molten fuel remains approximately constant from the left to right

extremes. Furthermore, due to larger reactivity insertion associated with uncontrolled CSR withdrawal in BOL core, the molten fuel acquires high enthalpy ($H_{f,max} = 1.89 \text{ MJ/kg}$). Therefore, during UTOP, the P-H data-points of molten fuel are either situated in proximity of the saturation vapour curve (best estimate) or situated within the vapour zone (conservative analysis). From the thermodynamic perspective, this shows that during UTOP, the probability of molten fuel vapour formation is greatest in case of BOL core.

Table 4.5: Molten fuel P-H data ($\Delta H =$ excess enthalpy required for vaporization).

Case study	P_{pin} (MPa)	H_{max} (MJ/kg)	H_{sat} (MJ/kg)	ΔH (MJ/kg)
E9bis	1.49	1.9	2.2	0.3
I	0.69	1.56	2.05	0.49
II	0.27	1.71	1.87	0.16
III	0.77	1.63	2.07	0.44
IV	0.27	1.89	1.87	-0.02

In the above context, it is useful to examine the state of molten fuel in the CABRI-E9bis test since numerical simulation revealed a maximum melt temperature of 4608 °C (Refer Section 3.3.3). The pressure-enthalpy data of molten fuel during the test is compared with the results of the above presented case studies in Table 4.5. It is evident that the existence of high pressure inside the OPHELIE-6 fuel pin results in a saturation enthalpy of 2.2 MJ/kg . Therefore, despite the high enthalpy (1.9 MJ/kg), the excess enthalpy required for fuel vapourization (ΔH) is 0.3 MJ/kg . It is evident that vapourization of melt may not have occurred in the CABRI-E9bis test. Consistent with this result, the corresponding experimental literature does not contain any observations with regards to the formation of a vapour phase [33].

4.2.6 Effect of reactor parameters

4.2.6.1 Effect of core burnup

This section presents a comparative study of the equilibrium and BOL cores in the aspects related to melt propagation as well as the whole-core feedback response during UTOP. Towards this purpose, it is important to isolate the effect of core burnup from the change in the banking depth of control rods. This is simply achieved by selecting the second and third case studies for comparison, since the external reactivity insertion is approximately equal in both the cases (~ 0.98 \$, Refer Table 4.3). The two cases are compared in Fig. 4.17.

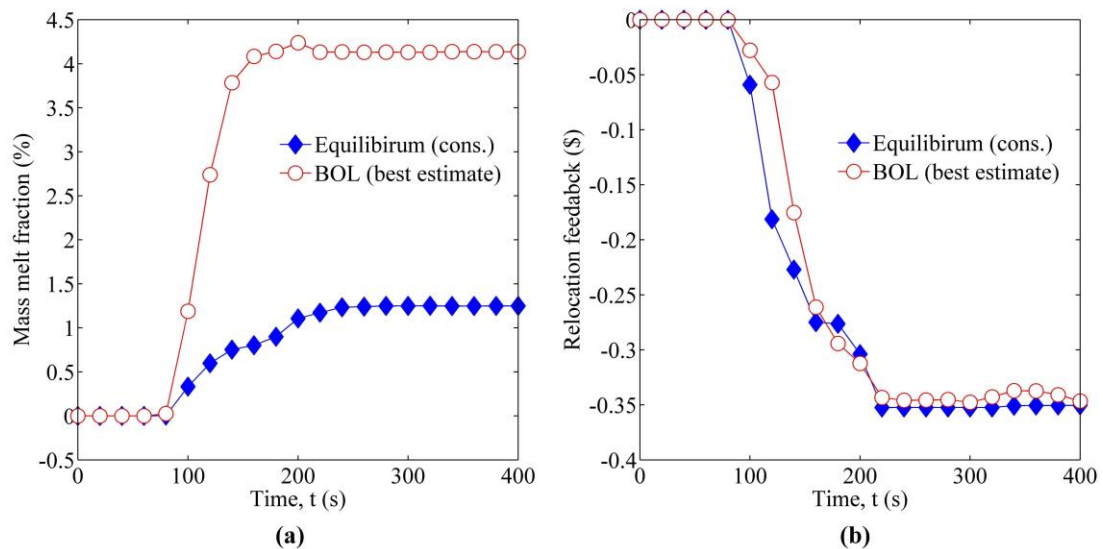


Figure 4.17: Comparison between BOL (best estimate) and equilibrium (conservative) cases (external reactivity insertion is approximately equal for both cases).

Time evolution of the core averaged melt mass fraction is presented in Fig. 4.17a (Refer Section 2.2 (iv) for definition). It is seen that the core averaged melt mass fraction is least in Case-III (equilibrium-conservative), despite the equivalent external reactivity insertion. The number of damaged subassemblies in Case-II are 85, in comparison with 61 subassemblies in Case-III. The reason can be seen in the relocation feedback curves

shown in Fig. 4.17b. From $t = 95 - 174$ s, the BOL core exhibits a significantly smaller relocation feedback compared to equilibrium core, with a maximum difference of ~ 0.12 \$. Due to the smaller relocation feedback, the net reactivity also remains higher in this period, leading to power excursion and greater melting in BOL core. It is apparent that the response of the BOL core is weaker in comparison with the equilibrium core under the above stated conditions and assumptions. The above differences are a consequence of the melt relocation characteristics specific to BOL and equilibrium fuel, as described in Chapter 3 of this thesis (Figure 3.14), which are not repeated here for the sake of brevity.

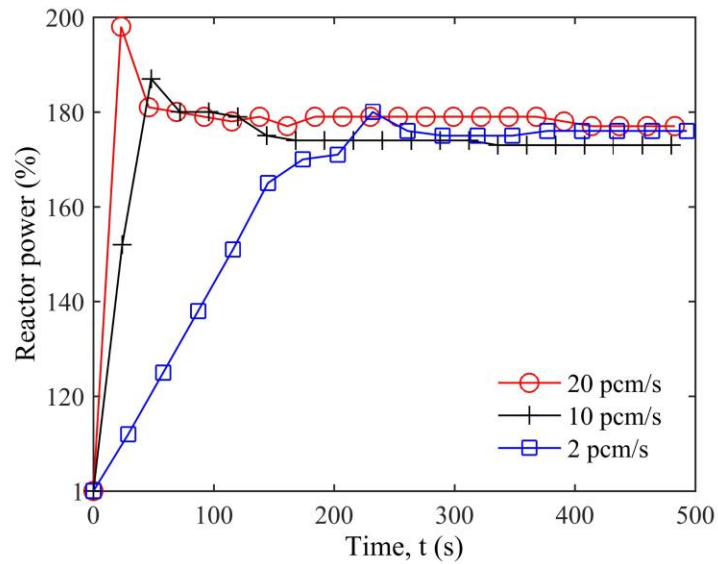
4.2.6.2 Effect of reactivity insertion rate

Under the postulated UTOP, the uncontrolled withdrawal of CSR leads to positive reactivity insertion typically of the order of $1 - 5$ pcm/s (Refer Section 2.3.3). The rate of reactivity insertion is proportional to CSR differential worth, banking depth, and withdrawal speed, which is generally constrained for safety purposes. As a test of the versatility of the developed algorithm, a parametric study of the reactor core under UTOP with different reactivity insertion rates is carried out. The study has resulted in estimations of the in-pin fuel motion feedback under highly conservative accident conditions. The parameters of the cases are detailed in Table 4.6.

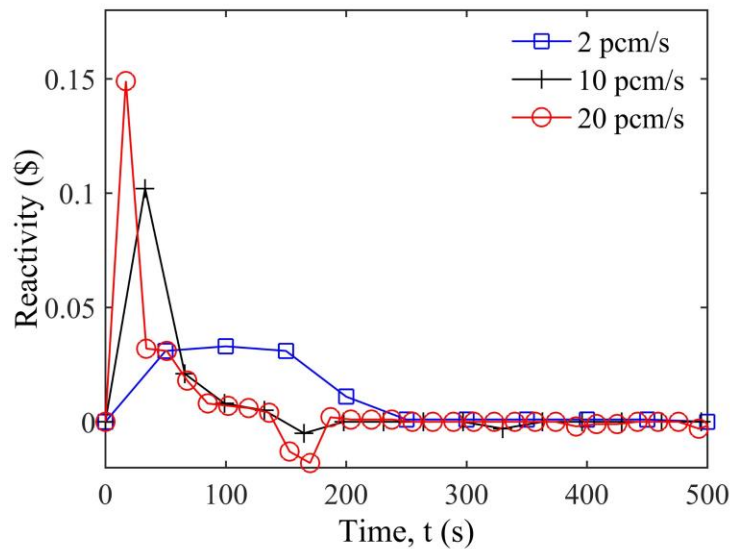
Table 4.6: Parametric analysis of reactivity insertion rate.

Insertion rate (pcm/s)	Withdrawal time (s)	No. of Damaged fuel subassemblies	Melt mass fraction (Zone-III, %)
2	239	95 (I, II, III, V)	2
10	48	95 (I, II, III, V)	4.1
20	24	125 (I, II, III, IV, V)	7.7

. In each case, although the withdrawal time changes, the maximum reactivity insertion remains constant (1.34 \$) for the single control rod. Results of the analysis are shown in Fig. 4.18a, which presents the reactor power history. It is observed that with increasing reactivity insertion rate, the peak reactor power increases.



(a)



(b)

Figure 4.18: Reactivity insertion rate study: (a) Power history, (b) Reactivity history.

For 20 pcm/s insertion rate, the maximum power level is 198 %, whereas for two pcm/s insertion rate, the peak reactor power is limited to 182 %. The reason is deduced from the net reactivity, which is presented in Fig. 4.18b. In both the ten pcm/s and

twenty pcm/s cases, there is a substantial net positive reactivity before initiation of in-pin fuel motion. The net positive reactivity is greatest for the twenty pcm/s case (0.149 \$), while it is least for the two pcm/s case. As a result, the reactor attains greatest power level in the twenty pcm/s case. It is noticeable that in the 10 pcm/s and 20 pcm/s, reactor power starts decreasing beyond $t = 47$ s and $t = 23$ s respectively, despite the net reactivity being positive during this time. This is a result of the dependence of power upon the rate of change of net reactivity. Although the net reactivity is positive, its time rate of change is negative (-0.006 \$/s for 10 pcm/s, -0.01 \$/s for 20 pcm/s case). The negative gradient in time causes the visible drop in power.

Upon initiation, the in-pin fuel motion feedback reduces the positive reactivity. However, the power level remains high until the external reactivity is completely neutralized (Refer Fig. 4.18b). As a result, the number of damaged fuel subassemblies is highest for the 20 pcm/s case (Refer Table 4.6). In this case, fuel subassemblies in the fourth zone have also melted. It is evident that with increasing CSR withdrawal speed, the damage spreads to the third and fourth zones. The analysis demonstrates the potential of in-pin fuel motion feedback to neutralize higher reactivity insertion rates.

4.3 Closure

In this chapter, a numerical algorithm for the simulation of mixed oxide fuel melting and its propagation inside sodium cooled, medium sized fast reactor during the unprotected transient overpower (UTOP) accident is presented. The algorithm accounts for the inherent coupling of fuel relocation with reactor neutronics, variations in fuel properties, heat generation and coolant flow rate throughout the reactor core using a dynamic coupling technique. The algorithm can capture the propagation of fuel melting in the reactor core as well as the impact of melt motion on the outcome of severe

accidents. This is a marked improvement over the corresponding studies available in literature, which have relied on broad assumptions of fuel squirting due to the absence of a benchmark-proven melt relocation model. A suitable data-exchange period is selected to minimize the computational efforts.

Four separate, whole-core, numerical simulations of UTOP are carried out using best and conservative estimates of the control rod banking depth for two basic types of core conditions: case studies I and III for the equilibrium core and case studies II and IV for the beginning-of-life (BOL) core. To measure the impact of in-pin fuel motion on the accident outcome, four equivalent, de-coupled numerical simulations are carried out by excluding the melt relocation feedback from the reactivity calculations. Furthermore, the effects of the core condition and the reactivity insertion rate on fuel melting, propagation and the resultant relocation feedback are studied. From the simulation results, the major conclusions are as follows:

- (i) The negative reactivity feedback of melt relocation (ρ_{rel}) improves the safety margin under UTOP, once melting initiates in multiple fuel subassemblies (~30 or more).
- (ii) The stabilized ρ_{rel} values for the case studies I, II III and IV are found to be -0.006 \$, -0.345 \$, -0.347 \$, and -0.55 \$, against the corresponding core-averaged melt mass fractions of 0.03 %, 4.15 %, 1.26 % and 17.15 % respectively.
- (iii) Inclusion of ρ_{rel} in the reactor kinetics calculations results in the prevention of coolant boiling and clad failure in all the case studies.
- (iv) The net positive reactivity is neutralized effectively in all cases except Case-IV (BOL, conservative, 1.48 \$), in which the reactor power reaches a peak level of

204 %, resulting in extensive propagation of melting up to 157 fuel subassemblies (out of 181).

- (v) The thermodynamic state of molten fuel at its highest temperature, determined by the pressure-enthalpy data of the case studies, shows that there is a significantly greater potential for vaporisation of molten fuel inside the pellet cavity in case of BOL core, as compared to the equilibrium core.

The study has clearly brought out the impact of in-pin fuel motion on the safety of a typical, sodium cooled, mixed oxide fuelled, medium sized fast reactor. Additionally, the characteristics of melt propagation throughout the reactor core have been established for both BOL and equilibrium configurations. A significant sensitivity of the melt propagation has been observed with regards to the condition of the reactor core. The next chapter attempts to address the sensitivity by a more consistent representation of the fission gas release induced pressurization forces.

Chapter 5

Development of a Fission Gas Release Solver and Investigation of Melt Relocation in Alternative Axial Blanket Designs

In this Chapter, suitable numerical algorithms are developed for consistent representation of the microstructural gas release processes involved in the pressurization of molten fuel. First, to represent the basic principles involved, a mechanistic fission gas release solver (FGR) is developed with sophisticated models for fission gas behaviour at both the intra-granular and inter-granular levels. The solver is integrated with the earlier developed multi-phase thermal hydraulic model, resulting in an improved numerical model that can capture the realistic effect of fission gas pressurization on the fluid flow. Numerical simulations are performed for the cases of isothermal gas release tests, FBTR mixed-oxide fuel irradiation test, and CABRI-E9 transient over-power test, employing the present model. The simulation results are compared with the corresponding experimental results as well as FEAST-OXIDE code predictions quoted in literature. As an illustration, the resultant algorithm, MITRA, is utilized to capture the realistic effects of transient fission gas release on the melt hydrodynamics and relocation during unprotected transient overpower accidents. To achieve the above goal, the following specific investigations are carried out:

- (a) Investigation of the effect of fission gas release on melt motion under a range of fuel burnup
- (b) Consolidated whole-core simulation of UTOP with MITRA in the equilibrium core to gauge the effect of the modelling improvements on the melt propagation and reactivity feedback.

The aim of the present study is to investigate the realistic impact of fission gas release on melting, fuel relocation, and the progression of UTOP accident. As a second illustration, MITRA is utilized to investigate the possibility of fuel relocation out of the active core through suitable axial blanket design modifications. To fulfil the above goal, the following tasks are carried out:

- (c) Incorporation of a bulk freezing model to simulate the penetration of fuel inside cold channels (for e.g., the cavity inside annular blanket pellets), and its experimental validation.
- (d) Investigation of melt displacement inside an alternative fuel pin geometry with a completely annular top blanket pellet.
- (e) Investigation of the effectiveness of partially annular top and bottom blanket columns on fuel relocation out of the active core.

The above study is aimed at investigating the potential for further improvement in the inherent safety of current and future fast reactors with fuel pin design modifications.

5.1 Modelling of fission gas pressurization force

5.1.1 Mathematical and numerical modelling

5.1.1.1 Underlying physical mechanisms

The present work investigates the pressurization of molten fuel during UTOP by the transient release of noble gases from within the fuel microstructure. Noble gas atoms are generated as by-products of nuclear fission inside fuel grains. These atoms remain insoluble within the fuel matrix, and depending upon the dynamics of solid-state diffusion, either remain pinned in their respective locations or diffuse through the grain matrix. A portion of the gas atoms reaches the grain boundaries, resulting in the formation of inter-granular bubbles. With continued fission, inevitably, the inter-

granular bubbles connect with the free volume inside the fuel pin, resulting in the release of fission gases to the free volume [125].

During UTOP, the reactor over-power may result in sufficient heat-up to initiate fuel melting. As this occurs, both the intra-granular and inter-granular gas bubbles overcome the surrounding fuel matrix through their internal pressure, resulting in extensive bubble coalescence and diffusion through the liquified fuel, which leads to a transient release of fission gases. With such a release, there is a rise in local density of the gas-phase inside the pellet cavity, resulting in a corresponding rise in local pressure (Refer Eq. (3.35)). The resultant pressure difference between the site of melting and other locations inside the cavity causes a pressure gradient, which results in the so-called fission gas pressurization force. The force is essentially dispersive in nature since it attempts to drive the fuel away from the original site of melting. Due to the pressure gradient, a flow initiates in the gas-phase, which attempts to equilibrate the pressure field inside the cavity by increasing the gas density in relatively low-pressure regions.

5.1.1.2 Intra-granular fission gas release

First, a mathematical model is developed for the gas release phenomena inside the fuel grain. The following intra-granular phenomena are considered in the present study: (I) noble gas atom generation (II) diffusion of gas atoms towards the grain boundaries (III) gas bubble nucleation and destruction (IV) bubble migration under the influence of a temperature gradient and (V) release of gas to the grain boundary. The governing equations of intra-granular gas release are as follows [126]:

$$\frac{\partial C_g}{\partial t} = \frac{1}{r^2} \frac{\partial}{\partial r} \left(D_g r^2 \frac{\partial C_g}{\partial r} \right) + K_g - D_g K_b^2 C_g - K C_t + b C_{gb} \quad \dots (5.1)$$

$$\frac{\partial C_{gb}}{\partial t} = D_g K_b^2 C_g + K C_t - b C_{gb} - \dot{G} \quad \dots (5.2)$$

$$\frac{dC_b}{dt} = KC_t - bC_b - \frac{\dot{G}}{n_b} \quad \dots (5.3)$$

$$D_g = 7.6 \cdot 10^{-10} \cdot e^{\left(\frac{-35000}{T_f}\right)} + \left(2.3 \cdot 10^{-20} \cdot e^{\left(\frac{-15000}{T_f}\right)} + 5 \cdot 10^{-25}\right) Q \quad \dots (5.4)$$

$$\dot{G} = 4\pi D'_g R_c C_t C_b Fr_{bu}, D'_g = \frac{0.973 D_g b}{D_g k_b^2 + b_{res}} \quad \dots (5.5)$$

$$Fr_{bu} = \frac{h_{bu}}{D_{grain}}, h_{bu} = \frac{v_b}{p_{de}}, v_b = \frac{3\delta_{su} D_{su} Q_{su} \nabla T_f}{(40 \times 10^{-19}) R_u T_f^2} \quad \dots (5.6)$$

In the above equations, C_g is the concentration of gas atoms in the fuel matrix, r is the radial coordinate inside the equivalent grain sphere, D_g is the gas atom diffusion coefficient, K_g is the rate of gas atom generation due to fission, K_b^2 is the sink strength of gas atoms in the gas bubbles, K is the nucleation rate constant of gas bubbles, C_t is the total concentration of gas atoms inside the fuel matrix ($C_t = C_g + C_{gb}$), b is the probability of destruction of gas bubble by a fission fragment, C_{gb} is the concentration of gas atoms trapped within gas bubbles, \dot{G} is the rate of gas atom deposition to the grain boundary due to bubble migration at high temperatures. Fr_{bu} is the fraction of bubbles that survive the journey to the grain boundary, h_{bu} is the average distance travelled by bubbles prior to their destruction, v_b is the bubble velocity, R_c is the effective bubble capture radius, δ_{su} is the effective surface thickness (3.4 nm), D_{su} is the surface diffusion coefficient of the bubbles, ∇T_f is the local temperature gradient, $R_u = 8.314 \frac{J}{mol} / K$, n_b is the average number of gas atoms trapped inside bubble ($n_b = \frac{C_{gb}}{C_b}$), where C_b is the concentration of gas bubbles within the fuel grain. All the above terms involving bubble dynamics are applicable to intra-granular bubbles. It should be noted that spatial variations of only three variables are considered within the fuel grain (C_g, C_{gb}, C_t). A uniform distribution is assumed for all other parameters inside the grain.

Each node of the fuel pellet stack is assigned a representative single grain with spherical geometry [127]. The grain sizes are a function of temperature, varying linearly from 32 μm ($T_f \geq 2000\text{ K}$) to 8 μm ($T_f \leq 1500\text{ K}$) respectively [126]. The migration of intra-granular gas bubbles is assumed to occur only above 1600 $^\circ\text{C}$, since at lower temperatures, the bubbles are found to remain pinned down and unable to migrate [126].

The boundary condition for the above equations are as follows:

$$\left. \frac{\partial C_g}{\partial r_{gr}} \right|_{r=0} = 0, \quad C_g \Big|_{r=R_{gr}} = 0 \quad \dots (5.7)$$

5.1.1.3 Inter-granular fission gas release

Fission gas atoms diffuse through the grain matrix and collect in the grain boundary. Intra-granular bubble migration under a temperature gradient may also result in the release of gas atoms to the grain boundary. Edge and face bubbles are formed in the boundary as a result. These bubbles grow with the continued arrival of fission gas, which results in fuel swelling. A vacancy emission and absorption model is adopted to describe the growth of the edge and face bubbles [128]. Upon sufficient enlargement, bubbles inter-link to form gas tunnels around the fuel grains. Fission gases escapes once an inter-linked edge tunnel connects with the free volume through a crack or an open pore. The following governing equations attempt to account for each of the above phenomena [128]:

$$\frac{dC_f}{dt} = (1 - F)(1 - X) \frac{dC_b}{dt} - \left(\frac{C_f - C_{f1}}{1 - F} \right) \frac{dF}{dt} + \frac{C_f}{A_f} \frac{dA_f}{dt} \quad \dots (5.8)$$

$$\frac{dC_e}{dt} = (1 - E) \left((F(1 - X) + X) \frac{dC_b}{dt} + \left(\frac{C_f - C_{f1}}{1 - F} \right) \frac{dF}{dt} - \frac{C_f}{A_f} \frac{dA_f}{dt} \right) - \left(\frac{C_e - C_{e1}}{1 - E} \right) \frac{dE}{dt} \quad \dots (5.9)$$

$$\frac{dC_r}{dt} = E \left((F(1 - X) + X) \frac{dC_b}{dt} + \left(\frac{C_f - C_{f1}}{1 - F} \right) \frac{dF}{dt} - \frac{C_f}{A_f} \frac{dA_f}{dt} \right) + \left(\frac{C_e - C_{e1}}{1 - E} \right) \frac{dE}{dt} \quad \dots (5.10)$$

Here, C_f, C_e = Gas atom concentrations in the face and edge bubbles. C_r = Gas atom concentration released to the free volume. C_b = Gas atom concentration arriving at the grain boundary from inside the grain, C_{f1} = Gas atom concentration inside face bubbles in case of complete inter-linkage with edge bubbles; F = Fraction of face-bubbles connected with edge bubbles; X = Fraction of intra-granular gas atoms arriving at face bubbles. A_f = Grain face area available for face bubble growth ($A_f = \pi e^2$); E = Fraction of edge bubbles linked with the free volume. C_{e1} = Gas atom concentration in case of complete linkage of edge bubbles with the free volume. The equation derived for inter-connecting the intra-granular and inter-granular models is as follows:

$$\frac{dC_b}{dt} = K_g(r, z, t) - \frac{dC_{t,avg}}{dt} \quad \dots (5.11)$$

The rate of arrival of gas atoms from within the grain to its boundary (C_b , atoms·m⁻³) is a function of the rate of gas atom generation (K_g , atoms·m⁻³s⁻¹) and the total intra-granular gas atom concentration (C_t , atoms·m⁻³) averaged over the grain volume ($C_{t,avg}$) [127]. Expressions for the above parameters are derived from the OGRES and FEAST-OXIDE model literature [126–128].

5.1.1.4 Transient fission gas release

As the fuel grains approach the solidus temperature, the material properties begin a transition towards liquid-phase properties. As a result, there is a rapid coalescence of dissolved gas atoms into bubbles since the diffusion coefficient for liquified fuel is large [46]. Both the intra-granular and inter-granular gas bubbles undergo random as well biased migration under the influence of buoyancy and capillary forces, resulting in a gradual separation and escape of gas bubbles from the liquid fuel. Previous studies have treated the intra-granular and inter-granular bubbles separately. Upon melting, the studies assumed that the inter-granular gases were released instantaneously through

inter-linked tunnels to the free volume. On the other hand, the intra-granular gas release was assumed to occur gradually, based on a coalescence formulation [129] or an exponentially decreasing rate of release [68,119].

In the present study, it is assumed that both the inter-granular and intra-granular gases are released instantaneously to the free volume once the fuel node temperature breaches the interface temperature (T_{int}). This assumption is considered for the following reasons: (a) An instantaneous entry of intra-granular and inter-granular gases along with the molten fuel in the pellet cavity will generate a large, localized pressure spike (Refer Eq. (3.35)). Consequently, a large pressure gradient will be set up, as compared to the case of gradual release, resulting in a correspondingly large pressure force. Such a modelling strategy will enable a conservative evaluation of the fission gas pressurization force. (b) If upon analysis, it is found that there is a significant sensitivity of the melt displacement towards pressure forces, further modelling efforts may be directed towards the resolution of the intra-granular gas bubble coalescence. Therefore, the local gas mass source term (S_g), physically equivalent to the transient, local gas release rate, is defined as follows:

$$S_g(z, t) = (n_{Xe}(r, z, t)Mol_{Kr} + n_{Kr}(r, z, t)Mol_{Xe})S_f(z, t) \quad \dots (5.12)$$

Here, n_{Xe}, n_{Kr} are the moles of Krypton and Xenon stored inside the control volume identified by the radial and axial coordinates (r, z), Mol_{Kr}, Mol_{Xe} are the molar masses ($\text{kg}\cdot\text{mol}^{-1}$), and the multiplication factor ($n_{Xe}(r, z, t)Mol_{Kr} + n_{Kr}(r, z, t)Mol_{Xe}$) is defined as the gas retention coefficient (F_g). It may be noted that S_g is utilized as a source term in the gas-phase mass and energy conservation equations developed for the multi-phase flow model (Refer Eq. (3.41, 3.44)).

Common to transient heat-up of nuclear fuel is the coalescence and migration of previously pinned intra-granular bubbles under the influence of a temperature gradient, due to a significant rise in fuel temperature. In fuel pins, this phenomenon assumes particular significance in the outer, unrestructured regions of fuel pellets. From the results of the CABRI reactor, it is reported that a considerable release of fission gases may occur from these regions, even without melting [33]. In the present study, such a transient gas release from the solid fuel is incorporated by the extension of the above described intra-granular and inter-granular gas release models towards transient heat-up. In the utilization of the above models, the following assumptions are considered:

- (i) The influence of the non-equilibrium conditions caused by UTOP on the intra-granular gas bubble coalescence and growth is neglected.
- (ii) Grain growth during the UTOP transient is insignificant.

The purpose of the above assumptions is to simplify the modelling framework for an initial application towards the experimental benchmark studies. As revealed from the results of the experimental validation studies presented in the subsequent sections, the present modelling framework adequately fulfils the main purpose of the present study, which is to capture the effect of the fission gas pressurization forces on the melt displacement. However, the above phenomena may be taken up for further development in a future work specifically targeted towards capturing the dynamics of transient fission gas release under upset conditions.

5.1.1.5 Development of a fission gas release solver (FGR)

Using the above-described mathematical framework, a fission gas release solver (FGR) is developed which can simulate the gas release behaviour of mixed-oxide, fast reactor fuel pins under both steady-state and transient conditions. The computational

grid of the solver is kept equivalent to the grid of the multi-phase thermal hydraulic model developed in Chapter 3, to enable seamless integration. However, it is observed that the magnitude of the fission gas release (Fr_{pin}) with the selected mesh remains convergent for coarser grid sizes, for e.g., 5×5 (radial \times axial) grid, which is in consistence with the optimal number of nodes specified for the FEAST-OXIDE code (6 radial) [126]. Therefore, the chosen grid (30×30) is adequate from the point of view of grid sensitivity. The details of the chosen grid have been presented in Chapter 3 and are not repeated here for the sake of brevity. For the intra-granular gas release equations (Refer Eq. 5.1-5.3), 15 spherical elements are considered inside each fuel grain, in consistence with the FEAST-OXIDE code. A fully explicit, finite difference method is used to develop the numerical solver. The fission gas release fraction for the entire fuel pin (Fr_{pin}) during steady state is calculated as follows:

$$Fr_{pin}(t)(\%) = \frac{100}{V_{fuel}} \int_{V_{fuel}} Fr(r, z, t) dV_{fuel}, \quad Fr(r, z, t) = \frac{C_{rel}(r, z, t)}{\int_0^t K_g(r, z, t) dt} \quad \dots (5.13)$$

In the above equation, the local fission gas release fraction (Fr) is defined as the ratio of released gas atom concentration (C_{rel}) and time integral of the rate of gas atom generation (K_g). The total fission gas release fraction (Fr_{pin}) is calculated by averaging the local release fraction over the total fuel volume (V_{fuel}). During the transient, the following procedures are carried out for a consistent representation of the gas release:

- (a) The radial position of each fuel node is compared with the location of the melt interface (R_{int}), which is defined in Chapter 2 (Section 2.2 (ii)). If a given fuel node radius lies inside the melt interface radius, it is considered to have undergone melting. In accordance with the above-described assumptions, the concentration of

released gas atoms (C_{rel}) is equated to the concentration of generated atoms ($\int_0^t K_g(r, z, t) dt$), resulting in 100 % gas release in the respective fuel node.

(b) To account for the transient gas release in solid fuel, the gas retention coefficient is modified at each solid fuel node as follows:

$$F_g(r, z, t) = F_g(r, z, 0) \left(\frac{1 - Fr(r, z, t)}{1 - Fr(r, z, 0)} \right) \quad \dots (5.14)$$

The time-step of steady-state computations is taken as 5 s, in view of the stability constraints observed during simulations as well as the recommended time step values available in literature [126]. For the UTOP transient, the time-step is reduced significantly (0.25 s) to capture the variation in F_g required in the multi-phase model.

5.1.1.6 Outline of MITRA algorithm

By assimilating the above developed FGR solver with the thermal hydraulic model presented in Chapter 3, an improved numerical algorithm is obtained which can capture the realistic effects of the fission gas pressurization forces on the melt displacement. It is named as Multi-phase In-pin Thermal hydraulic Relocation Algorithm (MITRA). Figure 5.1 shows a flowchart of the algorithm. Salient features are highlighted in Chapter 2 (Section 2.5). Essential input data are: (I) Pin geometry (for e.g., pellet radii, clad radii, length of fuel and blanket pellet columns, volume of fission gas plenum, etc.) (II) fuel thermo-physical parameters (for e.g., mole fraction of PuO_2) (III) fuel enthalpy-temperature data (IV) fuel removal worth data (V) irradiation time history (VI) power rise and (VII) coolant flow rate. The grid consists of 930 points in the fuel column, 102 points in the cladding steel and 128 points in the axial blankets. This mesh is chosen based on a rigorous mesh convergence study (Refer Section 3.3.1). First, the FGR module evaluates fission gas data before the start of the accident. The output of steady simulations is: (a) Gas release (b) Variation of fission gas retention at

the intra-granular and inter-granular levels inside solid fuel (c) Pin internal pressure and (d) Grain size distribution. Furthermore, essential data for transient simulations, such as the spatial distributions of Bu, Fr, F_g , inter-granular and intra-granular gas atom concentrations (for e.g., C_g, C_{gb}, C_t), and the moles of gases present in free volume (n_{Xe}, n_{Kr}, n_{He}) are written in the output file. Using the output files, the corresponding variables are initialized for transient simulations in the MITRA algorithm. The gap conductance module utilizes n_{Xe}, n_{Kr}, n_{He} values for calculating h_{gap} . The thermal conductivity module uses the Bu distributions imported from the input files for calculating K_f .

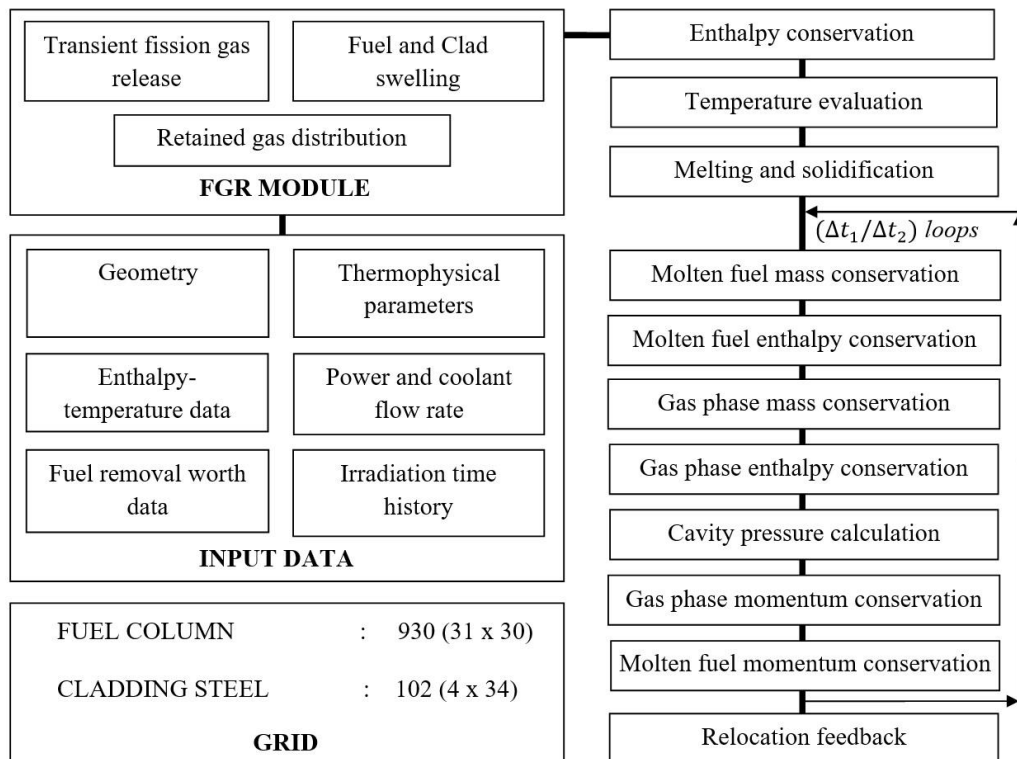


Figure 5.1: A brief outline of the developed code.

Based on the input and FGR (output) data, MITRA simulates the behaviour of mixed-oxide fuel pin during given UTOP conditions. The solver marches in time until the end of the transient. During the time march, the melt relocation feedback is

calculated at the end of each time step through Eq. (2.10–2.14). MITRA is encoded as a FORTRAN subroutine in PREDIS [30] as well as capable of parallel simulations by means of a data exchange mechanism [89]. Both these methods enable the integration of relocation feedback with reactor dynamics. The subroutine version is intended for the institutional repository, wherein multiple users can access the code for future use. The methodology of the subroutine is therefore enclosed in Appendix-C for the sake of future reference. The core is divided in seven fuel channels (or zones) and three blanket channels to reflect the radial variations in reactor power, coolant flow rate, enrichment and fuel mass removal worth (Refer Table 2.3 and Table 2.6) [13].

5.1.2 Results and discussion

5.1.2.1 Model validation and inter-code verifications

For validation of the algorithm, numerical simulations are first performed for the steady-state, isothermal gas release tests conducted in the FR2 reactor (Karlsruhe) [130]. To ensure consistency of the formulation, the simulation results are also compared with the predictions of the FEAST-OXIDE code quoted in literature. Next, the steady-state, mixed-oxide fuel irradiation test conducted in the FBTR reactor is simulated using the algorithm [131]. To verify the suitability of the algorithm towards transient overpower accidents, further numerical simulations are carried out for the CABRI-E9 test [33]. Finally, to ensure consistency between the melt displacement predictions of the current algorithm and the experimental observations, simulations are carried out for the CABRI-E9bis test.

(a) Steady-state validation and inter-code verification

The FGR module is benchmarked against both the FEAST-OXIDE code and isothermal gas release data [126,130]. The inter-code verifications ensure a sufficient

degree of conformance between the developed code and FEAST-OXIDE at different temperatures. Annular fuel pellets were loaded into irradiation capsules designed for exposing fuel to various burnup levels (2 to 10 atom percent) and temperatures (1000 to 2100 K) in the FR-2 reactor [130]. The fuel temperature was regulated by controlling the temperature of gas surrounding the pellets. Temperature was measured with a thermocouple passing through the annular pellet cavity. Constant temperature conditions were hence maintained. The pellets were axially separated with molybdenum rings to prevent axial temperature gradients. These efforts minimized the axial and radial temperature gradients of the fuel samples. The gas release was measured through a pin puncture test. Gas chromatography was carried out to determine the content of Xenon and Krypton. Table 5.1 presents the details of fuel samples and irradiation conditions. This data is used to carry out simulations of both intra-granular and inter-granular gas dynamics. Results of simulations are presented in Fig. 5.2. The gas release curves obtained from FGR are in general agreement with the experimental data.

Table 5.1: Verification data for fuel samples irradiated in FR-2 reactor [127,128].

Parameter	Value
Pellet outer periphery, m	5.1×10^{-3}
Pellet inner periphery, m	2.1×10^{-3}
Heat generation rate, W/kg	2×10^5
Pellet height, m	1×10^{-3}
Plutonium mole-fraction, %	15
As fabricated grain diameter, μm	10
Compressive stress, MPa	-
Fuel porosity, %	1.8 %

The curves are also in proximity with the FEAST-OXIDE curves. At 1350 K, the effect of JOG is considered in FEAST-OXIDE from two atom percent. This effect is

neglected in FGR. The simulations show that intra-granular gas bubble migration at 2000 K is crucial to obtain the rapid rise in gas release rate observed in the experiment. The verifications indicate a good level of conformance between MITRA and FEAST-OXIDE.

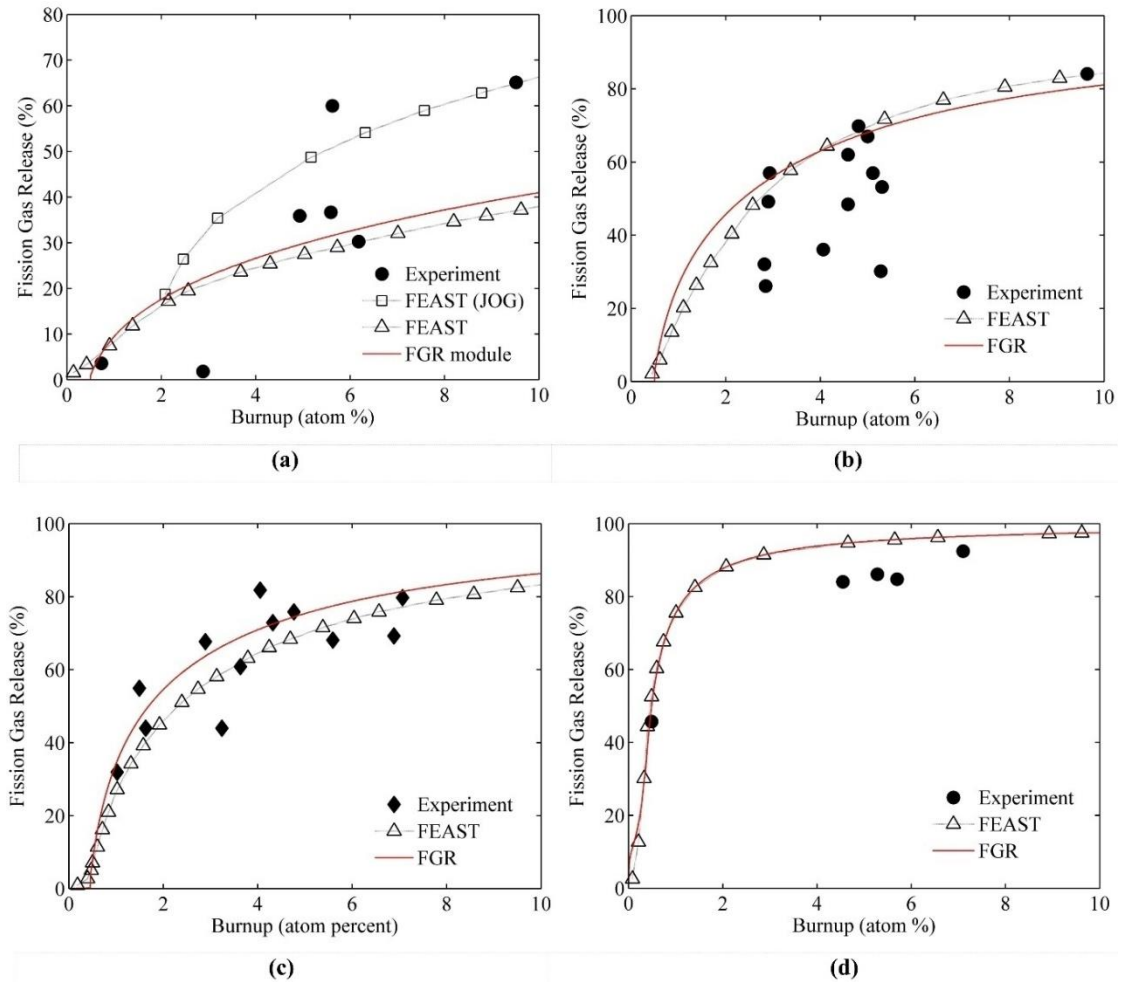


Figure 5.2: Results of verifications against UO₂ sample irradiation tests. Fission gas release curves of FGR are compared with FEAST-OXIDE curves along with experimental data [126,130].

To verify the suitability of the FGR solver towards the simulation of steady-state, fission gas release in mixed oxide, annular fuel pins, verification is performed using the experimental data from FBTR reactor [131]. A single, mixed oxide fuel subassembly (containing thirty-seven annular pins) was irradiated with a fast neutron flux (Refer Fig. 5.3 for axial power profile).

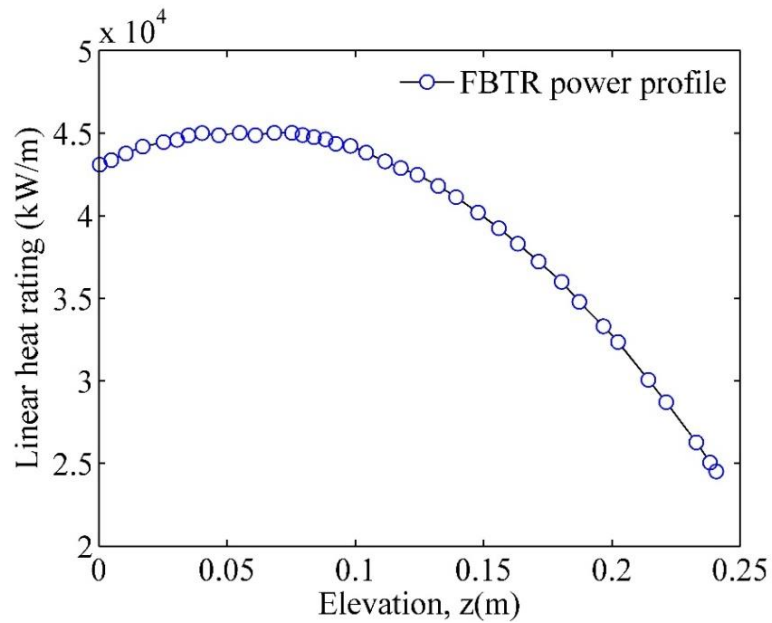


Figure 5.3: Power profile for the FBTR MOX fuel irradiation test [131].

Table 5.2: Specifications of FBTR-MOX test pins [131].

Parameter	FBTR-MOX test
Outer radius of pellet (m)	2.78×10^{-3}
Inner radius of pellet (m)	0.8×10^{-3}
Outer radius of clad (m)	3.3×10^{-3}
Inner radius of clad (m)	2.85×10^{-3}
Plutonium mole-fraction (%)	29.0
Length of fuel pellet cavity (m)	0.24
Length of blanket pellet column (m)	-
Maximum burnup (atom percent)	11.2
Upper plenum volume (m ³)	1.94×10^{-6}
Lower plenum volume (m ³)	2.95×10^{-6}
Peak steady state power (kW/m)	45
Coolant inlet temperature (°C)	365
Coolant flow rate (10 ⁻² kg·s ⁻¹)	8.2

The objective was to assess the performance of MOX fuel pin and D9 cladding steel [132] up to a burnup level of 11.2 atom percent. Table 5.2 enlists the parameters of the test used in the simulation. In the post-irradiation analysis, four fuel pins were punctured. Gas chromatography tests provided the partial pressure of each gas species. By determining the exact free volume inside the pin and the quantity of released gases, internal pressure estimates at room temperature (300 K) were calculated.

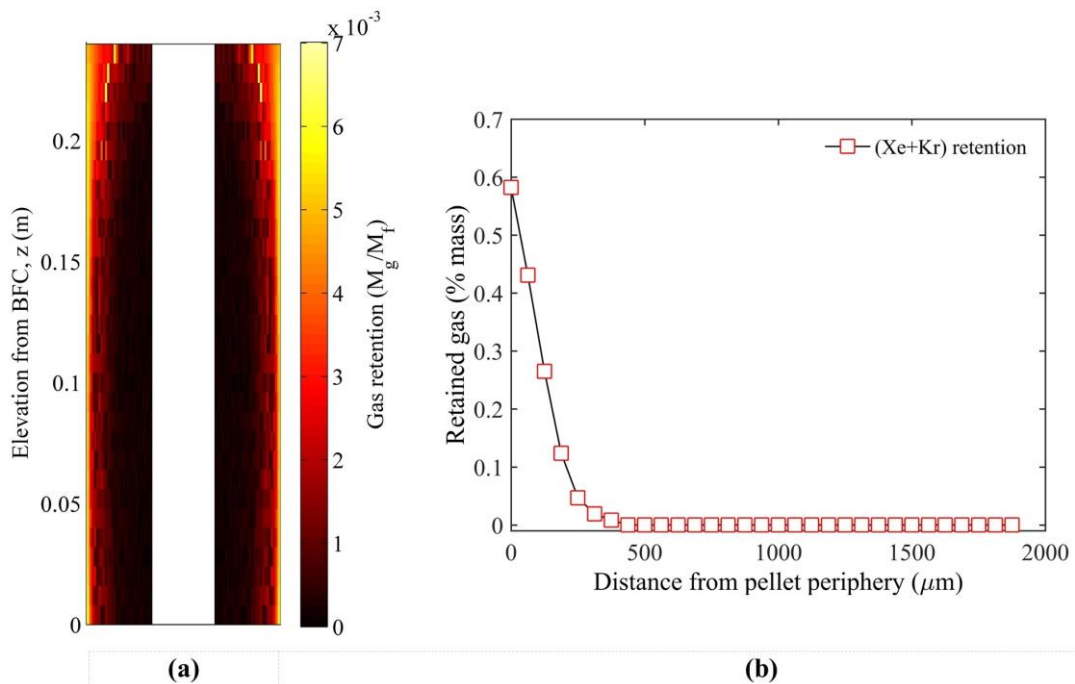


Figure 5.4: State of gas retention in FBTR MOX test pin. (a) Distribution of retained gases within the fuel pellet stack. (b) Retention of fission gases along the radius of the fuel pellet at the location of peak power. (dark regions signify minimum quantity of retained gas.)

Figure 5.4a presents the distribution of retained fission gases ($Xe + Kr$) inside the fuel microstructure at the end of irradiation. Figure 5.4b presents the gas retention profile at the peak power location ($z = 0.1 \text{ m}$). The retention is close to zero in the inner regions of the fuel pellet. The primary reasons are two-fold: high temperature leading to intra-granular bubble migration across the temperature gradient and high diffusion coefficient for fission gases. The behaviour falls in line with the isothermal benchmark

study at 2000 K (Figure 5.2d). The code predicted a total gas release of 83 % (experimental: 85 %) and an internal pin pressure of 2.3 MPa (experimental: 2.4–2.8 MPa). These results show that the simulation results of the algorithm agree with experimental gas release data for mixed-oxide fuel pins.

(b) *CABRI-E9 test*

The E9 test was conducted on a mixed oxide fuel pin with annular fuel pellets and fully solid blanket pellets (OPHELIE-6, Refer Table 2.8–2.9). The experimental data published in Ref. [33] and [72] have been used for benchmarking. In the test, a uniform power ramp of 1.1 % P_n/s ($P_n = 60.3 \text{ kW/m}, t = 0 \text{ s}$) was implemented over the pin until the power level reached 234 % ($P_{max} = 134.7 \text{ kW/m}, t = 119 \text{ s}$). A constant coolant mass flow rate was maintained throughout ($m_{ct} = 0.643 \text{ m}^3/\text{kg}$). Fuel melting was first detected at $\sim 73 \text{ kW/m}$. Post-irradiation analysis revealed that despite the maximum melt mass fraction reaching 57 %, the melt remained completely confined inside the fuel column.

Table 5.3: E9 validation results [33].

PARAMETER	MITRA	EXPERIMENT
Melt mass fraction, %	54.6	57
Radial melt extent at 0.18 m, %	79.8	79.8
Radial melt extent at 0.37 m, %	85.4	86.2
Radial melt extent at 0.59 m, %	82	75
Upper axial melt extent, m BFC	0.725	0.69
Lower axial melt extent, m BFC	0.025	0.016
Transient fission gas release, %	84	82.6
Power to melt, kW/m	71.5	73

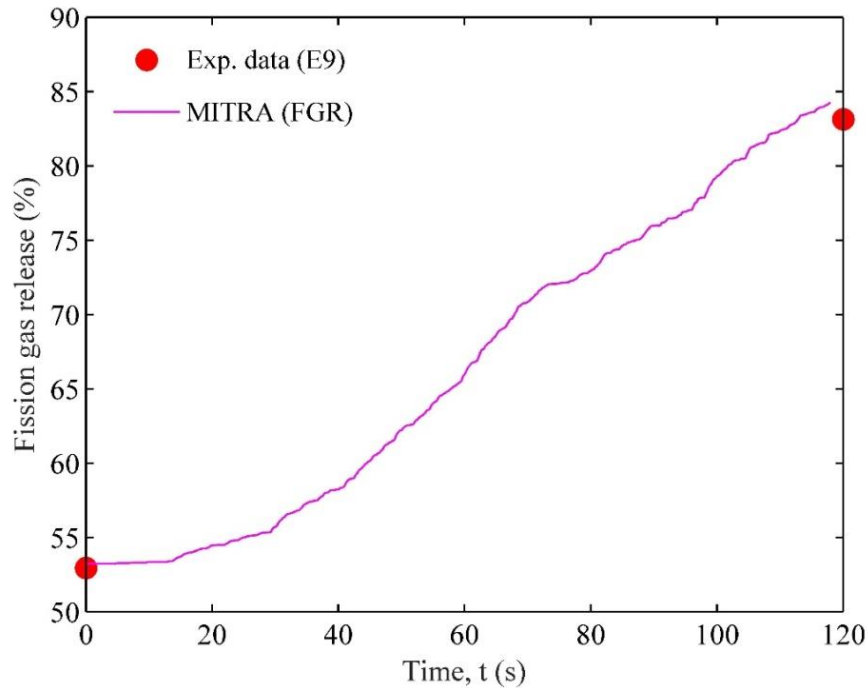


Figure 5.5: Comparison of E9 test data with gas release obtained from MITRA simulation [33].

Up to 82 % of gases were released during the test. In the molten regions, fission gases were liberated completely, whereas in the unmolten regions, the gases were released partially [33]. From the comparison of the experimental and simulation results, it is seen that the simulation results agree appreciably with the experimental data (Refer Table 5.3). In a previous study [77], only the thermal parameters were validated. Now, the validation extends to fission gas behaviour.

The time history of gas release is compared with experimental data in Fig. 5.5. Comparison with the results published in Ref. [72] shows that the predictions are in reasonable agreement with the ASTEC-Na code. The radial melt extent is compared with experimental data in Fig. 5.6. The results are in good agreement in lower and central regions of the fuel column ($z < 0.4 m$). The deviation in the upper region is due to over-prediction of inter-granular porosity.

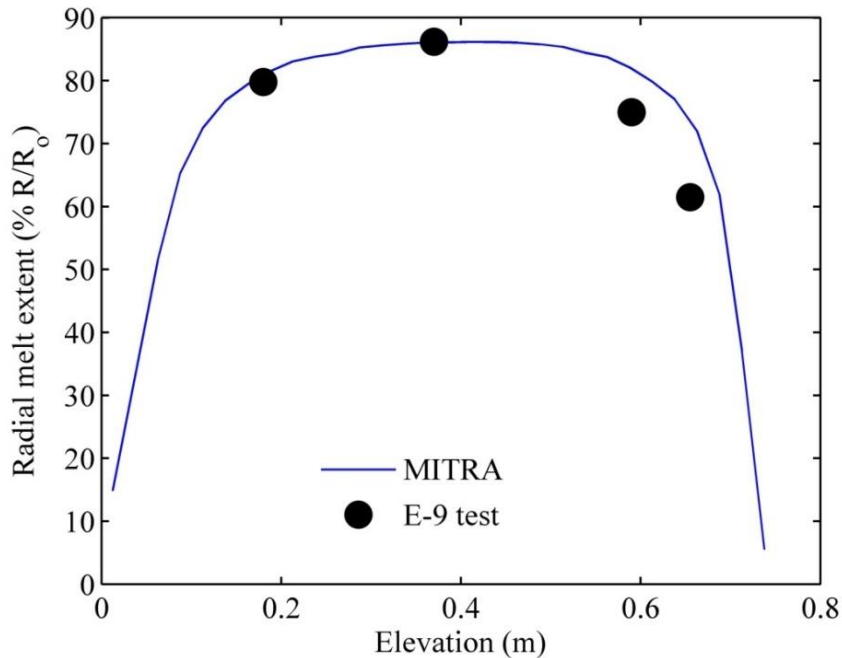


Figure 5.6: Comparison of E9 test data with melt profile obtained from MITRA simulation [33].

(c) *E9bis test*

Validation of the earlier developed advanced numerical algorithm with the experimental data of the E9bis test has been presented in Chapter 3 (Refer Section 2.4.2 for details of the E9bis test conditions). However, the previous model utilized an empirical correlation for the evaluation of the fission gas release fraction as well as F_g [12]. Therefore, the model ignored radial variations in the retained gas mass, which are quite significant. In the present model, these variations are incorporated through FGR solver. Consequently, the pressurization forces caused by transient gas release are also modified as compared to the previous validation. Therefore, to ensure consistency with experimental data regarding melt displacement, numerical simulations are carried out for the E9bis test, employing the present model.

Figure 5.7a presents the growth of the molten fuel column as a function of time [98]. The growth of melt columns is smooth and devoid of perturbations. The time of occupation of the topmost fuel node is in excellent agreement with the experimentally

observed time (65 – 69 s). As mentioned earlier, the source term (S_g) comprises both intra-granular and inter-granular gas mass release to obtain a conservative estimate of the fission gas pressurization forces (Refer Section 5.1.1.4). Despite this, the melt relocation is smooth (Refer Fig. 5.7b for melt mass time history). This indicates that the dispersive pressure forces are insignificant as compared to the viscous forces (due to solidification).

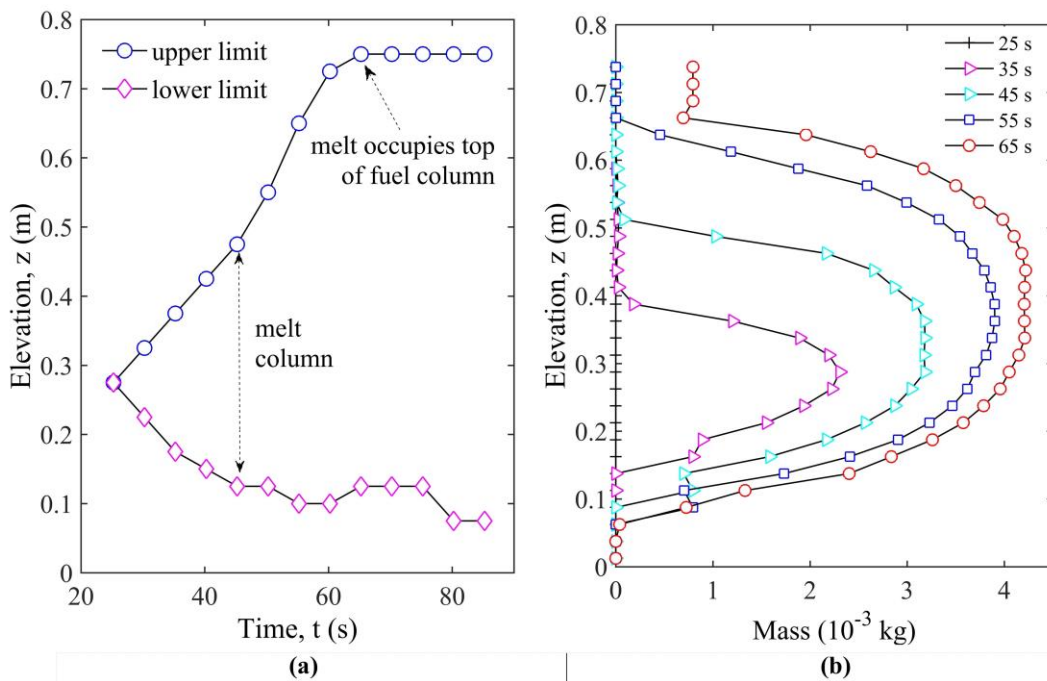


Figure 5.7: E9bis test: (a) Melt column time history (b) Melt mass as a function of time (upper and lower limits specify the respective extents of the melt column; $z = 0.75\text{ m}$ signifies top of fuel column, $z = 0\text{ m}$ signifies bottom of fuel column).

5.1.2.2 Transient fission gas release during UTOP

The validated algorithm is utilized to simulate the transient fission gas release in fast reactor fuel pins under UTOP conditions. The conditions are kept identical to the case studies presented in Chapter 3 (Section 2.3.3), except for the axial power profile utilized for the fresh fuel under the BOL core condition. Important parameters of the BOL core and fuel specifications have been detailed in Chapter 2 and are hence not repeated for the sake of brevity (Refer Section 2.1.1–2.1.2). Typically, power

generation in a BOL core condition is concentrated near the core mid-plane, as opposed to the equilibrium condition in which the power generation is comparatively increased in the top and bottom regions. Consequently, the axial peak factor is greater in case of BOL core (~ 1.246 , Zone-1) as compared to equilibrium core (~ 1.241 , Zone-1). However, since the main aim of the present study is to capture the effects of transient fission gas release on the melt motion, it is essential to isolate the sensitivity from the changes in the axial power distribution. Therefore, in the present study, the BOL fuel is also subjected to the typical axial power profile utilized for the equilibrium fuel. Furthermore, numerical simulations are also performed for a range of fuel conditions varying from fresh to intermediate burnup (0 – 7 atom percent), to capture the gas release phenomena effectively.

Table 5.4: Response of annular MOX fuel pin under UTOP at various burnup levels ($FGR_{t=0}$, $FGR_{t=120}$ are the fission gas release before and after the transient; radial melt is at $t = 120$ s, S_f , S_g , $F_{g,avg}$ are at peak power location ($z = 0.75$ m)).

Bu_{max} (at. %)	0	1	2	3	4	5	6	7
$F_{pin,t=0}$ (%)	-	51	71	77	79	79	80	83
<i>Retention</i> (%)	-	49	29	23	21	21	20	17
$MMF_{t=120}$ (%)	37	24	37	35	39	41	43	45
$F_{pin,t=120}$ (%)	-	54	75	81	83	84	86	86
<i>Melt extent</i> (% R/R_o)	80	74	79	75	79	79	79	82
$S_{f,avg}$ (10^{-4} kg·m ⁻¹ ·s ⁻¹)	20.6	21.5	19.6	15.9	16.5	15.8	15.2	14.8
$S_{g,avg}$ (10^{-8} kg·m ⁻¹ ·s ⁻¹)	0.0	4.6	9.3	12.4	15.4	18.7	21.0	17.6
$F_{g,avg}$ (10^{-5})	0.0	2.1	4.7	7.8	9.3	11.8	13.8	11.9

The results of the numerical simulations are presented in Table 5.4 [98]. The values of S_f , S_g and Bu_{max} are shown for the core mid-plane ($z = 0.75$ m). The time-

averaged values of S_f, S_g and $F_{g,avg}$ (from the start of melting to $t = 120$ s) and the peak melt mass fractions (MMF) are shown. The parameter $S_{f,avg}$ depends on the power ramp rate (primarily), fuel thermal conductivity (K_f) and the pellet-clad gap conductance (h_g). It is seen that $S_{f,avg}$ varies within a range of $14.8 - 20.6 \times 10^{-4} \text{ kg}\cdot\text{m}^{-1}\cdot\text{s}^{-1}$. Eq. (3.47) reveals that S_g additionally depends on the gas retention factor (F_g), defined in Eq. (5.12).

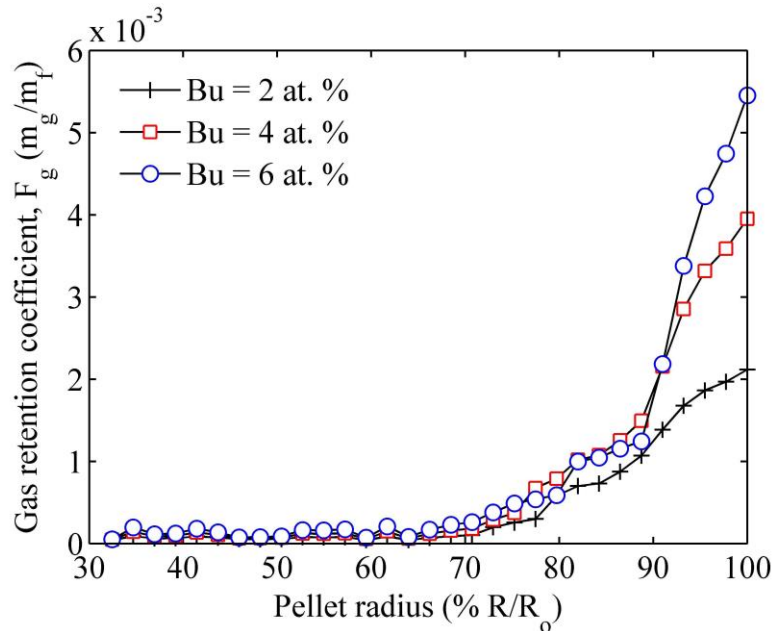


Figure 5.8: Gas retention coefficient, F_g , as a function of the dimensionless pellet radius (R/R_o) and fuel burnup level. (peak power location).

Figure 5.8 presents F_g as a function of the fuel pellet radius and the burnup level. From the figure, it is observed that in the inner region of the fuel pellet, fission gas retention in fuel microstructure is minimal, due to the high ambient fuel temperatures. In the outer pellet region, F_g attains higher magnitude due to reduced steady-state fission gas release at low temperature. As observed in Table 5.4, the radial melt extent ($\% R/R_o$) ranges from 74 % to 82 %, for 1-7 atom percent, respectively. Consequently,

when melting advances to the outer pellet region, the factor F_g in Eq. (3.47) increases.

This results in a greater variation in S_g as compared to S_f with respect to burnup level.

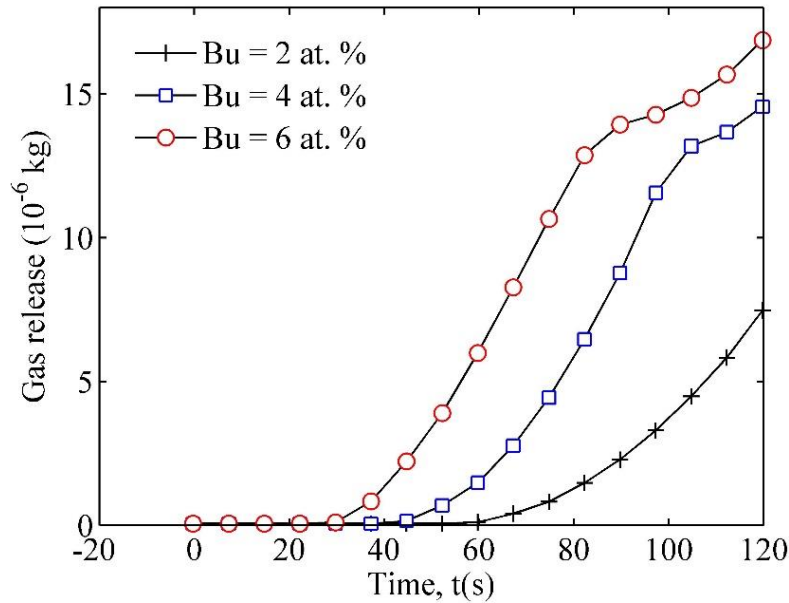


Figure 5.9: The release of fission gases due to melting as a function of transient time and peak fuel burnup.

Figure 5.9 presents the transient gas release during UTOP as a function of burnup level and time. It is observed that the slope of the release curves is minimum at the beginning. This is a consequence of the incorporation of the radial variations in F_g via the FGR solver. Since the magnitude of F_g is least at the pellet inner surface, the rate of gas release is correspondingly decreased. With further melting, the slopes of the curves continuously increase, due to the increased magnitude of F_g in the outer pellet regions (Figure 5.8). It is also found that with increasing burnup levels, the slopes of the curves tend to increase. From the above result, it is deduced that the case study with 7 atom percent burnup represents the maximum transient gas release rate, which corresponds to the highest fission gas pressurization force. Using the above-described transient fission gas release characteristics, the microstructural mechanisms responsible for the

fission gas pressurization forces are appropriately addressed. The effects of these forces on the melt displacement are addressed in the next section.

5.1.2.3 Effect of fission gas pressurization on melt hydrodynamics and relocation

The main purpose of the present study is to determine the realistic impact of fission gas pressurization on the melt motion, under the entire range of fresh to intermediate levels of fuel burnup, that may exist inside a fast reactor core. To fulfill this purpose, first the melt motion is presented as a function of the fuel burnup (Bu , atom percent) and melt mass fraction (%) in Table 5.5 [98].

The table breaks down the melting and motion behaviour into a set of numerical parameters, so that the variations can be quantitatively tracked across the range of fuel burnup levels. The power level ($\% P/P_n$) at which the respective melt fraction is achieved is also mentioned. The fuel volume fraction (averaged within the melt column, $(\alpha_{f,col})$), length of the melt column (Δz_{col}), elevation of the melt column center (z_{col} , from BFC) and ρ_{rel} obtained for Zone-I from Eq. (2.10) are detailed. Blank entries in the table indicate that the corresponding amount of melting did not occur. The simulation for fresh fuel ($Bu = 0$ atom percent) represents melt motion in the absence of the fission gas pressurization force, whereas the simulation for intermediate burnup ($Bu = 7$ atom percent) represents melt motion in the presence of highest gas release and pressurization force (Refer Section 5.1.2.2). It may be noted that in the present study, burnup and space dependent variations in the gas release fraction (Fr), fuel thermal conductivity (K_f), gap conductance (h_{gap}) and plenum pressure (P_{pl}) are also taken in account, based on the methodology of the MITRA algorithm (Refer Section 5.1.1.6). The following major observations are drawn from Table 5.5:

Table 5.5: Melt motion as a function of the melt mass fraction and fuel burnup.

<i>MMF</i>	<i>Bu_{max}</i> (at. %)	0	1	2	3	4	5	6	7
5 %	P/P_n (%)	171	185	168	159	152	147	143	139
	$\alpha_{f,col}$	0.93	0.98	0.93	0.91	0.95	0.95	0.95	0.96
	$\Delta z_{col,m}$	0.07	0.10	0.10	0.13	0.10	0.10	0.13	0.13
	$z_{col,m}$	0.62	0.63	0.63	0.65	0.67	0.63	0.65	0.65
	$T_{f,max}$ (°C)	3164	3332	3279	3267	3257	3236	3224	3201
	$\rho_{reloc,pcm}$	-0.43	-0.43	-0.43	-0.37	-0.30	-0.29	-0.35	-0.36
	10 %	P/P_n (%)	183	196	178	168	160	155	151
$\alpha_{f,col}$		0.95	0.98	0.97	0.95	0.99	0.97	0.96	0.97
$\Delta z_{col,m}$		0.27	0.27	0.23	0.27	0.23	0.27	0.27	0.27
$z_{col,m}$		0.58	0.62	0.63	0.65	0.63	0.65	0.65	0.65
$T_{f,max}$ (°C)		3517	3674	3586	3577	3522	3480	3434	3411
$\rho_{reloc,pcm}$		-1.47	-1.01	-0.86	-0.77	-0.59	-0.60	-0.58	-0.57
15 %		P/P_n (%)	189	205	186	175	168	163	158
	$\alpha_{f,col}$	0.89	0.98	0.98	0.98	0.98	0.98	0.98	0.99
	$\Delta z_{col,m}$	0.43	0.40	0.40	0.40	0.37	0.37	0.37	0.37
	$z_{col,m}$	0.67	0.65	0.65	0.65	0.67	0.67	0.67	0.67
	$T_{f,max}$ (°C)	3874	3961	3837	3769	3751	3723	3672	3656
	$\rho_{reloc,pcm}$	-1.48	-1.19	-1.14	-1.07	-0.93	-0.98	-0.85	-0.86
	20 %	P/P_n (%)	196	214	194	182	175	169	164
$\alpha_{f,col}$		0.98	0.98	0.99	0.99	0.99	0.99	0.99	0.99
$\Delta z_{col,m}$		0.47	0.50	0.50	0.50	0.47	0.47	0.47	0.47
$z_{col,m}$		0.65	0.67	0.67	0.67	0.68	0.68	0.68	0.68
$T_{f,max}$ (°C)		4023	4173	4057	3973	3942	3894	3842	3836
$\rho_{reloc,pcm}$		-1.95	-1.69	-1.42	-1.13	-1.09	-1.08	-1.00	-0.97
25 %		P/P_n (%)	204	-	201	189	181	175	170
	$\alpha_{f,col}$	0.99	-	0.99	0.99	0.99	0.99	0.99	0.99
	$\Delta z_{col,m}$	0.57	-	0.63	0.60	0.60	0.60	0.60	0.60
	$z_{col,m}$	0.67	-	0.70	0.72	0.72	0.72	0.72	0.72
	$T_{f,max}$ (°C)	4305	-	4180	4126	4075	4029	3980	3980
	$\rho_{reloc,pcm}$	-2.84	-	-1.67	-1.63	-1.69	-1.55	-1.40	-1.30
	30 %	P/P_n (%)	210	-	208	196	187	181	176
$\alpha_{f,col}$		0.99	-	0.99	0.99	0.99	0.99	0.99	0.99
$\Delta z_{col,m}$		0.63	-	0.73	0.73	0.73	0.73	0.73	0.70
$z_{col,m}$		0.70	-	0.75	0.75	0.75	0.75	0.75	0.73
$T_{f,max}$ (°C)		4441	-	4343	4252	4195	4151	4113	4110
$\rho_{reloc,pcm}$		-2.92	-	-2.74	-2.53	-2.43	-2.34	-2.23	-2.08

- i. The over-power required for arriving at a given melt mass fraction reduces with increasing burnup level, except for slightly burnt fuel (1 at. %). This is a result

of the decrease in fuel thermal conductivity with increasing burnup [79]. On the contrary, the rise in overpower in case of 1 atom percent fuel is due to (a) absence of steady-state, fission gas release at such low burnup and (b) reduction in the fuel pellet-clad gap width, which is a consequence of cracking and radial relocation of fuel pellets [126].

- ii. The length of the melt column is a strong function of the melt mass fraction and a weak function of the fuel burnup level. In addition, the averaged fuel volume fraction ($\alpha_{f,col}$) is close to unity at almost all points. This shows that the increase in transient fission gas release and the corresponding increase in the fission gas pressurization force do not impact the melt motion significantly, under typical UTOP conditions in annular mixed-oxide fuel pins.
- iii. Within the range of analysis ($Bu_{max} = 0 - 7 \text{ at. } \%$, melt mass = 0 – 30 %), the melt column continues to remain centered below the core mid-plane ($z_{col} < z_m$). However, the centre comes closer to the core mid-plane ($z_m = 0.8 \text{ m}$) with increasing melt mass. This is due to the upward growth of the melt column.
- iv. The maximum temperature ($T_{f,max}$), located inside the melt column near the peak power position ($z = 0.77 \text{ m}$), increases with the melt mass and the power level.
- v. The melt relocation feedback, evaluated with respect to Zone-1, is negative in all the cases ($\rho_{reloc} < 0$). Magnitude of the feedback is a strong function of the melt mass. It is higher for low burnup fuel as compared to high burnup.

Through these observations, the major findings are as follows:

- i. The fission gas pressurization forces are unable to influence the melt motion in a significant manner.

- ii. The tendency of the melt to agglomerate slightly below the core mid-plane remains unchanged, despite the changes in the transient fission gas release. Therefore, for all burnup levels, the melt motion essentially resembles the motion of fresh fuel, in which transient fission gas release is absent.
- iii. Gravity is the driving force responsible for the downward relocation of the melt. Viscous forces originating from the inter-molecular cohesion of partially solidified fuel restrict the relocation.
- iv. A favourable reactivity feedback emerges from both the downward melt relocation and thermal expansion of liquid fuel under high temperature. The feedback magnitude continues to increase with the level of overpower.
- v. The decreasing trend in the required power level with Bu is due to the reduction in thermal parameters (K_f, h_{gap}). More melting is likely to occur in a shorter period for high burnup fuel.

Observing the melt column position as a function of fuel burnup and melt mass fraction provides a clear picture of the sensitivity (Refer Fig. 5.10). The top ($z_{col} + 0.5\Delta z_{col}$) and bottom ($z_{col} - 0.5\Delta z_{col}$) locations reflect the growth of the melt column. At any melt fraction, the melt occupies the lower-most position in case of fresh fuel ($Bu = 0 \text{ at. \%}$). The physical origin of this variation lies in the restrictive particle viscosity, which depends on the wall-fluid surface interaction temperature ($T_{w,i}$) (Figure 5.11). In the region below the melt column, $T_{w,i}$ is significantly higher for fresh fuel as compared to burnt fuel. This deviation originates from the case-wise changes in the gap conductance (Refer Section 3.1.11). Eq. (3.11) predicts a correspondingly higher wall heat flux on entry of melt in this region.

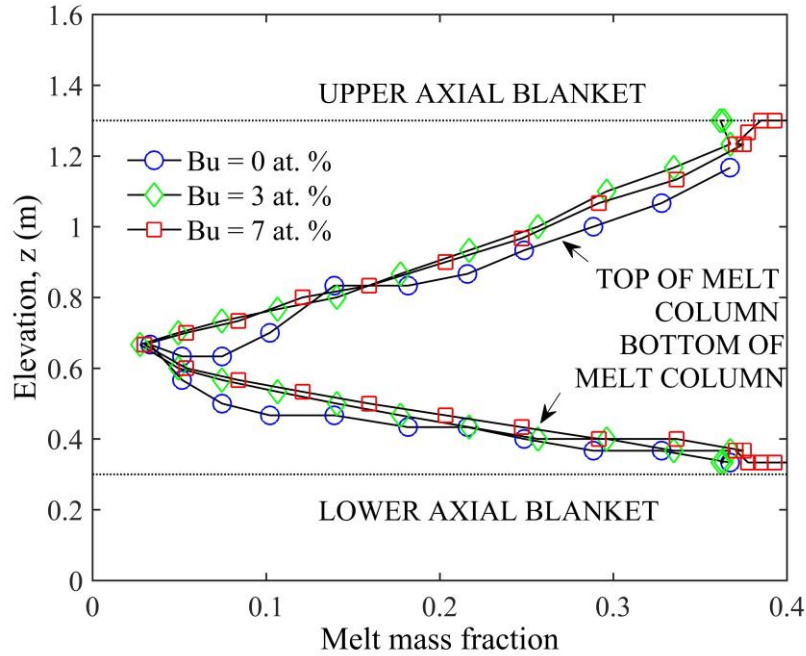


Figure 5.10: Evolution of the melt column as a function of the melt mass fraction and peak fuel burnup. Melt occupies the region between the top and bottom curves. (Core mid-plane is located at $z = 0.5 \text{ m}$)

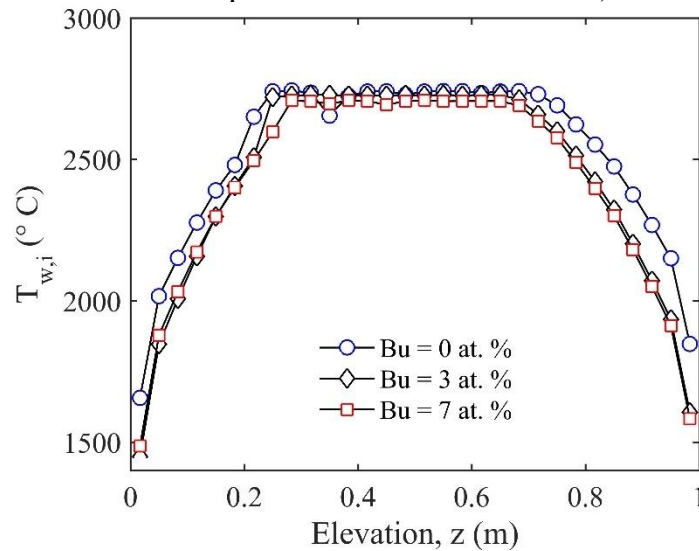


Figure 5.11: Pellet inner surface temperature ($T_{w,i}$) as a function of z and Bu_{max} . Each plot represents the temperature when melt mass = 5 %. The region occupied by melt is indicated by the flat profile (Elevation is with respect to z_b).

The resultant rise in melt temperature (T_f) implies a reduced viscous resistance, in line with the particle viscosity model [112] (Refer Eq. (3.25)). Consequently, the melt travels further downward. The results indicate a moderate sensitivity of the melt relocation with respect to the change in fuel burnup, due to the associated change in

thermal parameters. Therefore, it is concluded that the fundamental nature of melt displacement is equivalent for all fuel burnup levels and can be summarized by the schematic presented in Fig. 5.12.

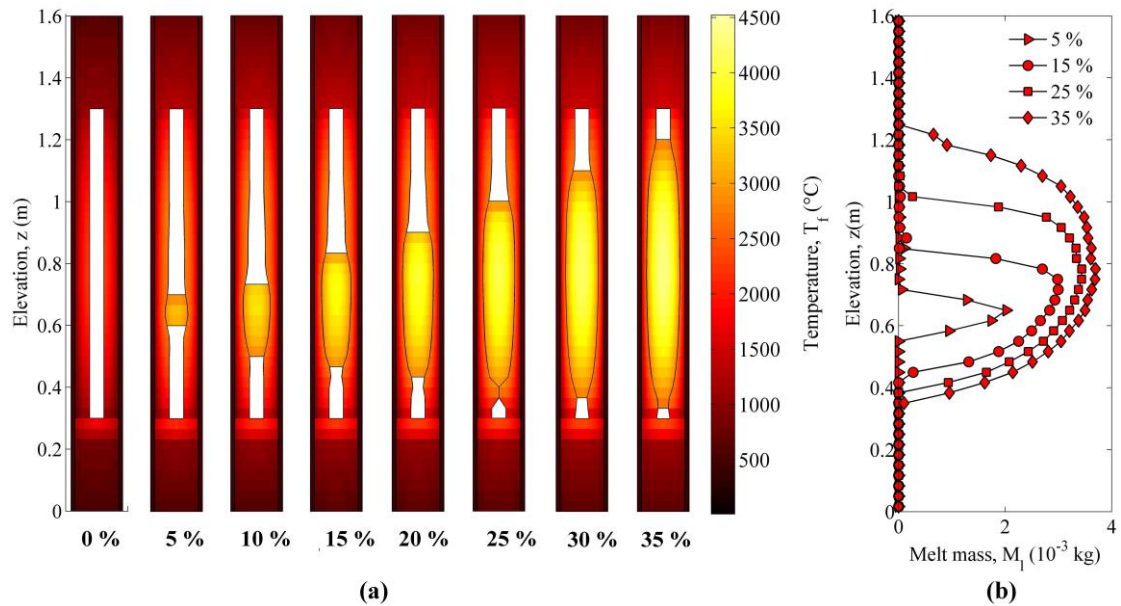
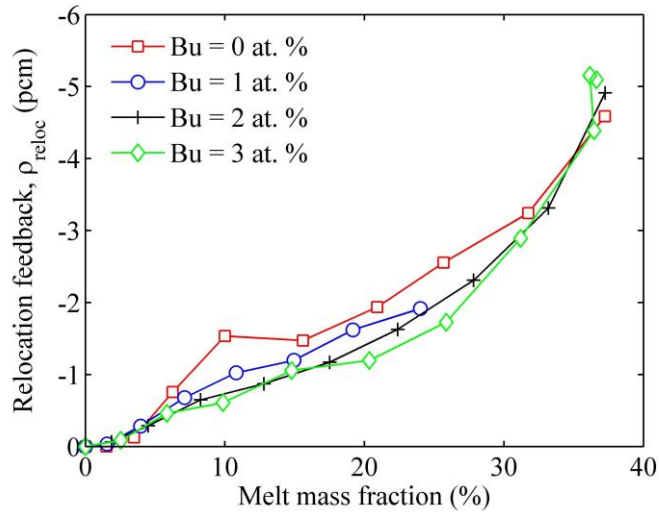
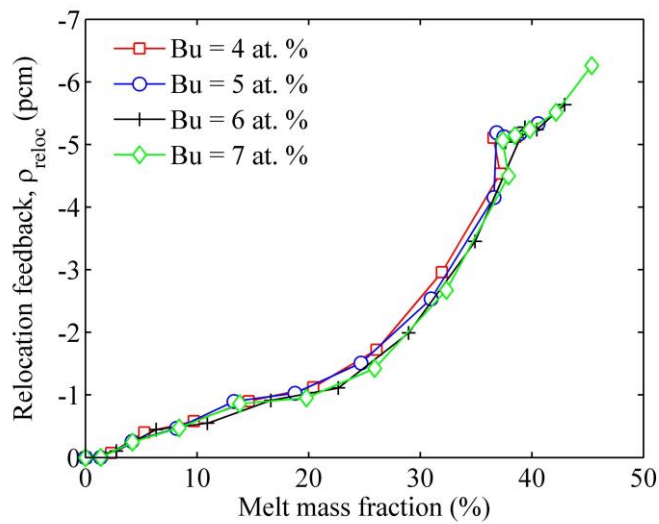


Figure 5.12: A generalized schematic of in-pin fuel motion in SFR conditions. (a) Thermal mapping of the fuel pellet stack during various stages of melting (0, 5, ... 35 % denote the melt mass fractions; pellet radius is exaggerated for clarity) (b) Axial variation of molten fuel mass (M_l) inside the cavity. (fuel mass = 0.225 kg/pin).

To illustrate the effect of the present modelling efforts on the melt relocation, the melt relocation reactivity feedback plots for the above case studies are presented in Fig. 5.13. Due to the above-described downward relocation in case of fresh fuel, the removal of fuel from the central region is also maximum. Therefore, up to 10 % melt mass fraction, the magnitudes of the melt relocation feedbacks are highest for fresh fuel. The above trend is clearly reflected in the feedback curves presented in Fig. 5.13a. On the other hand, ρ_{rel} magnitudes tend to converge for equilibrium and intermediate burnup values (Refer Fig. 5.13b), which is essentially a consequence of gap closure during transient heat-up and melting.



(a)



(b)

Figure 5.13: Melt relocation feedback as a function of fuel burnup and melt mass fraction (a) 0–3 atom percent (b) 4–7 atom percent (fuel mass removal worth analyses are constrained to central subassembly, $W_{max} = -41$ pcm).

It can be noted that the feedback trends presented in Fig. 5.13 are a reversal of the trends presented earlier in Chapter 3 of this thesis (Figure 3.14). Earlier, the equilibrium fuel had exhibited a significant downward melt motion, resulting in a greater feedback greater magnitude as compared to BOL case study. As discussed earlier, the difference between the accident conditions of the present study and Chapter 3 is the utilization of a uniform axial power profile for fresh as well as burnt fuel. It is deduced that this change is responsible for such a reversal.

5.1.2.4 Effect on whole-core melt propagation

The results of whole-core numerical simulations of UTOP have been presented earlier in Chapter 4. However, the multi-phase flow model employed in the earlier simulations utilized an empirical correlation for fission gas release [12] and assumed a constant F_g along the radius of the fuel pellet (Refer Section 3.1.10). From the results of the present study, the radial variations in F_g are substantial $\left(\frac{F_g|_{r=R_o}}{F_g|_{r=R_i}} \cong 60\right)$. Therefore, whole-core simulation of UTOP in the equilibrium core condition is performed with the present algorithm, to investigate the effects of the radial variations in the gas retention coefficient (F_g) on the whole-core melting and propagation behaviour. The BOL core is not studied since transient fission gas release is absent in fresh fuel. The simulation is performed for a conservative, unprotected withdrawal of a control rod in the equilibrium core. Therefore, the details of the simulation (for e.g., fuel specifications, methodology, accident parameters, delayed neutron fractions, reactivity feedback assumptions) are identical to the Case study III presented in Chapter 4 and are not repeated here to maintain brevity. The subassembly distribution, coolant mass flow rates, power distribution and fuel removal mass worth for the fuel channels of a typical sodium cooled fast reactor are detailed in Table 2.3 and Table 2.5 [82].

Figures 5.14 and 5.15 summarize the response of the equilibrium core (Zones 1-7) [98]. Melting initiates in the first, second, third, fourth and fifth zones due to relatively higher power as compared to other zones. Melt fractions in Zones 1, 2, 3, 4 and 5 reach up to 19, 12, 9, 1 and 5 %. The resultant melt relocation feedback limits the power excursion to 183 % by 200 s and reduces it further to 175 % (750 s). The feedback

response in Zone-2 is largest due to the respective fuel mass removal worth magnitude and greater amount of melting as compared to Zone-3 and Zone-5.

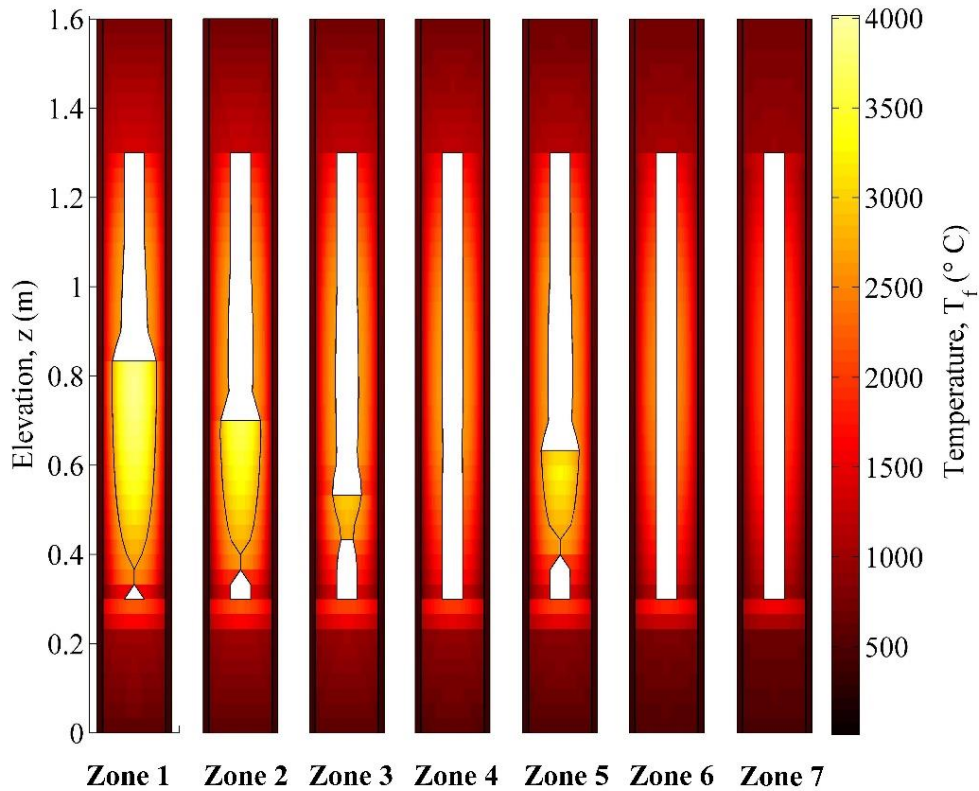


Figure 5.14: Thermal mapping of FBR core (equilibrium state) subjected to UTOP ($t = 750$ s); Zone 1, 2, 3 and 5 undergo fuel melting. Maximum melting occurs in Zone 1 (central subassembly).

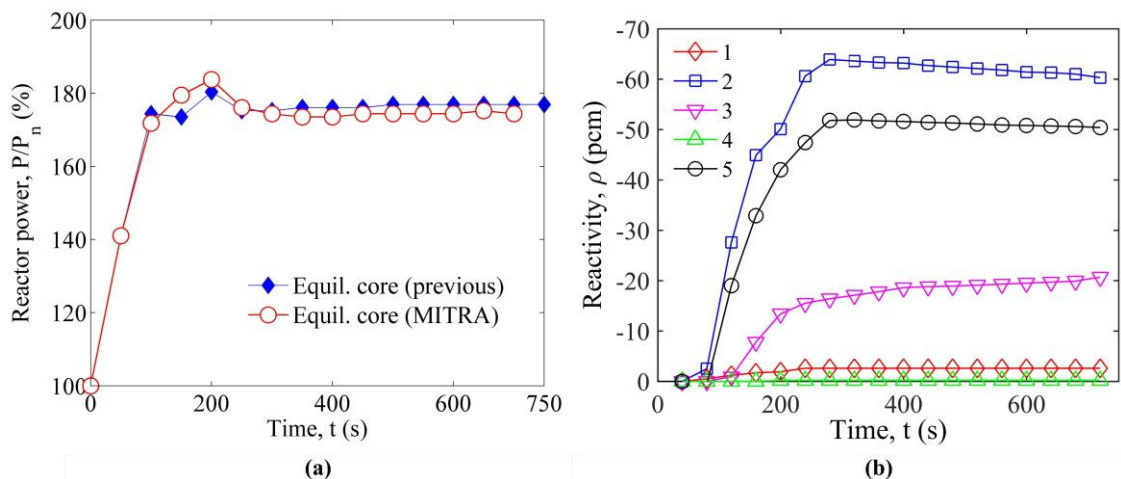


Figure 5.15: Reactor response a function of time (a) Reactor power history (b) Relocation feedback for zones (1-5). (Equilibrium core (previous) represents results where radial variation in gas retention is neglected; Equilibrium core (MITRA) represents results where the radial variation is incorporated)

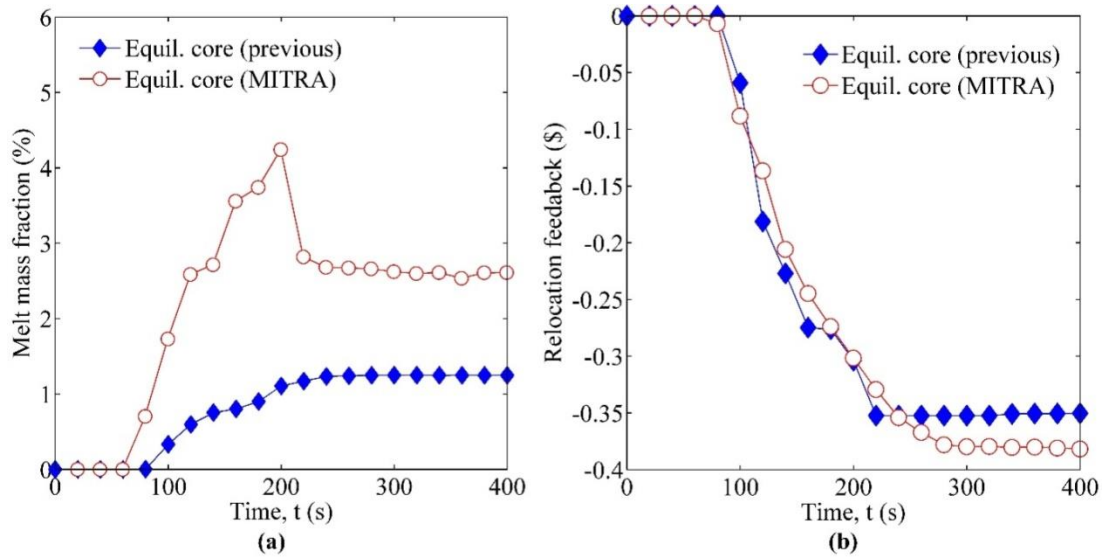


Figure 5.16: Comparison between earlier and current UTOP simulations; (a) Core averaged melt fraction history (b) Whole core melt feedback history.

Figures 5.16a, 5.16 present a comparative analysis of the present and earlier reactor core responses. There is a rise of $\sim 1.4\%$ in the stabilized value of the core averaged melt mass fraction. Similarly, the peak power has risen by 3% ($t = 200\text{ s}$). While melting had remained confined to zones 1, 2 and 5 in the earlier study, it is now spread to five innermost zones (118 subassemblies). These changes are the result of reduction in the melt relocation feedback (of the whole core) for an extended period (Refer Fig. 5.16b, $t = 110 - 180\text{ s}$). From a comparison of the current and previous reactivity feedback characteristics, it is deduced that the above reduction in the melt relocation feedback is caused by a slower, downward displacement of melt with the current model (Figure 5.13a, Figure 3.14).

5.2 Modelling of melt motion in alternative geometrical designs

5.2.1 Mathematical and numerical modelling

As discussed earlier, the main objective of the present study is to investigate the possibility of melt relocation out of the active core through suitable axial blanket design modifications. The modelling required to represent such a phenomenon is best

described through the definition of an initial physical problem. Previous studies have reported the most optimal geometrical design for enhancing annular fuel squirting out of the active core [26]. The studies have reported maximum fuel squirting for the following arrangement: solid bottom blanket pellets/annular fuel pellets/annular upper blanket pellets and plenum). Therefore, to recreate similar geometrical conditions under UTOP, first the following problem definition is outlined:

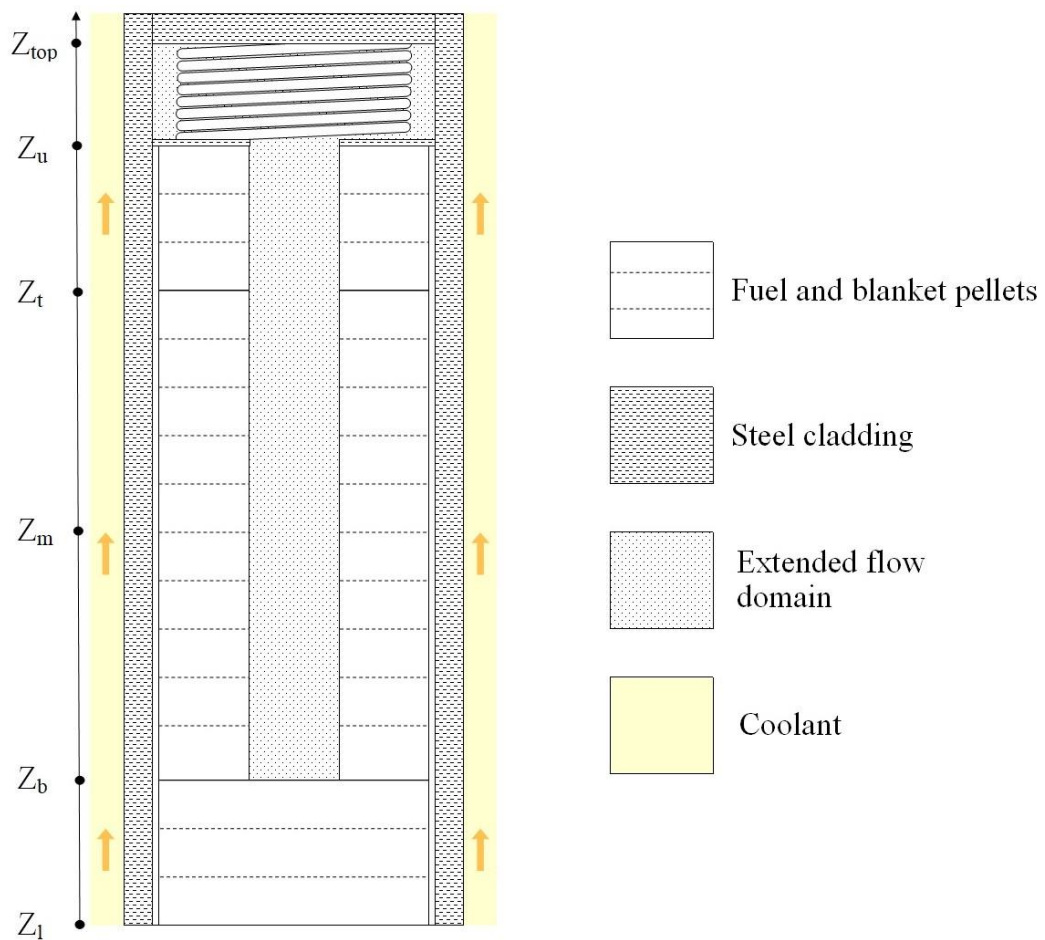


Figure 5.17: Problem domain.

5.2.1.1 Problem definition and assumptions

A typical mixed-oxide, fast reactor fuel pin consisting of annular pellets in the fuel column and solid pellets in both the top and bottom blankets is geometrically modified by introducing annular pellets in the top blanket column. Therefore, the multi-

phase flow domain now extends from the bottom-most fuel pellet up to the upper plenum, where it is closed by the top plug of the fuel pin. The inner and outer radii of the top blanket pellets are identical to the corresponding fuel pellet radii (Refer Fig. 5.17). Since melting initiates near the core mid-plane, along with the associated fission gas release, a negative pressure gradient is set up ($\frac{\partial P_{cav}}{\partial z} < 0$), resulting in an upward flow of fission gases. Consequently, the melt mass experiences pressure forces biased towards the upward direction along with other hydrodynamic effects.

Table 5.6: Geometrical parameters of the modified fuel pin.

Parameter	Sign	FBR-500 (Modified)
Fuel inner radius, mm	R _I	0.9
Fuel outer radius, mm	R _O	2.775
Top blanket inner radius, mm	R _{BI}	0.9
Top blanket outer radius, mm	R _{BO}	2.775
Bottom blanket inner radius, mm	-	0
Bottom blanket outer radius, mm	-	2.775
Inner clad radius, mm	R _{CI}	2.85
Outer clad radius, mm	R _{CO}	3.3
Fuel column length, m	L	1
Upper blanket column length, m	L _{UB}	0.3
Lower blanket column length, m	L _{LB}	0.3
Length of upper plenum	L _{UP}	0.2
Length of lower plenum	L _{LP}	0.71

From the schematic shown in Fig. 5.17, it is observed that a helical spring is present within the upper plenum. Material of construction is equivalent to the cladding steel (D9 steel). The spring will offer a minor resistance to the flow of the gas phase

until the surrounding temperature remains well below the steel melting temperature. For simplicity of treatment, it is assumed that there is no flow resistance due to the presence of the helical spring. For the sake of clarity, the numerical dimensions of the modified fuel pin are presented in Table 5.6. The thermophysical specifications remain identical to the earlier described FBR-500 fuel pin (Table 2.4).

5.2.1.2 Governing equations and boundary conditions

It is apparent that the mathematical model for the above presented problem requires modifications in the boundary conditions applicable to a typical annular fuel pin. The modified boundary conditions for the above problem are as follows:

$$K_f(T_f) \frac{\partial T_f}{\partial r} \Big|_{r=R_{int}} = \frac{(h_{w,f}A_{w,f}(T_{f,i}-T_{f,l})+h_{w,g}A_{w,g}(T_{f,i}-T_g))}{2\pi R_{int}} \quad (Z_t < z < Z_u) \quad \dots (5.15)$$

$$\frac{\partial v_i}{\partial z} \Big|_{z=Z_{top}} = 0, \quad q_i \Big|_{z=Z_{top}} = 0 \quad \dots (5.16)$$

$$K_c \frac{\partial T_c}{\partial r} \Big|_{r=R_{ci}} = \frac{(h_{w,f}A_{w,f}(T_{ci}-T_{f,l})+h_{w,g}A_{w,g}(T_{ci}-T_g))}{2\pi R_{ci}} \quad (Z_u < z < Z_{top}) \quad \dots (5.17)$$

From the above equation, the phase-specific heat transfer terms in Eq. (5.15) are utilized to replace the wall heat interactions terms in the energy conservation equations (Eq. (3.43–3.44)). The top-most flow boundary is shifted to the top of the upper plenum (Z_u). In case of alternative geometrical arrangements, modifications akin to the above equations are carried out for the lower plenum or the partially annular blanket columns. Furthermore, depending upon the geometry of blanket columns (completely annular/partially annular/completely solid), the wall-fluid interaction temperature ($T_{w,i}$) and contact area ($A_{w,i}$) are initialized. The expressions for the governing equations, remaining boundary conditions, closure terms, and wall-fluid contact areas have been detailed in Chapter 3 and are therefore not repeated for the purpose of brevity.

5.2.1.3 Incorporation of a bulk freezing model

The gradual entrance of molten liquid in a cold channel, with a temperature below the liquid's freezing point, is followed by the emergence of solid nuclei at the channel's inner surface. The nuclei grow into equiaxed crystals, which begin to grow radially inwards from the vicinity of the wall, resulting in the formation of a columnar zone known as the crust [57,133]. If the crust grows and covers the entire flow channel, the flow is considered as blocked due to solidification. However, if a completely solidified crust experiences a significant shear force exerted by the (still molten) liquid, it gets peeled from the surface of the cold wall and undergoes advection along with the melt in the form of a solid aggregate. From the experimental observations of the E9bis test, it is evident that such an aggregate (or bulk) motion would have occurred during the entry of molten fuel in the top blanket column (Refer Section 2.4.2). The temperatures of both the melt and blanket pellets are significantly smaller as compared to the solidus temperature at the point of entry (Figure 3.8), and the motion is laminar (is ~ 0.01 m/s [89]). Mathematically, these effects have been incorporated in Chapter 3 by the utilization of a particle viscosity expression, whereas the downward motion has been represented with a crust formation model. In the present study, the aggregate motion in both the upward and downward directions is incorporated through a bulk freezing model. In doing so, the crust formation model is replaced, since the breakage of crust cannot be represented with it. Furthermore, the freezing in both the upward and downward directions is represented by the introduction of a null velocity condition as follows:

$$\mu_f = \left\{ \begin{array}{l} V_f = 0 \quad (\alpha_p > \alpha_{p,max}) \\ \mu_f|_{T_{liq}} \left\{ (1 - \alpha_p) + \frac{f \alpha_{p,max} \alpha_p}{\alpha_{p,max} - \alpha_p} \right\}, \alpha_p = \frac{T_{liq} - T_f}{T_{liq} - T_{sol}} \quad (\alpha_p < \alpha_{p,max}) \\ 0.000988e^{4620T_f^{-1}} \quad (T_f > T_l) \end{array} \right\} \quad \dots (5.18)$$

In the above expression, if the fraction of solid particles exceeds the maximum allowable fraction ($\alpha_{p,max} = 0.62$), the viscosity increases rapidly [112]. This is mathematically captured by imposing a null velocity on the corresponding location. The value of $\alpha_{p,max}$ is consistent with the observations of Kamiyama [57]. The aggregate motion in cold regions (for e.g., annular blanket pellet) is represented by the prescription of flux corrections, based on the local mass conservation residual (Refer Section 3.2.2). With the above outlined approach, the bulk freezing model can accommodate the solid aggregate movement in both the upward and downward directions, under the effect of molten fuel thermal expansion. The present approach is distinct from the corresponding models available in literature since it incorporates the possibility of melt motion after the occurrence of bulk freezing.

5.2.1.4 Grid modifications

The details of the computational grid utilized for the present numerical simulations is presented in Table 5.7. The basic dimensions are based on the results of a grid sensitivity study presented in Chapter 3. To maintain a uniform axial grid throughout the extended multi-phase flow domain, the grid dimensions specific to the fuel column are applied to the blanket columns as well as the upper and lower plena. Therefore, a uniform mesh extends throughout the fuel and blanket pellets.

Table 5.7: Grid size details for the alternative fuel pin geometry.

Model region	Δr (mm)	Δy (mm)
Fuel column	0.0625	33.33
Top/bottom blanket column	0.0625	33.33
Upper/lower plenum		33.33
Fuel pellet cavity	-	33.33
Clad	0.15	33.33
Coolant	-	33.33

The clad and coolant domains are discretized with a corresponding mesh size to maintain numerical accuracy. Depending upon the fuel pin geometry, the plenum meshes can be activated or deactivated.

5.2.2 Results and Discussion

5.2.2.1 Validation of bulk freezing model

To validate the model, numerical simulation is performed for the E9bis test, employing the present model. Figure 5.18 shows the melt column evolution by utilizing bulk freezing model and compares it with the results of MITRA (Refer Section 5.1.2.1(c)). The time of complete occupation of the top-most fuel node with the bulk freezing model is 68.5 s, whereas the experimental time of penetration of the top blanket is 65 – 69 s.

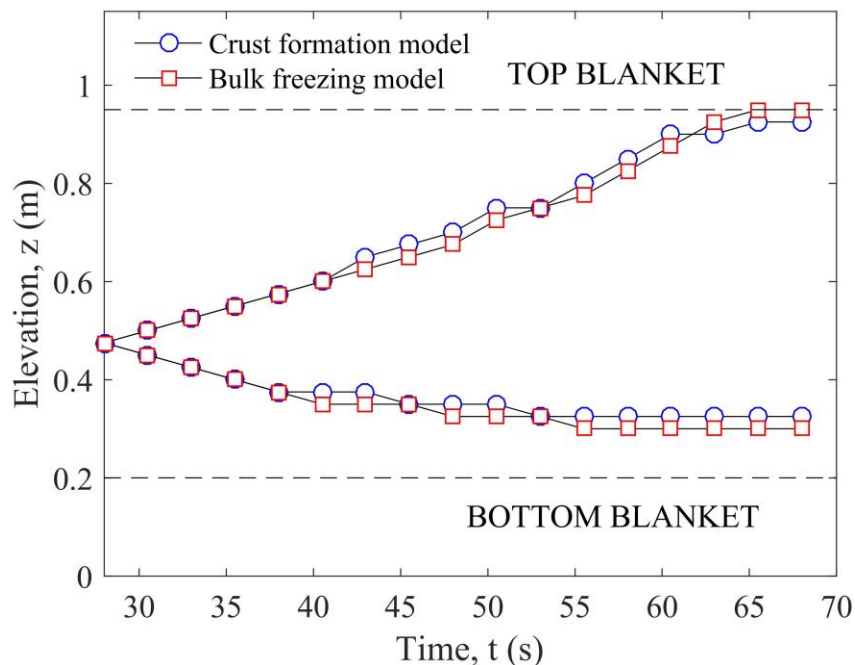


Figure 5.18: Comparison of the melt column evolution with the crust formation and bulk freezing models. Results are for E9bis test.

From Fig. 5.18, it is evident that the bulk freezing model can replicate the slow, downward motion of molten fuel caused by cyclic blockage and re-melting, which was

simulated by the crust formation model. Minor deviations emerge in the upper and lower column limits after $t = 40$ s, due to axial boundary modifications imposed by the crust formation model in case of flow blockage. However, the location of the column as well as the transient evolution of melting are equivalent for both models. In this context, it is important to mention that the crust formation model involves a laborious and time-consuming grid modification mechanism [77], which is not required with the bulk freezing model. Therefore, the present model is simpler and can be employed for similar applications with relative ease.

5.2.2.2 Effect of completely annular blanket column

Under the nominal annular fuel pin design, the melt relocation remains highly restricted due to the relative dominance of the viscous forces (of solidification) over the fission gas pressurization forces, which are dispersive by nature. The presence of high temperature within the molten fuel causes significant thermal expansion, resulting in extension of the melt column up to the top of the active core. Post-irradiation data of the CABRI tests indeed shows the presence of relocated fuel up to the top of the fissile column, where upward penetration is stopped by solid blanket pellets. However, if the blanket pellets are in a fragmented state prior to the test, fuel fills the gaps between the fragments [33]. This section presents the melt motion behaviour for the initial problem defined earlier in Section 5.2.1.1). The alternative geometry consists of annular pellets in the fuel and top blanket columns, with solid pellets in the bottom blanket column. All other fuel specifications and accident conditions are identical to Sections 5.1.2.2-5.1.2.3 for isolating the effects of geometrical modification. The effect of geometrical modification is presented in Fig. 5.19 and Fig. 5.20 [98].

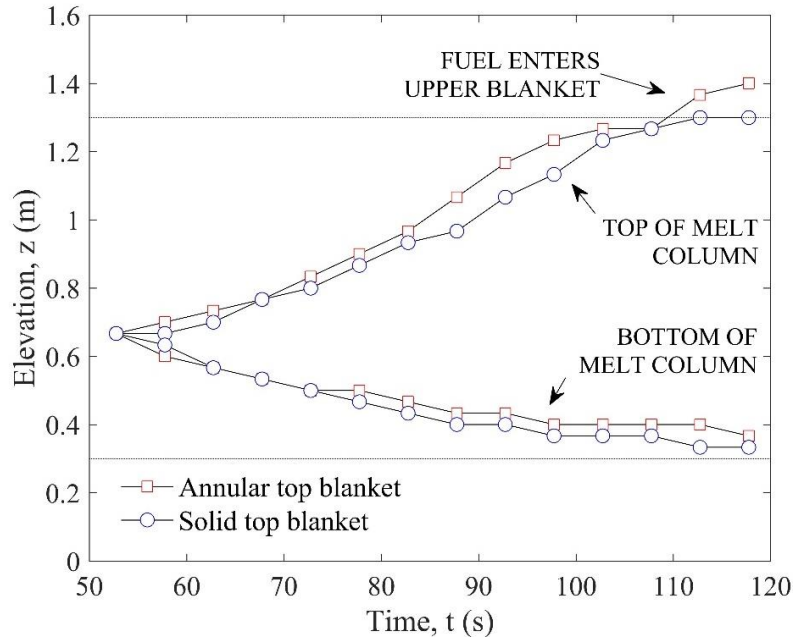


Figure 5.19: Sensitivity of melt relocation to geometric design variation (entry of fuel in annular top blanket occurs at melt fraction = 34.2 %).

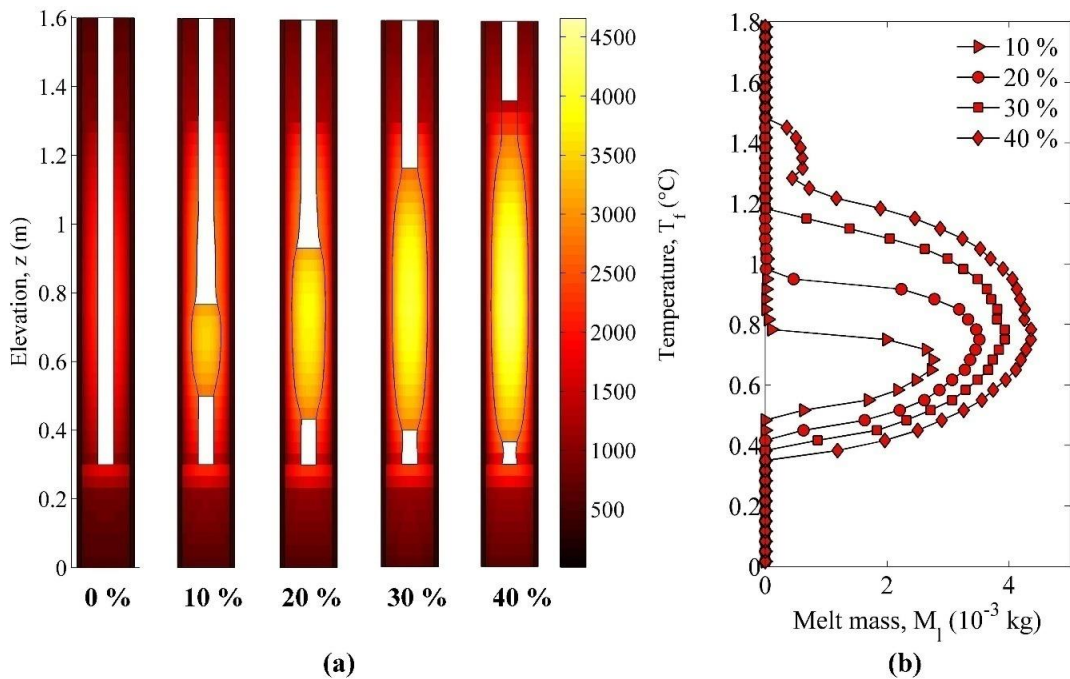


Figure 5.20: In-pin fuel motion in case of annular upper blanket pellets. (a) Thermal mapping of the fuel and axial blanket columns during various stages of melting (0, 10, ... 40 % denote the melt mass fractions). (pellet radius is exaggerated for clarity) (b) Axial variation of melt mass inside a single fuel subassembly ($z_t = 1.3 \text{ m}$).

As discussed earlier, the presence of an open pathway up to the top plenum leads to the generation of negative, axial pressure gradients at the site of melting (Refer

Section 5.2.1.1). Consequently, an upward shift appears in the melt column evolution, as shown in Fig. 5.19. A thermal map of the fuel pin under these circumstances is shown in Fig. 5.20. Melt freezing and the resultant viscous resistance continue to constrain the relocation. The melt behaviour remains unchanged up to 34.2 % melting, beyond which the melt column enters the top blanket.

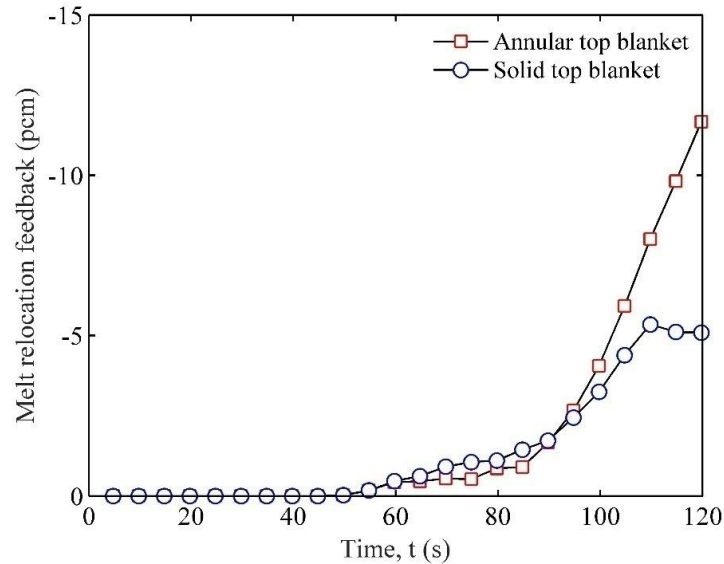


Figure 5.21: Sensitivity of the melt relocation feedback to geometric variation.

After a substantial amount of melting (~34.2 %), the melt relocates up to the top of the fissile column and enters the blanket region. Further rise in power leads to more melting and greater penetration of the blanket pellets. The relocation inside the blanket pellets occurs due to aggregate motion, driven by the thermal expansion of molten fuel. Therefore, the extent of fuel removal from the active core is an apparent function of the melt mass fraction, which is dependent on the reactor overpower. The melt does not enter the fission gas plenum, despite the presence of a direct flow pathway. Fuel removal from the fissile region immediately provides a substantial rise in the safety feedback (Figure 5.22).

Note that in the transient overpower tests conducted in the CABRI reactor; annular pins exhibited a high threshold to failure [53]. Power rise up to 315 % in the

MF2 test, as well as melting up to 57 % in E9 test did not induce clad failure [33,34]. A 500 μm thick solid fuel layer separated the molten fuel and cladding near the peak power position (Refer Table 5.3, radial melt extent at $z = 0.37 \text{ m}$). Table 5.4 displays the maximum melt fractions and radial melt extent of the FBR-500 fuel pin up to 220 % transient power level. The data obtained at the end of overpower ($P = 220 \% P_n$; $t = 120 \text{ s}$) are well within the bounds of failure thresholds established in the CABRI tests. Moreover, the enhancement in safety feedback is found to occur much earlier ($P = 200 \% P_n$; $t = 100 \text{ s}$). Considering both failure threshold and top blanket penetration time, we find that the use of annular top blanket pellets gives rise to a substantial safety feedback once the melting crosses a threshold ($\sim 34 \%$). In a worst-case scenario, if this threshold is somehow breached, the rise in negative feedback will limit the power rise and prevent cladding failure. Therefore, such a geometrical design variation can be beneficial for the mitigation of a worst-case UTOP scenario.

5.2.2.3 Effectiveness of partially annular top and bottom blanket columns

From the results of the previous case study, it is evident that a significant enhancement occurs in the melt relocation feedback, even if the top blanket column is only partially occupied with relocated fuel (Figure 5.22). From Fig. 5.19, it can be observed that the influence of the biased fission gas pressurization on the melt motion is negated to a large extent by restrictive effects of solidification. Therefore, the provision of a direct opening between the fuel cavity and fission gas plena does not impact the relocation appreciably. Since the incorporation of annular blanket pellets has a corresponding impact on the efficacy of breeding, a more optimized blanket design is needed to improve the safety margin without affecting the breeding significantly.

To fulfill the above purpose, six modified annular pin geometries with a variable number of annular pellets in the top and bottom blankets are investigated to examine the effectiveness of melt relocation out of the active core. Among these, three pins comprise of 0.033, 0.066 and 0.1 m length cavities in the top blanket column with a fully solid bottom blanket column. The remaining three pins contain equivalent cavities in the bottom blanket column and a fully solid top blanket column. The blanket cavity acts as an extension of the annular fuel pellet cavity. Figures 5.22 and 5.23 present the simulation results of melt motion inside the above-described fuel pin geometries (top blanket modifications). It is observed that the total amount of fuel removal from the active core is a function of the melt mass fraction and length of annular blanket cavity (Z_{bl} , Refer Fig. 5.23). It is additionally observed that the upward shift in the melt column extension in case of direct opening ($Z_{bl} = 0.3 \text{ m}$) does not result in an earlier penetration of the blanket column, as compared to the closed cases.

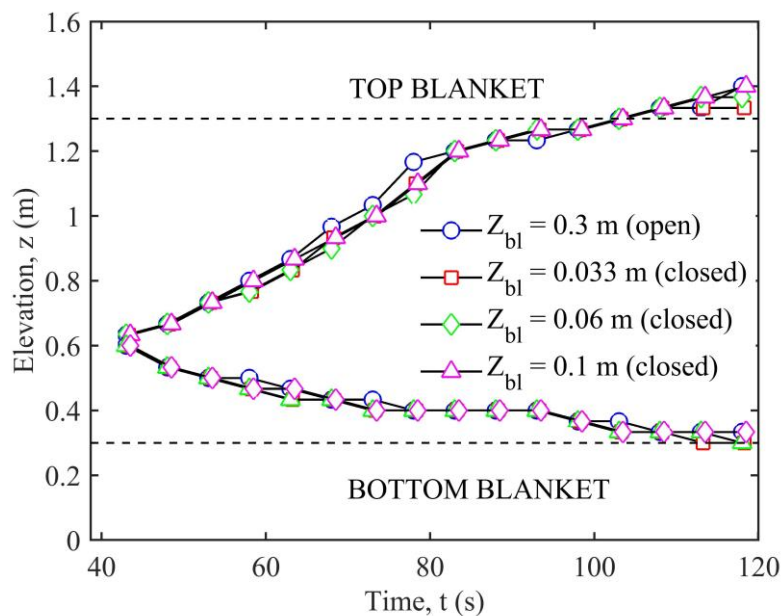


Figure 5.22: Melt column evolution as a function of the top blanket geometry (Z_{bl} = length of top blanket cavity).

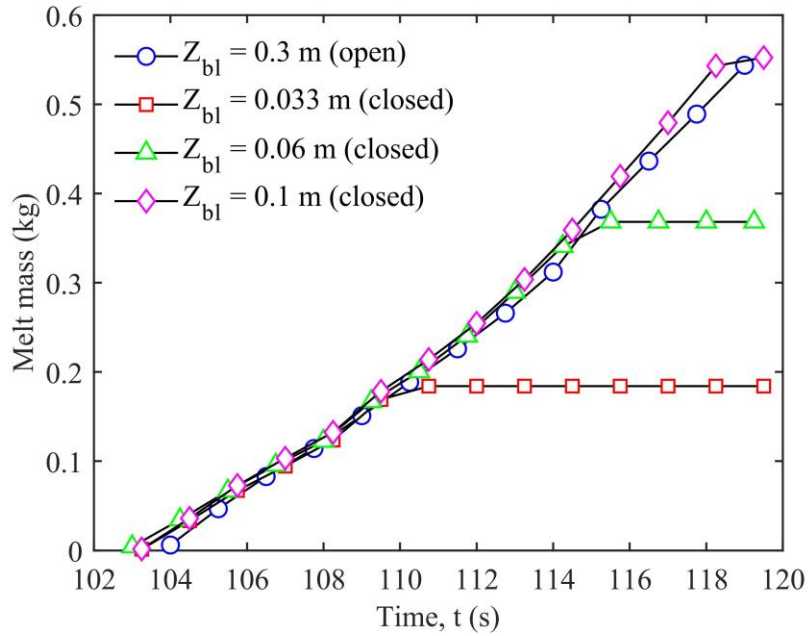


Figure 5.23: Fuel relocation in top blanket column as a function of top blanket geometrical design (melt mass is specific to central subassembly; total fuel mass is 48.8 kg).

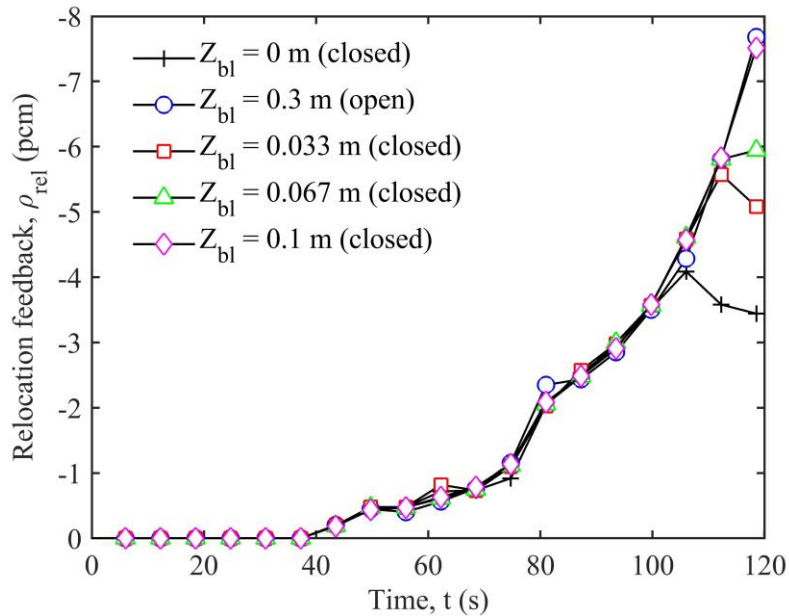


Figure 5.24: Melt relocation feedback as a function of top blanket geometrical configuration and time.

The pin with ~ 15 annular pellets ($Z_{bl} = 0.1 \text{ m}$) in the top blanket removes the same amount of fuel mass from the active core as the pin with fully annular top blanket ($Z_{bl} = 0.3 \text{ m}$). The pin with ~ 5 annular pellets ($Z_{bl} = 0.033 \text{ m}$) in the top blanket

removes comparatively smaller amount of melt mass (0.37 % of Zone-1). Improvements in the negative reactivity feedback range between 36-84 % ($Z_{bl} = 0.033 - 0.1 \text{ m}$) in comparison with the current annular fuel pin design ($Z_{bl} = 0 \text{ m}$; Refer Fig. 5.24). From these results, it is concluded that a minimal number of annular blanket pellets situated next to the fuel pellets can be an effective and optimal choice for relocating fuel out of the active core. The optimal number of annular blanket pellets can be determined based on the desired improvement in the safety margin.

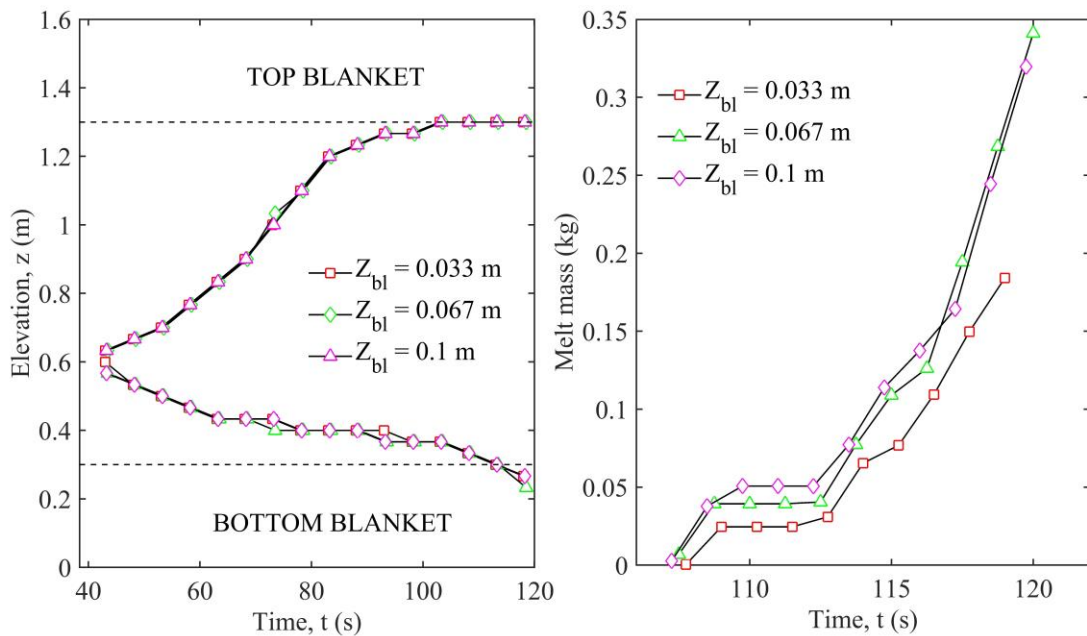


Figure 5.25: Simulation results for partially annular bottom blanket case studies. (a) Melt column evolution. (b) Mass of fuel removed from the active core (melt mass is specific for the central subassembly).

Figure 5.25 presents the melt motion behaviour for the partially annular bottom blanket geometries. Basic characteristics of melt motion in these cases are analogous to the above presented results (Figure 5.22-5.23). However, it is found that fuel relocation out of the active core is considerably slowed down with the bottom blanket cases as compared to the top blanket cases. The results are consistent with the previous experimental studies on annular fuel squirting, which reported that the annular top blanket geometry was most optimal for obtaining maximum fuel relocation out of the

active core [26]. In a physical sense, the decrease in fuel removal for bottom blanket as compared to top blanket modification cases is a consequence of lower molten fuel temperature ($T_{f,t}$) near the bottom of the fuel column (2597°C) as compared to the top of the fuel-column (2708°C) (220 % P/P_n , $t = 120$ s). High coolant temperature at the top of the fuel column ($T_{ct} = 755^\circ\text{C}$, $t = 120$ s) ensures the above-mentioned difference in melt temperature, due to which aggregate motion is relatively easier near the top region.

5.3 Closure

In this chapter, an improved numerical algorithm (MITRA) is presented that can capture the physically consistent effects of fission gas pressurization force on the melt motion. The algorithm is validated against experimental results pertaining to the isothermal fission gas release tests (steady-state), FBTR mixed-oxide fuel irradiation test (steady-state), CABRI-E9 and E9bis tests (transient overpower), and numerical results of the FEAST-OXIDE code. To capture the effects of fission gas pressurization on melt motion under fast reactor accident (UTOP) conditions, the algorithm is utilized to simulate fuel melting and multi-phase flow under a range of burnup levels (0 – 7 atom percent). The sensitivity of accident outcome towards core condition (observed earlier in Chapter 4) is addressed with a consolidated, whole-core UTOP simulation for the equilibrium core (conservative), employing the present model. From the results, the following major conclusions are drawn:

- (i) Regardless of the burnup level, the fission gas release-induced pressurization force is unable to disperse the melt significantly, and the agglomerated melt column remains constrained by the effects of solidification.

- (ii) The fundamental nature of melt motion remains unchanged for all fuel burnup levels, including fresh fuel, in which transient fission gas release is absent.
- (iii) A negative reactivity feedback emerges for all fuel burnup levels with the improved algorithm, due to downward relocation driven by gravity and melt thermal expansion at high temperature.
- (iv) The melt motion exhibits a moderate sensitivity towards change in fuel burnup, due to the associated change in thermal parameters.
- (v) An increase in the whole-core melt propagation occurs in the equilibrium core, upon employing the present model. The stabilized, core-averaged melt mass fraction is $\sim 2.6\%$, as compared to the earlier assessment ($\sim 1.2\%$).

As a second illustration, the model is utilized to investigate the possibility of fuel relocation out of the active core through suitable axial blanket design modifications. For a consistent representation of melt penetration in annular blanket pellets, a bulk freezing model is incorporated in the model framework. Using the resultant algorithm, simulations are performed for the E9bis test. The results are compared with the test data as well as the results of the previous algorithm (MITRA), and the level of agreement is excellent. The validated algorithm is subsequently utilized towards the numerical simulation of melt motion in a modified fuel pin consisting of a completely annular top blanket column. Furthermore, the study is extended to alternative axial blanket configurations with a variable number of annular pellets in both the top and bottom blanket columns. From the results, the major conclusions are as follows:

- (i) The presence of an opening between the pellet cavity and gas plenum does not lead to a rapid fuel squirting under typical UTOP accident ($\sim 1 - 5\text{ pcm/s}$), as the melt motion remains constrained by the effects of freezing.

- (ii) However, once melting exceeds a threshold, fuel relocates out of the active core region, because of the continuous growth of the melt column inside the pellet cavity.
- (iii) The threshold melt mass fraction is 34 % for FBR-500 annular fuel pin, and 26 % for the OPHELIE-6 fuel pin irradiated in Phénix reactor.
- (iv) The mass of fuel relocated out of the active core is a function of the amount of melting, which in turn is a function of the reactor power level.
- (v) The entry of molten fuel in the blanket column gives rise to a substantial enhancement in the negative reactivity feedback magnitude (36-84 %).
- (vi) The provision of a minimal number of annular blanket pellets (~ 5–15) situated next to the annular fuel pellets can be an effective and optimal choice for relocating fuel out of the active core and enhancing the negative reactivity feedback.
- (vii) The provision of a few annular pellets in the bottom blanket can also provide the desired removal of melt from the active core. However, the removal is slowed down by melt freezing near the bottom of the fuel column.

The study has established that the impact of fission gas pressurization force on molten fuel hydrodynamics in case of annular fuel is insignificant during UTOP. A much simpler model for capturing the effects of fuel freezing has been presented, which does not require complicated grid modifications. Furthermore, the study has predicted an advantageous melt relocation out of the active core by employing suitable geometrical changes. The benefits of this relocation can be obtained by providing a few annular axial blanket pellets next to the fuel pellets. The next chapter concludes the key outcomes of the research work and describes the future scope of work

Chapter 6

Concluding Remarks and Future Work

6.1 Conclusions

The main objective of this thesis has been to systematically investigate the melting and relocation of annular, mixed oxide ((U-Pu)-O₂) nuclear fuel during UTOP in sodium-cooled fast reactors. Emphasis has been placed on capturing the complex interaction of hydrodynamic forces, including the pressure forces generated due to transient fission gas release, as well as addressing the realistic impact of melt relocation on reactor safety. A mathematical model has been developed that adequately resolves the hydrodynamics of in-pin fuel motion and supplements the experimental findings of the CABRI test reactor. An excellent validation of the model against the benchmark test data is achieved. Experimentally consistent predictions of in-pin fuel motion under SFR conditions are reported using the developed model. Results have shown that essentially, there is a net relocation of molten fuel from the highest neutron density region (around the core-mid plane) to relatively lower neutron density regions (i.e., the top and bottom regions of the fissile column), which averts an undesirable increase in fuel mass near the core mid-plane. The motion has been found to be advantageous towards the inherent safety of SFR. A numerical algorithm has been presented to address the intrinsic coupling between the hydrodynamics and reactor dynamics of in-pin fuel motion. A parallel computing technique with a suitable data-transfer period is selected to reduce the computational efforts. The findings from whole-core, numerical simulations of UTOP have revealed the nature of propagation of fuel melting in the SFR core and the dynamics of the melt relocation reactivity feedback. Major influencing parameters of this feedback are the whole-core melt mass fraction and core condition (beginning-of-

life or equilibrium). The potential of molten fuel vaporisation under UTOP conditions has also been brought out clearly.

A fission gas release model (FGR) has been developed to address the apparent sensitivity of the melt relocation reactivity feedback towards the core condition. The model has been incorporated with the thermal hydraulic framework, and the resultant algorithm (MITRA) is validated with steady-state and transient benchmark data. Results have shown that under a physically consistent representation, the effect of pressure forces on the melt motion remains insignificant as compared to the effect of melt freezing, due to which the melt motion is essentially similar for a wide range of fuel burnup levels (0 – 7 atom percent). The propagation of melting in the SFR core is found to increase in comparison with that of the earlier reported assessment upon utilizing MITRA for a consolidated whole-core simulation. Axial blanket design modifications are investigated to examine the possibility of fuel relocation from the fissile to the fertile region of the core, which is a highly desirable outcome from the perspective of SFR safety. A simple bulk freezing model is also incorporated to represent melt penetration in annular blanket pellets satisfactorily. Results have shown that in annular SFR fuel pins, the provision of a direct flow path between the fuel pellet cavity and gas plenum does not lead to the well-known squirting effect during UTOP. However, if a threshold amount of melting is breached, the melt can relocate from the fissile to the fertile region. It is concluded that the provision of a small number of annular blanket pellets situated next to the annular fuel pellets can be an effective and optimal choice for enhancing the inherent safety of SFR. Figure 6.1 gives a brief glimpse of the research work as well as its major outcomes.

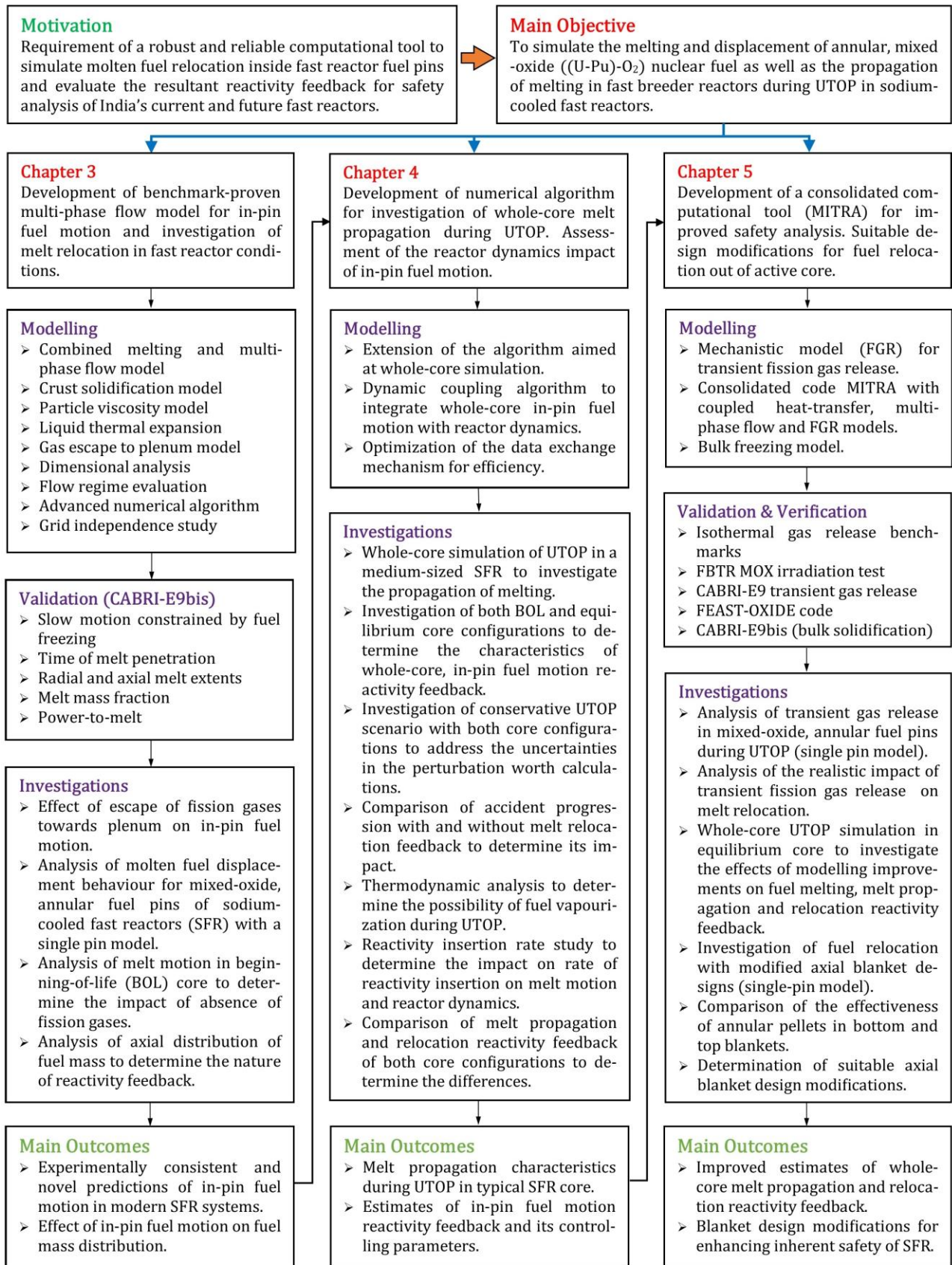


Figure 6.1: Summary and highlights of the thesis.

6.2 Scope for future work

During the validation studies, it was noticed that after a threshold level of melting (~ 27 % for CABRI-E9 and E9bis), the melt occupies the entire fuel pellet cavity, resulting in subsequent pressurization of the solid fuel pellets by means of liquid thermal expansion. Such a pressurization may result in a small amount of fuel squirting under extremely high overpower conditions (> 300 %), as evidenced in the CABRI-MF2 test. Furthermore, during steady-state irradiation and accident conditions, the fuel pellets and steel clad undergo both elastic and plastic deformations, due to pellet-clad mechanical interaction, creep, void swelling, transient fuel swelling, and thermal stresses, resulting in an associated impact on the fuel mass relocation characteristics. However, incorporation of these effects is not possible under the present modelling paradigm since the resolution of the associated mechanics requires a complex structural mechanics investigation of mixed-oxide fuel pins under upset conditions. For a better understanding of the process, these effects need to be addressed in detail in the investigations to follow. Coolant boiling and clad failure models need to be incorporated for investigations pertaining to the unprotected loss of flow accident. Intra-granular gas bubble coalescence models need to be incorporated for the representation of fission gas pressurization forces under rapid reactivity insertion rates. Models pertaining to Joint Oxide Grain (JOG) need to be included for an end-of-life (EOL) fuel pin simulation. Numerical instabilities in the code framework need to be investigated further using techniques such as the method of characteristics and linear stability analysis. A probabilistic analysis of MITRA is needed to quantify the uncertainties in code predictions.

Appendix A: Thermo-physical properties

This appendix details the thermophysical properties used in the calculations. For solid, mushy and molten phases of mixed oxide fuel, the correlations recommended by Carbajo have been incorporated [79]. All properties are in S.I. units. All temperatures are in Kelvin scale.

Mixed oxide fuel (U, Pu)O₂:

$$(T_f \leq T_{sol})$$

$$K_f(T_f, Bu, x, p) = 1.158 \left(\frac{1}{A+Ct} + \frac{6400}{t^2} e^{-\frac{16.35}{t}} \right) \mathbf{FD}(Bu, T_f) \mathbf{FP}(Bu, T_f) \mathbf{FM}(p) \mathbf{FR}(T_f) \quad (\text{A.1})$$

$$(T_f \geq T_{liq})$$

$$K_f(T_f, Bu, x, p) = 2.5 \quad (\text{A.2})$$

$$(T_{solidus} \leq T_f \leq T_{liq})$$

$$K_f(T_f, Bu, x, p) = (1 - o)K_f(T_{sol}, Bu, x, p) + oK_f(T_{liq}) \quad (\text{A.3})$$

$$\text{Here, } \mathbf{FD}(Bu, T_f) = \omega [\arctan(1/\omega)], \omega = \frac{1.09}{Bu^{3.265}} + 0.0643 \left(\frac{T_f}{Bu} \right)^{0.5}, \mathbf{FM}(p) = \frac{1-p}{1+2p},$$

$$\mathbf{FP}(Bu, T_f) = 1 + \frac{0.019Bu}{(3-0.019Bu)[1+e^{-(T_f-1200)/100}]}, \mathbf{FR}(T_f) = 1 - \frac{0.2}{1+e^{(T_f-900)/80}}, o =$$

$$\frac{T_f - T_{sol}}{T_{liq} - T_{sol}}, A(x) = 2.85x + 0.035, C(x) = (-0.715x + 0.286), t = \frac{T_f}{1000}$$

Expressions for the fuel specific enthalpy (H_f) are as follows [134–137]:

$$H_f(T_f, y) = (1 - y)H_{UO_2} + yH_{PuO_2} \quad (T_f < T_{sol}) \quad (\text{A.4})$$

$$H_{PuO_2} = H_{PuO_2}|_{T=T_a} + c_{Pu1} + c_{Pu2}t + c_{Pu3}t^2 + c_{Pu4}t^3 + c_{Pu5}t^4 + c_{Pu6}t^5 + c_{Pu7}t^{-1} \quad (\text{A.5})$$

$$H_{UO_2} = H_{UO_2}|_{T=T_a} + c_{U1} + c_{U2}t + c_{U3}t^2 + c_{U4}t^3 + c_{U5}t^4 + c_{U6}t^5 + c_{U7} \quad (\text{A.6})$$

$$H_f(T_f, y, o) = (1 - o)H_f(T_f, y)|_{T_f=T_s} + oH_f(T_f)|_{T_f=T_l} \quad (T_{sol} \leq T_f \leq T_{liq}) \quad (\text{A.7})$$

$$H_f = 2.977 \times 10^6 + 0.931T_f - 4.9215 \times \frac{10^9}{T_f} \quad (T_f > T_{liq}) \quad (\text{A.8})$$

$$T_{liq} = 3120.0 - 388.1y - 30.4y^2 - 5Bu \quad (\text{A.9})$$

$$T_{sol} = 3120.0 - 655.3y + 336.4y^2 - 99.9y^3 - 5Bu \quad (\text{A.10})$$

$$T_{int} = oT_l + (1 - o)T_s \quad (\text{A.11})$$

In the above equations $t = \frac{T_f}{1000}$; y is the mole-fraction of PuO_2 in mixed oxide fuel ($o = 0.2 - 0.5$); T_{sol}, T_{liq} are the solidus and liquidus temperatures, T_a is the room temperature (298.15 K). The latent heat of fusion is implicit in the enthalpy-temperature relationship (~ 248 KJ/kg). As an example, the temperature-enthalpy plot applicable towards FBR-500 inner core is shown in Fig. A1.

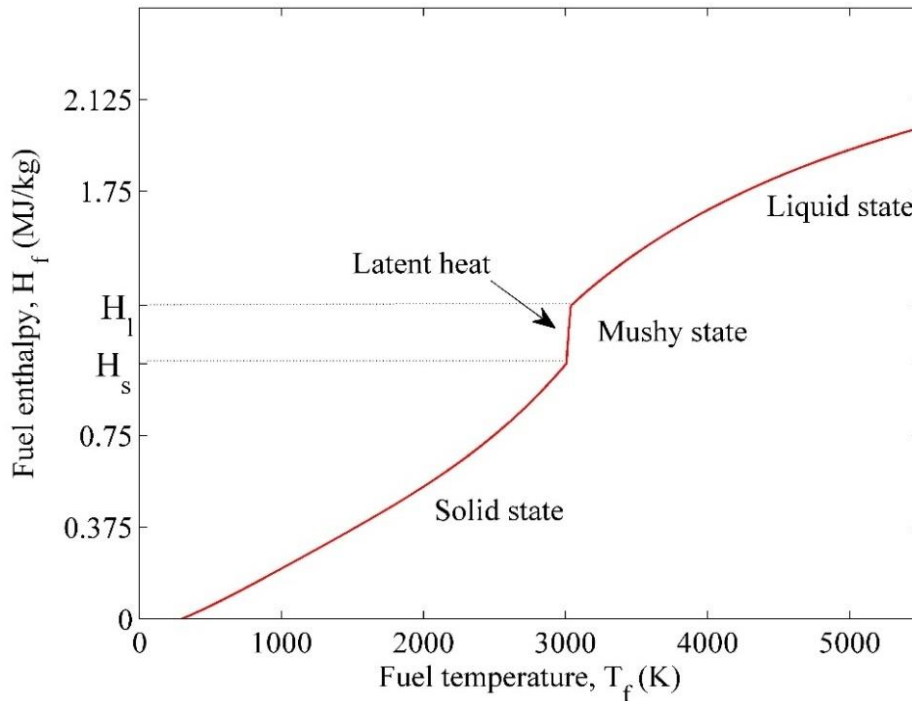


Figure A1: Enthalpy versus temperature plot for mixed oxide fuel. In the mushy state, latent heat and sensible heat exchange occur simultaneously.

The various polynomial coefficients are as follows:

$$c_{Pu1} = -118.2062, c_{Pu2} = 311.7866, c_{Pu3} = 19.629, c_{Pu4} = -0.752, c_{Pu5} = 0, c_{Pu6} = 0, c_{Pu7} = 7.0131, c_{U1} = -78.4303, c_{U2} = 193.238, c_{U3} = 162.8647, c_{U4} = -104.0014, c_{U5} = 29.2056, c_{U6} = -1.9507, c_{U7} = 2.644$$

Density correlations [110,134]:

$$\rho_f = \rho_{f,s}(273)(0.99734 + 9.802 * 10^{-6}T_f - 2.705 * 10^{-10}T_f^2 + 4.391 * 10^{-13}T_f^3)^{-3} \quad (273 \leq T_f < 923) \quad (A.12)$$

$$\rho_f = \rho_{f,s}(273)(0.99672 + 1.179 * 10^{-5}T_f - 2.429 * 10^{-9}T_f^2 + 1.219 * 10^{-12}T_f^3)^{-3} \quad (923 \leq T_f < T_{sol}) \quad (A.13)$$

$$\rho_f = (1 - o)\rho_f(T_{sol}) + o\rho_{f,l}(T_{liq}) \quad (T_{sol} \leq T_f \leq T_{liq}) \quad (A.14)$$

$$\rho_{f,l} = 8860 - 0.9285(T_f - T_{liq}) \quad (T_f > T_{liq}) \quad (A.15)$$

Expressions for pellet outer radius are based on integrated thermal expansion coefficients [79]:

$$R_o^t = R_f^{t=0} \left(0.99734 + 9.802 \times 10^{-6}(T_{f,m}) - 2.705 \times 10^{-10}(T_{f,m})^2 + 4.391 \times 10^{-13}(T_{f,m})^3 \right) \quad (T_f \leq 650) \quad (A.16)$$

$$R_o^t = R_f^{t=0} \left(0.99672 + 1.179 \times 10^{-5}(T_{f,m}) - 2.429 \times 10^{-9}(T_{f,m})^2 + 1.219 \times 10^{-12}(T_{f,m})^3 \right) \quad (T_f > 650) \quad (A.17)$$

Here, $T_{f,m}$ is the mean pellet temperature at a given axial position.

Cladding steel:

The thermophysical properties for cladding steel (D9) are as follows [138,139]:

$$K_c(T_c) = \begin{cases} 7.598 + (2.391 \times 10^{-2})T_c - (8.899 * 10^{-6})T_c^2 & (500 < T_c < 1030) \\ 7.260 + (1.509 \times 10^{-2})T_c & (1030 \leq T_c < 1030) \end{cases} \quad (A.18)$$

$$\rho_c(T_c) = \rho_c(293) \left(1 + 10^{-2} (-0.4247 + 1.282 * 10^{-3} * T_c + 7.362 * 10^{-7} * T_c^2 - 2.069 * 10^{-10} * T_c^3) \right)^{-3} \quad (\text{A.19})$$

$$R_{ci}^t = R_{ci}^{t=0} \left(1 + \alpha_{c,m}(T_{c,m}) \right) \quad (\text{A.20})$$

$$\alpha_{c,m} = (C_{c_1} + C_{c_2} T_c + C_{c_3} T_c^2) \times 10^{-5} \quad (\text{A.21})$$

$$C_c(T_c) = 291.9 + 3.792 * 10^{-1} * T_c - 1.345 * \frac{10^{-4}}{T_c^2} \quad (300 < T_c < 1300) \quad (\text{A.22})$$

Here, $\rho_c(293) = 7966 \text{ kgm}^{-3}$ and the range of validity of Eq. (A.19) is 400–1300 K. The polynomial coefficients are as follows: $C_{c_1} = 1.53$, $C_{c_2} = 6.82278 \times 10^{-4}$, $C_{c_3} = -4.06195 \times 10^{-8}$

Fission gases:

Expressions for thermal conductivities are as follows [113,140,141] (SAS4A-DEFORM):

$$K_{Xe} = 0.00515 + 1.69 \times 10^{-5} (T_g) - 3.5 \times 10^{-9} (T_g)^2 \quad (\text{A.23})$$

$$K_{He} = 2.682 \times 10^{-3} \left(1 + (1.123 \times 10^{-8} \times P_g) \right) T_g^{0.71(1-(2P_g \times 10^{-9}))} \quad (\text{A.24})$$

$$K_{Kr} = \frac{(0.716 \times 10^{-3}) T_g^{0.5}}{C_{Kr_1}} \left(1 + \frac{b_{Kr_0} \beta_{Kr} P_g}{R_{Kr} T_g} \right) \quad (\text{A.25})$$

In the above equations, the coefficients are as follows:

$$\beta_{Kr} = 10^{(q_{Kr_1} + q_{Kr_2} \log_{10} t^* + q_{Kr_3} (\log_{10} t^*)^2 + q_{Kr_4} (\log_{10} t^*)^3)}$$

$$C_{Kr_1} = e^{(b_{Kr_1} + b_{Kr_2} \ln(t^*) + b_{Kr_3} (\ln(t^*))^2 + b_{Kr_4} (\ln(t^*))^3 + b_{Kr_5} (\ln(t^*))^4)}$$

$$t^* = \frac{T_g}{197.8}, b_{Kr_0} = 0.00069, b_{Kr_1} = 4.6841 \times 10^{-1}, b_{Kr_2} = -5.6991 \times 10^{-1}, b_{Kr_3} =$$

$$1.9591 \times 10^{-1}, b_{Kr_4} = -3.879 \times 10^{-2}, b_{Kr_5} = 2.59 \times 10^{-3}, q_{Kr_1} = 0.47, q_{Kr_2} =$$

$$-1.59, q_{Kr_3} = 1.26, q_{Kr_4} = -0.37, R_{Kr} = 99.22$$

Appendix B: Discretized equations

Heat transfer and phase-change:

Governing equations

$$H_{i,k}^{t+\Delta t} = H_{i,k}^t + D_{radial}^t [q_{west}^t - q_{east}^t] + D_{axial}^t [q_{south}^t - q_{north}^t] + C_X^t X_{i,k}^t \quad (B.1)$$

$$T_{C_{i,k}}^{t+\Delta t} = T_{C_{i,k}}^t + D_c \left(\frac{r_{c,i+}}{r_{c,i}} \right) (T_{C_{i+1,k}}^t - T_{C_{i,k}}^t) + D_c \left(\frac{r_{c,i-}}{r_{c,i}} \right) (T_{C_{i-1,k}}^t - T_{C_{i,k}}^t) \quad (B.2)$$

$$H_{ct,k}^{t+\Delta t} = H_{ct,k}^t + D_{ct1} (T_{co,k}^{t+\Delta t} - T_{ct,k}^t) + D_{ct2} \left(H_{ct,k-\frac{1}{2}}^t - H_{ct,k+\frac{1}{2}}^t \right) \quad (B.3)$$

Flux definitions

$$q_{east}^t = -K_{i+}^t r_{i+\frac{1}{2}} \left(\frac{T_{i+1}^t - T_i^t}{r_{i+1} - r_i} \right), \quad q_{west}^t = -K_{i-}^t r_{i-\frac{1}{2}} \left(\frac{T_i^t - T_{i-1}^t}{r_i - r_{i-1}} \right), \quad q_{north}^t = -K_{k+}^t \left(\frac{T_{i,k+1}^t - T_{i,k}^t}{z_{k+1} - z_k} \right), \quad q_{south}^t = -K_{k-}^t \left(\frac{T_{i,k}^t - T_{i,k-1}^t}{z_k - z_{k-1}} \right)$$

Term definitions

$$D_{radial} = \frac{2\Delta t_1}{\rho_{f,s} \left(r_{i+\frac{1}{2}}^2 - r_{i-\frac{1}{2}}^2 \right)}; \quad D_{axial} = \frac{\Delta t_1}{\rho_{f,s} \left(z_{k+\frac{1}{2}} - z_{k-\frac{1}{2}} \right)}; \quad C_X^t = \frac{\Delta t_1}{\rho_{f,s} A_{pel}}$$

$$X_{i,k}^t = \dot{q}_k A_{pel}, \quad D_c = \frac{\Delta t K_c}{\rho_c C_c \Delta r_c^2}; \quad D_{ct1} = \frac{h_{ct} 2\pi R_{co} \Delta t}{\rho_{ct} A_{ct}}; \quad D_{ct2} = \frac{\dot{m}_{ct} \Delta t}{\rho_{ct} A_{ct} \Delta z}$$

$$H_{ct,k+\frac{1}{2}}^t = f_{ct1} H_{ct,k+1}^t + f_{ct2} H_{ct,k}^t; \quad H_{ct,k-\frac{1}{2}}^t = f_{ct3} H_{ct,k-1}^t + f_{ct4} H_{ct,k}^t$$

$$K_{i+} = \frac{K_{i+1,k} K_{i,k}}{f_{r+} K_{i+1,k} + (1-f_{r+}) K_{i,k}}, \quad K_{i-} = \frac{K_{i-1,k} K_{i,k}}{f_{r-} K_{i-1,k} + (1-f_{r-}) K_{i,k}}$$

$$K_{k+} = \frac{K_{i,k+1} K_{i,k}}{f_{z+} K_{i,k+1} + (1-f_{z+}) K_{i,k}}, \quad K_{k-} = \frac{K_{i,k-1} K_{i,k}}{f_{z-} K_{i,k-1} + (1-f_{z-}) K_{i,k}}, \quad f_{r+} = \frac{r_{i+1} - r_{i+\frac{1}{2}}}{r_{i+1} - r_i}$$

$$f_{r-} = \frac{r_{i-\frac{1}{2}} - r_{i-1}}{r_i - r_{i-1}}; \quad f_{z+} = \frac{z_{k+1} - z_{k+\frac{1}{2}}}{z_{k+1} - z_k}; \quad f_{z-} = \frac{z_{k-\frac{1}{2}} - z_{k-1}}{z_k - z_{k-1}}, \quad r_{i+\frac{1}{2}} = \frac{r_{i+1} + r_i}{2}$$

$$r_{i-\frac{1}{2}} = \frac{r_{i-1} + r_i}{2}, \quad r_{c,i+} = r_{c,i} + 0.5\Delta r_c, \quad r_{c,i-} = r_{c,i} - 0.5\Delta r_c, \quad f_{ct1} = \frac{\Delta z/2}{z_{k+1} - z_k}$$

$$f_{ct2} = \frac{(z_{k+1} - z_k - \Delta z/2)}{z_{k+1} - z_k}, \quad f_{ct3} = \frac{\Delta z/2}{z_k - z_{k-1}}, \quad f_{ct4} = \frac{(z_k - z_{k-1} - \Delta z/2)}{z_k - z_{k-1}}, \quad \rho_{f,s} = \rho_f \quad (273)$$

$$D_{c1} = \frac{4D_c(R_{ci} + \frac{\Delta r_c}{2})}{(2R_{ci} + \frac{\Delta r_c}{2})}; D_{c2} = \frac{4\Delta t h_{gap,k} R_m}{\rho_c C_c \Delta z (2R_{ci} + \frac{\Delta r_c}{2})}; D_{c3} = \frac{4\Delta t h_{ct} R_{co}}{\rho_c C_c \Delta z (2R_{co} - \frac{\Delta r_c}{2})}, D_{c4} = \frac{4D_c(R_{co} - \frac{\Delta r_c}{2})}{(2R_{co} - \frac{\Delta r_c}{2})}$$

Boundary Conditions:

$$T_{ci,k}^{t+\Delta t} = T_{ci,k}^t + D_{c1}(T_{c2,k}^t - T_{ci,k}^t) + D_{c2}(T_o^t - T_{ci,k}^t)$$

$$T_{co,k}^{t+\Delta t} = T_{co,k}^t + D_{c3}(T_{ct,k}^t - T_{co,k}^t) + D_{c4}(T_{cNc,k}^t - T_{co}^t)$$

$$q_{Rint}^t = -\left(h_{w,f}^t A_{w,f}(T_{int,k}^t - T_{f,l,k}^t) + h_{w,g}^t A_{w,g}(T_{int,k}^t - T_{g,k}^t)\right) / 2\pi$$

$$q_{Ro}^t = -R_m \left(h_{gap}^t (T_{ci,k}^t - T_{o,k}^t)\right), \quad R_m = \frac{R_{ci} + R_o}{2}$$

$$q_{north}^t = 0 \quad (z = Z_u), \quad q_{south}^t = 0 \quad (z = Z_l), \quad q_{west}^t = 0 \quad (r = 0)$$

$$T_{ct}(z = Z_l) = T_{ct,in}$$

In-pin fuel motion:

Governing equations

$$G_{fk}^{t+\Delta t} = C_{F1} G_{fk}^t + C_{F2} \left((G_f AV_f)_{k-\frac{1}{2}}^t - (G_f AV_f)_{k+\frac{1}{2}}^t \right) + C_{F3} S_f^t \quad (B.4)$$

$$\alpha_f^{t+\Delta t} = \frac{G_{fk}^{t+\Delta t}}{\rho_{fk}^t}, \quad \alpha_g^{t+\Delta t} = 1 - \alpha_f^{t+\Delta t} \quad (B.5)$$

$$H_{f,k}^{t+\Delta t} = H_{f,k}^t + C_{FH1} \left[\left((\alpha_f \rho_f A H_f V_f)_{k-\frac{1}{2}}^t - (\alpha_f \rho_f A H_f V_f)_{k+\frac{1}{2}}^t \right) + \right.$$

$$H_{fk}^t \left((\alpha_f \rho_f A V_f)_{k+\frac{1}{2}}^t - (\alpha_f \rho_f A V_f)_{k-\frac{1}{2}}^t \right) + (q_f'')_{k-\frac{1}{2}}^t - (q_f'')_{k+\frac{1}{2}}^t \left. \right] + C_{FH2} \left[S_f^t (e_{sf} - \right.$$

$$H_{fk}^t) + \frac{\alpha_f^t A_{cav} \rho_f^t X_k^t}{A_{pel} \rho_{f,s}} + h_{f-g}^t A_{f-g}^t (T_{gk}^t - T_{fk}^t) + h_{w,f}^t A_{w,f}(T_{w,k}^t - T_{fk}^t) \left. \right] \quad (B.6)$$

$$\rho_{gk}^{t+\Delta t} = C_{G1} \rho_{gk}^t + C_{G2} S_g^t + C_{G3} \left((\alpha_g \rho_g A V_g)_{k-\frac{1}{2}}^t - (\alpha_g \rho_g A V_g)_{k+\frac{1}{2}}^t \right) \quad (B.7)$$

$$\begin{aligned}
H_{g,k}^{t+\Delta t} &= H_{g,k}^t + C_{GH1} \left[\left((\alpha_g \rho_g A H_g V_g)^t_{k-\frac{1}{2}} - (\alpha_g \rho_g A H_g V_g)^t_{k+\frac{1}{2}} \right) + \right. \\
&H_{g,k}^t \left((\alpha_g \rho_g A V_g)^t_{k+\frac{1}{2}} - (\alpha_g \rho_g A V_g)^t_{k-\frac{1}{2}} \right) + (q_g'')^t_{k-\frac{1}{2}} - (q_g'')^t_{k+\frac{1}{2}} \left. \right] + C_{GH2} [S_g^t (e_{sg} - \\
&H_{g,k}^t) + h_{g-f}^t A_{g-f}^t (T_{f,k}^t - T_{g,k}^t) + h_{w,g}^t A_{w,g}^t (T_{w,k}^t - T_{g,k}^t)] \tag{B.8}
\end{aligned}$$

$$\begin{aligned}
V_{G_k}^{t+\Delta t} &= \frac{C_{GV2}}{C_{GV1}} V_{G_k}^t + \frac{C_{GV3}}{C_{GV1}} \left((\alpha_g \rho_g A V_g V_g)^t_{k-1} - (\alpha_g \rho_g A V_g V_g)^t_k \right) + \frac{C_{GV4}}{C_{GV1}} (P_{k-1}^{t+\Delta t} - \\
&P_k^{t+\Delta t}) - \frac{C_{GV5}}{C_{GV1}} + \frac{C_{DRAG}}{C_{GV1}} V_{f,k}^t - \frac{C_{VM2}}{C_{GV1}} \tag{B.9}
\end{aligned}$$

$$\begin{aligned}
V_{f,k}^{t+\Delta t} &= \frac{C_{FV2}}{C_{FV1}} V_{f,k}^t + \frac{C_{FV3}}{C_{FV1}} \left((\alpha_f \rho_f A V_f^2)^t_{k-1} - (\alpha_f \rho_f A V_f^2)^t_k \right) + \frac{C_{FV4}}{C_{FV1}} (P_{k-1}^{t+\Delta t} - P_k^{t+\Delta t}) - \\
&\frac{C_{FV5}}{C_{FV1}} + \frac{C_{DRAG}}{C_{FV1}} (V_{g,k}^{t+\Delta t} - V_{f,k}^t) + \frac{C_{VM1}}{C_{FV1}} (V_g^{t+\Delta t} - V_g^t) + \frac{C_{VM2}}{C_{FV1}} \tag{B.10}
\end{aligned}$$

Flux definitions

$$(\alpha_g \rho_g A V_g^2)^t_{k-1} = \begin{cases} \alpha_{g_{k-1}}^t A_{k-1}^t \rho_{g_{k-1}}^t V_{g_{k-1}}^t V_{g_{k-1}}^t, & V_{g_k}^t + V_{g_{k-1}}^t \geq 0 \\ \alpha_{g_{k-1}}^t A_{k-1}^t \rho_{g_{k-1}}^t V_{g_k}^t V_{g_k}^t, & V_{g_k}^t + V_{g_{k-1}}^t < 0 \end{cases}$$

$$(\alpha_g \rho_g A V_g^2)^t_k = \begin{cases} \alpha_{g_k}^t A_k^t \rho_{g_k}^t V_{g_k}^t V_{g_k}^t, & V_{g_k}^t + V_{g_{k+1}}^t \geq 0 \\ \alpha_{f_k}^t A_k^t \rho_{g_k}^t V_{g_{k+1}}^t V_{g_{k+1}}^t, & V_{g_k}^t + V_{g_{k+1}}^t < 0 \end{cases}$$

$$(\alpha_f \rho_f A V_f^2)^t_{k-1} = \begin{cases} \alpha_{f_{k-1}}^t A_{k-1}^t \rho_{f_{k-1}}^t V_{f_{k-1}}^t V_{f_{k-1}}^t, & V_{f_k}^t + V_{f_{k-1}}^t \geq 0 \\ \alpha_{f_{k-1}}^t A_{k-1}^t \rho_{f_{k-1}}^t V_{f_k}^t V_{f_k}^t, & V_{f_k}^t + V_{f_{k-1}}^t < 0 \end{cases}$$

$$(\alpha_f \rho_f A V_f^2)^t_k = \begin{cases} \alpha_{f_k}^t A_k^t \rho_{f_k}^t V_{f_k}^t V_{f_k}^t, & V_{f_k}^t + V_{f_{k+1}}^t \geq 0 \\ \alpha_{f_k}^t A_k^t \rho_{f_k}^t V_{f_{k+1}}^t V_{f_{k+1}}^t, & V_{f_k}^t + V_{f_{k+1}}^t < 0 \end{cases}$$

$$(G_f A V_f)^t_{k-\frac{1}{2}} = \begin{cases} G_{f_{k-1}}^t A_{k-1}^t V_{f_k}^t, & V_{f_k}^t > 0 \\ G_{f_k}^t A_k^t V_{f_k}^t, & V_{f_k}^t < 0 \end{cases}$$

$$(G_f A V_f)^t_{k+\frac{1}{2}} = \begin{cases} G_{f_k}^t A_k^t V_{f_{k+1}}^t, & V_{f_{k+1}}^t > 0 \\ G_{f_{k+1}}^t A_{k+1}^t V_{f_{k+1}}^t, & V_{f_{k+1}}^t < 0 \end{cases}$$

$$(\alpha_g \rho_g A V_g)^t_{k-\frac{1}{2}} = \begin{cases} \alpha_{g_{k-1}}^t A_{k-1}^t \rho_{g_{k-1}}^t V_{g_k}^t, & V_{g_k}^t > 0 \\ \alpha_{g_k}^t A_k^t \rho_{g_k}^t V_{g_k}^t, & V_{g_k}^t < 0 \end{cases}$$

$$(\alpha_g \rho_g A V_g)^t_{k+\frac{1}{2}} = \begin{cases} \alpha_{g_k}^t A_k^t \rho_{g_k}^t V_{g_{k+1}}^t, & V_{g_{k+1}}^t > 0 \\ \alpha_{g_{k+1}}^t A_{k+1}^t \rho_{g_k}^t V_{g_{k+1}}^t, & V_{g_{k+1}}^t < 0 \end{cases}$$

$$(\alpha_f \rho_f A H_f V_f)^t_{k-\frac{1}{2}} = \begin{cases} \alpha_{f_{k-1}}^t A_{k-1}^t \rho_f H_{f_{k-1}} V_{f_k}^t, & V_{f_k}^t > 0 \\ \alpha_{f_k}^t A_k^t \rho_f H_{f_k} V_{f_k}^t, & V_{f_k}^t < 0 \end{cases}$$

$$(\alpha_f \rho_f A H_f V_f)^t_{k+\frac{1}{2}} = \begin{cases} \alpha_{f_k}^t A_k^t \rho_f H_{f_k} V_{f_{k+1}}^t, & V_{f_{k+1}}^t > 0 \\ \alpha_{f_{k+1}}^t A_{k+1}^t \rho_f H_{f_{k+1}} V_{f_{k+1}}^t, & V_{f_{k+1}}^t < 0 \end{cases}$$

$$(q_f'')^t_{k-\frac{1}{2}} = -K_f \alpha_{f_{k-\frac{1}{2}}}^t A_{k-\frac{1}{2}}^t \left(\frac{T_{f_k}^t - T_{f_{k-1}}^t}{\Delta Z} \right); (q_f'')^t_{k+\frac{1}{2}} = -K_f \alpha_{f_{k+\frac{1}{2}}}^t A_{k+\frac{1}{2}}^t \left(\frac{T_{f_{k+1}}^t - T_{f_k}^t}{\Delta Z} \right)$$

$$(\alpha_g \rho_g A H_g V_g)^t_{k-\frac{1}{2}} = \begin{cases} \alpha_{g_{k-1}}^t A_{k-1}^t \rho_g H_{g_{k-1}} V_{g_k}^t, & V_{g_k}^t > 0 \\ \alpha_{g_k}^t A_k^t \rho_g H_{g_k} V_{g_k}^t, & V_{g_k}^t < 0 \end{cases}$$

$$(\alpha_g \rho_g A H_g V_g)^t_{k+\frac{1}{2}} = \begin{cases} \alpha_{g_k}^t A_k^t \rho_g H_{g_k} V_{g_{k+1}}^t, & V_{g_{k+1}}^t > 0 \\ \alpha_{g_{k+1}}^t A_{k+1}^t \rho_g H_{g_{k+1}} V_{g_{k+1}}^t, & V_{g_{k+1}}^t < 0 \end{cases}$$

$$(q_g'')^t_{k-\frac{1}{2}} = -K_g \alpha_{g_{k-\frac{1}{2}}}^t A_{k-\frac{1}{2}}^t \left(\frac{T_{g_k}^t - T_{g_{k-1}}^t}{\Delta Z} \right); (q_g'')^t_{k+\frac{1}{2}} = -K_g \alpha_{g_{k+\frac{1}{2}}}^t A_{k+\frac{1}{2}}^t \left(\frac{T_{g_{k+1}}^t - T_{g_k}^t}{\Delta Z} \right)$$

Boundary Flux definitions

$$(\alpha_g \rho_g A H_g V_g)^t_{k-\frac{1}{2}} \Big|_{k=L_{bs}} = 0; (\alpha_g \rho_g A H_g V_g)^t_{k+\frac{1}{2}} \Big|_{k=L_{ts}} = 0$$

$$(\alpha_f \rho_f A H_f V_f)^t_{k-\frac{1}{2}} \Big|_{k=L_{bs}} = 0; (\alpha_f \rho_f A H_f V_f)^t_{k+\frac{1}{2}} \Big|_{k=L_{ts}} = 0$$

$$(\alpha_g \rho_g A V_g^2)^t_{k-1} \Big|_{k=L_{bs}+1} = \begin{cases} 0.25 \alpha_{g_{k-1}}^t A_{k-1}^t \rho_{g_{k-1}}^t V_{g_k}^t V_{g_k}^t, & V_{g_k}^t \geq 0 \\ \alpha_{g_{k-1}}^t A_{k-1}^t \rho_{g_{k-1}}^t V_{g_k}^t V_{g_k}^t, & V_{g_k}^t < 0 \end{cases}$$

$$(\alpha_g \rho_g A V_g^2)^t_k \Big|_{k=L_{ts}} = \begin{cases} \alpha_{g_k}^t A_k^t \rho_{g_k}^t V_{g_k}^t V_{g_k}^t, & V_{g_k}^t \geq 0 \\ 0.25 \alpha_{g_k}^t A_k^t \rho_{g_k}^t V_{g_k}^t V_{g_k}^t, & V_{g_k}^t < 0 \end{cases}$$

$$(\alpha_f \rho_f A V_f^2)^t_{k-1} \Big|_{k=L_{bs}+1} = \begin{cases} 0.25 \alpha_{f_{k-1}}^t A_{k-1}^t \rho_{f_{k-1}}^t V_{f_k}^t V_{f_k}^t, & V_{f_k}^t \geq 0 \\ \alpha_{f_{k-1}}^t A_{k-1}^t \rho_{f_{k-1}}^t V_{f_k}^t V_{f_k}^t, & V_{f_k}^t < 0 \end{cases}$$

$$(\alpha_f \rho_f A V_f^2)^t_k \Big|_{k=L_{ts}} = \begin{cases} \alpha_{f_k}^t A_k^t \rho_{f_k}^t V_{f_k}^t V_{f_k}^t, & V_{g_k}^t \geq 0 \\ 0.25 \alpha_{f_k}^t A_k^t \rho_{f_k}^t V_{f_k}^t V_{f_k}^t, & V_{g_k}^t < 0 \end{cases}$$

$$(G_f A V_f)^t_{k=L_{bs}} = 0; (G_f A V_f)^t_{k=L_{ts}} = 0; (\alpha_g \rho_g A V_g)^t_{k=L_{bs}} = 0; (\alpha_g \rho_g A V_g)^t_{k=L_{ts}} = 0$$

$$(q_f'')^t_{k=L_{bs}} = -K_f \alpha_{f_k}^t A_k^t \left(\frac{T_{f,l_k}^t - T_{f,k-1,avg}^t}{\Delta z/2} \right); (q_f'')^t_{k=L_{ts}} = -K_f \alpha_{f_k}^t A_k^t \left(\frac{T_{f,k+1,avg}^t - T_{f,l_k}^t}{\Delta z/2} \right)$$

$$(q_g'')^t_{k=L_{bs}} = -K_g \alpha_{g_k}^t A_k^t \left(\frac{T_{g_k}^t - T_{f,k-1,avg}^t}{\Delta z/2} \right); (q_g'')^t_{k=L_{ts}} = -K_g \alpha_{g_k}^t A_k^t \left(\frac{T_{f,k+1,avg}^t - T_{g_k}^t}{\Delta z/2} \right)$$

$$T_{f,k,avg}^t = \frac{\sum_{i=1}^{i=N_{cav}+1+D_{int,k}} (T_{f,i,k}^t 2\pi r_{i,k} \Delta r)}{\pi R^2 (N_{cav}+1+D_{int,k})}$$

Term definitions

Table B.1: Definition of discretized multi-phase flow coefficients (drag term for (a) annular and (b) bubbly flow is specified)

C_{F1}	$\left(\frac{A_k^t}{A_k^{t+\Delta t}} \right)$	C_{F2}	$\frac{\Delta t}{\Delta z A_k^{t+\Delta t}}$	C_{F3}	$\frac{\Delta t}{A_k^{t+\Delta t}}$
C_{G1}	$\left(\frac{\alpha_{g_k}^t A_k^t}{\alpha_{g_k}^{t+\Delta t} A_k^{t+\Delta t}} \right)$	C_{G2}	$\frac{\Delta t}{\alpha_{g_k}^{t+\Delta t} A_k^{t+\Delta t}}$	C_{G3}	$\frac{\Delta t}{\Delta z \alpha_{g_k}^{t+\Delta t} A_k^{t+\Delta t}}$
C_{FH1}	$\frac{\Delta t}{\Delta z \alpha_{f_k}^t A_k^t \rho_{f_k}^t}$	C_{FH2}	$\frac{\Delta t}{\alpha_{f_k}^t A_k^t \rho_{f_k}^t}$	C_{GH1}	$\frac{\Delta t}{\Delta z \alpha_{g_k}^t A_k^t \rho_{g_k}^t}$
C_{GH2}	$\frac{\Delta t}{\alpha_{g_k}^t A_k^t \rho_{g_k}^t}$	C_{FV1}	$G_{f_{k-\frac{1}{2}}}^{t+\Delta t} A_{k-\frac{1}{2}}^{t+\Delta t} + \frac{\Delta t}{8} (\rho_f A_{w,f} f_{Darcy,f})_{k-\frac{1}{2}}^t V_{f_k}^t $		
C_{FV2}	$G_{f_{k-\frac{1}{2}}}^t A_{k-\frac{1}{2}}^t$	C_{FV3}	$\frac{\Delta t}{\Delta z}$	C_{FV4}	$\alpha_{f_{k-\frac{1}{2}}}^{t+\Delta t} A_{k-\frac{1}{2}}^{t+\Delta t} \frac{\Delta t}{\Delta z}$
C_{FV5}	$G_{f_{k-\frac{1}{2}}}^{t+\Delta t} A_{k-\frac{1}{2}}^{t+\Delta t} g \Delta t$	C_{DRAG} (a)	$\frac{\Delta t C_{Dk}^{t+\Delta t} \rho_{g_{k-\frac{1}{2}}}^{t+\Delta t} A_{f-g_{k-\frac{1}{2}}}^{t+\Delta t} \alpha_{g_{k-\frac{1}{2}}}^{t+\Delta t} V_{rel_k}^t }{2}$		
C_{DRAG} (b)	$\frac{3C_{Dk}^{t+\Delta t} \Delta t \alpha_{g_{k-\frac{1}{2}}}^{t+\Delta t} V_{rel_k}^t \rho_{f_{k-\frac{1}{2}}}^{t+\Delta t} A_{k-\frac{1}{2}}^{t+\Delta t}}{4d_g}$	C_{VM2}	$\frac{1}{2} (\alpha_g \rho_f A)_{k-\frac{1}{2}}^{t+\Delta t} V_{gk}^t \Delta t \left(\frac{(V_{g_{k+1}}^t - V_{g_{k-1}}^t)}{2\Delta z} - \frac{(V_{f_{k+1}}^t - V_{f_{k-1}}^t)}{2\Delta z} \right)$		
C_{VM1}	$\frac{\alpha_{g_{k-\frac{1}{2}}}^{t+\Delta t} \rho_{f_{k-\frac{1}{2}}}^{t+\Delta t} A_{k-\frac{1}{2}}^{t+\Delta t}}{2}$	C_{GV1}	$(\alpha_g A \rho_g)_{k-\frac{1}{2}}^{t+\Delta t} + C_{VM1} + C_{DRAG} + \frac{\Delta t}{8} (\rho_g A_{w,g} f_{Darcy,g})_{k-\frac{1}{2}}^{t+\Delta t} V_{gk}^t $		
C_{GV2}	$(\alpha_g A \rho_g)_{k-\frac{1}{2}}^t + C_{VM1}$	C_{GV3}	$\frac{\Delta t}{\Delta z}$	C_{GV4}	$\frac{(\alpha_g A)_{k-\frac{1}{2}}^{t+\Delta t} \Delta t}{\Delta z}$
C_{GV5}	$(\alpha_g A \rho_g)_{k-\frac{1}{2}}^{t+\Delta t} g \Delta t$		-		-

Appendix C: User instruction manual

This appendix provides the user instructions for MITRA subroutine as well as guidance on data input/output. The essential input and output files are as follows:

Table C.1: MITRA input files (n=1: IRN; IRN = total number of fuel and blanket channels in the core).

S.N.	Name	Role	Description
1	“pfbr15-bol.n1”	Input	Grid size, coolant flow rate
2	“pfbr16-bol.n1”	Input	Power and worth distribution
3	“pfbr27-bol.n1”	Input	Fuel properties, time periods and transient time steps
4	“n_enthalpy_data_1.txt”	Input	Fuel temperature-enthalpy data below solidus
5	“n_enthalpy_data_2.txt”	Input	Fuel temperature-enthalpy data between solidus and liquidus
6	“n_enthalpy_data_3.txt”	Input	Fuel temperature-enthalpy data beyond liquidus

```

File Edit Format View Help
MITRA INPUT DATA
BU_FRESH      BU_EQ      T_HEAT      T_STEADY    T_SOLIDIF    T_MAXPOWER
.00000e+00    .30000e+01 .00000e+00  .30000e+02  .20000e+01    .00000e+00
DELT_HT_1     DELT_HT_2  DELT_1      DELT_2      DELT_3
.10000e-02    .10000e-02 .15000e-03  .50000e-04  .50000e-04
molefr_inr    molefr_otr molefr_bl   x_fuel      x_blanket
.21000e+00    .27400e+00 .00000e+00  .20000e-01  .00000e+00
diluent_1     diluent_2
  3           8
poros_init    poros_blk
.50000e-01    .70000e-01

```

Figure C.1: An example input file (‘pfbr27-bol.n1’).

Input files provide essential data for simulation. Core axial and radial distributions of power, fuel mass removal worth and mass flow rate are available in PREDIS input files. The number of fuel and blanket channels, axial nodes, fuel pin dimensions, and

coolant thermophysical properties are available in PREDIS input. MITRA utilizes this data by reading PREDIS input files and storing data in its arrays.

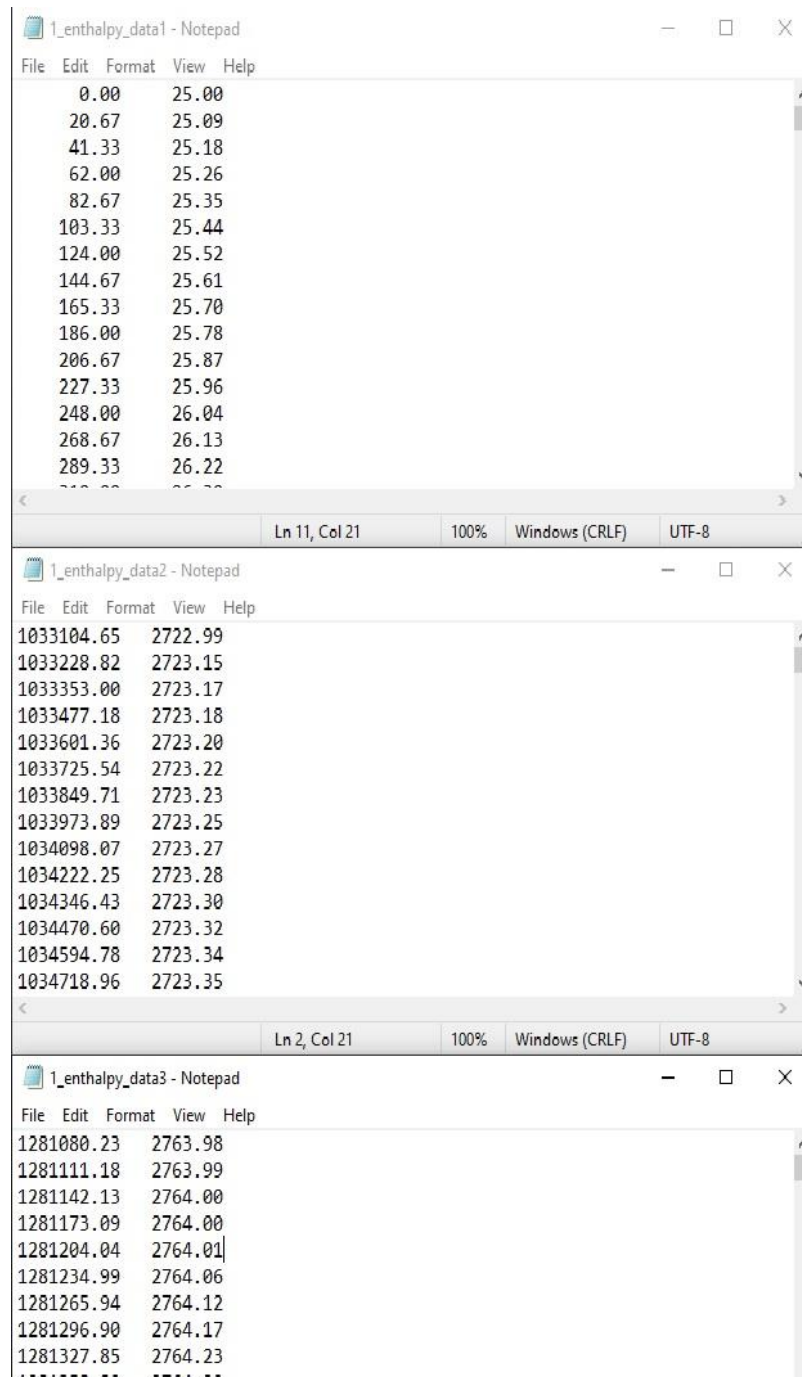


Figure C.2: Enthalpy-temperature data input files.

However, several parameters are not present in PREDIS input files. MITRA imports this data directly from a separate input file (Figure C.1). Reactor dynamics

parameters such as control rod withdrawal worth and rate of reactivity insertion are determined within the PREDIS code. Essentially, during transient simulation, MITRA only imports the level of over-power from PREDIS. Conversion of fuel enthalpy to temperature requires an Enthalpy-temperature database. It is stored in three basic input files (Refer Table C.1, S. No. 4-6). A separate code, “enthalpy_data_generator.f95” writes these files during pre-processing. This code requires the input file “pfbr27-bol.n1” for proper execution (Figure C.1). It generates the enthalpy-temperature database for all the fuel and blanket channels by utilizing the mathematical expressions defined in Appendix-A (Refer Eq. (A4-A10)). Figure C.2 displays the resultant input files. Table C.2 details the input parameters necessary for MITRA to perform its calculations. It presents the recommended time steps for various modules. Units and suggested values of the variables are also detailed. If the time-steps need to be changed, they must not violate the stability criteria (Refer Section 3.2.1) The in-pin fuel motion time steps (Delt_1, Delt_2, and Delt_3) can either be greater or equal to their recommended values, since the corresponding equations develop large coefficients, once the melt volume fraction approaches unity (Refer Eq. (B.8-B.10)). The use of recommended values of storage_factor and progress_display_factor results in data storage at every 0.25 seconds, and data display at every 2.5 seconds of transient time. Increase in the storage_factor results in reduction of the size of output files. Care should be taken that the product of storage_factor with Delt_ht_1 should be less than 1 s. MITRA works inside PREDIS architecture in the form of a group of subroutines. Table C.3 gives a list of these subroutines and briefly mentions the calculations performed in each. The main transient calculations occur inside MITRA subroutine. Data storage at regular intervals occurs inside MITRA_RECORD. Geometrical parameters for fuel pellets, cladding, and gap

width are calculated in MITRA_STEADY_CHANGES prior to the accident (steady state). The subroutine GAPCOND_M evaluates the gap conductance based on the model detailed in Section 3.1.11.

Table C.2: MITRA input variables

S. No.	Variable	Description	Units	Value
1	Bu_Fresh	Burnup of fresh fuel	Atom %	.000e+00
2	Bu_Eq	Burnup of fuel at beginning of equilibrium	Atom %	.300e+01
3	T_Heat	Time period between zero to steady power	s	.000e+00
4	T_Steady	Time period for initialization of steady state	s	.300e+02
5	T_Solidif	Time period for post-transient solidification	s	.200e+01
6	T_Maxpower	Time period for maximum power hold-up	s	.000e+00
7	Delt_Ht_1	Heat transfer time step before melting	s	.500e-03
8	Delt_Ht_2	Heat transfer time step after start of melting	s	.500e-03
9	Delt_1	Relocation time step before melting	s	.150e-03
10	Delt_2	Relocation time step after melting begins	s	.250e-04
11	Delt_3	Relocation time step after end of transient	s	.250e-04
12	Time_exchange	Data exchange period	s	0.05
13	storage_factor	Number of time loops between successive calls of MITRA_RECORD		250
14	progress_display_factor	Number of MITRA_RECORD calls between successive run-time displays		10
13	Radial_zones	Number of radial channels	-	IRN
14	LENGTH	Length of fuel column	m	1.0

15	RO	Outer radius of fuel pellet	m	0.2775e-02
16	RI	Inner radius of fuel pellet	m	0.8000e-03
17	RCO	Outer radius of fuel pin cladding	m	0.3300e-03
18	RCI	Inner radius of fuel pin cladding	m	0.2850e-03
19	Lower_blanket_bength	Length of lower blanket column	m	0.3
20	Upper_blanket_length	Length of upper blanket column	m	0.3
21	Lower_plenum_volume	Volume of lower plenum	m ³	1.8117e-05
22	Upper_plenum_volume	Volume of upper plenum	m ³	0.5103e-05
23	RO_BL	Outer radius of radial blanket pellet	m	0.6450e-02
24	RI_BL	Inner radius of radial blanket pellet	m	0
25	RCI_BL	Inner radius of blanket pin cladding	m	0.6550e-02
26	RCO_BL	Outer radius of blanket pin cladding	m	0.7150e-02
27	Molefr_Inr	PuO2 mole-fraction of inner core	-	.210e+00
28	Molefr_Otr	PuO2 mole-fraction of inner core	-	.274e+00
29	Molefr_Bl	PuO2 mole-fraction of depleted UO ₂	-	.000e+00
30	X_Fuel	Deviation from stoichiometry for fuel	-	.200e-01
31	X_Blanket	Deviation from stoichiometry for blanket	-	.000e+00
32	Diluent_1	Number of inner diluent channel	-	-
33	Diluent_2	Number of outermost diluent channel	-	-
34	Poros_Init	Initial porosity of fuel	-	.500e-01
35	Poros_Blkt	Initial porosity of blanket	-	.700e-01
36	KC	Thermal conductivity of clad	W·m ⁻¹ ·K ⁻¹	21
37	CP_CLAD	Specific heat of cladding steel	J·kg ⁻¹ ·K ⁻¹	570
38	RHO_CLAD	Density of cladding steel	Kg·m ⁻³	7700
39	A_NA	Effective coolant flow area (per pin)	m ²	-
40	RHO_NA	Density of coolant	kg·m ⁻³	-
41	CP_NA	Specific heat of coolant	J·kg ⁻¹ ·K ⁻¹	1268
42	TNA_MIN	Coolant inlet temperature	°C	397
43	Escape_constant	Parameter which governs the rate of escape of fission gases	-	-0.1
44	Assigned_worth	fuel mass removal worth distribution	pcm	(Array)
45	X_M	Fuel power distribution	W·m ⁻¹	(Array)
46	M_flow	Coolant mass flow rates (per pin)	Kg·s ⁻¹	(Array)

```

Command Prompt
Linear Heat Rating 0.1232E+05 0.4446E+05 0.7923E+04 0.4362E+05 0.4115E+05
Cavity pressure (MPa) = 0.2751E+00 0.2837E+00 0.2652E+00 0.2831E+00 0.2823E+00

Processing time_m= 96.75 s
Transient time_m= -2.50 s

Gap conductance 0.4021E+04 0.6639E+04 0.3680E+04 0.6543E+04 0.6277E+04
Plenum Pressure is 0.2751E+06 0.2837E+06 0.2652E+06 0.2831E+06 0.2823E+06
GAP_M(:,1,8) 0.7162E-04 0.4262E-04 0.7315E-04 0.4334E-04 0.4548E-04
Fuel Inner Temperature 0.1005E+04 0.2282E+04 0.7547E+03 0.2254E+04 0.2174E+04
Linear Heat Rating 0.1232E+05 0.4446E+05 0.7923E+04 0.4362E+05 0.4115E+05
Cavity pressure (MPa) = 0.2751E+00 0.2837E+00 0.2652E+00 0.2831E+00 0.2823E+00

Processing time_m= 105.42 s
Transient time_m= 0.00 s

Gap conductance 0.4021E+04 0.6639E+04 0.3680E+04 0.6543E+04 0.6277E+04
Plenum Pressure is 0.2751E+06 0.2837E+06 0.2652E+06 0.2831E+06 0.2823E+06
GAP_M(:,1,8) 0.7162E-04 0.4262E-04 0.7315E-04 0.4334E-04 0.4548E-04
Fuel Inner Temperature 0.1005E+04 0.2282E+04 0.7547E+03 0.2254E+04 0.2174E+04
Linear Heat Rating 0.1232E+05 0.4446E+05 0.7923E+04 0.4362E+05 0.4115E+05
Cavity pressure (MPa) = 0.2751E+00 0.2837E+00 0.2652E+00 0.2831E+00 0.2823E+00

```

Figure C.3: MITRA Run time output- steady state variables (Transient time = 0.0 s).

Figure C.3 presents an example of the run-time, steady-state output. The data shown at zero seconds represents the steady state data. The simulations prior to this time are for convergence of steady state data. The total period spent for convergence is $\text{TIME_HEAT} + \text{TIME_STEADY}$. The input file “pfbr27-bol.n1” contains these parameters. Convergence periods required for fuel and blanket channels are 30 s and 80 s, respectively. Convergence in the blanket channels is optional since melting does not occur in this part of the core. Table C.4 details the output files. The file ‘MITRA data summary.txt’ provides a summary of the steady-state and transient results. It provides the steady state temperature distribution in the core. It provides the melt mass fraction, radial melt extent, internal pressure, average fuel, coolant, and clad temperatures as a function of time. The file ‘Predis_mitra_comp.txt’ provides a comparison of the temperature distributions of PREDIS and MITRA, to identify discrepancies between the two. The files ‘Zone n.txt’ and ‘Zone n para.txt’ contain all the recorded data, which is internal to MITRA and data control parameters, respectively.

Table C.3: MITRA subroutines and functions

S. No.	Subroutine	Function
1	MITRA	Transient calculation of melting and relocation
2	MITRA_RECORD	Data storage at regular intervals
3	MITRA_STEADY_CHANGES	Change in fuel and clad radial dimensions at steady state
4	MITRA_DATA_ENTRY	Entry of data in text files
5	MITRA_INITIALIZATION	Initialization of variables
6	TEMP_TO_ENTHALPY_ROUTINE	calculation of fuel enthalpy from temperature
7	PELLETCOND	fuel and blanket thermal conductivity calculations
8	ENTHALPY_TO_TEMPERATURE_CONVERTER	conversion of fuel enthalpy to temperature using input data files
9	PELLET_DENSITY	Calculation of fuel and blanket densities
10	XENON_COND	Calculation of thermal conductivity of Xenon as a function of temperature
11	HELIUM_COND	Calculation of thermal conductivity of Helium
12	GAPCOND_M	Evaluation of gap conductance with jump distance model
13	COMPRESS_MODULE	Evaluation of reduction in fuel thermal density for accommodation of excess molten fuel in limited volume
14	POROSITY_DISTRIBUTION	Evaluation of fuel porosity changes due to melting and temperature induced porosity migration
15	PRESSURE_CALCULATIONS	Free volume calculations
16	FUEL_MOVEMENT_DATA	Entry of relocation data in text file

Table C.4: Output files (n=1: IRN; IRN = total number of fuel and blanket channels in the core).

S. No.	Name	Function
1	“MITRA data summary.txt”	Steady state data, melting and relocation feedbacks
2	“Predis_mitra_comp.txt”	Inter-code temperature comparison
3	“Zone n.txt”	Time history of all parameters
4	“Zone n para.txt”	Data for importing “Zone n.txt”

Bibliography

- [1] B. Merk, A. Stanculescu, P. Chellapandi, R. Hill, Progress in reliability of fast reactor operation and new trends to increased inherent safety, *Appl. Energy*. 147 (2015) 104–116. doi:10.1016/j.apenergy.2015.02.023.
- [2] J.F. Marchaterre, Overview of core disruptive accidents, *Nucl. Eng. Des.* (1977). doi:10.1016/0029-5493(77)90057-7.
- [3] P. Chellapandi, G.S. Srinivasan, S.C. Chetal, Primary containment capacity of Prototype Fast Breeder Reactor against core disruptive accident loadings, *Nucl. Eng. Des.* (2013). doi:10.1016/j.nucengdes.2012.12.014.
- [4] Basic Safety Principles for Nuclear Power Plants 75-INSAG-3 Rev. 1 | IAEA, (n.d.). <https://www.iaea.org/publications/5811/basic-safety-principles-for-nuclear-power-plants-75-insag-3-rev-1> (accessed March 10, 2021).
- [5] S. Banerjee, H.P. Gupta, The evolution of the Indian nuclear power programme, *Prog. Nucl. Energy*. 101 (2017) 4–18. doi:10.1016/j.pnucene.2017.02.008.
- [6] P. Puthiyavinayagam, P. Selvaraj, V. Balasubramaniyan, S. Raghupathy, K. Velusamy, K. Devan, B.K. Nashine, G. Padma Kumar, K. V. Suresh kumar, S. Varatharajan, P. Mohanakrishnan, G. Srinivasan, A.K. Bhaduri, Development of fast breeder reactor technology in India, *Prog. Nucl. Energy*. 101 (2017) 19–42. doi:10.1016/j.pnucene.2017.03.015.
- [7] S.C. Chetal, P. Chellapandi, P. Puthiyavinayagam, S. Raghupathy, V. Balasubramaniyan, P. Selvaraj, P. Mohanakrishnan, B. Raj, Current status of fast reactors and future plans in India, in: *Energy Procedia*, Elsevier Ltd, 2011: pp. 64–73. doi:10.1016/j.egypro.2011.06.009.

- [8] G. Srinivasan, K. V. Suresh Kumar, B. Rajendran, P. V. Ramalingam, The Fast Breeder Test Reactor-Design and operating experiences, *Nucl. Eng. Des.* 236 (2006) 796–811. doi:10.1016/j.nucengdes.2005.09.024.
- [9] M. Matsuura, M. Hatori, M. Ikeda, Design and modification of steam generator safety system of FBR MONJU, *Nucl. Eng. Des.* 237 (2007) 1419–1428. doi:10.1016/j.nucengdes.2006.09.046.
- [10] A.M. Judd, K.F. Ainsworth, Fast reactors in the U.K. 1946-1996, *Energy*. 23 (1998) 609–617. doi:10.1016/S0360-5442(97)00072-8.
- [11] A. Waltar, D. Todd, Fuel pin and assembly design, in: *Fast Spectr. React.*, Springer US, 2012: pp. 189–234. doi:10.1007/978-1-4419-9572-8_8.
- [12] T. Ozawa, T. Abe, Development and verifications of fast reactor fuel design code CEPTAR, *Nucl. Technol.* (2006). doi:10.13182/NT156-39.
- [13] S.C. Chetal, V. Balasubramaniyan, P. Chellapandi, P. Mohanakrishnan, P. Puthiyavinayagam, C.P. Pillai, S. Raghupathy, T.K. Shanmugham, C.S. Pillai, The design of the Prototype Fast Breeder Reactor, *Nucl. Eng. Des.* (2006). doi:10.1016/j.nucengdes.2005.09.025.
- [14] A. Lázaro, L. Ammirabile, G. Bandini, G. Darmet, S. Massara, P. Dufour, A. Tosello, E. Gallego, G. Jimenez, K. Mikityuk, M. Schikorr, E. Bubelis, A. Ponomarev, R. Kruessmann, M. Stempniewicz, Code assessment and modelling for Design Basis Accident Analysis of the European sodium fast reactor design. Part I: System description, modelling and benchmarking, *Nucl. Eng. Des.* 266 (2014) 1–16. doi:10.1016/j.nucengdes.2013.10.019.
- [15] V. Prakash, M. Thirumalai, M. Anandaraj, P.A. Kumar, D. Ramdasu, G.K. Pandey, G. Padmakumar, C. Anandbabu, P. Kalyanasundaram, Experimental

- qualification of subassembly design for Prototype Fast Breeder Reactor, *Nucl. Eng. Des.* 241 (2011) 3325–3332. doi:10.1016/j.nucengdes.2011.04.040.
- [16] P. Tsvetkov, A. Waltar, M. Salvatores, Fuel management, in: *Fast Spectr. React.*, Springer US, 2013: pp. 135–185. doi:10.1007/978-1-4419-9572-8_7.
- [17] A. Waltar, D. Todd, Fuel pin thermal performance, in: *Fast Spectr. React.*, Springer US, 2012: pp. 235–262. doi:10.1007/978-1-4419-9572-8_9.
- [18] V. Vinod, S. Sathishkumar, R.K. Mourya, S. Chandramouli, G. Padmakumar, B.K. Nashine, P. Selvaraj, Performance evaluation of decay heat removal system of PFBR with partial availability of air side dampers, *Nucl. Eng. Des.* 318 (2017) 174–181. doi:10.1016/j.nucengdes.2017.04.021.
- [19] V. Rajan Babu, R. Veerasamy, S. Patri, S. Ignatius Sundar Raj, S.C.S.P. Kumar Krovvidi, S.K. Dash, C. Meikandamurthy, K.K. Rajan, P. Puthiyavinayagam, P. Chellapandi, G. Vaidyanathan, S.C. Chetal, Testing and qualification of Control & Safety Rod and its drive mechanism of Fast Breeder Reactor, *Nucl. Eng. Des.* 240 (2010) 1728–1738. doi:10.1016/j.nucengdes.2010.02.037.
- [20] Deterministic Safety Analysis for Nuclear Power Plants | IAEA, (n.d.). <https://www.iaea.org/publications/12335/deterministic-safety-analysis-for-nuclear-power-plants> (accessed March 10, 2021).
- [21] J. Sackett, General safety considerations, in: *Fast Spectr. React.*, Springer US, 2013: pp. 411–426. doi:10.1007/978-1-4419-9572-8_13.
- [22] J. Sackett, Unprotected transients, in: *Fast Spectr. React.*, Springer US, 2012: pp. 451–463. doi:10.1007/978-1-4419-9572-8_15.
- [23] P. Tsvetkov, A. Waltar, D. Todd, Kinetics, reactivity effects, and control requirements, in: *Fast Spectr. React.*, Springer US, 2013: pp. 111–133.

doi:10.1007/978-1-4419-9572-8_6.

- [24] H.P.J.P. Planchon, G.H.H. Golden, J.I.I. Sackett, Demonstration of Passive Safety Features in EBR-II, in: 1987.
- [25] D.R. Porten, A. Padilla, R.E. Baars, E.H. Randklev, G.E. Culley, PINEX-2 Experiment: Concept Verification of an Inherent Shutdown Mechanism for HCDA's., Proc. - IEEE Reg. 6 Conf. (1979).
- [26] D.E. Smith, Comparative analysis of internal fuel motion in annular fuel designs, 1983. https://inis.iaea.org/search/search.aspx?orig_q=RN:15049687 (accessed March 1, 2020).
- [27] A.E. Waltar, A. Padilla, Mathematical and Computational Techniques employed in the Deterministic Approach to Liquid-Metal Fast Breeder Reactor Safety., Nucl. Sci. Eng. 64 (1977) 418–451. doi:10.13182/NSE77-A27381.
- [28] H. Tsai, L.A. Neimark, T. Asaga, S. Shikakura, Behavior of mixed-oxide fuel elements during an overpower transient, J. Nucl. Mater. 204 (1993) 217–227. doi:10.1016/0022-3115(93)90220-S.
- [29] A.L. Pitner, P.C. Ferrell, G.E. Culley, E.T. Weber, TS-1 and TS-2 transient overpower tests on FFTF fuel, in: United States, 1985. <https://www.osti.gov/biblio/6277874>.
- [30] T. Sathiyasheela, K. Natesan, G.S. Srinivasan, K. Devan, P. Puthiyavinayagam, Analysis of unprotected transients with control and safety rod drive mechanism expansion feedback in a medium sized oxide fuelled fast breeder reactor, Nucl. Eng. Des. 291 (2015) 1–9. doi:10.1016/j.nucengdes.2015.04.022.
- [31] H. Tsai, L.A. Neimark, K. Yamamoto, K. Hirai, S. Shikakura, Behavior of mixed-oxide fuel elements during the TOPI-1E transient overpower test,

- (1993). https://inis.iaea.org/search/search.aspx?orig_q=RN:25056026 (accessed July 21, 2017).
- [32] J. Dadillon, J.P. Chaudat, M. Schwarz, A. Tattegrain, G. Heusener, B. Kuczera, G. Kussmaul, J. Wolff, The CABRI test facility. Experimental fuel pin program, its objectives and present results, (1979).
http://inis.iaea.org/Search/search.aspx?orig_q=RN:11558712 (accessed March 10, 2021).
- [33] J. Charpenel, F. Lemoine, I. Sato, D. Struwe, W. Pfrang, Fuel pin behavior under the slow power ramp transients in the CABRI-2 experiments, *Nucl. Technol.* (2000). doi:10.13182/nt00-a3092.
- [34] Y. Fukano, Y. Onoda, I. Sato, J. Charpenel, Fuel pin behavior under slow-ramp-type transient-overpower conditions in the cabri-fast experiments, *J. Nucl. Sci. Technol.* 46 (2009) 1049–1058.
doi:10.1080/18811248.2009.9711615.
- [35] J. Papin, Behavior of fast reactor fuel during transient and accident conditions, in: *Compr. Nucl. Mater.*, 2012. doi:10.1016/B978-0-08-056033-5.00047-1.
- [36] A.M. Tentner, E. Parma, T. Wei, R. Wigeland, SNL, INL, Severe accident approach - final report. Evaluation of design measures for severe accident prevention and consequence mitigation., Argonne National Laboratory, Argonne, IL (United States), 2010. doi:10.2172/973483.
- [37] C.L. Pope, C.B. Jensen, D.M. Gerstner, J.R. Parry, Transient Reactor Test (TREAT) Facility Design and Experiment Capability, *Nucl. Technol.* 205 (2019) 1378–1386. doi:10.1080/00295450.2019.1599615.
- [38] A. De Volpi, R.J. Pecina, R.T. Daly, Fast neutron hodoscope at TREAT:

- development and operation, *Nucl. Technol.* 27 (1975) 449–487.
doi:10.13182/NT75-1.
- [39] L.C. Walters, Thirty years of fuels and materials information from EBR-II, *J. Nucl. Mater.* (1999). doi:10.1016/S0022-3115(98)00760-0.
- [40] J.I. Sackett, Operating and test experience with EBR-II, the IFR prototype, *Prog. Nucl. Energy.* (1997). doi:10.1016/0149-1970(96)00006-6.
- [41] G. Kayser, Jo. Papin, The reactivity risk in fast reactors and the related international experimental programmes CABRI and SCARABEE, *Prog. Nucl. Energy.* 32 (1998) 631–638. doi:10.1016/s0149-1970(97)00067-x.
- [42] CABRI Facility, (n.d.). <https://www.irsn.fr/EN/Research/Research-organisation/Research-programmes/CABRI-International-program/Pages/CABRI-Facility.aspx> (accessed March 29, 2021).
- [43] A. Flores Y Flores, V. Matuzas, S. Perez-Martin, G. Bandini, S. Ederli, L. Ammirabile, W. Pfrang, Analysis of ASTEC-Na capabilities for simulating a loss of flow CABRI experiment, *Ann. Nucl. Energy.* 94 (2016) 175–188. doi:10.1016/j.anucene.2016.02.032.
- [44] J.P. Hudelot, J. Lecerf, Y. Garnier, G. Ritter, O. Guéton, A.C. Colombier, F. Rodiac, C. Domergue, A complete dosimetry experimental program in support of the core characterization and of the power calibration of the CABRI reactor, 2015 4th Int. Conf. Adv. Nucl. Instrum. Meas. Methods Their Appl. ANIMMA 2015. (2015) 2–7. doi:10.1109/ANIMMA.2015.7465504.
- [45] O. Clamens, J. Lecerf, J. Couybes, J. Hudelot, B. Duc, L. Pantera, P. Blaise, B. Biard, Analysis of the CABRI power transients -Prediction improvements using a combination of measurements and calculation, in: *Int. Conf. Adv. Nucl.*

- Instrum. Meas. Methods Their Appl., International conference on advancements in nuclear instrumentation measurement methods and their applications, Liege, Belgium, 2017. <https://hal.archives-ouvertes.fr/hal-02418137>.
- [46] L. Vath, Modeling Transient Fission Gas Behavior for Solid, Melting, and Molten Fuel in the Computer Program LAKU, Nucl. Technol. 98 (1992) 44–53. doi:10.13182/NT92-A34649.
- [47] A. Prosperetti, G. Tryggvason, eds., Computational Methods for Multiphase Flow, Cambridge University Press, Cambridge, 2007. doi:10.1017/CBO9780511607486.
- [48] L.M. Wickens, Molten fuel dispersal in hypothetical fast reactor accidents, Nucl. Eng. Des. (1987). doi:10.1016/0029-5493(87)90060-4.
- [49] U. States., D. of Energy., O. of S. and T. Information., U. States., D. of Energy., O. of S. and T. Information., Experimental Studies of Transient Effects in Fast Reactor Fuels. Series III. Pre-Irradiated Mixed Oxide (PuO₂--UO₂) Irradiations. Final Report. Transient Irradiations., (1967). <http://www.osti.gov/servlets/purl/4520426/>.
- [50] T. Hikido, J.H. Field, Molten Fuel Movement in Transient Overpower Tests of Irradiated Oxide Fuel., United States, 1969. <https://www.osti.gov/biblio/4175346>.
- [51] P.C. Ferrell, D.R. Porten, F.J. Martin, Internal fuel motion as an inherent shutdown mechanism for LMFBR accidents: PINEX-3, PINEX-2, and HUT 5-2A experiments, (1981). https://inis.iaea.org/search/search.aspx?orig_q=RN:12641444 (accessed July

- 21, 2017).
- [52] L. Ravi, K. Velusamy, P. Chellapandi, A robust thermal model to investigate radial propagation of core damage due to total instantaneous blockage in SFR fuel subassembly, *Ann. Nucl. Energy*. 62 (2013) 342–356.
doi:10.1016/j.anucene.2013.06.032.
- [53] I. Sato, F. Lemoine, D. Struwe, Transient fuel behavior and failure condition in the CABRI-2 experiments, *Nucl. Technol.* (2004). doi:10.13182/NT04-A3464.
- [54] C. An, F.C. Moreira, J. Su, Thermal analysis of the melting process in a nuclear fuel rod, *Appl. Therm. Eng.* (2014). doi:10.1016/j.applthermaleng.2014.04.005.
- [55] A. Shrivastava, B. Williams, A.S. Siahpush, B. Savage, J. Crepeau, Numerical and experimental investigation of melting with internal heat generation within cylindrical enclosures, *Appl. Therm. Eng.* 67 (2014) 587–596.
doi:10.1016/j.applthermaleng.2014.02.039.
- [56] D. McCord, J. Crepeau, A. Siahpush, J.A. Ferres Brogin, Analytical solutions to the Stefan problem with internal heat generation, *Appl. Therm. Eng.* 103 (2016) 443–451. doi:10.1016/j.applthermaleng.2016.03.122.
- [57] K. Kamiyama, D.J. Brear, Y. Tobita, S. Kondo, Establishment of freezing model for reactor safety analysis, *J. Nucl. Sci. Technol.* 43 (2006) 1206–1217.
doi:10.1080/18811248.2006.9711213.
- [58] X. Manchon, F. Bertrand, N. Marie, M. Lance, D. Schmitt, Modeling and analysis of molten fuel vaporization and expansion for a sodium fast reactor severe accident, *Nucl. Eng. Des.* (2017). doi:10.1016/j.nucengdes.2017.07.010.
- [59] S.P. Saraswat, P. Munshi, C. Allison, Nonhyperbolicity of conservation equations of RELAP5 two-fluid model in nuclear reactor safety results

- (investigation and eigenvalue analysis), *J. Nucl. Eng. Radiat. Sci.* 7 (2021).
doi:10.1115/1.4047161.
- [60] S.P. Saraswat, P. Munshi, C. Allison, Linear stability analysis of RELAP5 two-fluid model in nuclear reactor safety results, *Ann. Nucl. Energy.* 149 (2020) 107720. doi:10.1016/j.anucene.2020.107720.
- [61] A. Trivedi, M. Perez Ferragut, Z. Fu, C. Allison, Implementation of Sodium Single Phase Thermodynamic and Transport Properties plus Heat Transfer Correlation in RELAP/SCDAPSIM for SFR Applications, 2018.
- [62] A. Srivastava, A.K. Trivedi, H.G. Lele, P. Munshi, K.K. Vaze, Best estimate plus uncertainty analysis of LBLOCA for Indian PHWR, *Kerntechnik.* 77 (2012) 333–338. doi:10.3139/124.110217.
- [63] P. Coddington, PINEX-AR, a fuel dynamics code applied to PINEX-2 prediction and reactor analysis, *Spec. Work. Predict. Anal. Mater. Dyn. LMFBR Saf. Exp.* (1979) 67–84.
- [64] A. V Jones, C. of the E.C.J.R.C.I. Establishment, Multiphase Processes in LMFBR Safety Analysis: Lectures from a Course Held at the Joint Research Centre, Ispra (Italy), 29 March-2 April 1982, Harwood Academic Publishers for the Commission of European Communities, 1984.
<https://books.google.co.in/books?id=a-02AQAAIAAJ>.
- [65] R. Leslie, T. Rudge, B. Klingert, Whole core accident analysis for a 1300 MW(e) LMFBR design using the FRAX-4 code, in: *Sci. Technol. Fast React. Safety. Vol. 2*, British Nuclear Energy Society, 1986.
- [66] D.E. Smith, F.J. Martin, A. Padilla, Internal Fuel Motion Phenomenology: FUMO-E Code Analysis of PINEX Experiments., in: *Trans. Am. Nucl. Soc.*,

1982.

- [67] A.E. Waltar, W.L. Partain, D.C. Kolesar, L.D. O'Dell, A.J. Padilla, J.C. Sonnichsen, N.P. Wilburn, H.J. Willenberg, MELT-III: a neutronics, thermal-hydraulics computer program for fast reactor safety analysis. Volume II, (1974). https://inis.iaea.org/search/search.aspx?orig_q=RN:7220361 (accessed March 12, 2021).
- [68] A.M. Tentner, D.J. Hill, PINACLE: a mechanistic model for the analysis of in-pin fuel relocation under LOF and TOP conditions for SAS4A, *Trans. Am. Nucl. Soc.; (United States)*. 49 (1985).
<https://www.osti.gov/scitech/biblio/5144397-pinacle-mechanistic-model-analysis-pin-fuel-relocation-under-lof-top-conditions-sas4a> (accessed August 3, 2017).
- [69] C.E. Brennen, *Fundamentals of multiphase flow*, 2013.
doi:10.1017/CBO9780511807169.
- [70] P. Chatelard, N. Reinke, S. Arndt, S. Belon, L. Cantrel, L. Carenini, K. Chevalier-Jabet, F. Cousin, J. Eckel, F. Jacq, C. Marchetto, C. Mun, L. Piar, ASTEC V2 severe accident integral code main features, current V2.0 modelling status, perspectives, *Nucl. Eng. Des.* 272 (2014) 119–135.
<https://www.sciencedirect.com/science/article/pii/S0029549313005621> (accessed June 6, 2018).
- [71] A. Moal, V. Georgenthum, O. Marchand, SCANAIR: A transient fuel performance code, *Nucl. Eng. Des.* 280 (2014) 150–171.
doi:10.1016/j.nucengdes.2014.03.055.
- [72] S. Perez-Martin, W. Pfrang, N. Girault, L. Cloarec, L. Laborde, M. Buck, V.

- Matuzas, A. Flores y Flores, P. Raison, A.L. Smith, N. Mozzani, F. Feria, L. Herranz, B. Farges, Development and assessment of ASTEC-Na fuel pin thermo-mechanical models performed in the European JASMIN project, *Ann. Nucl. Energy*. 119 (2018) 454–473. doi:10.1016/j.anucene.2017.12.061.
- [73] S. Perez-Martin, W. Pfrang, G. Bandini, S. Ederli, P. Balestra, C. Parisi, Single and two-phase sodium flow analysis for two tuocp cabri tests using the ASTEC-Na code, in: *Int. Top. Meet. Nucl. React. Therm. Hydraul. 2015, NURETH 2015*, American Nuclear Society, 2015: pp. 4299–4312.
- [74] D. Moxon, F. Camous, A new cavity model for SAS4A, (1994). https://inis.iaea.org/search/search.aspx?orig_q=RN:31055589 (accessed January 18, 2021).
- [75] R. Kruessmann, A. Ponomarev, W. Pfrang, D. Struwe, J. Champigny, B. Carlucci, D. Schmitt, D. Verwaerde, Assessment of SFR reactor safety issues: Part II: Analysis results of ULOF transients imposed on a variety of different innovative core designs with SAS-SFR, *Nucl. Eng. Des.* 285 (2015) 263–283. doi:10.1016/j.nucengdes.2014.11.037.
- [76] A.M. Tentner, K.J. Miles, D.J. Hill, Fuel Relocation Modelling in the SAS4A Accident Analysis Code System., in: 1986: pp. 85–90. https://inis.iaea.org/search/search.aspx?orig_q=RN:19002352 (accessed March 12, 2021).
- [77] A. Dubey, A.K. Sharma, Melting and multi-phase flow modelling of nuclear fuel in fast reactor fuel rod, *Int. J. Therm. Sci.* 125 (2018) 256–272. doi:10.1016/j.ijthermalsci.2017.10.009.
- [78] N. Choudhry, A. Riyas, K. Devan, P. Mohanakrishnan, 3D core burnup studies

- in 500 MWe Indian prototype fast breeder reactor to attain enhanced core burnup, *Nucl. Eng. Des.* 255 (2013) 359–367.
doi:10.1016/j.nucengdes.2012.11.011.
- [79] J.J. Carbajo, G.L. Yoder, S.G. Popov, V.K. Ivanov, A review of the thermophysical properties of MOX and UO₂ fuels, *J. Nucl. Mater.* (2001).
doi:10.1016/S0022-3115(01)00692-4.
- [80] K. Devan, A. Riyas, P. Mohanakrishnan, Approach to equilibrium fuelling scheme of 500 MWe PFBR based on 3-D core burnup modeling, *Nucl. Eng. Des.* 241 (2011) 1596–1605. doi:10.1016/J.NUCENGDES.2011.02.026.
- [81] G.K. Pandey, D. Ramdasu, G. Padmakumar, V. Prakash, K.K. Rajan, Development of honeycomb type orifices for flow zoning in PFBR, *Nucl. Eng. Des.* 262 (2013) 63–71. doi:10.1016/j.nucengdes.2013.03.046.
- [82] R. Harish, G.S. Srinivasan, A. Riyas, P. Mohanakrishnan, A comparative study of unprotected loss of flow accidents in 500 MWe FBR metal cores with PFBR oxide core, *Ann. Nucl. Energy.* 36 (2009) 1003–1012.
doi:10.1016/J.ANUCENE.2009.06.004.
- [83] K. Natesan, T. Sundararajan, A. Narasimhan, K. Velusamy, Turbulent flow simulation in a wire-wrap rod bundle of an LMFBR, *Nucl. Eng. Des.* 240 (2010) 1063–1072. doi:10.1016/j.nucengdes.2009.12.025.
- [84] A.E. Waltar, D.R. Todd, P. V. Tsvetkov, *Fast spectrum reactors*, 2012.
doi:10.1007/978-1-4419-9572-8.
- [85] P.M. Khot, G. Singh, B.K. Shelke, B. Surendra, M.K. Yadav, A.K. Mishra, M. Afzal, J.P. Panakkal, Development of recycling processes for clean rejected MOX fuel pellets, *Nucl. Eng. Des.* 270 (2014) 227–237.

doi:10.1016/j.nucengdes.2013.12.060.

- [86] V. Alexiades, A.D. Solomon, V. Alexiades, A.D. Solomon, Problem Formulation, in: *Math. Model. Melting Freez. Process.*, Routledge, 1993: pp. 1–32. doi:10.1201/9780203749449-1.
- [87] A. Gandini, A generalized perturbation method for bi-linear functionals of the real and adjoint neutron fluxes, *J. Nucl. Energy.* 21 (1967) 755–765. doi:10.1016/0022-3107(67)90086-X.
- [88] A. Riyas, K. Devan, P. Mohanakrishnan, Perturbation analysis of prototype fast breeder reactor equilibrium core using IGCAR and ERANOS code systems, *Nucl. Eng. Des.* 255 (2013) 112–122. doi:10.1016/j.nucengdes.2012.09.020.
- [89] A. Dubey, T. Sathiyasheela, A.K. Sharma, Reactor dynamics of in-pin fuel motion in fast breeder reactors, *Nucl. Eng. Des.* 340 (2018) 431–446. doi:10.1016/j.nucengdes.2018.10.010.
- [90] V.R. Babu, R. Veerasamy, S. Patri, S.I.S. Raj, S.C.S.P.K. Krovvidi, S.K. Dash, C. Meikandamurthy, K.K. Rajan, P. Puthiyavinayagam, P. Chellapandi, G. Vaidyanathan, S.C. Chetal, Testing and qualification of Control & Safety Rod and its drive mechanism of Fast Breeder Reactor, *Nucl. Eng. Des.* 240 (2010) 1728–1738. doi:10.1016/j.nucengdes.2010.02.037.
- [91] K. Devan, A. Riyas, P. Mohanakrishnan, Approach to equilibrium fuelling scheme of 500 MWe PFBR based on 3-D core burnup modeling, in: *Nucl. Eng. Des.*, North-Holland, 2011: pp. 1596–1605. doi:10.1016/j.nucengdes.2011.02.026.
- [92] R. Harish, T. Sathiyasheela, G.S. Srinivasan, O.P. Singh, KALDIS: A Computer Code System for Core Disruptive Accident Analysis of Fast

Reactors, Kalpakkam, 1999.

- [93] P. Mohanakrishnan, O.P. Singh, Eigenvalue Separation and Spatial Neutronic Coupling, 2000.
- [94] J.F. Jackson, R.B. Nicholson, VENUS-II: AN LMFBR DISASSEMBLY PROGRAM., Argonne, IL (United States), 1972. doi:10.2172/4578510.
- [95] M. Schneider, Fast breeder reactors in France, *Sci. Glob. Secur.* (2009). doi:10.1080/08929880902953013.
- [96] J.R. Matthews, M.H. Wood, Modelling the transient behaviour of fission gas, *J. Nucl. Mater.* 84 (1979) 125–136. doi:10.1016/0022-3115(79)90156-9.
- [97] A. Dubey, T. Sathiyasheela, A.K. Sharma, In-pin fuel motion dynamics for beginning-of-life core in fast breeder reactors, *Nucl. Eng. Des.* 347 (2019) 31–44. doi:10.1016/j.nucengdes.2019.03.014.
- [98] A. Dubey, A.K. Sharma, Modelling, verifications and safety feedback assessment of annular fast reactor fuel pins with severe accident code MITRA, *Nucl. Eng. Des.* 364 (2020) 110684. doi:10.1016/j.nucengdes.2020.110684.
- [99] A. Dubey, T. Sathiyasheela, A.K. Sharma, IHMTC2019-NSA-031 Modelling and Verifications of Fast Reactor Fuel Melting and Multi-phase Flow Code MITRA, in: *Proc. 25th Natl. 3rd Int. ISHMT-ASTFE Heat Mass Transf. Conf.*, Begel House Inc., 2019.
- [100] A. Dubey, T. Sathiyasheela, A.K. Sharma, Reactivity effects of in-pin fuel motion in modern fast breeder reactors, in: *Lect. Notes Mech. Eng.*, Pleiades Publishing, 2019: pp. 49–57. doi:10.1007/978-981-13-6577-5_6.
- [101] F.P. Incropera, D.P. DeWitt, T.L. Bergman, A.S. Lavine, Introduction to Conduction, *Fundam. Heat Mass Transf.* (2007).

- [102] S. V. Patankar, Numerical heat transfer and fluid flow., (1980).
doi:10.13182/nse81-a20112.
- [103] V. Voller, M. Cross, Accurate solutions of moving boundary problems using the enthalpy method, *Int. J. Heat Mass Transf.* (1981). doi:10.1016/0017-9310(81)90062-4.
- [104] V. Alexiades, A.D. Solomon, V.J. Lunardini, *Mathematical Modeling of Melting and Freezing Processes*, 1993.
doi:<https://doi.org/10.1201/9780203749449>.
- [105] I. Lunati, D. Or, Gravity-driven slug motion in capillary tubes, *Phys. Fluids.* (2009). doi:10.1063/1.3125262.
- [106] Y.A. Çengel, J.M. Cimbala, *Fluid Mechanics A Fundamental Approach*, 2018.
- [107] *Thermophysical Properties of Materials for Nuclear Engineering: A Tutorial and Collection of Data*, INTERNATIONAL ATOMIC ENERGY AGENCY, Vienna, 2009. <https://www.iaea.org/publications/7965/thermophysical-properties-of-materials-for-nuclear-engineering-a-tutorial-and-collection-of-data>.
- [108] N. Brauner, D.M. Maron, Identification of the range of ‘small diameters’ conduits, regarding two-phase flow pattern transitions, *Int. Commun. Heat Mass Transf.* 19 (1992) 29–39. doi:[https://doi.org/10.1016/0735-1933\(92\)90061-L](https://doi.org/10.1016/0735-1933(92)90061-L).
- [109] H. Ide, A. Kariyasaki, T. Fukano, Fundamental data on the gas–liquid two-phase flow in minichannels, *Int. J. Therm. Sci.* 46 (2007) 519–530.
doi:10.1016/J.IJTHEMALSCI.2006.07.012.
- [110] W. Breitung, K.O. Reil, *The Density and Compressibility of Liquid (U,Pu)-*

- Mixed Oxide, Nucl. Sci. Eng. 105 (1990) 205–217. doi:10.13182/NSE90-A19186.
- [111] M. Ramacciotti, C. Journeau, F. Sudreau, G. Cognet, Viscosity models for corium melts, Nucl. Eng. Des. (2001). doi:10.1016/S0029-5493(00)00328-9.
- [112] M.K. Hossain, Y. Himuro, K. Morita, K. Nakagawa, T. Matsumoto, K. Fukuda, W. Maschek, Simulation of molten metal penetration and freezing behavior in a seven-pin bundle experiment, J. Nucl. Sci. Technol. (2009). doi:10.1080/18811248.2007.9711588.
- [113] The SAS4A/SASSYS-1 Safety Analysis Code System, (2012). <https://www.osti.gov/servlets/purl/1231510>.
- [114] J.A. Boure, Constitutive equations for two-phase flows, (1974). https://inis.iaea.org/search/search.aspx?orig_q=RN:8281522 (accessed January 19, 2021).
- [115] N.I. Kolev, Multiphase flow dynamics 2: Mechanical interactions, 2012. doi:10.1007/978-3-642-20598-9.
- [116] J.B. Joshi, K. Nandakumar, A.W. Patwardhan, A.K. Nayak, V. Pareek, M. Gumulya, C. Wu, N. Minocha, E. Pal, M. Kumar, V. Bhusare, S. Tiwari, D. Lote, C. Mali, A. Kulkarni, S. Tamhankar, Computational fluid dynamics, in: Adv. Comput. Fluid Dyn. Nucl. React. Des. Saf. Assess., 2019. doi:10.1016/B978-0-08-102337-2.00002-X.
- [117] H.S. Isbin, One-dimensional two-phase flow, Graham B. Wallis, McGraw-Huill, New York (1969), AIChE J. 16 (1970) 896–1105. doi:10.1002/aic.690160603.
- [118] G. Dharmadurai, Acoustic Mismatch Theory for Heat Flow across Fuel-

- Cladding Interfaces in Fast Reactors., Nucl. Sci. Eng. (1983).
doi:10.13182/NSE83-A15455.
- [119] K.J. Miles, D.J. Hill, DEFORM-4: fuel pin characterization and transient response in the SAS4A accident analysis code system, (1986).
<https://www.osti.gov/scitech/biblio/5737020-deform-fuel-pin-characterization-transient-response-sas4a-accident-analysis-code-system> (accessed August 3, 2017).
- [120] A. Ross, R. Stoute, Heat transfer coefficient between UO₂ and Zircaloy-2, At. Energy Canada Ltd. (1962).
- [121] S. Song, M. Yovanovich, Correlation of thermal accommodation coefficient for engineering surfaces, 1 (1987) 107–116.
- [122] R. Courant, K. Friedrichs, H. Lewy, Über die partiellen Differenzgleichungen der mathematischen Physik, Math. Ann. 100 (1928) 32–74. doi:10.1007/BF01448839.
- [123] Y.-M. Kwon, H.-Y. Jeong, W.-P. Chang, C.-H. Cho, Y.-B. Lee, Control Rod Driveline Reactivity Feedback Model for Liquid Metal Reactors, (2008).
https://inis.iaea.org/search/search.aspx?orig_q=RN:39121525 (accessed January 20, 2021).
- [124] W. Breitung, K.O. Reil, Vapor pressure measurements on liquid uranium oxide and (U,Pu) mixed oxide, Nucl. Sci. Eng. 101 (1989) 26–40.
doi:10.13182/NSE89-A23592.
- [125] D.R. Olander, Fundamental aspects of nuclear reactor fuel elements, United States, 1976. doi:10.2172/7343826.
- [126] A. Karahan, J. Buongiorno, Modeling of thermo-mechanical and irradiation

- behavior of mixed oxide fuel for sodium fast reactors, *J. Nucl. Mater.* 396 (2010) 272–282. doi:10.1016/j.jnucmat.2009.11.021.
- [127] M.H. Wood, J.R. Matthews, A simple operational gas release and swelling model. I. Intragranular gas, *J. Nucl. Mater.* 91 (1980) 35–40. doi:10.1016/0022-3115(80)90029-X.
- [128] J.R. Matthews, M.H. Wood, A simple operational gas release and swelling model. II. Grain boundary gas, *J. Nucl. Mater.* 91 (1980) 241–256. doi:10.1016/0022-3115(80)90224-X.
- [129] L. Våth, Modelling fission gas behaviour in mixed oxide fuel under normal and off-normal conditions in fast reactors, *J. Nucl. Mater.* 188 (1992) 308–311. doi:10.1016/0022-3115(92)90489-8.
- [130] H. Zimmermann, Investigations on swelling and fission gas behaviour in uranium dioxide, *J. Nucl. Mater.* (1978). doi:10.1016/0022-3115(78)90039-9.
- [131] C.N. Venkiteswaran, V. V. Jayaraj, B.K. Ojha, V. Anandaraj, M. Padalakshmi, S. Vinodkumar, V. Karthik, R. Vijaykumar, A. Vijayaraghavan, R. Divakar, T. Johny, J. Joseph, S. Thirunavakkarasu, T. Saravanan, J. Philip, B.P.C. Rao, K. V. Kasiviswanathan, T. Jayakumar, Irradiation performance of PFBR MOX fuel after 112 GWd/t burn-up, *J. Nucl. Mater.* (2014). doi:10.1016/j.jnucmat.2014.01.045.
- [132] S. Latha, M.D. Mathew, P. Parameswaran, K. Bhanu Sankara Rao, S.L. Mannan, Thermal creep properties of alloy D9 stainless steel and 316 stainless steel fuel clad tubes, *Int. J. Press. Vessel. Pip.* 85 (2008) 866–870. doi:10.1016/j.ijpvp.2008.07.002.
- [133] F.B. Cheung, L. Baker, Transient Freezing of Liquids in Tube Flow, *Nucl. Sci.*

- Eng. 60 (1976) 1–9. doi:10.13182/NSE76-A26851.
- [134] J.K. Fink, Thermophysical properties of uranium dioxide, *J. Nucl. Mater.* (2000). doi:10.1016/S0022-3115(99)00273-1.
- [135] J.K. Fink, Enthalpy and heat capacity of the actinide oxides, *Int. J. Thermophys.* (1982). doi:10.1007/BF00503638.
- [136] E.H.P. Cordfunke, R.J.M. Konings, Thermochemical data for reactor materials and fission products: The ECN database, *J. Phase Equilibria.* (1993). doi:10.1007/BF02671964.
- [137] M.G.G. Adamson, E.A.A. Aitken, R.W.W. Caputi, Experimental and thermodynamic evaluation of the melting behavior of irradiated oxide fuels, *J. Nucl. Mater.* 130 (1985) 349–365. doi:10.1016/0022-3115(85)90323-X.
- [138] L. Leibowitz, R.A. Blomquist, Thermal conductivity and thermal expansion of stainless steels D9 and HT9, *Int. J. Thermophys.* (1988). doi:10.1007/BF00503252.
- [139] A. Banerjee, S. Raju, R. Divakar, E. Mohandas, G. Panneerselvam, M.P. Antony, Thermal property characterization of a titanium modified austenitic stainless steel (alloy D9), *J. Nucl. Mater.* 347 (2005) 20–30. doi:10.1016/j.jnucmat.2005.06.009.
- [140] J.R. Tallackson, Thermal transport properties of helium, helium--air mixtures, water, and tubing steel used in the CACHE program to compute HTGR auxiliary heat exchanger performance, (1976).
- [141]. International Atomic Energy Agency - IAEA, Thermophysical Properties of Materials for Water Cooled Reactors, 1997.